Monte Carlo investigations of a high resolution Small Field-Of-View gamma camera

Thesis submitted for the degree of
Doctor of Philosophy
at the University of Leicester

by

Bahadar S. Bhatia
Space Research Centre
Department of Physics & Astronomy
University of Leicester

May 2019

Declaration

The work described in this thesis is my own work. All sentences or passages quoted in this project dissertation from other people's work have been specifically acknowledged by clear cross referencing to author.

Name:	Bahadar S. Bhatia
Signed:	Bahadar Bhatia
Date:	29/05/2019

For Toshi and Nayan.

Abstract. **Monte Carlo investigations of a high resolution Small Field-Of-View gamma camera. Bahadar S. Bhatia.**

At the time of writing there have been no publications describing Monte Carlo simulations tracking low energy gamma and X-ray photons (less than 200 keV) through Small Field-Of-View (SFOV) photon detection systems. A literature search using the Web of Science (1970-2019) and Scopus (1960-2019) with the keywords "gamma, camera" AND "monte carlo" AND "small" OR "compact" showed 200 and 215 results respectively, but without any photon tracking studies. Two SFOV systems were modelled using PENELOPE v2008 Monte Carlo: the Portable Imaging X-ray Spectrometer detector, a pre-scintillator detector system for non-medical use, and a thallium doped caesium iodide scintillator based Compact Gamma Camera used for medical imaging. Each system uses an electron multiplying charge coupled device modelled as an 8 mm x 8 mm x 5 μm thick monolithic silicon detector. These simulations demonstrated the Fano-limited energy spectrum, and that the modelled fluorescence do not record some of the caesium and iodine K_α and K_β fluorescence photons if the source event originated closer to the boundary of the Monte Carlo accumulator. The corroborative experimental response of the PIXS detector using cadmium-109 showed broadening of the Ag K_α, K_β peaks, consistent with the energy resolution being broadened owing to incomplete charge collection, drift and transfer through the shift and gain registers, and also due to noise from the detector readout. As the distribution of photoelectrons from the EMCCD output is stochastic, a premise of distinguishing between zero and single photoelectron as an input, with thresholding using noise peak plus 5σ worked well for a gain potential difference Φ_{HV} between 33.5 V and 39.5 V, with the system cooled to 256.0 ± 0.1 K. Finally, a GEANT4 v10.5 simulation of caesium iodide crystal comprised of columns 100 μm x 100 μm x 1500 μm thick demonstrated a greater number of optical photons propagating by internal reflection to the 5 μm silicon detector, when laterally wrapped with 1 μm aluminium compared either to an unwrapped columnar crystal, laterally wrapped monolithic or unwrapped monolithic crystals.

Acknowledgements

I am sincerely grateful for the invaluable academic advice and mentoring provided throughout the production of thesis by Emeritus Professor John Lees, University of Leicester and Emeritus Professor Alan Perkins, University of Nottingham. Alongside them, I wish to thank both Dr Sarah Bugby and Dr Simon Lindsay, University of Leicester for their additional peer support throughout this work.

This research would have not been possible without the encouragement of Dr Adam Lovick, Dr Bill Thomson and Jonathan Walters, all at Sandwell & West Birmingham NHS Trust.

I am grateful to have worked within the professional environment of the Space Research Centre with colleagues Dr Mohammed Alqahtani, Dr Steve Leach, and in particular for the technical support provided by Bill McKnight in the Bioimaging laboratory.

Finally I am grateful for the review and guidance provided by Professor Mark Sims, University of Leicester and Professor Spyros Manolopoulos, University College London.

Contents

List of Tables

List of Figures

Nomenclature

ADU	Analogue to Digital Unit
Aluminium	Aluminium-13
Caesium	Caesium-55
CCD	Charge Coupled Device
CGC	Compact Gamma Camera (University of Leicester)
CTE	Charge Transfer Efficiency
EANM	European Association of Nuclear Medicine
EMCCD	Electron Multiplying Charge Coupled Device
ERF	Edge Response Function
EURATOM	European Atomic Energy Community
FOM	Figure Of Merit
FWTM	Full-Width Tenth-Maximum
GFOV	Geometric Field Of View
IEC	International Electrotechnical Commission
Iodine	Iodine-53

IPEM	Institute of Physics and Engineering in Medicine
Lead	Lead-82
LFOV	Large Field-Of-View
LSF	Line Spread Function
NEMA	National Electrical Manufacturers' Association
PIXS	Portable Imaging X-ray Spectrometer detector (University of Leicester)
PLES	Parallel Line Equal Spacing
PSF	Point Spread Function
PSPMT	Position Sensitive Photo-Multiplier Tube
SFOV	Small Field-Of-View
Silicon	Silicon-14
SPAD	Single Photon Avalanche Diode
TCAD	Technology Computer Aided Design
Tungsten	Tungsten-74
UFOV	Useful Field-Of-View
VOV	Variance Of the Variance
Z	Atomic Number

Introduction

This thesis describes the systematic investigation of two Small Field-Of-View (SFOV) low energy photon detection systems (less than 200 keV) developed at the University of Leicester using Monte Carlo simulations - the first was a pre-scintillator silicon detector called the Portable Imaging X-ray Spectrometer detector [PIXS detector], and the second, a scintillator based silicon detector called the Compact Gamma Camera [CGC]. The CGC was designed for clinical imaging in nuclear medicine and contains the same silicon detector as the PIXS detector, but in addition has a columnar caesium iodide crystal and front-end tungsten collimator. The CGC design allows it to image scintillation photons created by the passage of gamma photons transmitted through the collimator into the caesium iodide crystal.

In this work Monte Carlo modelling was used to understand and predict the underlying physics as impinging gamma photons transport through these SFOV systems. These methods are powerful because they can be used to investigate different physical processes independently, and used to track photon transport using different materials and geometries; such an approach may not easily be translated into an experiment, would be costly and would be beneficial to avoid design errors before construction. These simulations were a first step towards more refined modelling described in the chapter on future work. Nonetheless they were performed using the University of Leicester ALICE computing cluster across an array of compute nodes. The array processing was used to perform simultaneous calculations across several CPUs within each compute node. Such an approach meant that the simulations were able to compute all the desired characteristics of the models. This applied research was used to understand the design of the current SFOV gamma camera and inform its development in order to improve its capability for clinical imaging.

The first chapter establishes the clinical context for use of such a medical device. As an aid to the subsequent corpus, Chapter 2 summarises the physics used in this thesis including photon interactions, fluorescence, sources of noise within an electron multiplying charge coupled device (EMCCD - a type of solid state detector), scintillator crystals, Monte Carlo simulations and an analytical model of a detector without a scintillator used for corroboration later in chapter 5.

The subsequent chapters 3 to 4 discuss several PENELOPE v2008 [Salvat et al., 2011] Monte Carlo investigations which were used to describe simulations of the transport of photons in various intervening materials used within the aforesaid SFOV systems. The key elements of a Monte Carlo computation require: a probability distribution function describing the physics of the photon interactions; a random number generator used to guide the tracking of the photon through the material; and a virtual accumulator recording the measured response. In Monte Carlo photon interaction events can be tracked like particle interactions whereas the physics of the photon interactions may require de Broglie wave properties to describe them. PENELOPE v2008 [Salvat et al., 2011] does not model the effect of scintillation photons nor detector noise. Chapter 3 describes Monte Carlo simulations used to determine the distribution of energy deposited within a silicon detector (representative of the PIXS detector) owing to impinging gamma photons and to determine its impact on the energy resolution. The detector efficiency as a function of energy deposited within the modelled CGC for a point source was also simulated. All Monte Carlo simulations require software development rather than just being off-the-shelf, and used the ALICE High Performance Computing facility at the University of Leicester.

A systematic approach was used to investigate the underlying physics as gamma and X-ray photons transport through the materials used within the camera, assisting with future designs. These are described in chapter 4, within which the distribution of energy deposited within caesium iodide was determined, and the fluence of photons from caesium iodide assessed. These fluence photons were then tracked to establish the energy deposited within a silicon detector.

It is important to corroborate findings where possible, either by experiment or by analytical means. In chapter 5 experimental responses were obtained using cadmium-109 and americium-241 sources in order to calibrate a bare silicon PIXS detector (without the scintillator being present). As an experimental design may be costly and time consuming to build, an alternative approach is to use an analytical calculation to describe the expected response of the PIXS detector for a given radionuclide. An analytical model of the expected response using a bare silicon detector was derived and used to compare against a PENELOPE Monte Carlo simulation using a cadmium-109 source. The final part of this chapter evaluated the amount of pixel charge sharing for incident events amongst the EMCCD pixel array.

The penultimate chapter addresses the optical photons generated by the scintillator using the Monte Carlo code GEANT4 v10.4 [Agostinelli et al., 2003]. This optical photon Monte Carlo transport code includes optical photon interactions at a boundary and is governed by Fresnel reflection into the same medium or Fresnel refraction into another medium. The simulation of each optical photon stops when either it is absorbed, escapes from any intervening medium or is impacting on the silicon detector. Chapter 6 investigates the transport of optical photons and this is used to assess its impact on performance parameters.

The last chapter 7 describes a baseline protocol for the clinical evaluation of SFOV gamma cameras in the absence of any previous schema [Bhatia et al., 2015]; experimental results obtained using this protocol are described elsewhere, [Bugby et al., 2014]. A summary of key findings and direction for future work completes the thesis.

Chapter 1

Clinical context and current imaging technology in nuclear medicine

1.1 Nuclear Medicine

In nuclear medicine the physiological function of an organ can be imaged by administrating a radiolabelled pharmaceutical either intravenously, intra-dermally, orally, by inhalation or by placement intra-cavity, and collecting the photons emitted from its distribution within the patient with a suitable detector system. The pharmaceutical component is chosen to follow the physiological process within the organ being imaged and for gamma camera imaging is usually labelled with technetium-99m. This radionuclide has a physical half-life of 6.02 hours and peak photon energy of 140.5 keV, and is chosen because as well as the being able to label the pharmaceutical, it results in a low effective dose and has a short physical half-life. These photons are either photoabsorbed, Compton scattered or Rayleigh scattered. These photopeak and scattered photons may be imaged by a Large Field-Of-View

(LFOV) Anger camera, [Anger, 1957], which usually consists of a lead collimated thallium-81 doped sodium iodide crystal coupled to an array of photomultiplier tubes. The image is reconstructed through appropriate digital processing of the photomultiplier outputs, and through iterative reconstruction software using detector profiles which are the counts detected at each polar angle. The capability of the imaging system to resolve the distribution of radioactivity depends upon the collection of these photons emitted from the patient (sensitivity), response of the detector to the energy of the photons (energy resolution), ability to accept photons as distinct events (count-rate capability), and the ability to spatially resolve adjacent areas of radioactivity as being distinct (spatial resolution). For current commercial Large Field-Of-View gamma cameras the system spatial resolution is about 10 mm, so imaging has limitations with regards to the detection of smaller tumorous lesions which for example may require surgical assessment. An important adjunct to imaging is in the use of non-imaging hand-held detectors to identify tumorous lesions of dimensions less than about 10 mm. These non-imaging hand-held detectors are called gamma probes and are often used to detect sentinel lymph nodes to allow the surgeon to biopsy and refer to histological assessment. This technique is known as radio-guided surgery and is important because it mitigates against complete excision of the affected tissue so reducing this risk of associative co-morbidity for the patient. However, there are limitations to using non-imaging hand-held detectors, for example their narrow field-of-view and poor spatial resolution at depth may cause the surgeon to miss deep seated lesions, or those near injection sites or nearby regions of high background activity, [Benjegard et al., 1999]. The following sections introduce radio-guided surgery using gamma probes, and Small Field-Of-View gamma photon imaging systems employing scintillators and solid state devices.

1.2 Radio-guided surgery

The preferential properties of a single photon counting gamma ray detector with sub-millimetre intrinsic resolution has important clinical use in radionuclide guided surgery, [Perkins and Hardy, 1996]. An essential feature is the need to detect and localise any small suspect lesions transcutaneously – as such a non-imaging gamma probe should be non-obtrusive, ergonomic and designed for the surgical approach and clinical need in mind, [Kotzassarlidou et al., 2004]. The gamma probe is essentially a gamma photon detector on a stem and shielded from extraneous photon scatter. The surgeon uses the gamma probe to detect and localise a suspect lesion using an audible bleep emitted by the gamma probe at sites of increased count-rates (called a "hot" lesion) above a user selected threshold. There are various designs of gamma probes specific to the clinical requirements and examples of available intra-operative gamma probes at the time of publication include:

- "C-Trak" Carewise
- "Neoprobe" Mammotome, and
- "Node Seeker" Intramedical.

High spatial resolution ensures that where hot lesions are close to each other, then they can be adequately separated and localised. An example of this is where the surgeon wishes to identify the sentinel lymph node in breast cancer patients where the radionuclide colloid injection is close to the lymphatic drainage basin. The requirement to discriminate against scattering means that the gamma probe should have good shielding and good energy resolution. Scattered photons which are detected add to background counts. Good temporal resolution ensures that detected responses are discriminated as single events within the counting duration. It is desirable to have a linear response between energy and count-rate. The dose limit to the patient and the operator aside from detection threshold also influences the sensitivity of a gamma probe. These factors all influence the design of the gamma probe but overall clinical requirements should be the main factor. For example, sensitivity is also important in detecting sentinel lymph nodes where there are often low count-rates and where there might be deep lesions which could be potentially missed. A comparative study of the designs of various non-imaging gamma probes was performed by Benjegard et al. [1999] who evaluated the detection of indium-111 octreotide hot lesions within a phantom. They found that their thallium-81 doped sodium iodide detector (8.2 mm diameter, 16 mm thick crystal) was better suited for identifying deep seated tumours than a cadmium telluride detector (4 mm diameter, 1 mm thick crystal) owing to its larger interaction cross-section. However the cadmium telluride detector performed better with superficial tumours as it has both higher spatial resolution and energy resolution. In the case of radio-guided parathyroidectomy high spatial resolution is the dominant requirement, [Rubello and Mariani, 2007, Rubello et al., 2007, Ortega et al., 2007a,b]. In this case tissue adjacent to the parathyroid adenoma often incorporates high radioactivity. Since background count-rates are higher than in sentinel lymph node staging, the gamma probe design should have thick collimation and adequate shielding to discriminate this.

The use of gamma probes is now advocated for several clinical areas [Povoski et al., 2009]. Hayashi et al. [2003] used a combined blue dye tracking and gamma probe for the localisation of gastric sentinel lymph node. Surgeons use blue dye to stain the lymphatic system to help isolate lymph nodes. Although the dual technique identified sentinel lymph nodes with high sensitivity, this study showed that there were significant differences in the distribution of blue dye and hot lesions. They concluded that radio-guided surgery should only be undertaken with blue dye tracking technique. Takeuchi et al. [2009] evaluated seventy five patients with primary oesophageal cancer with early stage tumour (grades T1N0M0 or T2N0M0)[1]. Trial patients were injected with technetium-99m colloid via an endoscope. Sentinel lymph nodes were successfully identified pre-operatively with lymphoscintigraphy (which is imaging of the distribution of administered radioactivity within the lymphatic system) and a gamma probe with diagnostic accuracy of 94%. Schilling et al. [2010] enrolled 463 patients in a study with histological proven prostate cancer. technetium-99m colloid was injected into the prostate under trans-rectal ultrasound guidance. As routine practice all lymph nodes with grades T3+Nx in the obturator fossa are dissected. However additional lymph nodes were identified by a gamma probe and in more than half the cases outside the obturator fossa. Terwisscha Van Scheltinga et al. [2006] evaluated 56 patients with colon carcinoma by sub-serosal injection of radio-colloid around the tumour site. Sentinel nodes were excised and their histological slides examined. The overall accuracy in combination with blue dye was 95.6%.

1.3 SFOV gamma cameras

Although radio-guided surgery with gamma probes is prevalent there is clinical requirement to improve sensitivity and the false negative rate, [Heller and Zanzonico, 2011]. Some sentinel nodes may be missed owing to the position of the sentinel nodes, which may be deep in tissue or near to injection sites or areas of increased uptake. The need for a compact device with good energy resolution is important in the clinical imaging of tumours and sentinel nodes, [Duch, 2011, Hruska et al., 2005, Ruano et al., 2008, Rubello and Mariani, 2007, Vermeeren et al., 2009, Vidal-Sicart et al., 2011]. The limitations of gamma probe which has a narrow field-of-view and may have insufficient collection of

[1]T0 to T4 represent tumours of increasing size with T0 as no palpable tumour, T1$<$2 cm and 2$<$T2$\leq$5 cm; N0 are no palpable lymph nodes; M0 are no clinically apparent metastases.

audible counts above a pre-selected threshold should be mitigated; indeed the surgeon can also benefit by rapidly review any areas of concern through imaging. The use of high resolution SFOV hand-held gamma cameras to provide dynamic images addresses some of the limitations of gamma probes and indeed their development has enabled imaging procedures to be undertaken at the bedside, within intensive care units, clinics and in the operating theatres, [Perkins and Hardy, 1996, Duch, 2011].

There are various designs of Small Field-Of-View (SFOV) gamma cameras which may use:

- Scintillators (these have high atomic number (Z), thick crystals but generally poor energy resolution) coupled to various types of solid state detectors
- Or solid state detectors alone such as cadmium zinc telluride (these have high Z, thin crystals and generally good energy resolution).

Some examples of typical performance parameters for two SFOV gamma cameras, one for the scintillator based silicon detector called the Compact Gamma Camera [CGC] and the other using a cadmium telluride solid state detector alone called the Solid State Gamma Camera [SSGC] are shown in Table 1.1.

	Solid State Gamma Camera	Compact Gamma Camera
	[Tsuchimochi and Hayama, 2013]	[Bugby et al., 2014]
System Spatial Resolution	6.8 mm FWHM at 100 mm away from camera face. High resolution parallel hole collimator	1.21 mm FWHM at 10 mm away from camera face (non-magnifying point). 0.5 mm pinhole collimator
System Sensitivity	150 counts.s^{-1}MBq^{-1} at the camera face. High resolution parallel hole collimator	214 counts.s^{-1}MBq^{-1} at the camera face. 0.5 mm pinhole collimator
Energy Resolution (at 140.5 keV)	6.9%	58%

Table 1.1: Typical performance parameters for two SFOV gamma cameras, one for the scintillator based silicon detector called the Compact Gamma Camera and the other using a cadmium telluride solid state detector alone called the Solid State Gamma Camera.

The drawback of using a scintillator with a solid state detector is that its energy resolution may be poor due to light collection losses from the scintillator and losses between the scintillator and solid state detector interface as shown in Table 1.1.

Often solid state detector based gamma cameras employ one or more pinhole collimators to increase the field-of-view since the detector has a small active area [Have and Beekman, 2004]. Several groups have reported designs for SFOV gamma cameras with high spatial resolution and low cost relative to LFOV gamma cameras that allow imaging for specific applications such as tumour resection and sentinel node localisation. Examples of designs are summarised in Table 1.2. These systems combine the advantages but also address some of the limitations of both LFOV gamma cameras and hand held gamma probes.

Although using a solid state detector alone has a better intrinsic spatial resolution and energy resolution compared to LFOV gamma cameras, it has much lower sensitivity and a front end scintillator may be used to improve sensitivity (since it has a high stopping power for incident gamma photons). Comparative results for the SFOV (Compact Gamma Camera) [Bugby et al., 2014] and for an example LFOV gamma camera (Siemens Ecam) from literature [Baechler et al., 2003] are shown later in Table 7.1.

Design of SFOV gamma camera	Reference
scintillators coupled to multi-anode PSPMT	[Williams et al., 2000, Porras et al., 2002, Garibaldi et al., 2003, Kieper et al., 2003, Sánchez et al., 2004, Trotta et al., 2007, Ferretti et al., 2013, Olcott et al., 2014];
scintillators coupled to SPAD-based PSPMT	[Yamamoto et al., 2011, Dinu et al., 2015, Massari et al., 2016]
scintillators coupled to an EMCCD	[de Vree et al., 2005, Lees et al., 2011];
cadmium (zinc) telluride detector	[Abe et al., 2003, Tsuchimochi et al., 2003, Gal et al., 2006, Wilson et al., 2010, Veale et al., 2012, Scuffham et al., 2012];

Table 1.2: Designs of SFOV gamma cameras

A current commercial application at the time of writing is the high resolution SFOV gamma camera called the Sentinella [Oncovision]. Its use has assisted several clinical studies which has included: sentinel node detection in breast cancer [Ghosh et al., 2017]; this study identified additional nodes missed by a gamma probe; the identification of non palpable invasive breast cancer [Lombardi et al., 2015] and the reliable identification of melanoma [Riccardi et al., 2015]. The next sections describe some of the types of solid state detectors used in SFOV gamma cameras at the time of publication.

1.4 SPAD-Based Silicon Position Sensitive Photomultipler

When a reverse bias voltage is applied to a silicon p-n junction an $\mathbf{E}-$field across the depletion layer accelerates any charge carriers generated by an incident photon. With a sufficiently high electric field within the depletion layer of $> 5 \times 10^5$ Vcm^{-1} these charge carriers will be accelerated to create secondary charge pairs through impact ionisation. A photodiode which operates in this Geiger mode with high gain is called a Single Photon Avalanche Diode (SPAD). Once the reverse bias approaches its nominal breakdown potential difference the device is quenched using a series resistor which limits the current drawn by the photodiode. The photodiode then returns to Geiger mode through the high $\mathbf{E}-$field. The SPAD therefore produces a signal which is independent of the number of incident photons impinging the device. However, if an array of several independent SPADs is used then this device is position sensitive because each photon interaction within an individual SPAD generates an independent spatial signal. This array is known as a modern silicon position sensitive photomultiplier[2]. An older type of position sensitive photomultiplier employs a multi-anode photomultiplier which is not discussed in this work. A schematic is shown in Figure 1.1 with an additional fast output node to the cathode and anode which has a nominally lower capacitance. This signal is used to trigger the arrival time of the first impinging photon. A detector system with high spatial resolution and comparable energy resolution to a conventional LFOV gamma camera is a PSPMT coupled to a scintillator. However, such a gamma camera system will require correction of both spatial uniformity and spatial distortion across its field-of-view owing to the non-uniformity in response of the SPADs across the photomultiplier.

[2] Hamamatsu-Photonics use the term multi-pixel photon counter [MPPC] for their commercial silicon position sensitive photomultipliers.

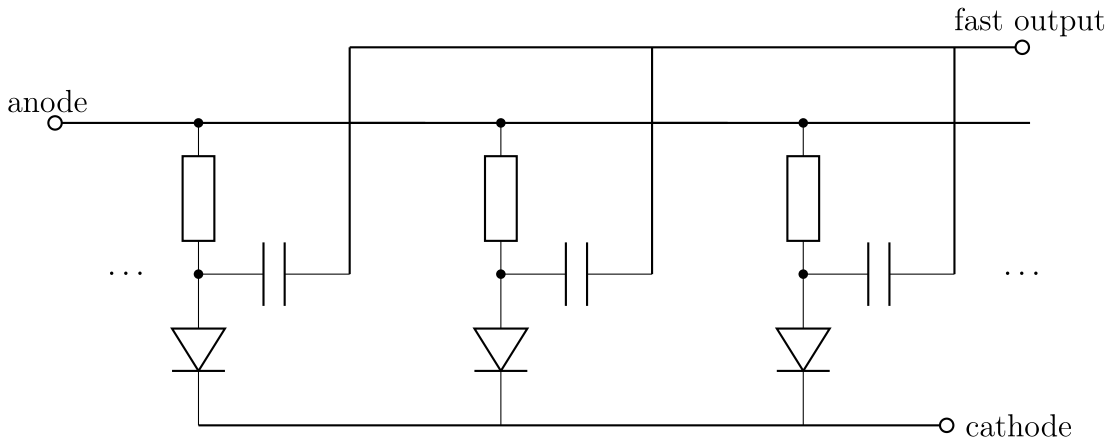

Figure 1.1: Schematic of a row segment of a silicon position sensitive photomultiplier

1.5 The Electron Multiplying Charge Coupled Device

In this work the detector used in our two SFOV systems is the e2v CCD97-00 back illuminated Electron Multiplying Charge Coupled Device (EMCCD) [e2vTechnologies, 2004]. Its choice was determined by its large signal to noise ratio and high spatial resolution. In the case of nuclear medicine, a scintillator is needed to create optical photons as described in section 2.4. When incident photons interact in the image area of a charge coupled device (CCD), electron holes pairs are created. Any accumulated charge is then transferred to the storage area of the CCD and then transferred vertically, line by line to the horizontal shift register onto the output amplifier as shown in Figure 1.2.

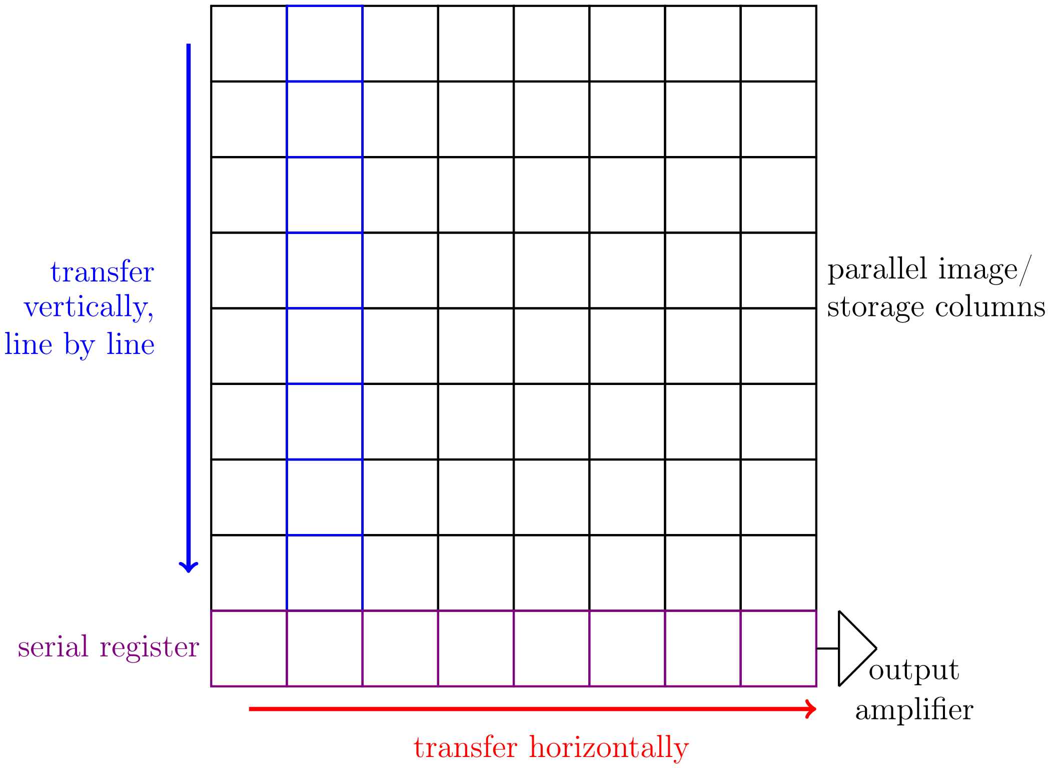

Figure 1.2: The transfer of accumulated charge from the storage area of the CCD vertically, line by line to the horizontal serial register onto the output amplifier.

In an electron multiplying charge coupled device, the shift register is extended with an additional horizontal gain register. Within this gain register there are three potential difference phases designated ϕ_1, ϕ_2, ϕ_3 which transfer the charge clocked across from the shift and across the gain register as shown for a single stage in Figure 1.3.

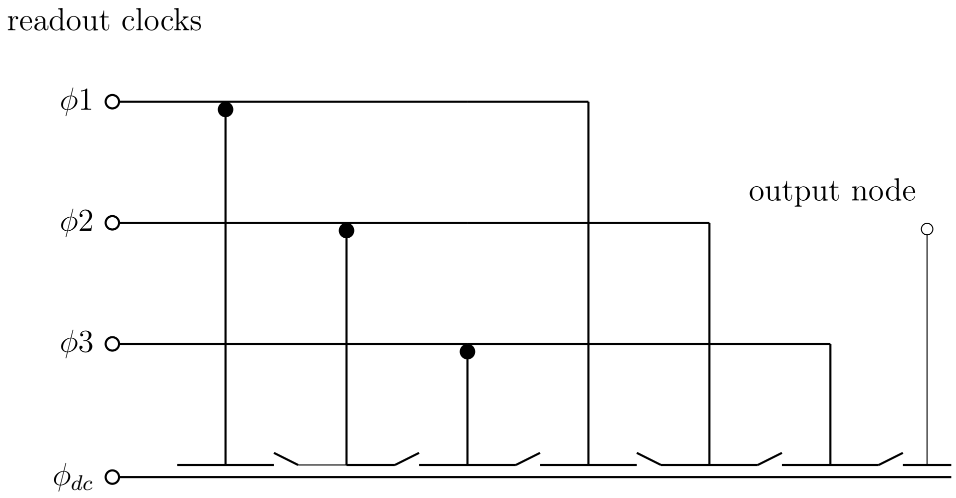

Figure 1.3: Schematic of a single stage comprising of three clock phases and a dc biased phase

A gain potential difference Φ_{HV} is established between ϕ_2 and ϕ_{dc} typically between 35 V to 60 V. The charge collected under ϕ_1 is then clocked over the ϕ_{dc} into the high potential difference. This accelerates the electrons in the gain register creating impact ionisation. The charge collected under ϕ_1 is then clocked out into the next stage through ϕ_3. Since a large signal is achieved relative to the readout noise large this provides a large signal to noise ratio [Tutt et al., 2013]. This effective readout noise is less than one electron r.m.s. relative to the input signal (before the amplifier stage). The variation of the gain of the EMCCD with its gain potential difference Φ_{HV} is demonstrated later in section 5.2.2.

During the process of the transfer of charge through the shift register and gain register, if the charge does not translate through part of either register it may be associated with the signal collected from another pixel. Although this charge transfer efficiency is almost unity, over several hundreds of cycles it will cause charge spreading over adjacent pixels; this is discussed in chapter 5.

At high gains the readout noise is also increased but this is counteracted by the large gain in signal. With an EMCCD operating at 10 frames per second, images of photon events may be detected such that individual photon events can be spatially resolved and their energy deposition determined [Heemskerk et al., 2007]. Thus the EMCCD acts as a photon counter and uses specific thresholding of the output signal. As the distribution of photoelectrons from the amplifier of the EMCCD is stochastic, a thresholding scheme of using noise peak plus 5σ is used for gain potential difference Φ_{HV} between 33.5 V and 39.5 V, discussed in chapter 5. This thresholding scheme is only valid for low input photon flux [Basden et al., 2003] due to pile-up at high count rates. The e2v CCD97-00 has 512 lines with 512 pixels, covering an active area of 8.192 mm by 8.192 mm. The intrinsic spatial resolution as described in chapter 7 is determined by the on-chip binning which provides pixels of size 64 μm by 64 μm covering the active area of 8.192 mm by 8.192 mm, [Lees et al., 2011]. So the best intrinsic spatial resolution this detector can achieve is 128 μm. The e2v CCD97-00 is a back illuminated EMCCD, such that incident photons are directly absorbed into the depletion layer where the charge cloud can be detected. This design differs from a front illuminated EMCCD where the polysilicon gates on the front of the device (which define the charge wells at each pixel) reduce the quantum efficiency of the device. The back illuminated EMCCD is also back thinned to 10 μm thickness so that photons are incident directly onto the depletion region of the EMCCD without the gate structure impeding. The temporal resolution is determined by the readout and clock speed, both of which create noise in the detection process.

Chapter 2

Theory

This chapter summarises the background physics used in subsequent chapters covering photon interactions, fluorescence, the Electron Multiplying Charge Coupled Device (EMCCD) used in this work (e2v CCD97-00 [e2vTechnologies, 2004]) and inorganic scintillators. In the absence of a scintillator, sources of noise within the EMCCD and the factors affecting the energy resolution are also discussed. Monte Carlo codes are also described and the selected one was used to construct two models of SFOV systems called the Portable Imaging X-ray Spectrometer detector [PIXS detector], and the Compact Gamma Camera [CGC]. It is good practice to corroborate Monte Carlo simulation either with experiment (if possible) or by analytical means; thus, in order to assist with validation an analytical model is described for a bare silicon detector.

2.1 Photon Interactions

In this work photon interactions used in the Monte Carlo simulation are photoabsorption, Compton (incoherent) scattering and Rayleigh (coherent) scattering. Pair production is not relevant for this work as the photon energy threshold for this to occur is 511 keV which is outside the range of energies detectable by the SFOV systems considered. For incident photons of energy

511 keV using 5 μm thick silicon with a linear attenuation coefficient of μ_{Si}= 5.0095x 10^{-1} cm^{-1}, the interaction probability $\ll$ 1%.

In photoabsorption the incident photon is absorbed by an individual electron and this photoelectron is ejected with a kinetic energy equal to the incident photon energy less its binding energy in the target atom [Krane, 1988]. For low energy incident gamma photons in the energy range 20 keV to 200 keV, the photoelectron tends towards the direction $\pi/3$ radians to $\pi/6$ radians respectively to the $\mathbf{E}-$field for the incident photon [Meyerhof, 1967]. The probability for photoabsorption is greater for K-shell where electrons are more tightly bound, and greater for lower incident energies (above the K-shell binding energy). Equation 2.1 shows the relationship between the incident energy E_0 and atomic number Z for the partial photon mass attenuation coefficient for photoabsorption μ_{photo}

$$\mu_{photo} \propto \left(\frac{Z^{(4-4.8)}}{{E_0}^3} \right) \tag{2.1}$$

In Compton or incoherent scattering, the incident photon interacts with a weakly bound electron in the scattering atom which then emits the secondary photon in a different direction to the incident photon with less energy; the freed electron is ejected with a kinetic energy equal to the incident photon energy less the sum of the electron binding energy and the energy of the secondary photon [Krane, 1988]. The Compton scattered photons have energy E_γ given by Equation 2.2

$$E_\gamma = \frac{E_0}{1 + E_0/m_0c^2(1 - \cos\,\theta)} \tag{2.2}$$

where E_0 is incident gamma photon energy, m_0c^2 is the rest mass of the target electron and θ is the scattering angle of the Compton scattered photon relative to the direction of the impinging photon. For example with gamma photons of energy E_γ= 150 keV with direction θ= 0 radians, Figure 2.1 shows the Klein-Nishina angular distribution function per steradian per electron. Large peaks are seen at θ= 0 radians and at θ= 2π. There is a small peak at θ= π radians (back-scattered photon) and this is more pronounced with increasing impinging gamma photon energy.

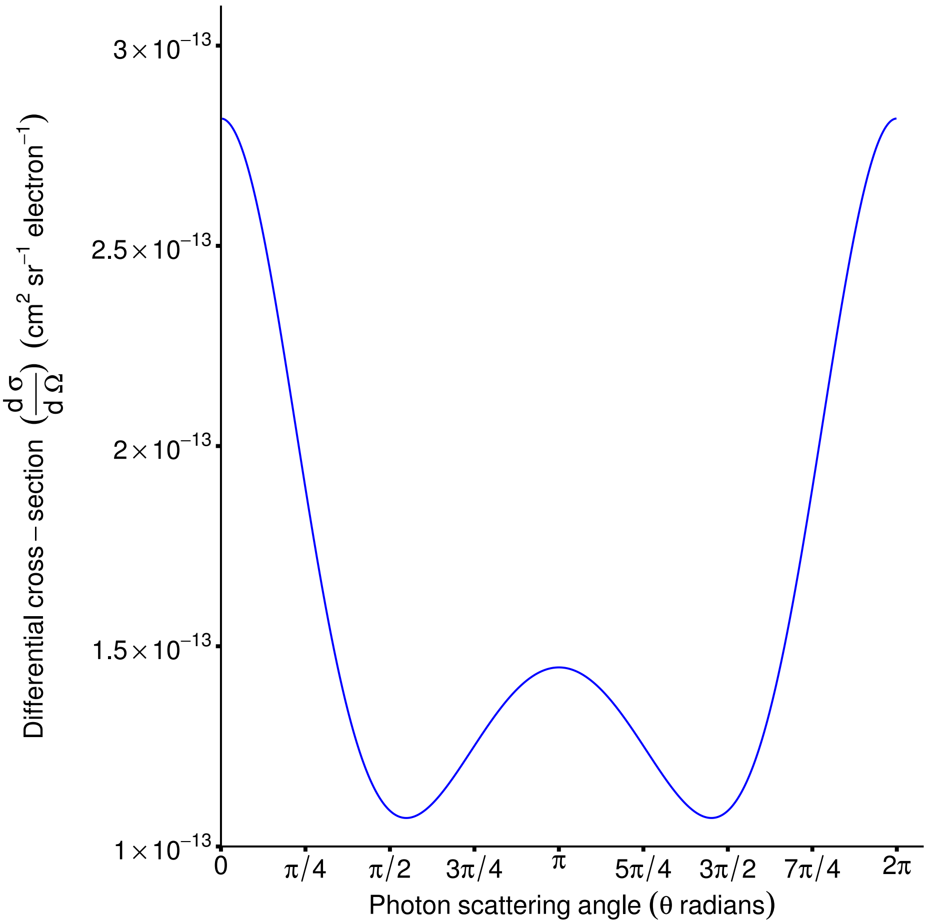

Figure 2.1: Klein-Nishina angular distribution function per steradian per electron for impinging gamma photons of energy E_γ=150 keV and θ is the scattering angle of the Compton scattered photon relative to the direction of the impinging photon.

In Rayleigh scattering the incident photons interfere coherently with the scattered photon field from the oscillation of the charge distribution of electrons. So the energy of the scattered photon energy is the same as the incident photon energy, and the target atom is not excited. Thus the bound electrons absorb energy from the incident beam of photons.

The partial photon mass attenuation coefficients for these interactions is given by Equation 2.3

$$\mu_i = N\kappa_i \tag{2.3}$$

where μ_i is the partial photon mass attenuation coefficient for $i=$ photoabsorption, Compton scattering or Rayleigh scattering, N is the number of atoms or molecules per unit volume and κ_i is the atomic or molecular cross section for that process i. The response of silicon can be considered in the context of its partial mass attenuation coefficients as shown in Figure 2.2 with the dominant interaction at energies less than less than 70 keV within silicon being photoabsorption, and Compton scatter between 80 keV to 200 keV. μ_i are the partial attenuation coefficients and ρ the target density. Note the binding energy in the target atom causes the edges in the photoabsorption curve. The Rayleigh scattering differential cross-section $d\sigma/d\Omega_{Ra}$ may be considered to be due to the product of the Thomson elastic scattering photon cross-section $d\sigma/d\Omega_T$ and a correction factor called the atomic form factor $f(q, Z)$ as Equation 2.4

$$\frac{d\sigma}{d\Omega_{Ra}} = \frac{d\sigma}{d\Omega_T}.|f(q, Z)|^2 \tag{2.4}$$

where $\hbar q$ is the momentum transferred to the atom when the incoming photon is scattered. The atomic form factor contains energy dependent real and imaginary anomalous scattering factors. For Rayleigh scattering the coherent differential cross-section includes the effect of this complex quantity around the absorption edge of the scattering called the “anomalous” scattering factor, [Salvat et al., 2011]. This is shown as an indent to the Rayleigh scattering curve.

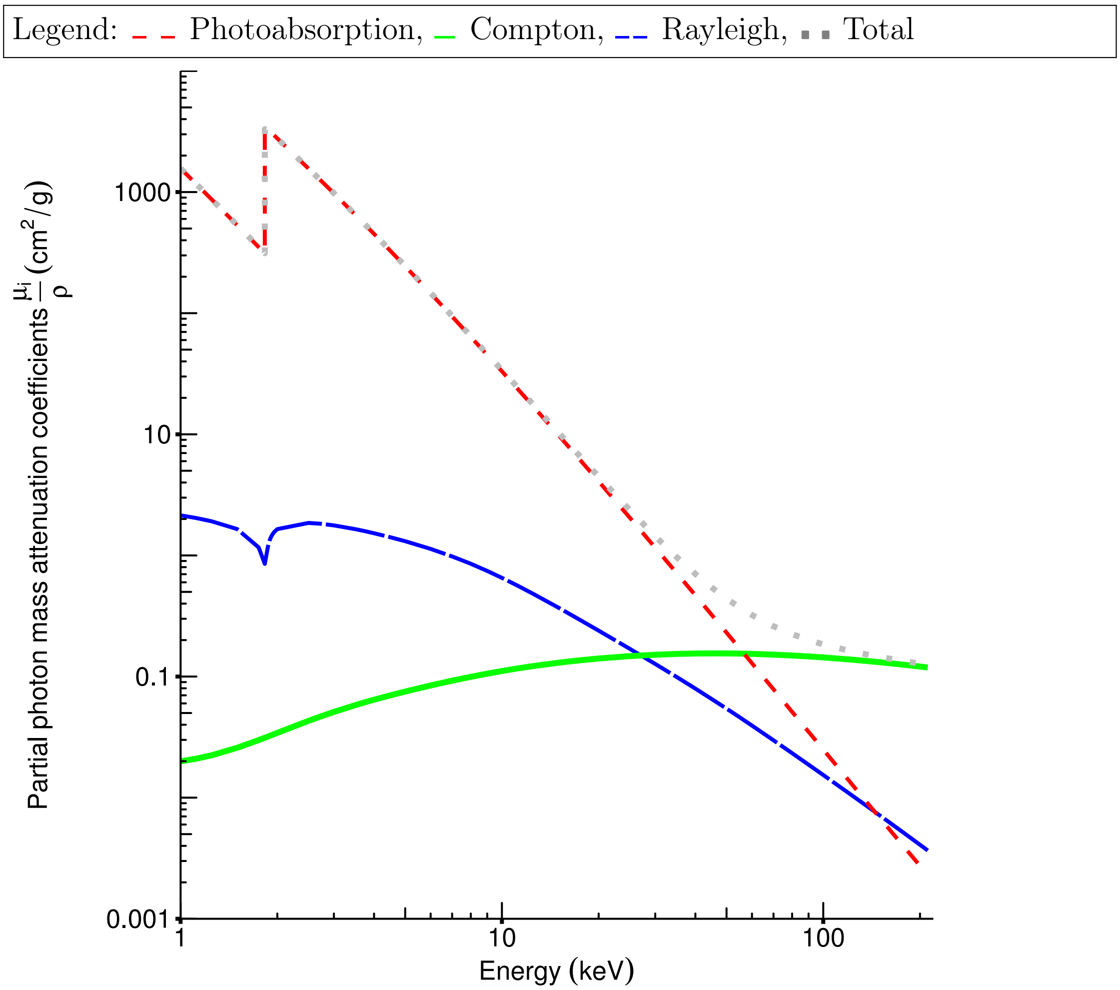

Figure 2.2: Partial photon mass attenuation coefficients μ_i with $i=$ photoabsorption, Compton scattering or Rayleigh scattering and ρ the target density for silicon up to 200 keV generated using PENELOPE

2.2 Fluorescence

Within each target materials' atoms the electrons occupy discrete energy levels which are designated as $K, L_1, L_2, L_3, M_1, \ldots, M_5, N_1, \ldots, N_7, \ldots$. When an electron is removed from a given energy level by an incident photon interaction or particle interaction, a vacancy is created in its energy level. This vacancy is then filled by an electron from an outer energy level with the energy difference between the binding energy of these energy levels creating a fluorescence X-ray or leading to Auger electrons. For example if an electron in the K energy level is removed by some interaction by a source photon or source particle, and this vacancy is filled by an electron from the L_3 energy level then the X-ray emitted is designated as $K_{\alpha 1}$. Where outer electrons fill vacancies in the K energy level, the X-rays emitted are designated as K series X-rays; similarly for electrons filling vacancies in the L energy level, the X-rays emitted are designated as L series X-rays. The major K series and L series X-rays are shown in Figure 2.3 with the energy levels dependent on the target material used.

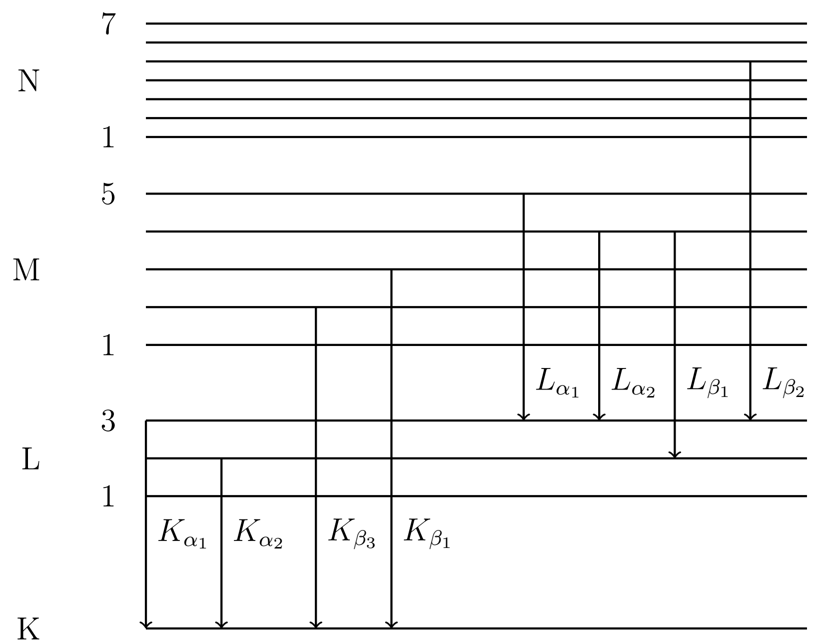

Figure 2.3: Major K series and L series fluorescence X-rays

2.3 Noise in the EMCCD

This noise can be considered to be comprised of two components - one which is inherent called dark current and the second due to sources of noise within the charge collection and electronics detection chain, [Zhang et al., 2009].

2.3.1 Dark Current noise

Within a silicon detector dark current noise occurs from surface states, from interface states between the valence and conduction band, and from the bulk of the depletion layer [Inglesfield, 1982]. Crystal imperfections and impurities creates interface states between the valence and the conduction band which provide a pathway for electrons with sufficient thermal energy to progress into the conduction band.

The dark current from surface states can be reduced by using a technique called inverted mode which creates a layer of holes between the surface and collection well. In an individual pixel three electrodes are used with one used as the charge collection well, and the other two electrodes inverted which creates a layer of holes between the surface and collection well. Any thermally excited electrons will recombine with this layer of holes rather than progressing into the collection well. This technique is used in the e2v CCD97-00 back illuminated EMCCD [e2vTechnologies, 2004] and used within our two SFOV systems. The dark current from surface states may also be reduced using chemical surface passivation of the silicon dioxide layer [Dong et al., 2015].

Dark current, I_D varies with temperature according to Equation 2.5, [Burt and Morcom, 1987]

$$I_D \propto \exp\left(\frac{-V_{bg}}{2kT/e}\right) \tag{2.5}$$

where V_{bg} is the band gap of silicon and e is the magnitude of the electron charge. Any localised inhomogeneities in the EMCCD will create fixed pattern noise which affects the uniformity in response across the detector. For the e2v CCD97-00 back illuminated EMCCD the dark noise is of the order of 400 electrons per pixel per second with each pixel size of 16 µm x 16 µm at a temperature of 293 K, cooling an EMCCD with a thermoelectric cooler.

2.3.2 Noise within the Detection Chain

For a stochastic process with an incident photon flux impinging the active detector area of a CCD, the uncertainty in the arrival and collection of these photons is given by Poisson statistics and can be expressed as Equation 2.6 where σ_{shot} is the shot noise and S is the signal, both in units of electrons,

$$\sigma_{shot} = \sqrt{S} \tag{2.6}$$

The process to generate electrons during the impact ionisation with the gain register is also stochastic. The number of electrons x out of the gain register will have a distribution $z(x)$ according to the n input electrons as approximated by as Equation 2.7 [Zhang et al., 2009]

$$z(x) = \frac{x^{n-1} exp(-x/G)}{G^n (n-1)!} \tag{2.7}$$

where G is the total mean electron gain in the gain register. The distribution $z(x)$ with n input electrons is shown in Figure 2.4.

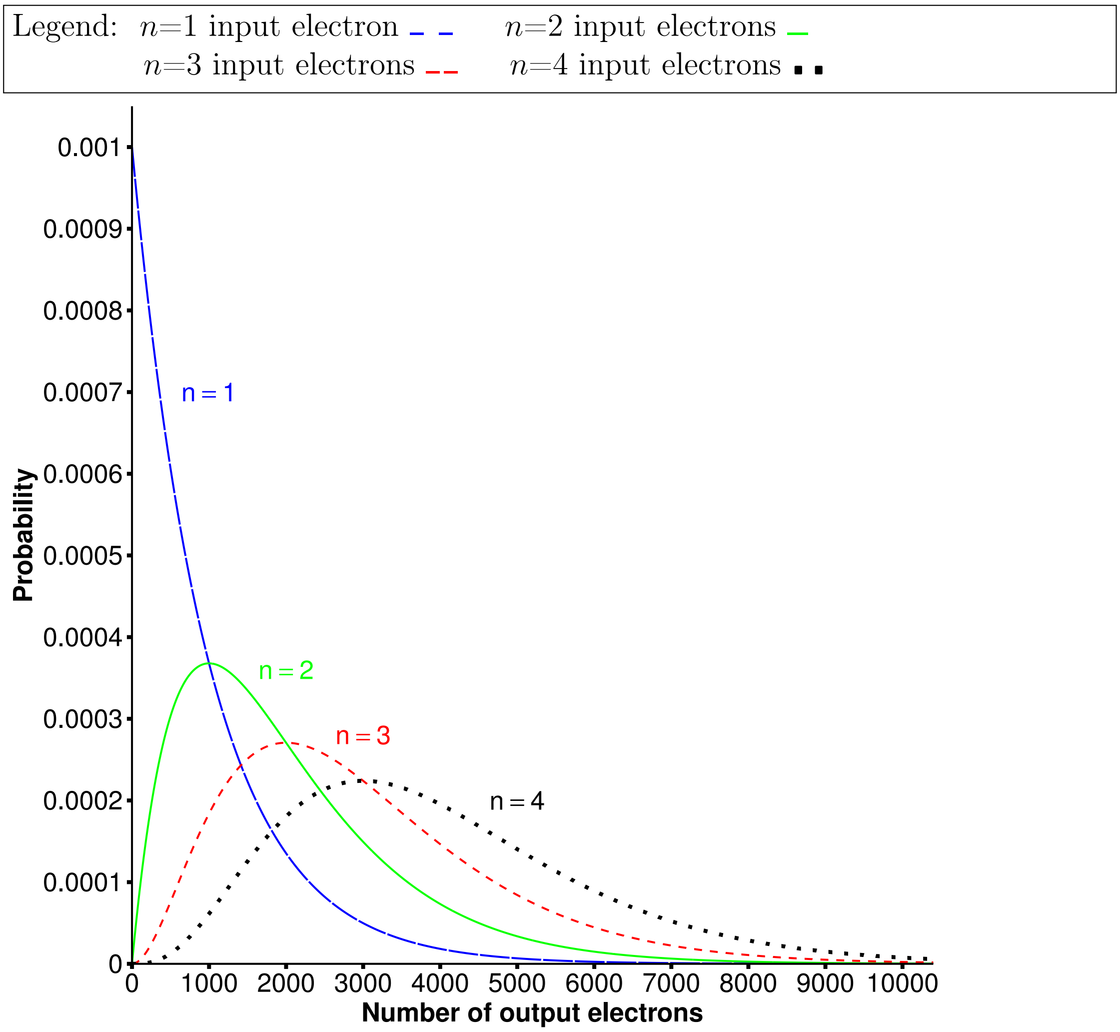

Figure 2.4: The number of electrons x out of the gain register will have a distribution $z(x)$ according to the n input electrons and gain G=1000.

This distribution in the number of electrons x out of the gain register is given by the excess noise factor ν as Equation 2.8 for more than a single input photoelectron [Zhang et al., 2009]

$$\nu = \frac{\sigma_{out}}{G\sigma_{in}} \tag{2.8}$$

where σ_{out} and σ_{out} are the standard deviations of the input and output signals respectively. For a single input photoelectron the ν can be estimated as $\sqrt{2}$ [Zhang et al., 2009] using G derived from the number of gain stages n each with gain g

according to Equation 2.9

$$G = g^n \tag{2.9}$$

The amplifier of a CCD has readout noise given by a Gaussian distribution with a variance determined by the readout rate. The output from the amplifier for an EMCCD is given by the Gaussian readout noise convolved with the output from the gain register. When an EMCCD operates with high gain, the shot noise is multiplied through the gain register and dominates the readout noise from the amplifier. As the gain register output depends on the incident photon flux and the probability distribution in the number of generated electrons introduced through the multiplication process in the gain register, the shot noise on the image is increased and this is the excess noise factor of $\sqrt{2}$ [e2vTechnologies, 2004]. An analytical expression for the excess noise factor has been derived [Robbins and Hadwen, 2003] and the variation of multiplication gain with the square of the excess noise factor ν^2 has been modified from [Robbins and Hadwen, 2003] and is shown in Figure 2.5.

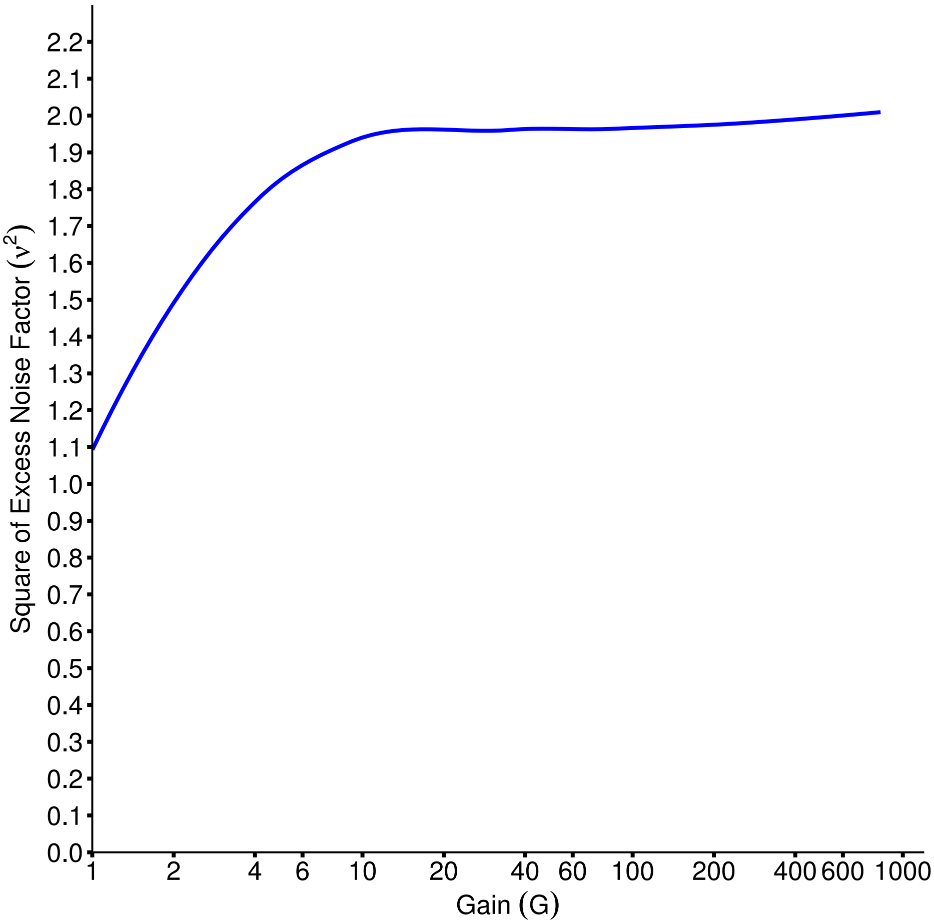

Figure 2.5: The square of the excess noise factor ν^2 versus gain G. Modified from [Robbins and Hadwen, 2003].

Clock-induced charge arises during the process of enabling and removing inversion of the surface states as charge is transferred from the image and storage registers; this also adds noise to the EMCCD but is typically less than one electron/pixel/frame [e2vTechnologies, 2004].

2.3.3 Energy Resolution

In the absence of a scintillator, the energy resolution of semiconductor detectors ΔE can be described by three terms as in Equation 2.10, [Owens et al., 1996, Lees, 2010].

$$\Delta E = 2.36\omega\sqrt{\frac{FE}{\omega} + R^2 + A^2} \tag{2.10}$$

with ω the electron hole pair creation energy, F is the Fano factor and E is the incident photon energy. The first term is the intrinsic variance of the number of primary electron hole pairs. The second term is due to readout noise due to incomplete charge collection, drift and transfer through the shift and gain registers. The last term due to noise from the detector readout. For the e2v CCD97-00 back illuminated EMCCD the readout noise is of the order of electrons per pixel per frame with each pixel size of 16 μm x 16 μm at a temperature of 293 K, 30 Hz frame rate and gain of 1000 [e2vTechnologies, 2004].

The Fano component originates within silicon owing to some of the incident energy creating phonons (energy given to the silicon lattice). This Fano noise represents an intrinsic limitation in the energy resolution. The Fano-limited root mean square line width within the distribution of energy deposition is given by Equation 2.11, [Devanathan et al., 2006].

$$\sigma_{Fano} = \sqrt{\omega F E} \tag{2.11}$$

For a scintillator based solid state detector the energy resolution can be attributed to the energy deposition from the impinging gamma photons, the presence of fluorescence, the gamma ray conversion efficiency to scintillation photons, transmission losses of these optical photons, as well as the detection efficiency at the EMCCD. Equation 2.10 would therefore need to account for the scintillator and optical transmission/detection stages.

2.4 Scintillator crystals.

A large number of materials have been found to scintillate when X-ray and gamma ray photons impinge upon them. The ideal scintillator for imaging should exhibit the following properties [van Eijk, 1998, Nikl et al., 1999, van Eijk, 2001, Nikl et al., 2006, Lecoq, 2016]:

- High absorption coefficient to detect impinging X-ray and gamma photons requires a high density and a high atomic number. With larger scintillation volumes, any scattering component owing to impurities and defects degrades the final image.
- High yield of optical light, which should be proportional to the energy over the impinging photon energy range.
- The position of the K edge should be outside the clinical range of the incident X-ray and gamma photons so that the total mass attenuation coefficient is high.
- Low variation of light yield with the temperature of the scintillator.
- Low afterglow caused by the delayed thermal release of trapped charge carriers and their recombination from impurities and defects.
- The decay time of the luminescence from a scintillator should have a short decay time to allow the collection of fast optical signals through the ADC.
- The scintillator should be radiation hard over the lifetime of the integrated radiation exposure.

- The scintillator should be transparent to its own light and this is done so using activation centres, for example using thallium in alkali halides.

- The emission spectrum should match the peak response curve of the absorption spectrum of the optical photon detector.

- The scintillator should be capable of being optically coupled to the photon detector in order to minimise light collection losses of the detected counts.

There are a variety of inorganic scintillators, [Derenzo et al., 2002, Lecoq, 2016, Dujardin et al., 2018] and ceramic scintillators available, [Greskovich and Duclos, 1997]. Organic scintillators are not suitable for gamma photon detection due to their low density which is of order 1 gcm^{-3}. The scintillation process converts impinging gamma photons to $E_0/(\beta.E_{bg})$ electron-hole pairs, where E_0 is the energy of incident photons, E_{bg} is the band gap energy of the material, and β an empirical property of each material has values between 3 and 7, [Blasse, 1994]. This is followed by transfer of energy to self-trapped excitons (coupled electron-hole pairs) or transfer of the electron-hole pair energy to luminescent ions. Radiative emission of optical photons occurs as the self-trapped excitons relax or as the excited luminescent ions returns to ground state. During thermalisation β accounts for the energy losses through coupling with lattice phonons [Lecoq, 2016].

In alkali halides trace amounts of thallium-81 are used to dope the halide lattice, as the migrating exciton is trapped by the Tl^{1+} ion, with emission occurring from these sites [Blasse, 1994]. In order to have optimal counting statistics within a detector, the optical photon light yield should be better than about 20,000 photons per absorbed ionising energy. This scintillator optical photon yield should be independent of energy otherwise it is difficult to determine the energy of the detected signal and its energy resolution will be degraded. Non-proportionality in scintillator response and its effect on energy resolution has been described elsewhere, [Dorenbos et al., 1994, 1995, Khodyuk et al., 2010]. Selected types of inorganic scintillators – alkali halides, tungstates, lanthanide silicates, and ceramics, [Blasse, 1994, Greskovich and Duclos, 1997] are summarised in Table 2.1.

	sodium iodide (thallium doped)	caesium iodide (thallium doped)	cadmium tungstate	lutetium silicate	gadolinium orthoxysulphide (praesidium, cerium doped)
Density/ gcm^{-3}	3.67	4.51	7.99	7.4	7.34
Emission peak/ nm	415	560	480	420	520
Light Yield/ photons per keV	40	54	14	25	50
Decay Time/ ns	230	2.1, 1000	5000	40	2400
After-glow/ % after 6 ms	0.3 - 5	0.5 - 5	$<$ 0.1		$<$ 0.1 after 3 ms
Notes	very hygroscopic	slightly hygroscopic	difficult to cleave	intrinsic radioactivity	ceramic, translucent

Table 2.1: Selected examples of monolithic inorganic scintillators from [Blasse, 1994, Greskovich and Duclos, 1997]

Thallium doped sodium iodide and caesium iodide are used in LFOV systems owing to its effectiveness in stopping gamma photons which depends not just its atomic number but also the scintillator thickness (usually between 1/4 inch and 1/3 inch). In nuclear medicine low energy gamma photons less than 200 keV are usually used. The 200 keV upper threshold is arbitrarily chosen covering the energy range for majority of radionuclides using in nuclear medicine including technetium-99m. The K edges for sodium are at 1.072 keV, for iodine at 33.169 keV and for caesium at 35.985 keV [Sanchez del Rio et al., 2003] and are well below the photopeak energies for the range of radionuclides used. The peak emissions for thallium doped sodium iodide and caesium iodide are well matched for the respective photomultipliers used to collect the scintillation photons. However the decay time of the light yield profile can cause overlapping of consecutive scintillations which affect the count-rate capability discussed in section 7.3.6. Nonetheless the high light yield improves the energy resolution which allows for better discrimination of Compton scattered events from photopeak events.. Lutetium orthoxysilicate has a high density and fast decay time of the light yield profile which makes it an attractive alternative to either alkali halide; however its light yield is comparatively less and it is intrinsically radioactive which degrades the image.

Cadmium tungstate has been traditionally used in CT scanners which are essentially an X-ray tube coupled opposite to a detector array with both source and detector fixed onto a rotating toroid about a supine or prone patient. The CT scanner acquires a large number of detector response profiles as the toroid rotates and this constrains both the decay time of the light yield profile and the afterglow. The detector sampling rate is $\geq$ 10 kHz so the decay time for cadmium tungstate is well suited. The low afterglow for cadmium tungstate ensures that the large number of detector response profiles do not overlap so that the image reconstruction algorithm can be optimised. More recently manufacturers of CT scanners have used gadolinium orthoxysulphide doped with rare earth ions to quench afterglow. The Pr^{3+} is a co-dopant whose sites compete with intrinsic traps such that 4f/5d level of the Pr^{3+} can be excited; this is followed by non-radiative de-excitation. The Ce^{3+} is added as a co-dopant to suppress any residual afterglow of the Gd_2O_2S $\{Pr^{3+}\}$ [Blahuta et al., 2011].

2.5 Monte Carlo

In this work Monte Carlo computation methods are used to describe simulations of the transport of photons within two models of SFOV systems. A Monte Carlo simulation requires: several probability distribution functions describing the physics of the photon interactions; a random number generator used to track the photons events through the materials; and a accumulator recording the measured response. As mentioned these methods are powerful because they can be used to investigate different physical processes independently, and often these may be difficult to evaluate with experimentally. There are a variety of Monte Carlo codes used in nuclear medicine [Buvat et al., 2005, Castiglioni et al., 2005] which may either be general codes adapted for use from those either in radiation dosimetry or high energy particle physics tracking, or purposely encoded ones. From a comparison perspective if one considers general codes, Berger originally described the transport of electrons with a global interaction effect over their track length, and then together with Seltzer determined the energy loss during this transport [Berger and Seltzer, 1964] so derived their ETRAN code. The simulation of electron transport was subsequently extended to include photon transport, as can now be found for example in the Electron Gamma Shower algorithms used in EGS5 and MCNP6.

Examples of general purpose codes are:

- EGS5 [Hirayama et al., 2016]
- MCNP6 [Goorley et al., 2013]
- GEANT4 [Agostinelli et al., 2003]
- PENELOPE [Salvat et al., 2011]

The Monte Carlo simulation of photon transport is usually averaged over a given number of secondary tracks from the primary event or N 'histories' and its statistical uncertainty decreases as $1/\sqrt{N}$. In the process of slowing down the secondary photon interactions produced may either be absorbed in the medium or escape from the intervening medium. The Monte Carlo codes listed above all consider the cumulative effects of several physical interactions along a defined step length for each of the secondary tracks within a primary event. The cumulative effect of these interactions is obtained by appropriate sampling of the photon's energy and displacement from analytical forms of multiple scattering distribution functions, [Berger and Seltzer, 1964]. As regards to dedicated Monte Carlo codes used in nuclear medicine, current examples (which are both equally used at the time of writing) include parameters to investigate LFOV gamma camera detector and collimator design are

- SIMIND v6.1 [Ljungberg, 2017]
- GATE v8.1 [Strul et al., 2003, Jan et al., 2004, Staelens et al., 2003]

As the requirement for nuclear medicine is to use low energy photons (less than 200 keV) reflecting the clinically useful radionuclides for imaging, the Monte Carlo codes should use accurate probability density functions and material cross-section tables within this energy range [Zaidi, 2000].

In this work, the radiation transport of gamma photons through SFOV systems is modelled using the PENELOPE v2008 Monte Carlo code [Salvat et al., 2011]. The appropriateness of using this Monte Carlo code is because it has accurate differential cross-sections from the Lawrence Livermore National Laboratory, Evaluated Photon Data Library (EPDL) [Hubbell et al., 1997] which describe the physics of the photon interactions modelled. These differential cross-sections characterise the mean free path between interactions, the type of interaction, the energy losses and subsequent orientation to the next event. The mean free path between interactions λ is the inverse of the total interaction probability per unit length $N\kappa$, as in Equation 2.12

$$\lambda = \frac{1}{N\kappa} \tag{2.12}$$

where N is the number of atoms or molecules per unit volume and κ is the total atomic or molecular cross section for that process.

The PENELOPE Monte Carlo code is able to handle tracking of events near interfaces i.e. only the simulation parameters (velocity, angular deflection, displacement between interactions) just preceding determine the future path. This is called a Markov process. The physics of the photon interactions modelled can be followed within the simulation because of the Markovian nature of the tracking. In PENELOPE photon interactions used are photoabsorption, Compton (incoherent) scattering and Rayleigh (coherent) scattering. For photoabsorption, when this photoelectron is in the K, L or M shells, the simulation proceeds with the excited atom relaxing to its ground state by emitting characteristic X-rays and Auger electrons. If the interaction occurs in an outer shell (outside the M shell), then PENELOPE approximates the simulation by assuming the photoelectron is ejected with kinetic energy equal to the incident energy less its binding energy and fluorescence is disregarded [Salvat et al., 2011]. Since the kinetic energy of the photoelectron is artificially increased then it is assumed to compensate for the fluorescence disregarded during relaxation. PENELOPE uses differential cross-sections based on the Klein-Nishina equation for Compton scattering. In addition it is modified to account for the fact that target electrons are not stationary but have momentum distribution, and also modified to allow only transitions for bound electrons where the energy difference between the incident and scattered photons is greater than the ionisation energy of the active shell. Detailed physics, analytical probability density functions and sampling algorithms for all these interactions are described within the PENELOPE documentation [Salvat et al., 2011]. Finally although the Lawrence Livermore Evaluated Atomic Data Library (`https://www-nds.iaea.org/epdl97/`) is still used in several Monte Carlo codes for example GEANT4 and MCNP6, PENELOPE uses a comprehensive model of atomic de-excitation [Bearden and Burr, 1967].

The following chapters describes PENELOPE simulations [Salvat et al., 2011] which are used to model the distribution of energy deposition and the distribution of photon fluence within separate accumulators when low energy gamma photons (less than 200 keV in these cases) impinge a caesium iodide crystal. The 200 keV upper threshold is arbitrarily chosen covering the energy range for the majority of radionuclides used in nuclear medicine including technetium-99m. PENELOPE does not model any scintillation photons and this is however discussed in later in chapter 6 using the GEANT4 Monte Carlo code.

2.6 Statistics and Convergence

In Monte Carlo modelling a random variable representing the quantity of interest is tracked and sampled from a function describing the interaction probability density function. This sampled random variable is accumulated in suitably sized bins for one complete photon interaction history. The estimate of the mean value of the Monte Carlo procedure samples x_i with a sample mean $\bar{x}$ derived from i to n independent observations for each bin is given by Equation 2.13,

$$\bar{x} = \frac{1}{n}\sum_{i=1}^{n} x_i \tag{2.13}$$

As the number of histories becomes large, the probability density function of the sample means $\bar{x}$ is a Gaussian distribution with mean $\langle x \rangle$ and variance $\hat{\mu}_2$ as given by the second central moment in Equation 2.14

$$\hat{\mu}_2 = \frac{1}{n-1}\sum_{i=1}^{n} (x_i - \bar{x})^2 \tag{2.14}$$

For large n, variance $\hat{\mu}_2$ is given by the second central moment as Equation 2.15

$$\hat{\mu}_2 \approx \frac{1}{n}\sum_{i=1}^{n} ({x_i}^2 - \bar{x}^2) \tag{2.15}$$

In PENELOPE for a large number of simulations n, the expectation value of the random variable and its standard deviation are reported within a confidence interval given by $\langle x \rangle \pm 3\sigma$ or 99.7%. This only applies asymptotically which leaves the determination of n to the Monte Carlo practitioner. This is known as the convergence of the simulation and there are some semi-empirical guidelines [Forster et al., 2004, Pederson et al., 1997]. The convergence of a simulation ensures that the interaction probability density function has been adequately sampled by the distribution of random numbers. One of these which is commonly used is the Relative Errors (E_R) which is given by the ratio of the sample standard deviation σ to the sample mean $\bar{x}$ as in Equation 2.16,

$$E_R = \frac{\sigma\sqrt{n}}{\bar{x}} \tag{2.16}$$

However [Pederson et al., 1997] advises that the E_R should not be used to estimate convergence as it does not stabilise sufficiently well. Instead it is recommended that the "figure of merit" FOM and the "variance of the variance" VOV should be used. The former is given by Equation 2.17,

$$FOM = \frac{1}{t(E_R)^2} \tag{2.17}$$

where t is the time taken to acquire n histories. The latter is given by Equation 2.18 where

$$VOV = \left(\frac{\hat{\mu}_4 - \sigma^4}{\sigma^4 n} \right) \tag{2.18}$$

$\hat{\mu}_4$ the fourth central moment given by Equation 2.19

$$\hat{\mu}_4 = \frac{1}{n}\sum_{i=1}^{n}(x_i - \bar{x})^4 \tag{2.19}$$

These metrics may be considered to be converged by assessing each of their trends over time over the last half of the simulation.

2.7 General analytical model of a silicon detector without a scintillator

While Monte Carlo simulations are useful computation methods to describe the transport of photons in materials, it is important to corroborate findings either with experiment or by analytical means. As experimental design may be costly to source materials and alternative approach is to use an analytical calculation. Thus, in order to assist with validation an analytical model is described for a bare silicon detector. A schematic of a detector without a scintillator or collimator is shown in Figure 2.6; there is an intervening entrance window designated layer a before the detector layer b. This approach allows different materials to be trialled before specifying materials for purchase.

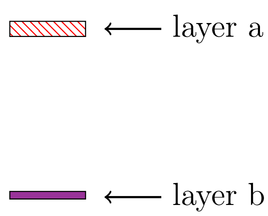

Figure 2.6: Simplified schematic of the bare silicon detector

Following Smith and Lucas [1999] one can determine the absolute photon detection efficiency η_{total} as Equation 2.20,

$$\eta_{total} = \frac{\Sigma \text{ photons within photopeak}}{\Sigma \text{ photons from source activity}} \tag{2.20}$$

The absolute photon detection efficiency η_{total} is the product of three terms excluding any self-absorption by the source as in Equation 2.21,

$$\eta_{total} = \Omega \, \eta_a \, \eta_b \tag{2.21}$$

where Ω is the fractional solid angle subtended from a point source by the detector Figure 2.7, η_a is the transmission coefficient in the layer a, η_b is the intrinsic efficiency in the detector layer b, and corresponds to probability that a gamma photon interaction in the detector gives the full energy photopeak.

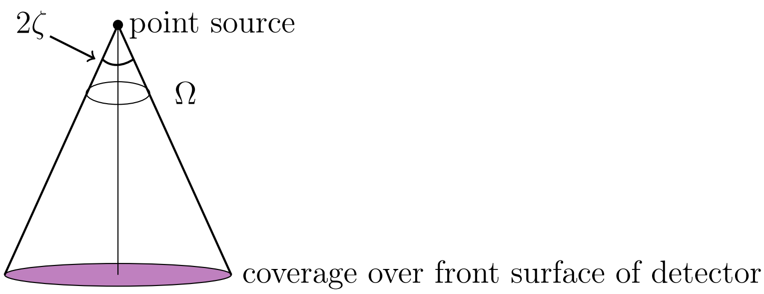

Figure 2.7: . The fractional solid angle Ω subtended from a point source by the detector. 2ζ is the apex angle of the cone.

Ω can be derived from the apex angle of the cone 2ζ subtended from a point source by the detector and is given by Equation 2.23 using conical coordinates with polar angle θ and azimuthal angle ϕ.

$$\begin{aligned}\Omega &= \int_0^{2\zeta}\int_0^{2\pi} \sin\theta \, d\theta d\phi &(2.22)\\ &= 2\pi\big[1-\cos(2\zeta)\big] &(2.23)\end{aligned}$$

The transmission coefficient term η_a for layer a is given by the Equation 2.24 where μ_a which is its mass absorption coefficient, ρ_a is its density and t_a is its thickness,

$$\eta_a = \exp\big[-(\mu_a\rho_a t_a)\big] \tag{2.24}$$

The term η_b is determined by Equation 2.25 where for layer b μ_b is its mass absorption coefficient, ρ_b is its density and t_b is its thickness, thus

$$\eta_b = 1 - \exp\big[-(\mu_b\rho_b t_b)\big] \tag{2.25}$$

The equations in this section are used in the following chapters to validate experimental and Monte Carlo simulations.

Chapter 3

Monte Carlo modelling of the Small Field-Of-View PIXS detector and CGC.

3.1 Models

Monte Carlo modelling can be used to understand and predict the underlying physics as impinging gamma photons transport through models of SFOV systems. These simulations to track photon transport can be performed using different materials and geometries within a model of the SFOV system; such an approach would not easily be translated into an experiment and would be costly. This chapter considers two models of SFOV systems which are described within separate sections - one pertaining to a bare silicon detector called the Portable Imaging X-ray Spectrometer detector [PIXS detector], and the second describing the Compact Gamma Camera [CGC]. The PIXS detector and CGC each use an e2v CCD97-00 back illuminated EMCCD [e2vTechnologies, 2004] and this is modelled as an 8 mm x 8 mm x 5 μm thick monolithic silicon detector.

A schematic of the PIXS detector is shown in Figure 3.1

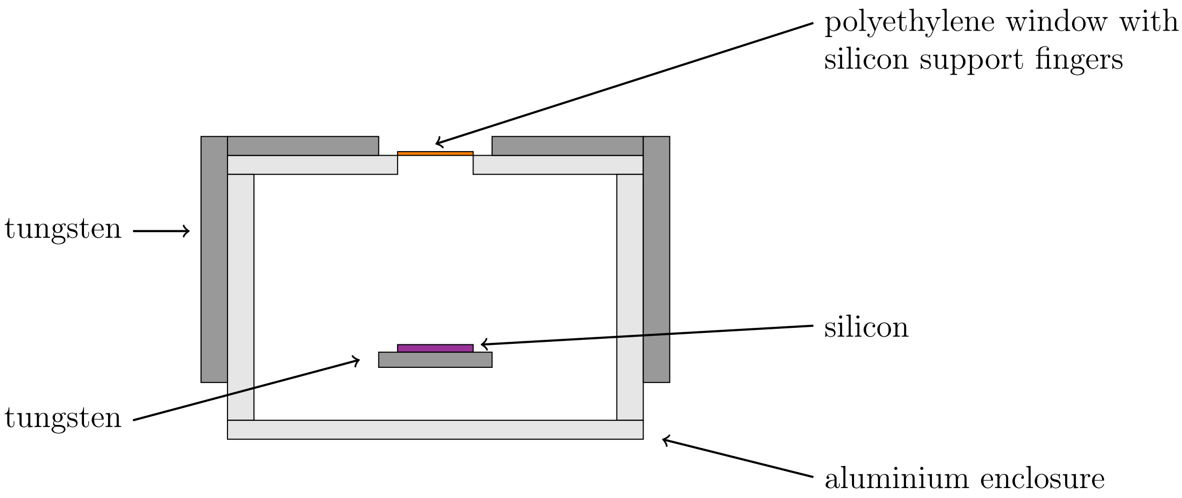

Figure 3.1: A schematic of the PIXS detector

The entrance window of the PIXS detector has a thin polyethylene cover with a 4 µm thick layer of interleaved silicon support fingers. These silicon support fingers are not included in the Monte Carlo model as their width and length were unknown. The 5 µm thick silicon detector with active area of 8 mm x 8 mm represents the depletion layer of the EMCCD and is within an evacuated aluminium chamber at 1.3 x 10^{-3} Pa. Another reason for the aluminium housing is to mitigate against fluorescence from the housing interfering with the silicon detector. Shielding from extraneous scatter is provided by a partial enclosure of tungsten 3 mm thick.

Monte Carlo modelling was used to determine the distribution of energy deposited within the silicon detector, and is described in section 3.4.1 firstly using 22 keV incident gamma photons, and then using the full spectral emission from a cadmium-109 source. The PENELOPE Monte Carlo code did not include the addition of detector noise although in reality there are several sources of noise present and these are discussed in section 2.3. The influence of noise is discussed in relation to the experimental response of the PIXS detector in chapter 5.

An additional aim of the simulation was to model the CGC in order to determine its detector sensitivity using technetium-99m. A schematic of the CGC is shown in Figure 3.2.

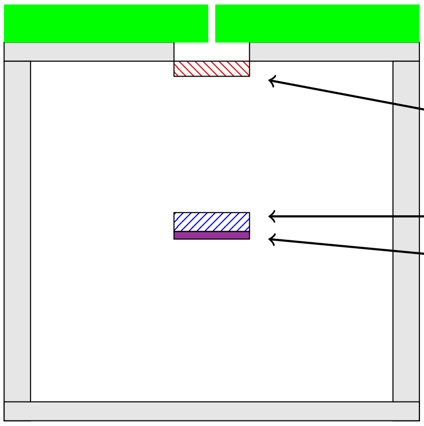

Figure 3.2: Schematic of the modelled Compact Gamma Camera

As shown in Figure 7.3 the columns of caesium iodide within the crystal are close-packed. Zhao et al. [2004] have reported an uncorroborated packing density of 75%, corresponding to average densities 3.38 gcm^{-3} for their HL (High Light) output provided by Hamamatsu-Photonics [Hamamatsu, 2016]. However, Hamamatsu-Photonics have not published the average density of columnar caesium iodide for the samples used in the CGC. For the Monte Carlo modelling performed in this chapter, the caesium iodide crystal is simplified for simulating the transport of gamma photons by replacing the columnar crystal by a monolithic crystal. In an improved model with columns of caesium iodide, one would expect less photoabsorption, less Rayleigh scattering owing to lower density but more Compton scattering owing to the increase of internal crystal surfaces. The other reason for modelling a monolithic caesium iodide crystal is that the construction of the columnar geometry in PENELOPE is cumbersome and the Monte Carlo tracking within the geometry is memory intensive. Nonetheless this should be considered for future work.

Omission of trace thallium-81 doping from the radiation transport simulations as a first order approximation does not affect the modelled spectrum within the caesium iodide crystal since the weighted proportion of thallium-81 of order 10^{-28} gcm^{-3} has a negligible impact. The modelled monolithic caesium iodide crystal was abutted directly (without a gap) to a 5 μm silicon depletion layer representing the EMCCD. Both the modelled monolithic crystal and silicon depletion layer have an area of 8 mm x 8 mm. Collimators are constructed of high Z materials (for example tungsten) are used to attenuate some of the tissue-scattered photons and have holes to allow mostly non-tissue scattered photons to pass through onto the detector. The most common types of collimators employ a single cylindrical hole ("pinhole"), or an array of several cylindrical holes ("parallel hole"), or a single tapered hole ("knife-edge pinhole"). Each of these types of collimators have different behaviours in their response to sensitivity and spatial resolution. [Anger, 1964, Beach, 1969, Levin, 2003, Shokouhi et al., 2009]. The physical knife-edge pinhole within the 6 mm thick collimator used in the CGC is simplified for the following Monte Carlo simulations to a cylindrical parallel hole collimator of diameter 0.5 mm. This was because the Monte Carlo simulation of photons through a collimator hole which is a thin tapered wedge will have a very low probability of interaction.

The simulations in this chapter use the PENELOPE Monte Carlo code [Salvat et al., 2011]. This Monte Carlo code has accurate differential cross-sections from the Lawrence Livermore National Laboratory, Evaluated Photon Data Library (EPDL) [Hubbell et al., 1997] which describe the physics of the photon interactions which are modelled. These include photoabsorption, Compton and Rayleigh scatter as discussed in section 2.1. The response of the silicon detector can be considered in the context of its partial mass attenuation coefficients as shown in Figure 2.2 with the dominant interaction for incident photon energies less than 70 keV within silicon being photoabsorption, and Compton scatter between 80 keV to 200 keV. Pair production is not relevant for this work as the photon energy threshold for this to occur is 511 keV. Secondly PENELOPE uses an up-to-date physics model of atomic de-excitation [Salvat, 2015]. The following section 3.2 provides an overview of how Monte Carlo simulations were performed. Detector noise was not considered in this chapter (noise in the PIXS detector is discussed in chapter 5), and another limitation of the PENELOPE Monte Carlo code [Salvat et al., 2011] is that scintillation photons are not included.

3.2 PENELOPE Monte Carlo simulations

In general there are several steps to perform Monte Carlo simulations which can be categorised as firstly preparing the model and secondly performing the simulation.

A flow chart of the steps to prepare the model is summarised in Figure 3.3.

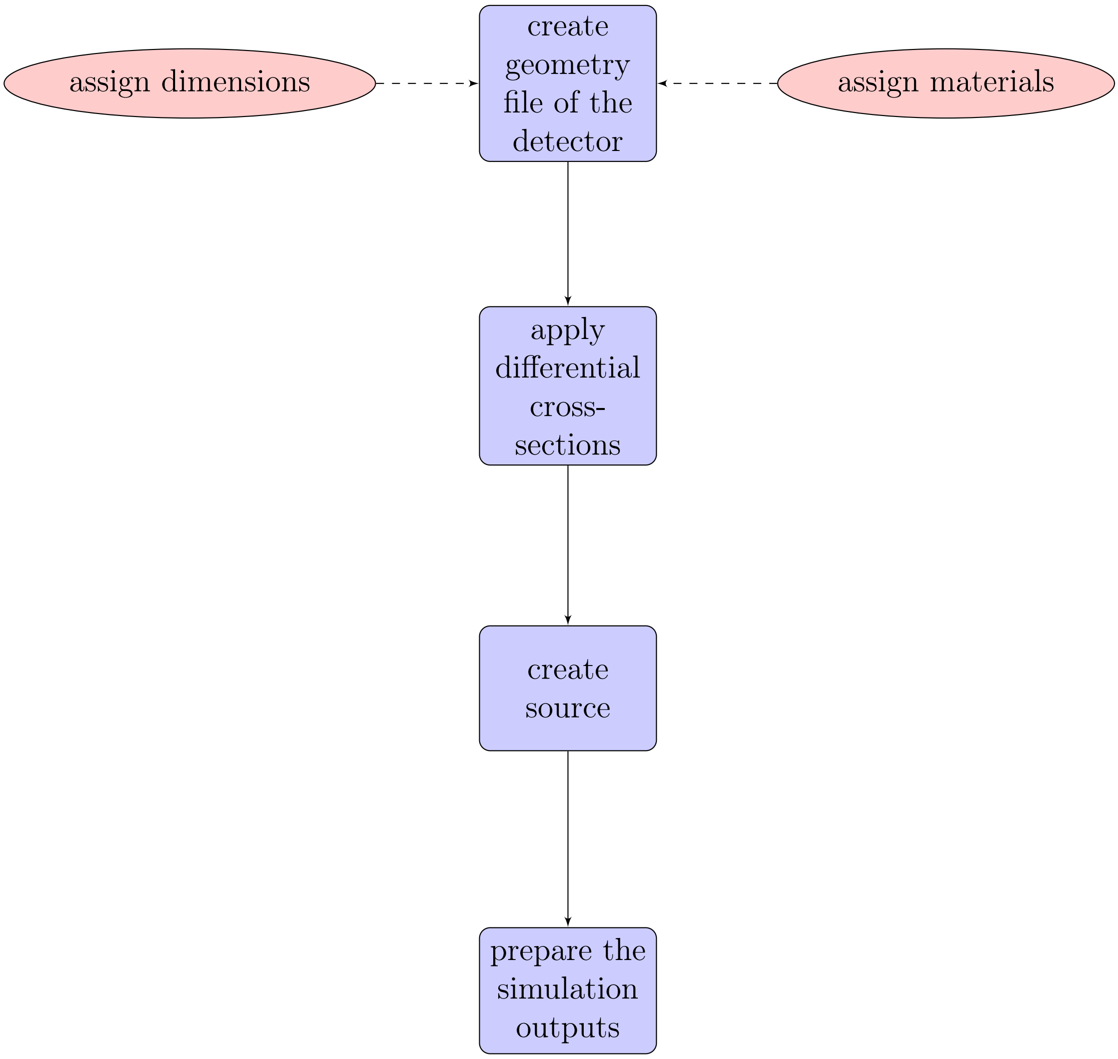

Figure 3.3: Flow chart showing how the Monte Carlo model is prepared.

The PENELOPE geometry file describes the model of the detector with dimensions assigned by the requirements of the simulation, and is based on quadric surfaces which may be rotated using Euler angles, ω, θ, ψ about orthogonal axes x, y, z respectively. Quadric surfaces $F_r(x, y, z)$ can be used to describe the shape of limiting surfaces and may be defined using coefficients $\{I_1, I_2, I_3, I_4, I_5\}$ [Salvat et al., 2011] as in Equation 3.1

$$F_r(x, y, z) = I_1x^2 + I_2y^2 + I_3z^2 + I_4z + I_5 \tag{3.1}$$

For example Table 3.1 shows the affect of changing these indices and the shape of the limiting surfaces they describe.

Reduced quadric	Indices $\{I_1, I_2, I_3, I_4, I_5\}$	Quadric surfaces
$z - 1 = 0$	0 0 0 1 -1	plane
$z^2 - 1 = 0$	0 0 1 0 -1	pair of parallel planes
$x^2 + y^2 + z^2 - 1 = 0$	1 1 1 0 -1	sphere
$x^2 + y^2 - 1 = 0$	1 1 0 0 -1	cylinder
$x^2 + y^2 - z^2 = 0$	1 1 -1 0 0	cone

Table 3.1: Quadric surfaces using reduced indices

For the following simulations PENELOPE geometry files were created to model the transport of gamma photons through each component using a combination of quadrics comprising of planes coefficients $\{0, 0, 0, 1, -1\}$, parallel planes coefficients $\{0, 0, 1, 0, -1\}$ and cylinders coefficients $\{1, 1, 0, 0, -1\}$. These PENELOPE geometry files are not shown for brevity. In a more complex geometry such as that in a patient phantom for example, a geometry file based on quadrics becomes more cumbersome. An alternative is to use GEANT4 for the Monte Carlo modelling, preserving the PENELOPE physics model as developed in chapter 6.

The second step is to construct the materials' files which list the media used in the simulation. These provide the differential cross-sections for each of the photon interactions simulated for the prescribed energy range up to 200 keV. The materials' files included the target medium (for example caesium iodide or silicon) and intervening air as an approximation to the evacuated chamber.

The source emits photons and its origin is positioned with an appropriate semi-angle to ensure that the photon flux irradiates the simulated geometry. For the initial simulation a wide-beam source was used to ensure the photon flux irradiated the whole of the simulated geometry.

The final step is to prepare the simulation output which describes the energy binning and includes two types of accumulators so as

- to accumulate the distribution of the number of photons entering a defined volume (fluence accumulator) or
- to accumulate the distribution of absorbed energy events for photons which enter and are absorbed within another defined volume (energy deposition event accumulator).

A flow chart of how the simulation is performed is summarised in Figure 3.4. After the simulation is prepared, the Monte Carlo software determines the mean free path between interactions, the type of photon interaction, the energy losses and subsequent orientation to the next event. The fate of the photon(s) is then decided:

- If the photon escapes from the simulation of the geometry or is absorbed within the materials that are used, then the simulation is halted.
- If the photons still have energy above a user defined threshold, then the Markovian tracking continues within the "update simulation" loop. These photons undergo scattering interactions.

As mentioned in section 2.5, a Markovian process is one where only the simulation parameters (velocity, angular deflection, displacement between interactions) just preceding the Monte Carlo calculation determine the future path. Non-Markovian processes are those which involve random walks (for example Brownian motion) or those which create particles (for example ionisation or fluorescence).

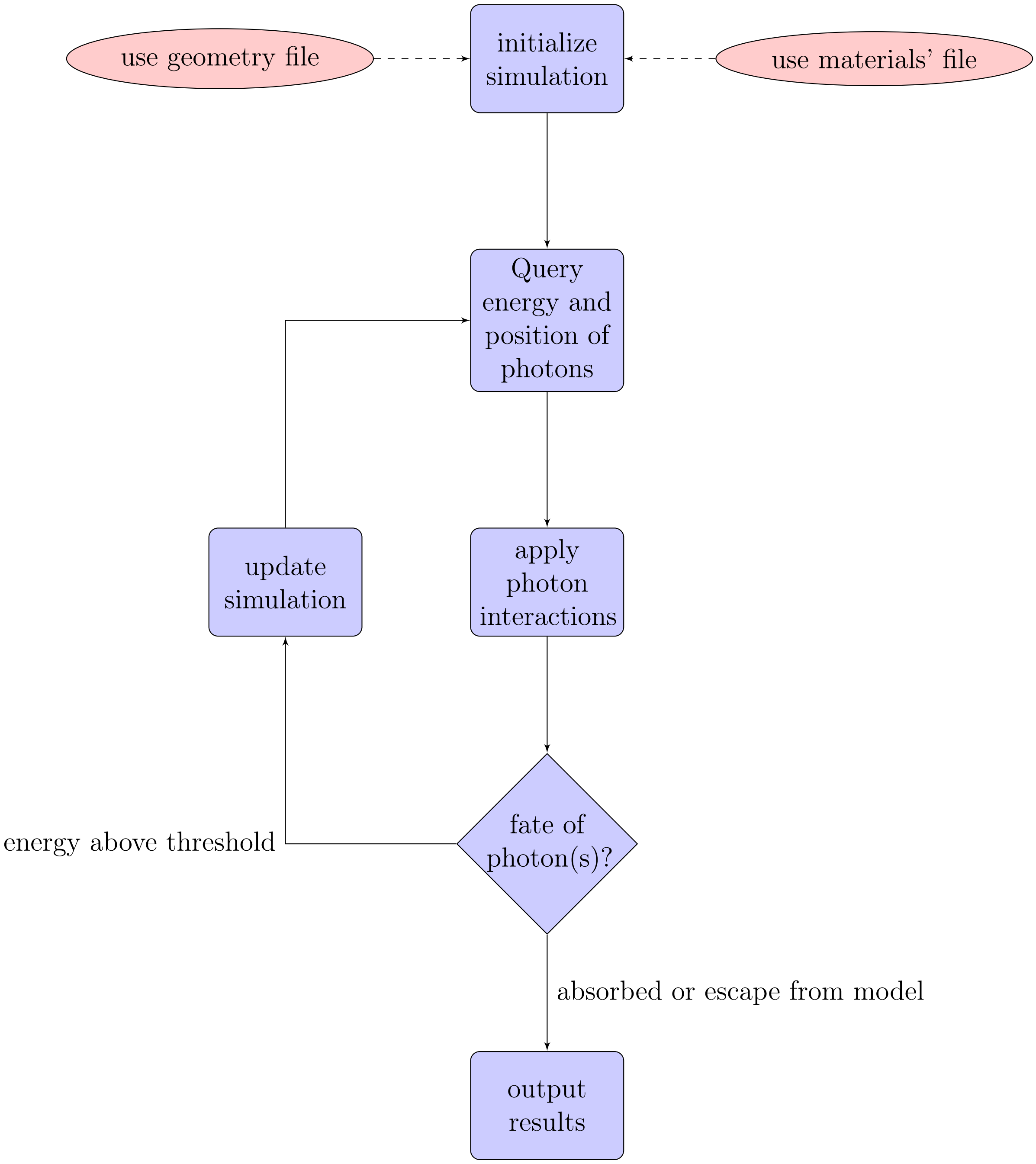

Figure 3.4: Flow chart of the Monte Carlo simulation

The physics models used in these simulations are described in chapter 2, section 2.1 for photon interactions and in section 2.2 for fluorescence.

The outputs of the simulations are determined using two Monte Carlo measurement accumulators as shown in Figure 3.5, which is to measure the photon fluence and in Figure 3.6, which is used to measure the photon energy deposition events.

Referring to Figure 3.5, measurement A is carried out to assess the fluence of photons across the detector cross-section into the detector bulk; the fluence $\Phi(\mathbf{r})$ at a point $\mathbf{r}$ is defined as Equation 3.2

$$\Phi(\mathbf{r}) = \frac{dN}{d\mathbf{A}} \tag{3.2}$$

where dN is the total number of photons incident on a surface element $d\mathbf{A}$ centred at $\mathbf{r}$, [Salvat et al., 2011]. Fluence has dimensions of [number of photons] x [distance]$^{-2}$.

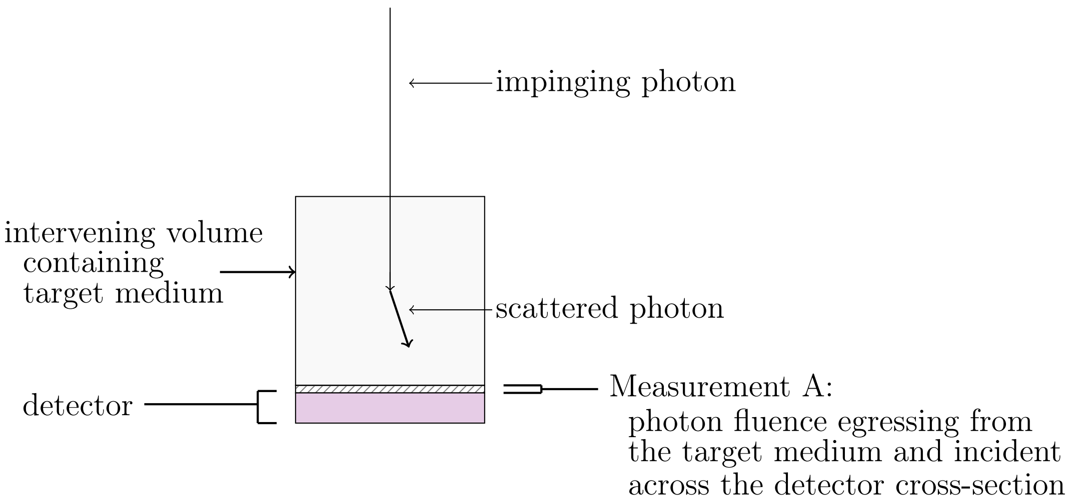

Figure 3.5: Measurement A: This Monte Carlo measurement accumulator records the photon fluence egressing from the target medium and incident across the detector cross-section into the detector bulk.

Referring to Figure 3.6 measurement B is used to determine the energy deposition of photons within a specified volume bounded by the detector cross-section.

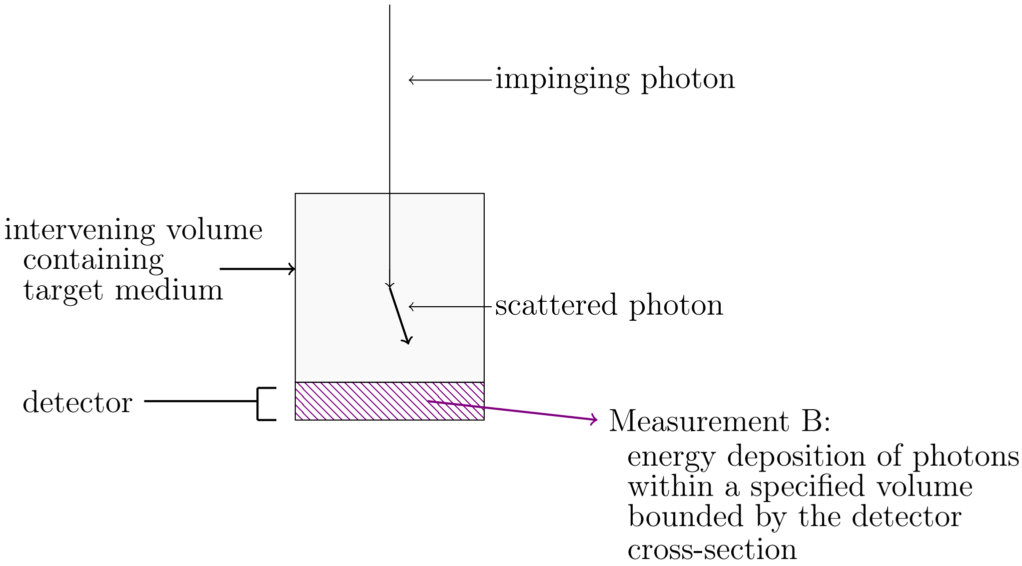

Figure 3.6: Measurement B: This Monte Carlo measurement accumulator records energy deposition of photons within a specified volume bounded by the detector cross-section.

The volumes of these accumulators are chosen to match the dimensions of the materials in the geometry file and hence the modelled detector. Any scattered photons which escape the target medium will not be recorded within either of these two accumulators. Both models of SFOV systems use a 5 μm thick silicon detector which represents the depletion layer of an EMCCD with active area of 8 mm x 8 mm. For fluence, its entrance area matches the surface area of the egress face of the intervening target material used. This fluence accumulator has an arbitrary thickness to accommodate the path length of photons which contribute when their trajectory intersects this volume for the duration of the simulation. For energy deposition events, this accumulator has its volume defined as that encompassing the dimensions of the detector.

The fluence and energy deposition are respectively accumulated within discrete energy intervals of fixed width called bins as described in section 2.6.

These bins accumulate either fluence events or energy deposition events as photons are tracked from the primary interaction within the intervening medium to the secondary tracks produced from the primary interaction. Thus measurement A records the photon fluence egressing from the target medium and incident across the detector cross-section into the detector bulk as a function of incident photon energy; measurement B provides an distribution of the energy deposition of photons within a specified volume bounded by the detector cross-section as a function of incident photon energy.

The PENELOPE Monte Carlo simulations included the tracking of photoelectrons with elastic scattering, inelastic scattering and bremsstrahlung emission. Detailed simulations were only considered at low energies as it is infeasible to simulate the transport of fast electrons owing to the large number of their interactions. The differential cross-sections for each of the processes is described in detail elsewhere [Salvat et al., 2011]. For the dominant process inelastic scattering, the differential cross-section is derived from a plane-wave Born approximation which creates excitations and fluorescence in the target medium. The elastic scattering of electrons is described by the scattering from a static-field approximation of the charge distribution of the target atom, provided the energy of the electrons is greater than a few hundred eV. Bremsstrahlung emission arises from the electrostatic field of the atoms creating braking radiation for fast electrons. In the following simulations, the energy deposited into bins was recorded for any events which created fluorescence or bremsstrahlung emission from the photoelectron interactions. Detailed analyses of the photoelectron interactions were not performed as the focus of this work was on the tracking of photons.

The PENELOPE Monte Carlo FORTRAN 90 coded [Salvat et al., 2011] simulations were performed using the University of Leicester ALICE computing cluster across an array of compute nodes. The array processing was used to perform simultaneous calculations across several CPUs within each compute node. One hundred standard compute nodes were used for each job execution with each standard compute node using Intel Xeon Ivy Bridge CPUs at 2.6 GHz, 64 GB RAM.

3.3 Assessment of the convergence of the simulations

3.3.1 Method

The duration of a Monte Carlo simulation is important to ensure the simulation converges as discussed in section 2.6. This was required to ensure that the probability distribution functions which describe the physics of the photon interactions were sufficiently sampled. So prior to simulating the complete SFOV systems, preliminary Monte Carlo experiments were performed to provide guidelines for how long to run each simulation for the SFOV systems. Consequently, four separate PENELOPE geometry files were created with components of the CGC added in sequence as follows:

1. 8 mm x 8 mm x 600 μm thick monolithic CsI crystal
2. 3 mm thick tungsten enclosure
3. 0.5 mm diameter cylindrical pinhole tungsten collimator 6 mm thick
4. 8 mm x 8 mm x 5 μm thick silicon detector

and a schematic is shown in Figure 3.7. This model was built in a piece-wise process to assess the effects of adding each additional component. The 120 μm inner aluminium entrance window was removed from these Monte Carlo simulations as its effect is to attenuate the incident photons; each individual Monte Carlo experiment above would therefore be slowed by the same duration. N.B. An aluminium entrance window creates fluorescence at 1.4 keV as shown for example for the PIXS detector in Figure 3.11, for a 40 hours' simulation of the distribution of energy deposition within 5 μm silicon layer using a full spectral cadmium-109 radionuclide. The amplitude of the aluminium fluorescence is small so would not introduce a significant systematic error to the convergence simulations. The volume within the tungsten enclosure was modelled with air.

A 140.5 keV photon source was sited 10 mm on-axis away from the collimator surface with a divergence of 150 degrees from the entrance face. For the initial simulation although these dimensions were arbitrarily selected, a wide-beam source was used to ensure the photon flux irradiated the whole of the simulated geometry; 140.5 keV represents the peak gamma emission for technetium-99m.

The energy binning was set to 0.5 keV with the simulation producing an output of the distribution of energy deposited within the 600 μm caesium iodide crystal.

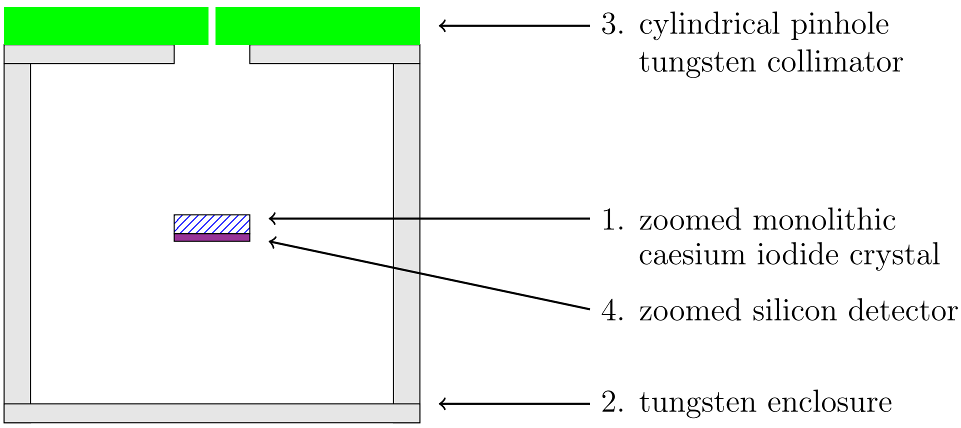

Figure 3.7: Schematic showing the modelled components of CGC added in a piece-wise order

One hundred concurrent simulations were performed using each of the four geometry files described above for 5 hours. This process was repeated for 10 hours, 20 hours, 30 hours, 40 hours, 60 hours, 80 hours and 100 hours.

3.3.2 Results

Three Monte Carlo simulation metrics as described in section 2.6 were calculated for the energy deposition accumulators for each of the simulations. These metrics were the relative error E_R, the figure of merit FOM and the variance of variance VOV and are shown in Table 3.2 for each of the durations simulated. Validation was confirmed from the convergence of the variation of the variance (VOV) parameter as recommended by [Pederson et al., 1997] recalling that these metrics may be considered to be converged by assessing each of their trends over time over the last half of the simulation.

Period	5 Hrs.	10 Hrs.	20 Hrs.	30 Hrs.	40 Hrs.	60 Hrs.	80 Hrs.	100 Hrs.
E_R	0.00473	0.00216	0.00235	0.00191	0.00193	0.00152	0.00179	0.00149
FOM	8949.8	21384.94	9045.1	9133.9	6691.1	7254.6	3890.4	4453.4
VOV	0.0153	0.0070	0.0080	0.0063	0.0063	0.0049	0.0059	0.0050

Table 3.2: Convergence for one hundred concurrent Monte Carlo simulations for the modelled CGC

3.3.3 Discussion

In Table 3.2 the relative error E_R does not settle sufficiently well so should not be used alone to assess whether the simulation has converged [Pederson et al., 1997]. Both the figure of merit, FOM and the variance of variance VOV parameter show a large variation at 5 hours and 10 hours suggesting under-sampling of the probability density functions describing the photon interactions. In Monte Carlo simulations the probability density functions describing the photon interactions must be appropriately sampled to ensure the simulation provides a true physical account of the interaction parameter being measured.

The energy binning was arbitrarily set to 0.5 keV for all the simulations which is wide enough to ensure sufficient events have been collected in each bin. Both the FOM and the VOV parameters for photon energy deposition events collected gradually settle after 60 hours of simulation. For subsequent simulations carried out in the following chapters, PENELOPE simulations were empirically performed for an additional 20 hours for each of the component added to the model in the path of the source photons, neglecting the volume of intervening air within the enclosure. It should be noted that the random number generator in PENELOPE guarantees that there is no recycling of a random number within a period of 10^{18} [Salvat et al., 2011]. Using both the FOM and the VOV parameters ensures that the probability density function for the photon interactions have been adequately sampled by the distribution of random numbers, within a reasonable simulation duration (as determined by the available compute nodes on the ALICE cluster).

3.4 Modelling of the PIXS detector

3.4.1 Method

Simulation using a mono-energetic 22 keV photon flux source

This section describes a Monte Carlo simulation of the distribution of energy deposited within an event accumulator located within a silicon detector with an impinging mono-energetic 22 keV photon flux source. The PENELOPE Monte Carlo simulation does not include detector noise. The silicon detector simulated here is representative of the PIXS detector as shown in Figure 3.1. This 22 keV photon emission serves as an approximation of the principal cadmium-109 peak ($AgK_{\alpha 1}$). The energy deposition event accumulator was placed entirely within the volume occupied by the 5 μm thick silicon detector with area 8 mm x 8 mm. The conical photon source was sited 23 mm away from a 5 μm thick silicon detector; these dimensions corresponds to a 0.05 radian semi-angle with full coverage of the 5 μm silicon detector by the incident photon source as shown in Figure 3.9. The narrow 0.05 radian cone semi-angle for this 22 keV photon source was used to aid the efficiency of the simulation from a geometrical perspective i.e. to allow the Monte Carlo simulation to track only those photons which are directed towards the silicon. The geometry did not include a tungsten enclosure as any scattered photons incident on it would be mostly absorbed. An 120 μm thick foil of aluminium was placed over the external entrance window of the physical PIXS detector (as it is sensitive to ambient optical photons); this aluminium foil was included in the Monte Carlo simulation. Note that there is no internal aluminium layer behind the entrance window in the PIXS detector. The external 120 μm thick foil of aluminium attenuates the transmission of source photons into the PIXS chamber. The transmission versus energy for aluminium for source photons at 22 keV is shown in Figure 3.8. The transmission of source photons at 22 keV through the 120 μm inner aluminium entrance window was 0.928, derived using Equation 2.24 with its mass absorption coefficient μ_{Al}= 2.3023 cm^{2}g^{-1}, its density ρ_{Al}= 2.7 gcm^{-3} and thickness t_{Al}= 120 µm.

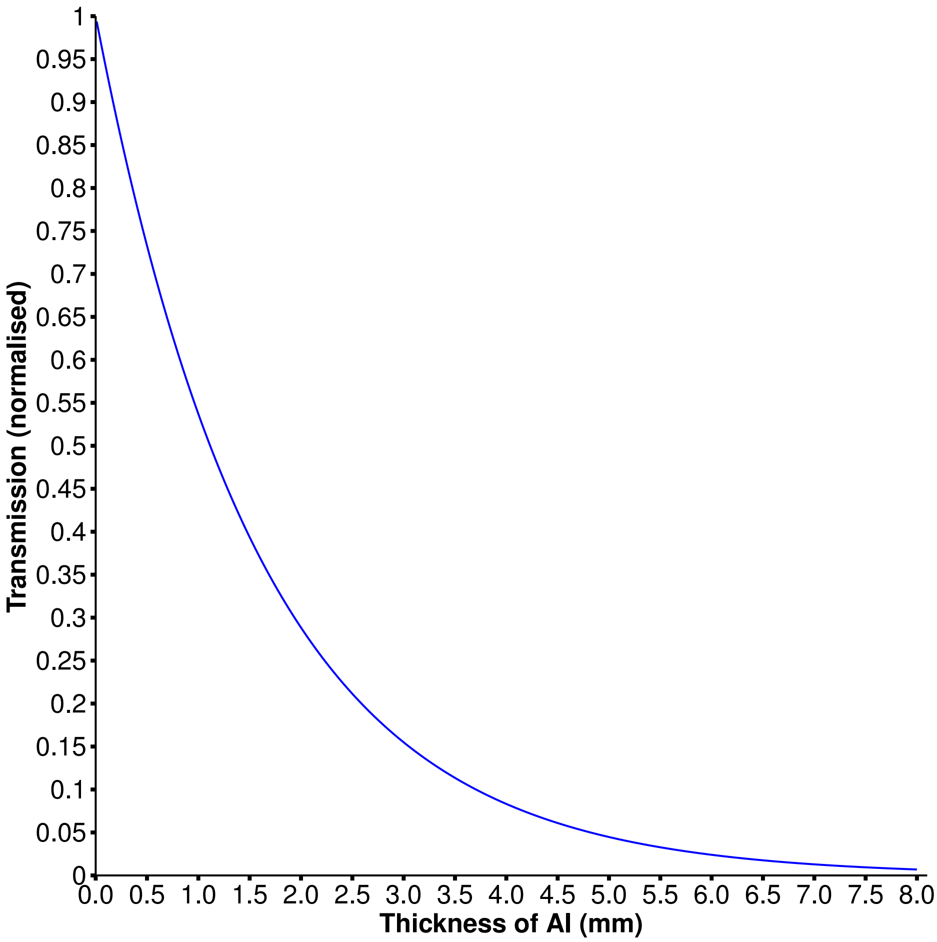

Figure 3.8: The transmission for aluminium with incident photons at 22 keV.

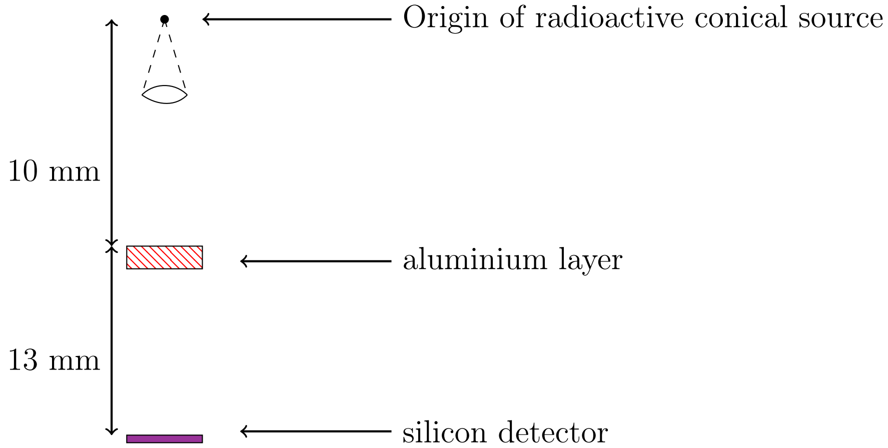

Figure 3.9: Schematic of the model to assess the distribution of energy deposited within an event accumulator positioned within a 5 μm silicon layer using a 22 keV mono-energetic conical source.

Within the Monte Carlo simulations, an event accumulator was set with 900 energy bins between an energy interval from 1 keV to 90 keV. Even though only 22 keV photons were simulated in this section, the energy interval was increased to 90 keV so as to allow this particular simulation to be compared with the full spectral cadmium-109 radionuclide source described in the following paragraph noting that there is a gamma photon emission at 88 keV. One hundred concurrent simulations were performed over a duration of 40 hours with each simulation generating a 22 keV source of photons. The simulation was performed for 40 hours based on the guidelines established in section 3.3, neglecting interactions with the intervening air. In the following graphs showing the distribution of energy deposition, the statistical uncertainty in the ordinate was $\pm 1/\sqrt{N}$ for N events per energy bin, and that for the abscissa was $\pm$ 0.1 keV but not shown for clarity.

Simulation using a full spectral cadmium-109 radionuclide

Following the methodology of the Monte Carlo simulation performed above, the mono-energetic 22 keV photon flux source was replaced with a full spectral cadmium-109 radionuclide and the simulation repeated. The spectrum was derived from Chu et al. [1999], including the gamma photon emission at 88 keV as shown in Table 3.3. In PENELOPE the photon energies and normalised line intensities are created line-by-line for the photon source in order of increasing energy.

X-rays from cadmium-109, Energy (keV)	Line Intensity (%)	Assignment
2.634	0.18 (3)	$Ag\ L_l$
2.978	0.50 (8)	$Ag\ L_{\alpha 2}$
2.984	4.5 (7)	$Ag\ L_{\alpha 1}$
3.151	2.62 (6)	$Ag\ L_{\beta 3}$
3.348	0.58 (9)	$Ag\ L_{\beta 2}$
3.520	0.28 (4)	$Ag\ L_{g1}$
21.990	29.5 (11)	$Ag\ K_{\alpha 2}$
22.163	55.7 (20)	$Ag\ K_{\alpha 1}$
24.912	4.76 (17)	$Ag\ K_{\beta 3}$
24.943	9.2 (3)	$Ag\ K_{\beta 1}$
25.455	2.30 (8)	$Ag\ K_{\beta 2}$
25.511	0.487 (24)	$Ag\ K_{\beta 4}$
Gamma from cadmium-109, Energy (keV)		
88.04	3.61 (0.36)	Gamma

Table 3.3: Principal X-ray and gamma emission peaks cadmium-109 from [Chu et al., 1999]

3.4.2 Results

Simulation using a mono-energetic 22 keV photon flux source

Using a mono-energetic 22 keV photon flux source the distribution of energy deposited within the event accumulator in the 5 μm silicon layer is shown in Figure 3.10. Of the 4.6 x 10^9 simulated primary photons, (1.057 ± 0.0001) x 10^9 were accumulated at 22 keV. The small peak has amplitude (3.448 ± 0.002) x 10^6 at 20.3 ± 0.1 keV is denoted by $\mathrm{Si}_{\mathrm{ep}}$. The energy of the Si $K_{\alpha 1}$ is 1.740 keV and Si $K_{\alpha 2}$ is 1.739 keV with probabilities 0.646 and 0.325. The energy of the Si $K_{\beta 1,2}$ is 1.8360 keV, noting that the probability for a Si K_{β} event is low, (0.019 for a Si $K_{\beta 3}$ and 0.01 for a Si $K_{\beta 1}$ event) [Sanchez del Rio et al., 2003]. The ratio of the small to large peak is 0.003 ± 0.001.

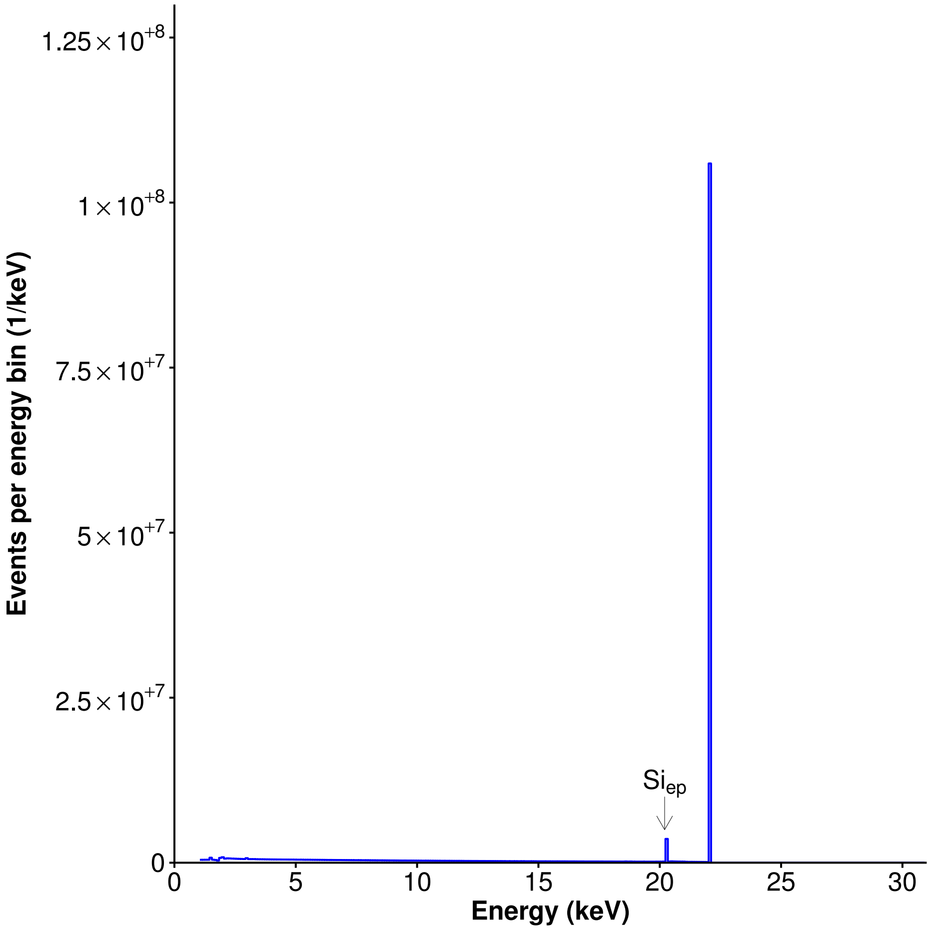

Figure 3.10: 40 hours' simulation of the distribution of energy deposition within an event accumulator in the 5 μm silicon layer using a 22 keV mono-energetic source. The number of simulated primary photon histories was 4.6 x 10^9. Si_{ep} is a silicon escape peak.

The Si_{ep} peak at 20.3 ± 0.1 keV occurs because the incident photons produce fluorescence in silicon (mostly K shell), and a proportion of the silicon K X-rays can escape from the silicon detector. The energy deposition accumulator resides within the volume of the silicon detector and when a escape event occurs, the accumulator records an event equivalent to a photon with energy given by the difference between the incident primary photon energy and the silicon K_α fluorescence photon. Using PENELOPE the photoabsorption mean free path was derived to be to 12 μm for a silicon K_α fluorescence photon at 1.74 keV. This proportion would however be determined by the origin of the escape peak within the silicon crystal and its range within the volume occupied by the accumulator. The spectral response below the Si_{ep} peak is discussed in the following section.

The intensity ratio k of the areas under the events collected in the energy bin for Si_{ep} compared to that for incident photon peak has been estimated by [Reed and Ware, 1972] using Equation 3.3

$$k = \frac{0.035\epsilon}{1 - 0.035\epsilon} \tag{3.3}$$

where ϵ is the fraction of silicon K X-rays that escape from a silicon detector. The factor 0.035 is determined from the product of two proportions:

- the proportion of K shell ionizations (= 0.92) [Heinrich, 1966],
- and the proportion of these which produce K shell fluorescence so yielding silicon K X-rays (= 0.038) [Fink et al., 1996].

Fioratti and Piermattei [1971] derived ϵ for incident photons impinging at an angle θ subtended from the crystal axis as Equation 3.4

$$\epsilon = 0.035\left[(1 - \cos\,\theta)(\frac{\sigma_{Si}}{\sigma_i})ln\left(1 + \frac{\sigma_i}{\sigma_{Si}\cos\,\theta}\right)\right] \tag{3.4}$$

where σ_{Si} and σ_i are the photoelectric cross-sections of the X-ray fluorescence photon and the incident photon respectively. This analytical derivation for the finite width detector above makes not distinction between either $K_{\alpha 1}$ or $K_{\alpha 2}$ silicon escape photons. For a finite width silicon detector of dimensions 5 µm thick with cross-section 8 mm x 8 mm and 23 mm away from the point source cos θ in Cartesian coordinates is given by Equation 3.5

$$\cos\,\theta = \frac{z}{\sqrt{x^2 + y^2 + z^2}} \tag{3.5}$$

Using Equation 3.4 with σ_i= 1.4193 x 10^{-22} cm^2 and σ_{Si}= 1.6657 x 10^{-20} cm^2 and Equation 3.5 with $\cos\,\theta = 0.897$, ϵ was calculated to be = 0.114. The values for σ_{Si} and σ_i which are the photoelectric cross-sections of the X-ray fluorescence photon and the incident photon respectively, were derived using PENELOPE. The ratio k can be calculated from Equation 3.3 as 0.004. In a real detector electronic noise would broaden the line widths and the escape peak is always narrower than the parent peak, [Reed and Ware, 1972].

In the Monte Carlo simulation which does not include detector noise, the relative heights of the Si_{ep} peak to the 22 keV peak was 0.003 $\pm$ 0.001. Table 3.4 shows a summary of these findings for the peak ratios which shows the Monte Carlo estimate of peak ratio ϵ is a good fit to the analytical one. A literature search at the time of writing did not reveal any comparative experiment to measure the peak ratio ϵ for a parent photon of incident energy 22 keV. However, an experiment could be performed to measure the peak ratio ϵ using a multichannel pulse height analyser and a mono-energetic source of photons from a synchrotron. The Monte Carlo model also takes account of the photon mass attenuation coefficients for silicon as a function of energy as shown in Figure 2.2.

peak ratio ϵ	
Monte Carlo Simulation	0.003 $\pm$ 0.001
Finite width detector	0.004

Table 3.4: Comparison of the peak ratios ϵ

Simulation using a full spectral cadmium-109 radionuclide

In Figure 3.11 the results from the energy deposition event accumulator within the 5 μm silicon layer is shown for the full spectrum of the cadmium-109 radionuclide. The spectrum was derived from Chu et al. [1999] as shown in Table 3.3. This figure shows a large peak at 3.05 ± 0.1 keV and relatively much smaller peaks at 2.6 ± 0.1 keV, 3.3 ± 0.1 keV and 3.5 ± 0.2 keV due to Ag L X-rays. Aside from the photoelectric cross-section, the relative heights of the Ag L X-rays and the Ag K X-rays can be determined by the line intensities and branching ratios using a reference database [Chu et al., 1999]. The relative line intensities of the $Ag\ K_{\alpha,\beta}$ peaks are evaluated further in Figure 3.12. There are also small peaks due to aluminium $K_{\alpha,\beta}$ approximately between 1.4 keV to 1.5 keV.

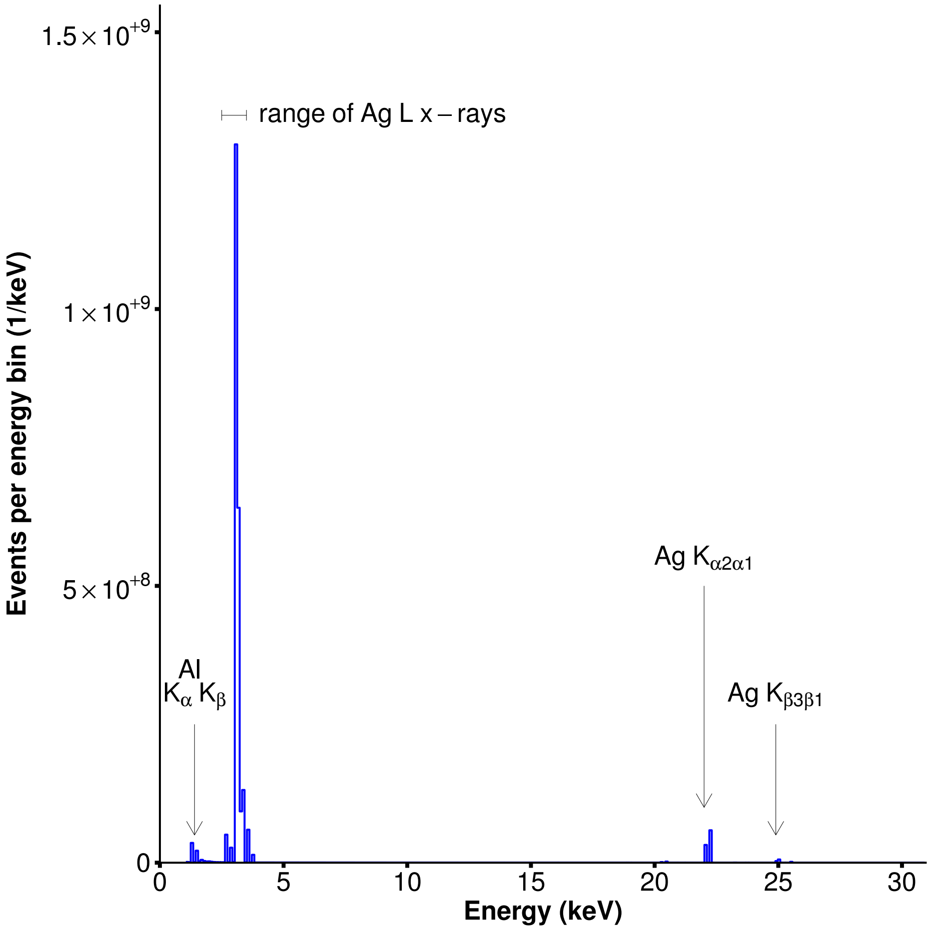

Figure 3.11: 40 hours' simulation of the distribution of energy deposition within an event accumulator in the 5 μm silicon layer using a full spectral cadmium-109 radionuclide. The two sets of adjacent $Ag\,K_\alpha$ and $Ag\,K_\beta$ peaks are close together as shown are in order of increasing energy. The number of simulated primary photon histories was 5.2 x 10^9.

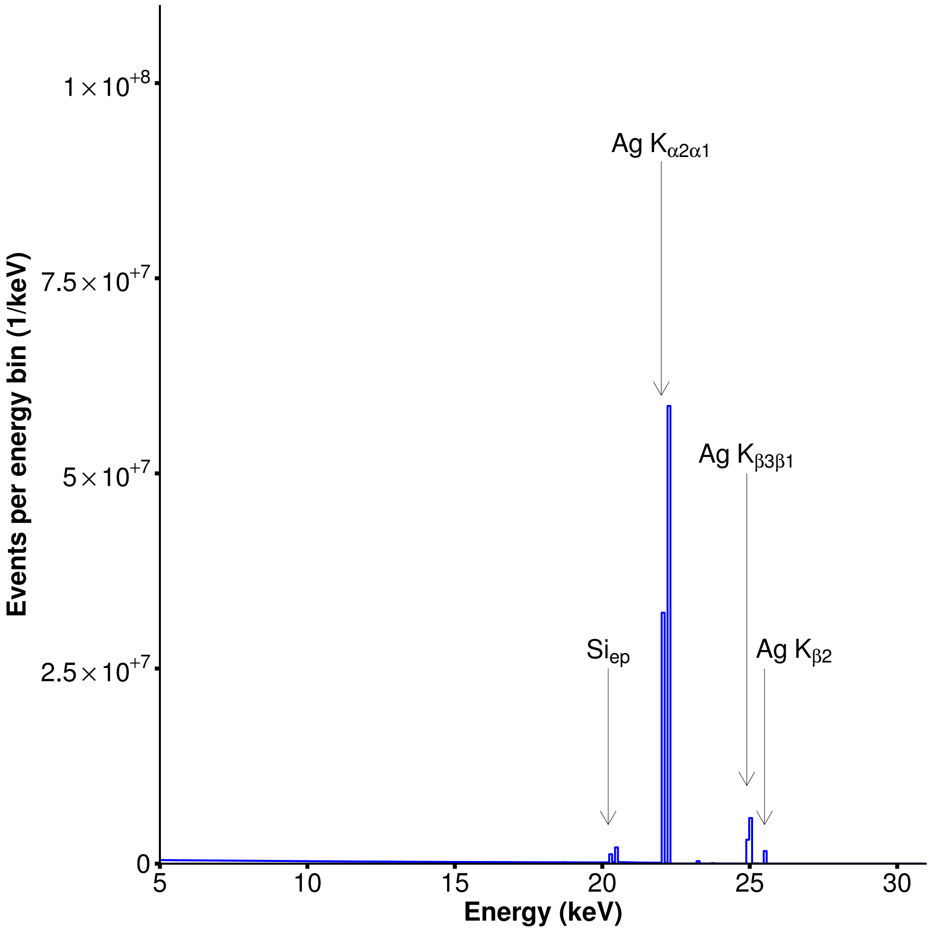

Figure 3.12: 40 hours' simulation of the distribution of energy deposition within an event accumulator in the 5 μm silicon layer using a full spectral cadmium-109 radionuclide for the portion of the principal $Ag\ K_{\alpha,\beta}$ peaks within the energy range 5 keV to 30 keV. The two sets of adjacent $Ag\,K_\alpha$ and $Ag\,K_\beta$ peaks are close together as shown are in order of increasing energy. The number of simulated primary photon histories was 5.2 x 10^9. $\mathrm{Si_{ep}}$ are the silicon escape peaks from the $Ag\ K_\alpha$ peaks.

In the recorded response for the 5 μm silicon layer as shown in Figure 3.12, one sees small adjacent peaks at 20.2 ± 0.1 keV and 20.3 ± 0.1 keV. The ratio of the 20.2 ± 0.1 keV and 20.3 ± 0.1 keV peak to their respective $Ag\ K_\beta$ peak $Ag\ K_\alpha$ peak is expected as fluorescence from each parent peak can cause escape events. In each case the accumulator records an event equivalent to a photon with energy given by the difference between the parent photon energy and the respective silicon K_α K_β fluorescence photons.

3.4.3 Discussion

Energy Bin widths

In PENELOPE there is a limit on the number of energy bins which can be assigned for a chosen incident photon energy range. The binning of the energy was arbitrarily chosen for all subsequent simulations for a cadmium-109 source using a bin width of 0.1 keV with energy range up to 90 keV, and for a technetium-99m source using a bin width of 0.5 keV with energy range up to 200 keV. The recorded events D_i in bin i is given by Equation 3.6

$$D_i \propto \ S_j V_j \Delta t \tag{3.6}$$

where the source flux of photons is S_j, the volume of the accumulator V_j and Δt is the duration of the recording. If one reduced the width of the energy bin then this would imply either increasing the duration of the recording or increasing the effective volume of the accumulator; both of these would reduce the variance in the events for each energy bin.

Simulation using the full spectral cadmium-109 radionuclide

For a simulation using 5.2 x 10^9 primary photon histories there is a large peak at 3.05 $\pm$ 0.1 keV as shown in Figure 3.11. The response of silicon can be considered in the context of its partial mass attenuation coefficients as shown in Figure 2.2 noting the silicon K edge at 1.84 keV, with the dominant interaction at energies less than 70 keV within silicon being photoabsorption.

The large peak at 3.05 $\pm$ 0.1 keV and smaller adjacent peaks (within approximately $\pm$ 0.5 keV) arise because the probability is greater for photoabsorption for lower incident energies from the *Ag L* series X-rays relative to the higher incident energies from the *Ag K* series X-rays. The Monte Carlo simulation however does not include detector noise, which would mask the aluminium fluorescence, and would also mask the silicon escape peaks.

3.5 Modelling of the Compact Gamma Camera

3.5.1 Method

Estimate of detector efficiency as a function of energy deposited

One recalls from section 3.2 that measurement B is used to determine the energy deposition of photons within a specified volume bounded by the detector cross-section as shown in Figure 3.6. The detection efficiency as a function of energy deposited is ratio of events recorded by measurement B to the incident primary photons. In the case of the Compact Gamma Camera, this is the proportion of the emitted photon flux which is directed towards the silicon detector with an intervening caesium iodide crystal in the absence of scintillation photons. In this section the detector efficiency as a function of energy deposited within the accumulator occupying the volume of the silicon detector is calculated using Monte Carlo simulation.

A schematic of the Compact Gamma Camera used in this simulation is shown in Figure 3.2. The CGC comprised of a 3 mm thick tungsten outer enclosure with a 0.5 mm diameter cylindrical pinhole tungsten collimator 6 mm thick. Internally, the CGC was modelled with a 120 μm inner aluminium entrance window, a 1500 μm caesium iodide monolithic crystal and a 5 μm thick silicon detector. A 1500 μm thick caesium iodide monolithic crystal was modelled as an approximation to a close-packed (85%) columnar crystal [Hamamatsu-Photonics, 2019]. The area of the 5 μm silicon detector and the 1500 μm thick caesium iodide monolithic crystal were both 8 mm^2.

The geometrical arrangement for this simulation is shown in Figure 3.13 where a 140.5 keV conical photon source was positioned centrally on-axis 10 mm away from the entrance face of the tungsten collimator; 140.5 keV is the photopeak energy of technetium-99m [Chu et al., 1999]. The silicon detector was about 23 mm away from the source. The 0.5 mm diameter cylindrical pinhole tungsten collimator 6 mm thick subtends a semi-angle of 0.025 radians.

A narrow conical beam of 0.05 radians for 140.5 keV photon source was used as a variance reduction technique to optimise the simulations. This conical beam just covers the outward facing hole of the tungsten collimator. If a much wider beam source of photons was used, any scattered photons would be absorbed by the tungsten enclosure and reduce the efficiency for the Monte Carlo simulation. Variance reduction techniques are designed to improve the statistics of the Monte Carlo simulation and are described in detail by [Salvat et al., 2011].

One hundred concurrent simulations were performed for 60 hours following the guidelines established in section 3.3. The energy binning was arbitrarily set to 0.5 keV for all the simulations which is wide enough to ensure sufficient events have been collected in each bin, and complies with the maximum number of bins available within PENELOPE.

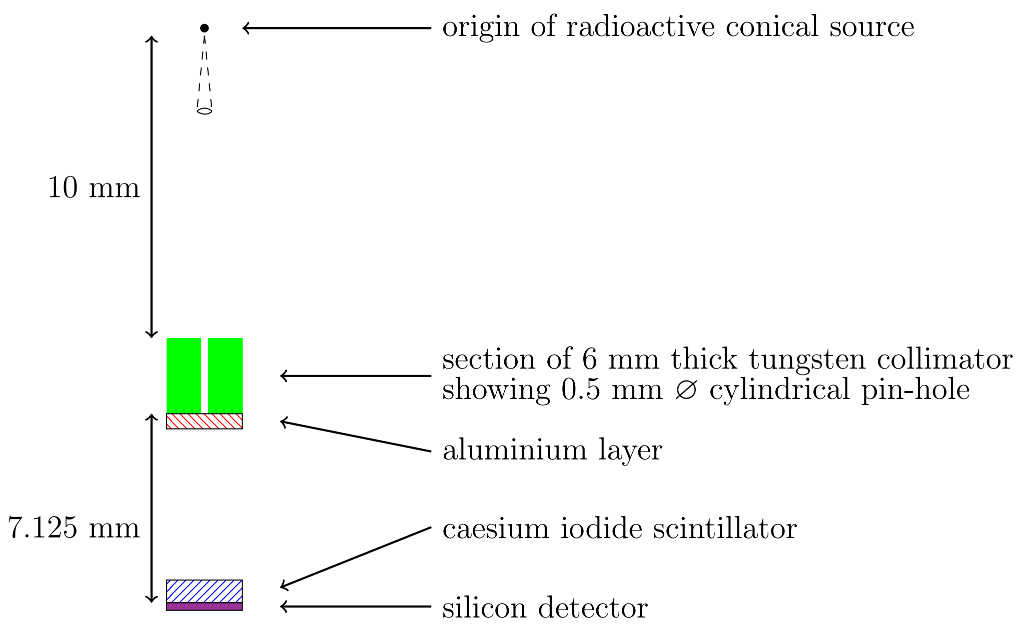

Figure 3.13: Schematic of the CGC model to assess the distribution of energy deposited within an event accumulator positioned within a 5 μm silicon layer using a 140.5 keV mono-energetic conical source and intervening 1500 μm thick caesium iodide monolithic crystal .

3.5.2 Results

The PENELOPE Monte Carlo code simulated 3.2 x 10^8 primary photons and directly produced its simulation results including the detector efficiency as a function of energy deposited within the 5 μm thick silicon detector. This value E_{Si} was computed to be (2.23 ± 0.06) x 10^{-3}. From the same simulation, the detector efficiency as a function of energy deposited within the cross-section of the 1500 μm thick caesium iodide monolithic crystal E_{CsI} was (4.165 ± 0.004) x 10^{-1}. This latter value takes into account the transmission of source photons through the 120 μm inner aluminium entrance window as 0.9998, derived using Equation 2.24 with its mass absorption coefficient μ_{Al}= 6.1575 x 10^{-3} cm^{2}g^{-1}, its density ρ_{Al}= 2.7 gcm^{-3} and thickness t_{Al}= 120 μm.

This estimate of the detector efficiency as a function of energy deposited for photons within the 5 μm thick silicon detector was determined for a 140.5 keV photon conical source. As mentioned the 0.5 mm diameter cylindrical pinhole tungsten collimator 6 mm thick subtends a semi-angle of 0.025 radians. Thus the solid angle ψ subtended by the cone with apex of $\alpha = 0.025$ radians is given by Equation 2.23 as 0.76 steradians. So the detector efficiency as a function of energy deposited for photons within the 5 μm silicon detector for a point source was derived to be (1.69 ± 0.05) x 10^{-3}.

3.5.3 Discussion

In the Monte Carlo simulation with a 140.5 keV source, the detector efficiency as a function of energy deposited for photons within the 5 μm thick silicon detector for a point source was derived to be 0.17%. This is consistent with the physical interpretation that most of the gamma photons at 140.5 keV pass through the 5 μm silicon detector. The detector efficiency as a function of energy deposited within the 1500 μm thick caesium iodide monolithic crystal E_{CsI} for a point source was 31.65% and is used to generate scintillation photons, discussed in detail in chapter 6. While using a thicker caesium iodide monolithic crystal might be considered beneficial for stopping incoming source photons, it also has a side effect of increasing Compton scatter which degrades the clinical image. This increase of Compton scatter with increasing thickness of crystal is demonstrated in the following chapter.

From geometric considerations [Lees et al., 2011] showed that using a point source at 25 mm on axis with incident 140.5 keV gamma photons and a 0.5 mm diameter pinhole tungsten collimator 6 mm thick with an acceptance angle of 60 degrees, the estimate for detector efficiency for fluence was 4.5 x 10^{-5}. The estimate provided by [Lees et al., 2011] of 4.5 x 10^{-5} included septal penetration by gamma photons using a more detailed analytical calculation [Metzler et al., 2001].

However, in this Monte Carlo simulation with a 140.5 keV source, the detector efficiency as a function of energy deposited within the 5 μm thick silicon detector, as opposed to fluence across the cross-section of the 5 μm silicon detector, for a point source was modelled with a cylindrical pinhole whereas the actual mechanical design of the collimator hole is tapered with a larger acceptance angle. Nonetheless, this should be considered for future work.

3.6 Conclusions

Two models of SFOV systems were simulated - one describing a bare silicon detector called the Portable Imaging X-ray Spectrometer detector which was used to assess the spectral response for both mono-energetic 22 keV photons and the full spectral cadmium-109 source; and the second describing the simulation of the Compact Gamma Camera.

For the simulation of the PIXS detector both the mono-energetic 22 keV photon source and the full spectral cadmium-109 source Monte Carlo simulations demonstrated the presence of $Ag\ K_\alpha$ and $Ag\ K_\beta$ peaks consistent with the line intensities for the referenced database [Chu et al., 1999].

With an incident photon source at 22 keV, an analytical derivation of the silicon K X-rays that escape from a finite 8 mm x 8 mm by 5 μm thick silicon detector, assuming that the width of the silicon escape peak and the incident parent peak are both 0.1 keV, the ratio of peak heights was determined to be 0.004. In the corresponding Monte Carlo simulation the relative heights of the $\mathrm{Si_{ep}}$ peak to the 22 keV peak was 0.003 ± 0.001 which was in good agreement. The Fano-limited Monte Carlo simulation however does not include readout noise due to incomplete charge collection and detector noise found in a real silicon detector (see section 2.3.3), which would mask the silicon escape peaks discussed further in chapter 5.

Lastly, the Monte Carlo simulation of the detector efficiency as a function of energy deposited for photons within the 5 μm thick silicon detector for a point source was derived to be 0.17%, consistent with the physical interpretation that the majority of gamma photons pass through the silicon. The detector efficiency as a function of energy deposited included photoabsorption and Compton scattering interactions which have not been previously modelled.

Chapter 4

The tracking of gamma and X-ray photons through a caesium iodide crystal to a silicon detector.

4.1 Introduction

In the chapter 3 Monte Carlo modelling was used to determine the distribution of energy deposited within a target silicon detector firstly using incident gamma photons with energy of 22 keV, and then using the full emission spectrum of cadmium-109 as the source. In this current chapter several PENELOPE Monte Carlo simulations were utilised to investigate individual materials used within the Compact Gamma Camera as incident photons were directed towards them. By selecting each target material, the energy deposited or the fluence from the material could be determined respectively using either energy deposition or fluence accumulators. These types of accumulators as described in section 3.2 in the previous chapter. Specifically, the PENELOPE Monte Carlo simulations were used to show the energy deposited within the caesium iodide crystal, the distribution of photon fluence from caesium iodide crystal and the distribution of energy deposited within a silicon detector.

The first part of this chapter considers a simulation with gamma photons of energy 140.5 keV incident upon a target monolithic caesium iodide crystal, 8 mm x 8 mm x 600 μm thick[1]. An energy deposition accumulator was positioned within the volume occupied by the caesium iodide crystal, and used to measure the energy deposited by photons in the crystal. These results were used for spectral verification of the Monte Carlo simulation by corroborating with available reference data, [Chu et al., 1999]. The energy deposited within the caesium iodide crystal creates scintillation photons which are discussed in chapter 6 using the GEANT4 Monte Carlo code.

In the second simulation a accumulator was positioned at the egress from the monolithic crystal and was used to determine the distribution of photon fluence from 600 μm thick caesium iodide. As mentioned in the previous chapter, the average fluence of photons across the detector cross-section and recorded within the volume of the fluence accumulator is given by a measurement of the total number of photons per unit area which contribute when their trajectory intersects this volume during the time of the simulation.

It was also interesting to assess the effects on the energy distribution for photon fluence with increasing thickness of the caesium iodide crystal. Thus, starting with the 600 μm crystal, the effects of increasing thickness were ascertained using selected thicknesses of 1500 μm and 8000 μm. The effectiveness of stopping incident gamma photons depends on both the density and thickness of the scintillator. A traditional LFOV gamma camera utilises a sodium iodide scintillator of between one quarter inch to about one third inch thickness for incident photons of energy 140.5 keV (which is the photopeak energy of technetium-99m). The upper limit for modelling was therefore

[1]As mentioned this CGC model initially consisted of a columnar caesium iodide crystal of 600 μm and then later replaced with 1500 μm thickness as these were commercially available at the time of the construction of the gamma camera [Hamamatsu, 2016].

arbitrarily chosen to be 8000 μm.

Finally, in order to assess the distribution of energy deposited within a silicon detector of area 8 mm x 8 mm and 5 μm thick, an event accumulator was positioned such that it occupied the whole volume of this silicon detector.

It should be noted that the PENELOPE Monte Carlo code [Salvat et al., 2011] does not include detector noise nor does it incorporate modelling of scintillation photons. In the following graphs showing the distribution of energy deposition, the statistical uncertainty in the ordinate was respectively $\pm 1/\sqrt{N}$ for N events per energy bin (for the energy deposition accumulator) or fluence per energy bin (for the fluence accumulator); the statistical uncertainty for the abscissa was ± 0.5 keV but both sets of error bars were not shown for clarity. In these simulations incident photons of energy 140.5 keV were used. We recall that within PENELOPE the number of energy bins is limited to 400 for incident low energy photons up to 200 keV, i.e. the bin width is 0.5 keV.

4.2 Modelling of the Energy Deposition within a monolithic caesium iodide crystal

4.2.1 Method

Energy Deposition within caesium iodide

A Monte Carlo model was created with an 8 mm x 8 mm monolithic caesium iodide crystal of thickness 600 μm positioned at 10 cm away from a 140.5 keV mono-energetic conical photon source with a 5 degree semi-angle and centrally directed orthogonal to the plane of the target crystal. These dimensions were arbitrarily selected so as to ensure a wide-beam photon flux irradiated the whole of the target caesium iodide crystal. A schematic of this set-up is shown in Figure 4.1. The 140.5 keV mono-energetic photon source corresponds to the principal gamma emission energy for technetium-99m, which is the most commonly used radionuclide in nuclear medicine. No enclosure was included in this simulation as the aim was to determine the distribution energy deposition events within the caesium iodide crystal.

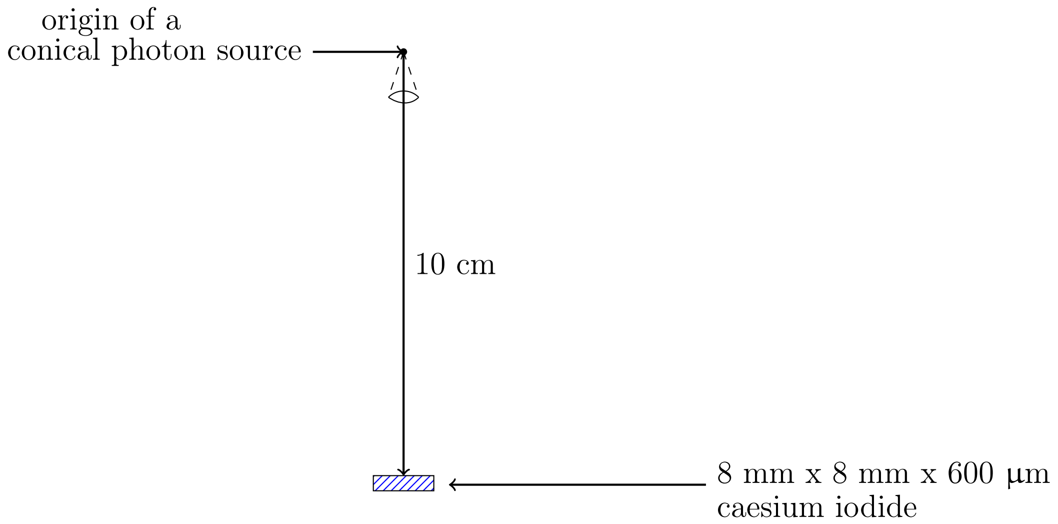

Figure 4.1: Schematic to assess the energy deposited within 8 mm x 8 mm x 600 μm caesium iodide crystal using a 140.5 keV mono-energetic conical photon source.

The Monte Carlo simulation was performed for 40 hours, following the simulation convergence guidelines established in section 3.3. In Monte Carlo simulations the probability density functions describing the photon interactions must be appropriately sampled to ensure the simulation provides a true physical account of the interaction parameter being measured. The energy binning was set to 0.5 keV with the simulation producing an output of the distribution of energy deposited within the 600 μm caesium iodide crystal. The Monte Carlo simulation was then repeated replacing the 600 μm thick caesium iodide crystal with the selected thickness of 1500 μm and then 8000 μm. For brevity the distribution of energy deposited within the caesium iodide are only shown for the 600 μm thick crystal since the energy spectra were found to be similar when using either 1500 μm or 8000 μm thick caesium iodide crystals.

4.2.2 Results

Distribution of the energy deposition within 600 μm caesium iodide

The energy deposition spectrum within the monolithic 600 μm caesium iodide crystal for a 40 hours' simulation period is shown in Figure 4.2.

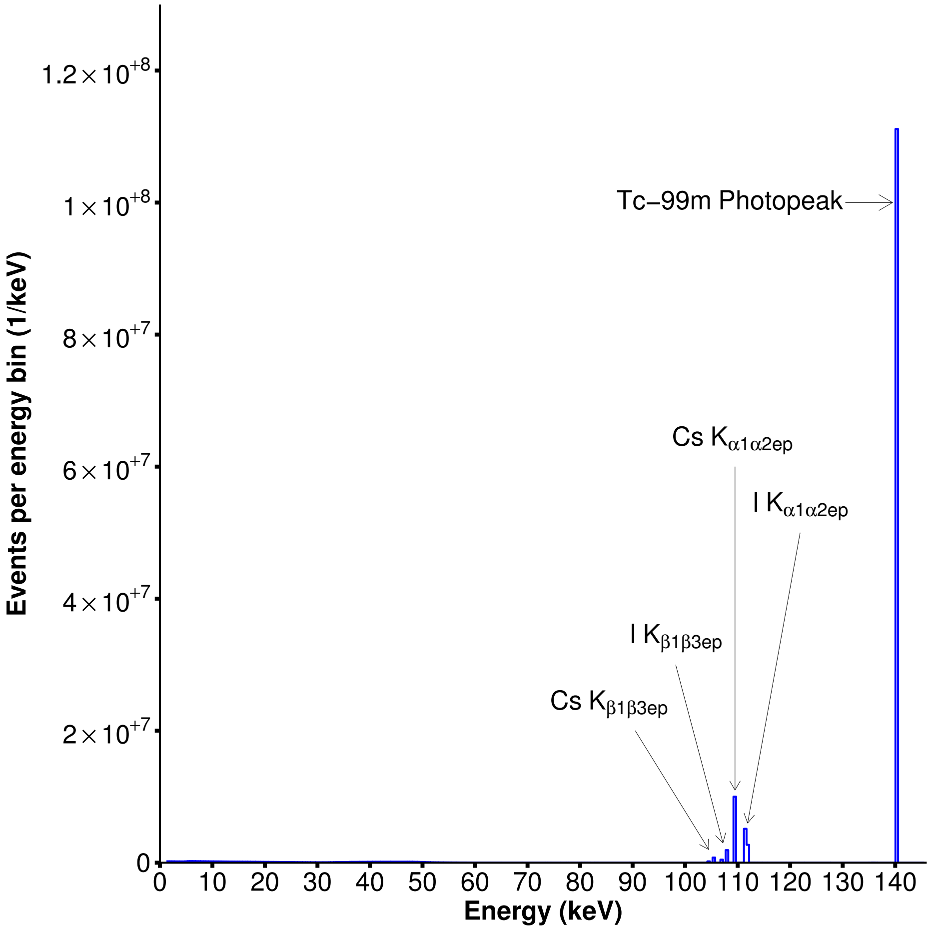

Figure 4.2: 40 hours' simulation of the distribution of energy deposition within an event accumulator in the 600 μm caesium iodide using a 140.5 keV mono-energetic photon source. The number of simulated primary photon histories was 1.4 x 10^8. caesium and iodine principal K_α, K_β escape peaks are also shown with subscript $_{\text{ep}}$.

The peaks in the simulated energy deposition spectrum were obtained by a energy deposition event accumulator sited within the volume occupied by the caesium iodide crystal and which subtended a 5 degree semi-angle from the position of the conical photon source. This distribution of the energy deposited demonstrates a very large photopeak at 140.0 ± 0.5 keV of amplitude (1.150 ± 0.006) x 10^8 events per energy bin (1/keV). The simulated number of primary photons was 1.4 x 10^8.

To aid the discussion the response of monolithic caesium iodide can be considered in the context of its partial mass attenuation coefficients as shown in Figure 4.3 with the dominant interaction at energies less than 200 keV being photoabsorption with μ_i the partial mass attenuation coefficients and the target density ρ= 4.51 gcm^{-3}.

Legend: Photoabsorption, Compton, Rayleigh, Total

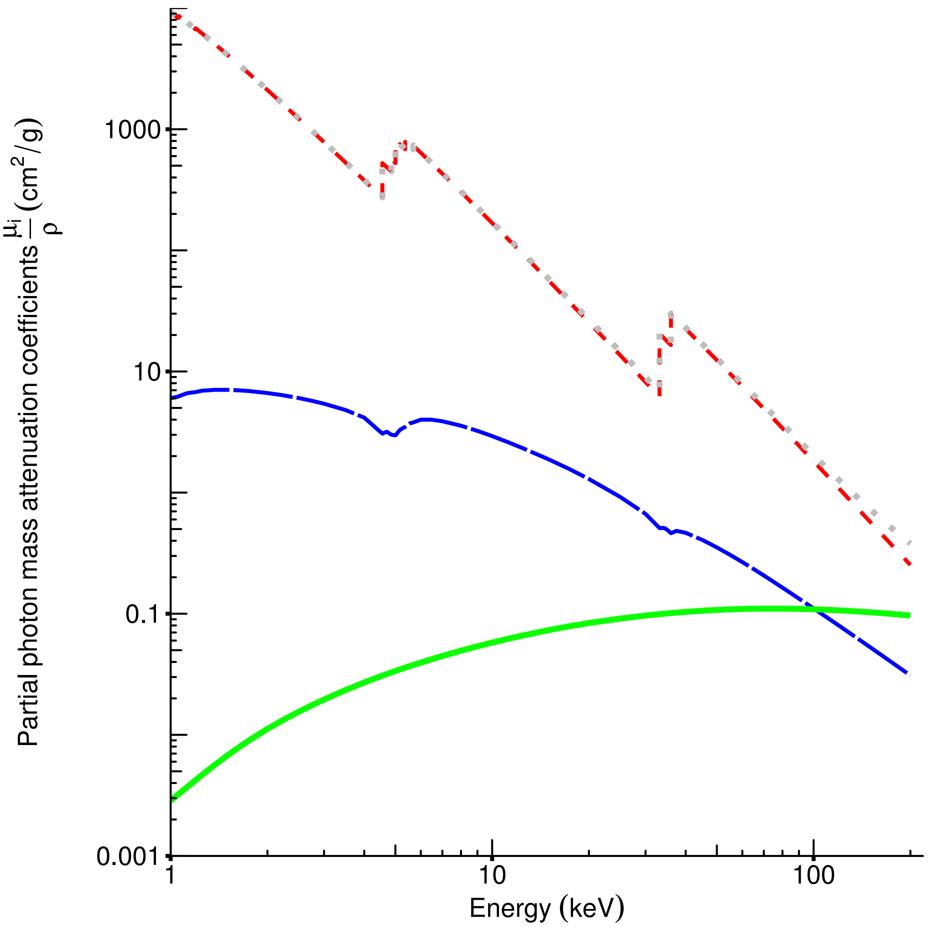

Figure 4.3: Partial photon mass attenuation coefficients μ_i with i= Photoabsorption, Compton scattering or Rayleigh scattering and ρ the target density for caesium iodide up to 200 keV generated using PENELOPE

The ratio of the measured photopeak amplitude to the total number of simulated primary photons was 0.82 for the 600 µm caesium iodide crystal. Using PENELOPE, the partial mass attenuation coefficients for caesium iodide were generated for source photons at 140.5 keV, as shown in Table 4.1.

	Partial photon mass attenuation coefficients for CsI/ cm^2g^{-1}
Photoabsorption	6.8956 x 10^{-1}
Compton scattering	1.0405 x 10^{-1}
Rayleigh scattering	5.961 x 10^{-2}

Table 4.1: Partial photon mass attenuation coefficients for photoabsorption, Rayleigh scattering and Compton scattering for caesium iodide for impinging photons at 140.5 keV generated using PENELOPE.

From these partial mass attenuation coefficients the expected analytical proportion of photopeak events to the sum of photoabsorption, Compton and Rayleigh events was estimated to be 0.81 which was consistent with the simulated photopeak amplitude. Note the photopeak events accumulated within the energy deposition accumulator includes those from photoabsorption, and there will be a very small proportion of events accumulated from Rayleigh elastically scattered photons near the inner surface of the crystal back into the volume occupied by the accumulator.

The escape peaks in the energy deposition events spectrum were analysed for the energy interval between 1 keV and 140 keV excluding the photopeak as shown in Figure 4.4 and these modelled peaks were tabulated in Table 4.2 in comparison with reference data, [Chu et al., 1999, Sanchez del Rio et al., 2003]. The caesium and iodine principal K_α, K_β escape peaks are shown with subscript $_{\mathrm{ep}}$. The region below 100 keV labelled as I + II was examined further in Figure 4.5.

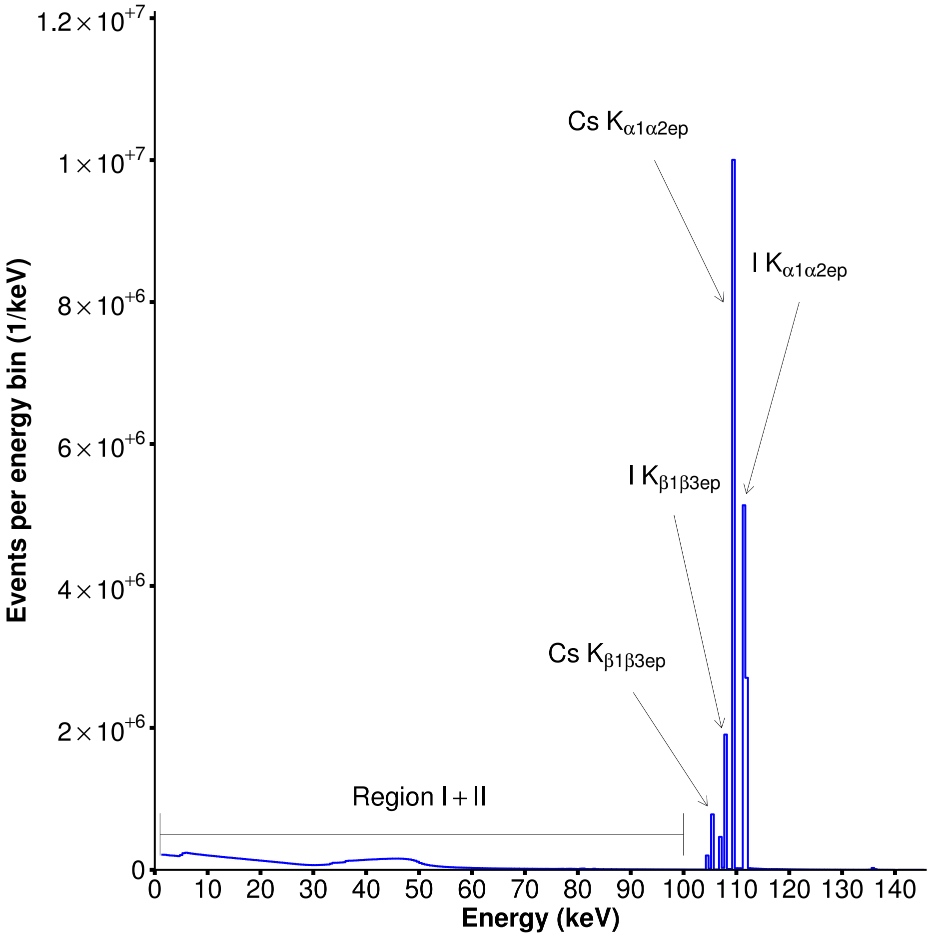

Figure 4.4: 40 hours' simulation of the distribution of energy deposition within an event accumulator in the 600 μm caesium iodide using a 140.5 keV mono-energetic photon source within the energy range 1 keV to 140 keV. The photopeak has been removed for clarity. The caesium and iodine principal K_α, K_β escape peaks are shown with subscript $_{\text{ep}}$. The region below 100 keV is labelled as Region I + II for descriptive purposes.

caesium and iodine escape peaks	Model / keV ± 0.5 keV	Reference/ keV	Model: relative escape peak intensities ±0.05 (arbitrary units)	Reference: relative escape peak intensities
caesium $K_{\alpha 1ep}$	109.5	109.5	0.47	0.524
caesium $K_{\alpha 2ep}$	109.5	109.9	*	0.283
caesium $K_{\beta 1ep}$	105.5	105.5	0.05	0.102
caesium $K_{\beta 3ep}$	105.5	105.6	0.01	0.052
iodine $K_{\alpha 1ep}$	112.0	111.9	0.25	0.526
iodine $K_{\alpha 2ep}$	112.0	112.2	0.13	0.283
iodine $K_{\beta 1ep}$	109.0	108.2	0.09	0.101
iodine $K_{\beta 3ep}$	109.0	108.3	0.02	0.052
			* unresolved	

Table 4.2: Measured peaks in the distribution of energy deposition within an event accumulator in the 600 µm caesium iodide using a 140.5 keV mono-energetic photon source. The caesium and iodine principal K_α, K_β escape peaks are shown with subscript $_{\mathrm{ep}}$. The relative escape peak intensities were ascribed to the modelled ratios of: caesium $K_{\alpha 1}$ and $K_{\alpha 2}$, caesium $K_{\beta 1}$ and $K_{\beta 3}$, iodine $K_{\alpha 1}$ and $K_{\alpha 2}$, iodine $K_{\beta 1}$ and $K_{\beta 3}$. These ratios were compared to the referenced databases, [Chu et al., 1999, Sanchez del Rio et al., 2003].

It is interesting to focus on the distribution of energy deposition within the event accumulator recording up to an arbitrary threshold of 3.0 x 10^5 events per energy bin for the 600 μm thick caesium iodide crystal within the energy range 1 keV to 140 keV. This is shown in Figure 4.5 where the amplitudes in this plot are very small relative to the photopeak and has been arbitrarily segmented in regions I to III for descriptive purposes. For clarity the photopeak together with the caesium and iodine principal K_α, K_β escape peaks (apart from the caesium $K_{\beta 4\mathrm{ep}}$) have also been removed for clarity. Since the energy deposition accumulator was positioned wholly within the volume occupied by the caesium iodide crystal, it accumulates the energy deposited by photons which undergo photoabsorption, Compton scatter, and from fluorescence in the crystal. This is discussed in detail in the following section bearing in mind the plot of partial photon mass attenuation coefficients for caesium iodide up to 200 keV as shown in Figure 4.3. At low energies the partial photon mass attenuation coefficients for photoabsorption and Rayleigh scattering is larger than at higher photon energies within this photon energy interval.

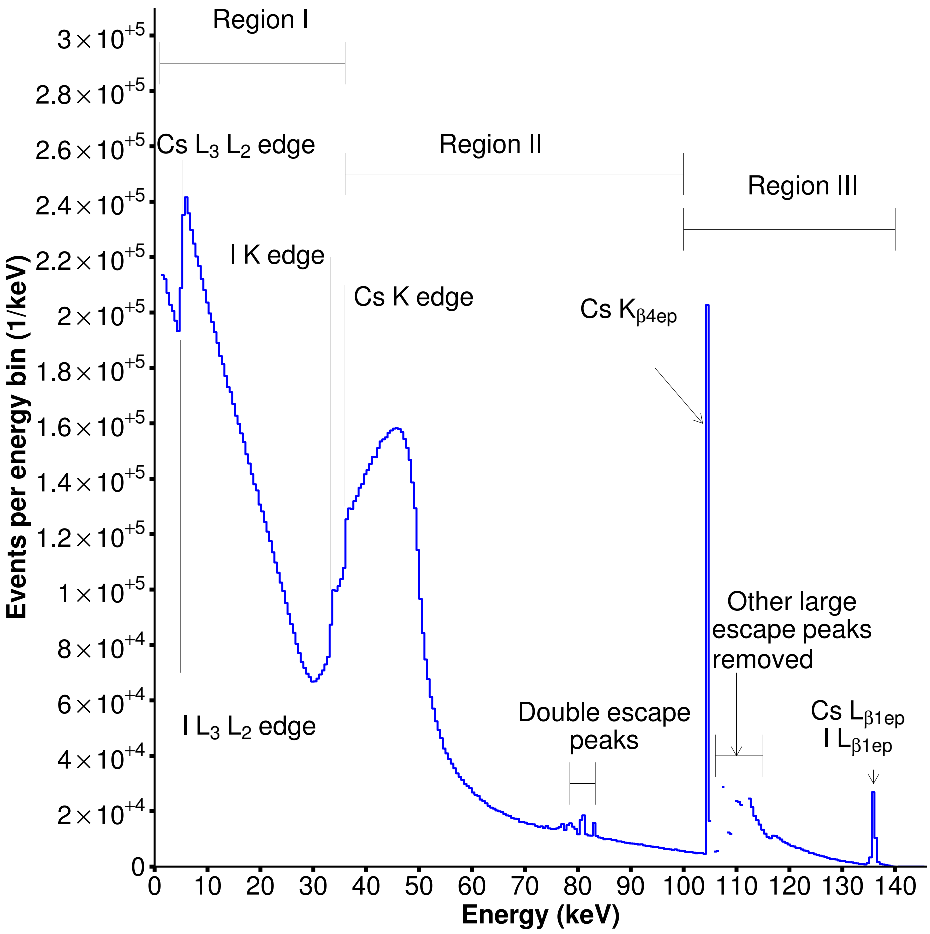

Figure 4.5: 40 hours' simulation of the distribution of energy deposition up to an arbitrary threshold of 3.0 x 10^5 events per energy bin within 600 µm thick caesium iodide crystal within the energy range 1 keV to 140 keV using a 140.5 keV mono-energetic photon source. The plot has been artificially segmented into three regions and labelled Region I, II and III for descriptive purposes. The photopeak together with the caesium and iodine principal K_α, K_β escape peaks (apart from the caesium $K_{\beta 4ep}$) have been removed for clarity. Both caesium and iodine $L_{\beta 1}$, and caesium $K_{\beta 4}$ escape peaks are shown with subscript $_{\mathrm{ep}}$.

4.2.3 Discussion

Distribution of the energy deposited within 600 μm caesium iodide

The ratio of the measured photopeak amplitude to the total number of simulated primary photons in Figure 4.2 was in good agreement with expected analytical proportion of photopeak events to the sum of photoabsorption, Compton and Rayleigh events.

In Figure 4.4 K_α and K_β escape peaks were observed from both caesium and iodine atoms which shows the energy interval up to 140 keV excluding the large photopeak. For photoabsorption events, when the photoelectron is in the K, L or M shells, the simulation proceeds with the excited atom relaxing to its ground state by emitting characteristic X-rays and Auger electrons. If these caesium and iodine fluorescence X-rays occur adjacent to the initial photoabsorption then they are recorded within the total photopeak energy. However if these fluorescence X-rays escape from the caesium iodide crystal, the energy distribution spectrum shows escape peaks as given by the difference between the energy of the source photon which are directed towards the crystal and the energy of the caesium or iodine K_α and K_β fluorescence. As shown in Table 4.2 the caesium and iodine principal K_α, K_β escape peak energies corroborated with two referenced databases, [Chu et al., 1999, Sanchez del Rio et al., 2003].

The relative escape peak intensities were ascribed to the modelled ratios of: caesium $K_{\alpha1}$ and $K_{\alpha2}$, caesium $K_{\beta1}$ and $K_{\beta3}$, iodine $K_{\alpha1}$ and $K_{\alpha2}$, iodine $K_{\beta1}$ and $K_{\beta3}$ as shown in Table 4.2. The intensity of these K_{α} and K_{β} escape peaks from caesium and iodine was found to be about half those in the referenced database. This can be considered in the context of the probability distribution function $p(s)$ of the path length s of the photon from its source position within the caesium iodide crystal as given by Equation 4.1 where λ^{-1} is the interaction probability per unit length. If a K_{α} or K_{β} fluorescence photon with path length s is sufficiently close to the crystal surface and does not undergo any further interaction, it can escape from the crystal.

$$p(s) = \lambda^{-1} exp(-s/\lambda) \tag{4.1}$$

Table 4.3 shows the calculated mean free path λ within caesium iodide for the K_{α} and K_{β} fluorescence photons from caesium and iodine. These values for λ were derived using PENELOPE. The modelled escape peak intensities may not record some of these K_{α} and K_{β} fluorescence photons if the source event originated close to the boundary of the accumulator i.e. less than its mean free path λ .

caesium and iodine fluorescence peaks	Reference/ keV	λ / mm
caesium		
$K_{\alpha 1ep}$	30.973	0.2968
$K_{\alpha 2ep}$	30.625	0.2875
$K_{\beta 1ep}$	34.987	0.1248
$K_{\beta 3ep}$	34.920	0.1241
iodine		
$K_{\alpha 1ep}$	28.612	0.2374
$K_{\alpha 2ep}$	28.318	0.2306
$K_{\beta 1ep}$	32.295	0.3340
$K_{\beta 3ep}$	32.240	0.3324

Table 4.3: The mean free path λ of photons within caesium iodide for the K_α and K_β fluorescence from caesium and iodine.

The distribution of energy deposition within an event accumulator recorded up to an arbitrary threshold of 3.0 x 10^5 events per energy bin is shown in Figure 4.5. In region I there is a sharp decrease between 5 keV and approximately 30 keV indicative of the dominant photoabsorption interaction within this energy interval as corroborated in Figure 4.3. In addition both the iodine and caesium $Cs\ L_3L_2$ edges are seen at approximately 5 keV.

In region II there is Compton continuum which occurs where the incident photons only deposit part of their energy within the crystal and there is a Compton edge at approximately 55 keV. The Compton continuum is truncated by the iodine and caesium $Cs\ L_3L_2$ edges are seen at approximately 5 keV, and the iodine and caesium K edges at 33.2 keV and 35.9 keV respectively. The Compton edge itself is not sharply truncated as the target electrons have a momentum distribution, and the Compton scatter model allows for transitions for bound electrons where the energy difference between the incident and scattered photons is greater than the ionisation energy of the active shell. Very small double escape K_α, K_β peaks are seen superimposed on the Compton valley at approximately 80 keV.

In region III the large caesium and iodine principal K_α, K_β escape peaks have been removed for clarity relative to the caesium $K_{\beta 4\mathrm{ep}}$ which is shown. The truncated tail (from the other large escape peaks) in this region also has a small unresolved caesium and iodine escape $L_{\beta 1}$ peak. These modelled features in regions I, II and III as demonstrated in Figure 4.5 would be masked by system noise in both LFOV and SFOV gamma camera systems.

4.3 Modelling of the photon fluence from caesium iodide

4.3.1 Method

Assessment of photon fluence from caesium iodide

In this Monte Carlo simulation to assess the photon fluence from the egress face of the monolithic caesium iodide crystal, the source to target arrangement shown in Figure 4.1 was used with the 140.5 keV mono-energetic conical photon source directed towards and perpendicular to the plane of the 8 mm x 8 mm x 600 μm caesium iodide crystal. A fluence accumulator of area 8 mm x 8 mm with thickness 600 μm was positioned at the egress from the monolithic crystal (no gap). The thickness of the fluence accumulator was sufficiently larger than the mean free path λ to accumulate any fluorescence X-rays as shown in Table 4.3. The fluence was measured within this accumulator such that it subtended a 5 degree semi-angle about 10 cm away from the conical photon source. If the volume of the fluence accumulator is too small then the simulation is inefficient because there would be too few events recorded. Scintillation photons were not included in the assessment of the photon fluence from the caesium iodide crystal.

4.3.2 Results

Distribution of photon fluence from 600 μm caesium iodide

The distribution of photon fluence within a measurement accumulator positioned at the egress face of the 600 μm caesium iodide crystal is shown in Figure 4.6. This spectrum is the energy distribution of photons that entered the virtual measurement accumulator from the caesium iodide crystal. The duration of the simulation was 40 hours as per guidelines discussed in section 3.3.

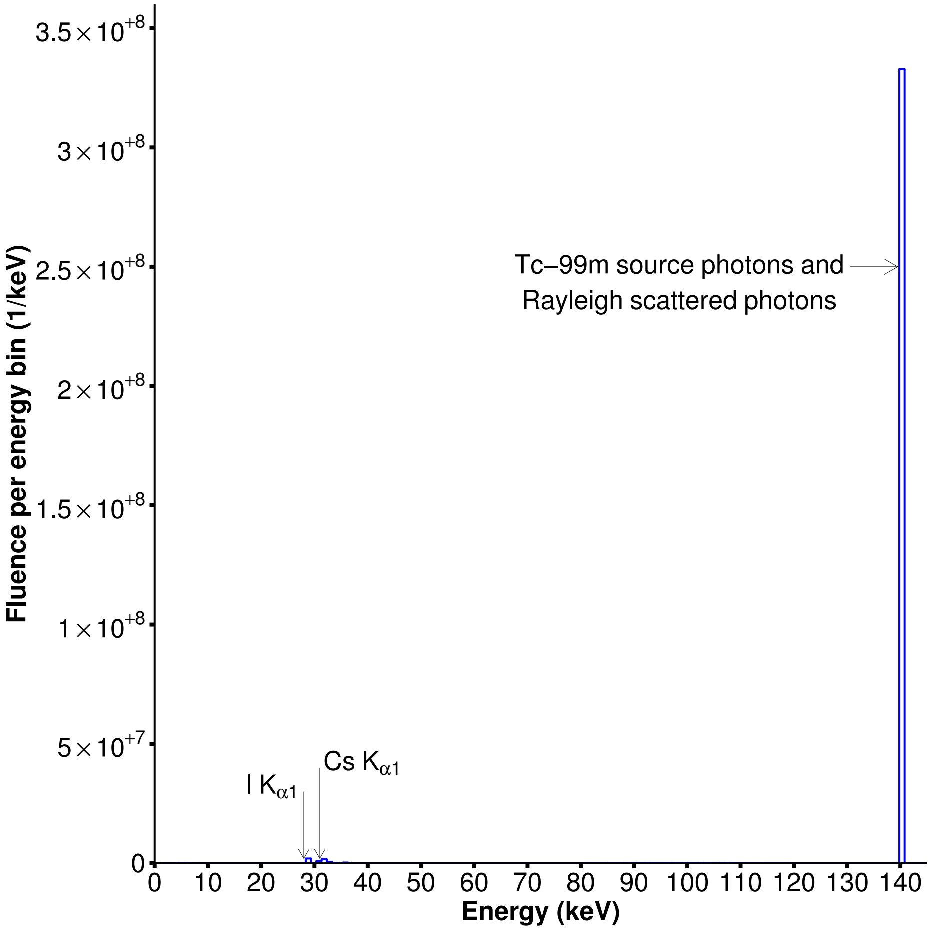

Figure 4.6: 40 hours' simulation of the distribution of photon fluence within a measurement accumulator from the 600 µm caesium iodide using a 140.5 keV mono-energetic photon source. The number of simulated primary photon histories was 3.62 x 10^8. The position of the caesium and iodine principal $K_{\alpha 1} K_{\alpha 2}$ peaks are shown.

There is a large peak of amplitude (3.30 $\pm$ 0.05) x 10^8 at 140.5 keV which corresponds to the energy of the source photons which are transmitted through the caesium iodide and Rayleigh scattered photons directed towards the accumulator. The virtual accumulator does not affect the tracking but the energy distribution of the photon fluence is averaged over the volume of the accumulator.

PENELOPE also directly outputs its numerical results as Table 4.4 for the transmitted, backscattered and absorbed photons within caesium iodide relative to the direction of the source photons. The transmitted photons are those which do not interact within the caesium iodide crystal. The absorbed photons are those which are photoabsorbed within caesium iodide, giving rise to fluorescence photons. The backscattered photons within caesium iodide relative to the direction of the source photons arise from Rayleigh scattered photons and Compton scattered photons. As Rayleigh scattered photons will be emitted over 4π, those forward scattered will contribute to the fluence accumulated at 140.5 keV.

Source photons	Transmitted photons*	Backscattered photons*	Absorbed photons
3.62 x 10^8	2.92 x 10^8	5.03 x 10^6	6.56 x 10^7
Fraction	8.19 x 10^{-1} ± 8.1 x 10^{-5}	2.56 x 10^{-2} ± 3.5 x 10^{-5}	1.81 x 10^{-1} ± 6.1 x 10^{-5}

Table 4.4: PENELOPE simulation results showing transmitted, backscattered and absorbed photons * relative to the direction of the source photons through 600 µm thick caesium iodide crystal. The simulated number of primary photons was 3.62 x 10^8.

Figure 4.7 shows the distribution of photon fluence for the energy interval between 1 keV and 140 keV, with the 140.5 keV photon peak excluded to assist the identification of the caesium and iodine principal K_α, K_β peaks; separate simulations of just atomic caesium and atomic iodine were used to confirm the identification of the spectral peaks in the energy spectrum. There are very small peaks of caesium fluorescence at about 5 keV corresponding to $L_{\alpha 1}$ and $L_{\beta 1}$. In order to simplify the Monte Carlo simulations they were only performed using pure caesium iodide.

It is important to note that trace amounts of thallium-81 are used to dope the halide lattice with scintillation emission occurring from these sites [Blasse, 1994]. This omission of trace thallium-81 doping in these radiation transport simulations as a first order approximation does not affect the modelled spectrum of the caesium iodide crystal since the weighted proportion of thallium-81 of order 10^{-28} gcm^{-3} has a negligible impact.

As the fluence accumulator has a finite area 8 mm x 8 mm with thickness 600 µm and subtends a 5 degree semi-angle, about 10 cm away from the conical photon source, any photons which are Compton scattered from within the caesium iodide crystal towards the fluence accumulator will be recorded. Figure 4.7 also shows fluence from Compton scattered photons originating from partial energy loss in the caesium iodide crystal. These Compton scattered photons have energy E_γ given by Equation 2.2 from section 2.1. As mentioned in chapter 2, the Klein-Nishina angular distribution of Compton scattered photons would be similar to Figure 2.1 which is shown for impinging photons of 150 keV. In this simulation any incident photons (with energy 140.5 keV) which are Compton scattered will have an angular distribution which peaks at $\theta = 0$ radians and a smaller back-scatter peak at $\theta = \pi$ radians. Bearing in mind the position of the fluence accumulator at the egress face of the caesium iodide crystal, the Compton scatter in Figure 4.7 shows only forward-scattered Compton photons relative to the direction of the impinging photons. Using Equation 2.2 the minimum Compton scattered photon energy $E_\gamma(min)$ is given by Equation 4.2

$$E_\gamma(min) = \frac{E_0}{1 + 2\alpha} \tag{4.2}$$

and calculated to be 90.6 keV where α is calculated as per Equation 4.3 as the ratio 140.5 keV to 511 keV.

$$\alpha = E_0/m_0c^2 \tag{4.3}$$

When $\theta = \pi/3$ is the scattering angle of the Compton scattered photon relative to the direction of the impinging photon, the Compton scattered photon has energy 124.3 keV which is consistent with the Compton profile in Figure 4.7.

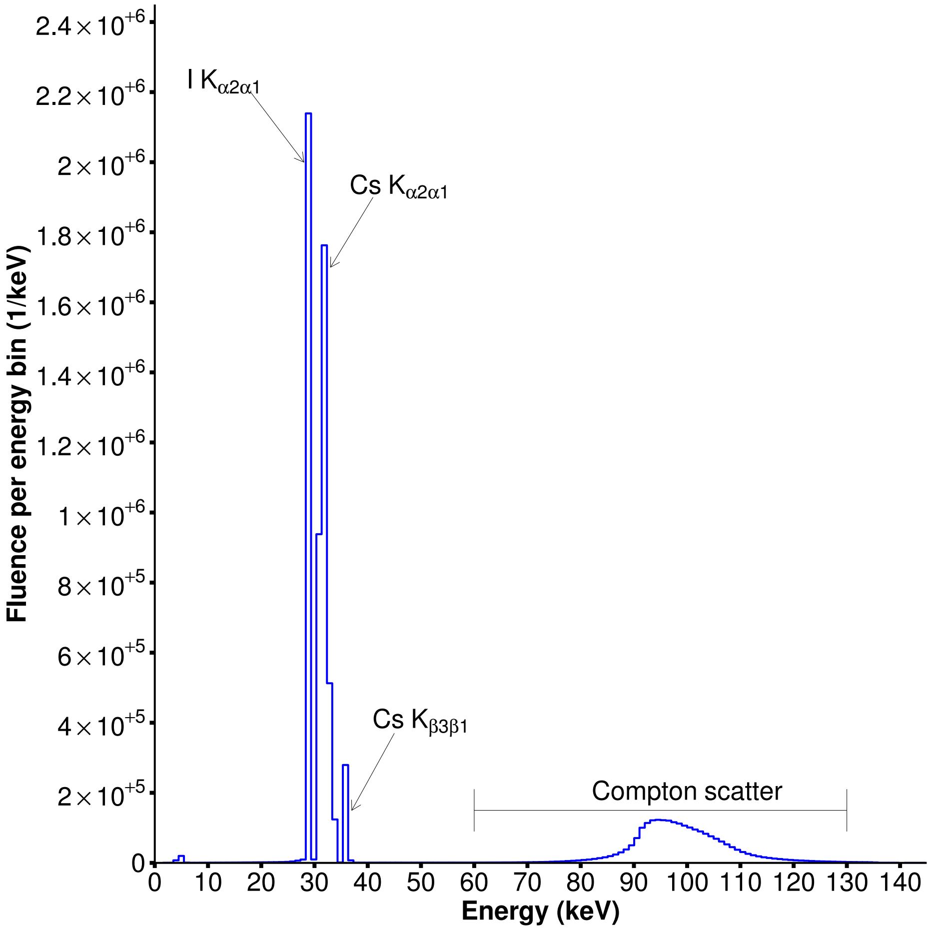

Figure 4.7: 40 hours' simulation of the distribution of photon fluence within a measurement accumulator from the 600 μm caesium iodide using a 140.5 keV mono-energetic photon source for the portion of the principal K_α, K_β peaks within the energy range 1 keV to 140 keV. The number of simulated primary photon histories was 1.7x 10^8. The caesium and iodine principal $K_{\alpha 1}$ peaks are shown. The caesium $K_{\beta 3\beta 1}$ peak is also shown. The large off-scale 140.5 keV photon peak was excluded. There are very small peaks of caesium fluorescence at about 5 keV corresponding to $L_{\alpha 1}$ and $L_{\beta 1}$.

4.3.3 Discussion

Distribution of photon fluence from 600 μm caesium iodide

This section described the distribution of photon fluence accumulated from the 600 μm caesium iodide crystal whereas in the previous section, it described the distribution of energy deposited within a accumulator encompassing the dimensions of the 600 μm caesium iodide crystal. We recall that for fluence, the fluence accumulator has an arbitrary thickness sufficient to accommodate the path length of photons which contribute when their trajectory intersects this volume for the duration of the simulation. The Monte Carlo simulation using the fluence accumulator at the egress face of the 600 μm caesium iodide crystal shows a large peak of amplitude $(3.30 \pm 0.05) \times 10^8$ at 140.5 keV owing to contribution of both source photons and Rayleigh scattered photons directed towards the accumulator. Table 4.4 shows the PENELOPE results for the transmitted photons within caesium iodide relative to the direction of the source photons as $(8.19 \times 10^{-1}) \pm (8.1 \times 10^{-5})$. This is consistent with the analytical transmission at 140.5 keV relative to the direction of the source photons for 600 μm caesium iodide crystal as shown in Figure 4.8. This transmission is 0.83, 0.63 and 0.08 respectively for the 600 μm, 1500 μm and 8000 μm thick caesium iodide crystals. However, the Monte Carlo fluence accumulator demonstrates the importance of incorporating both Compton and Rayleigh scattered photons in the modelling. Referring back to Figure 4.7 this distribution of photon fluence demonstrated the Compton scatter in the energy interval between about 90 keV and 125 keV, recalling that there is no sharp truncation in the Compton profile as the target electrons are not stationary but have momentum distribution, and also modified to allow only transitions for bound electrons where the energy difference between the incident and scattered photons is greater than the ionisation energy of the active shell.

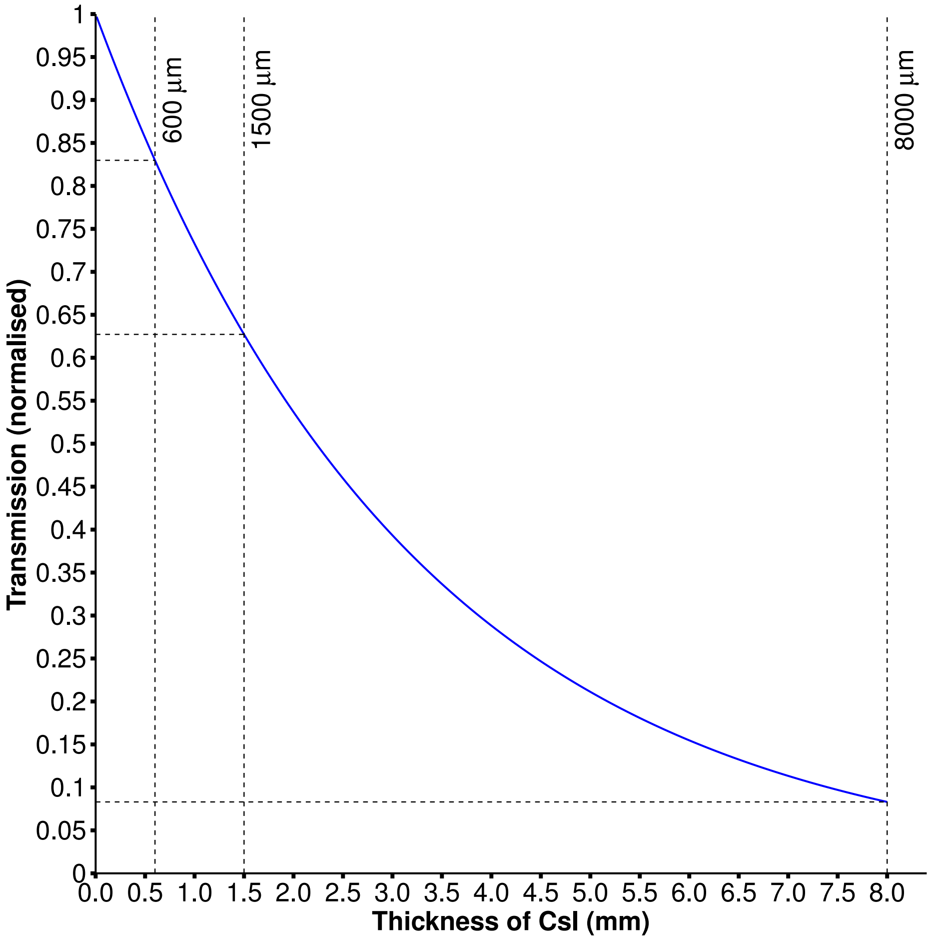

Figure 4.8: The transmission for caesium iodide crystal with incident photons at 140.5 keV

Fluorescence X-rays are seen in the distribution of photon fluence corresponding to the iodine $K_{\alpha 1}$ fluorescence peak and caesium $K_{\alpha 1}$ fluorescence peak respectively at 28.5 $\pm$ 0.5 keV and 31.3 $\pm$ 0.5 keV, and a caesium $K_{\beta 1,\beta 3}$ fluorescence peak 35.4 $\pm$ 0.5 keV. For each modelled fluorescence peak, their amplitudes is likely to be less than that for their corresponding values in the reference database, [Sanchez del Rio et al., 2003]. This is because some of the K_α and K_β fluorescence photons escape from the caesium iodide crystal, and so are not recorded within the fluence accumulator.

4.4 The effect on fluence measurements with increasing thickness of the crystal

4.4.1 Method

Effect of increasing crystal thickness.

Two further 40 hours' simulations were performed of the distribution of photon fluence within a measurement accumulator sited at the egress from a 1500 μm thick caesium iodide crystal and also separately from a 8000 μm thick caesium iodide crystal using a 140.5 keV mono-energetic conical photon source. The area of the fluence accumulator was 8 mm x 8 mm with thickness 600 μm. The number of simulated primary photon histories for the simulation using the 1500 μm thick and 8000 μm thick caesium iodide crystal were 1.60 x 10^8 and 6.89 x 10^7 respectively. These Monte Carlo simulations were performed for a defined time interval of 40 hours for each simulation.

4.4.2 Results

These results of the distribution of photon fluence within a measurement accumulator sited at the egress from a 1500 μm caesium iodide crystal and from 8000 μm are shown in Figure 4.9, and in Figure 4.10 respectively; in both cases the energy range was 1 keV to 140 keV with the 140.5 keV photon peak excluded to show the principal caesium and iodine K_α, K_β peaks. As before PENELOPE also directly outputs its numerical results respectively for 1500 μm caesium iodide crystal and from 8000 μm as Tables 4.5 and 4.6 for the transmitted, backscattered and absorbed photons within caesium iodide relative to the direction of the source photons.

Source photons	Transmitted photons*	Backscattered photons*	Absorbed photons
1.60 x 10^{8}	9.42 x 10^{7}	2.63 x 10^{6}	6.35 x 10^{7}
Fraction	5.99 x 10^{-1} ± 1.4 x 10^{-4}	2.88 x 10^{-2} ± 5.6 x 10^{-5}	3.96 x 10^{-1} ± 1.2 x 10^{-4}

Table 4.5: PENELOPE simulation results showing transmitted, backscattered and absorbed photons * relative to the direction of the source photons through the 1500 µm thick caesium iodide crystal. The simulated number of primary photons was 1.60 x 10^{8}.

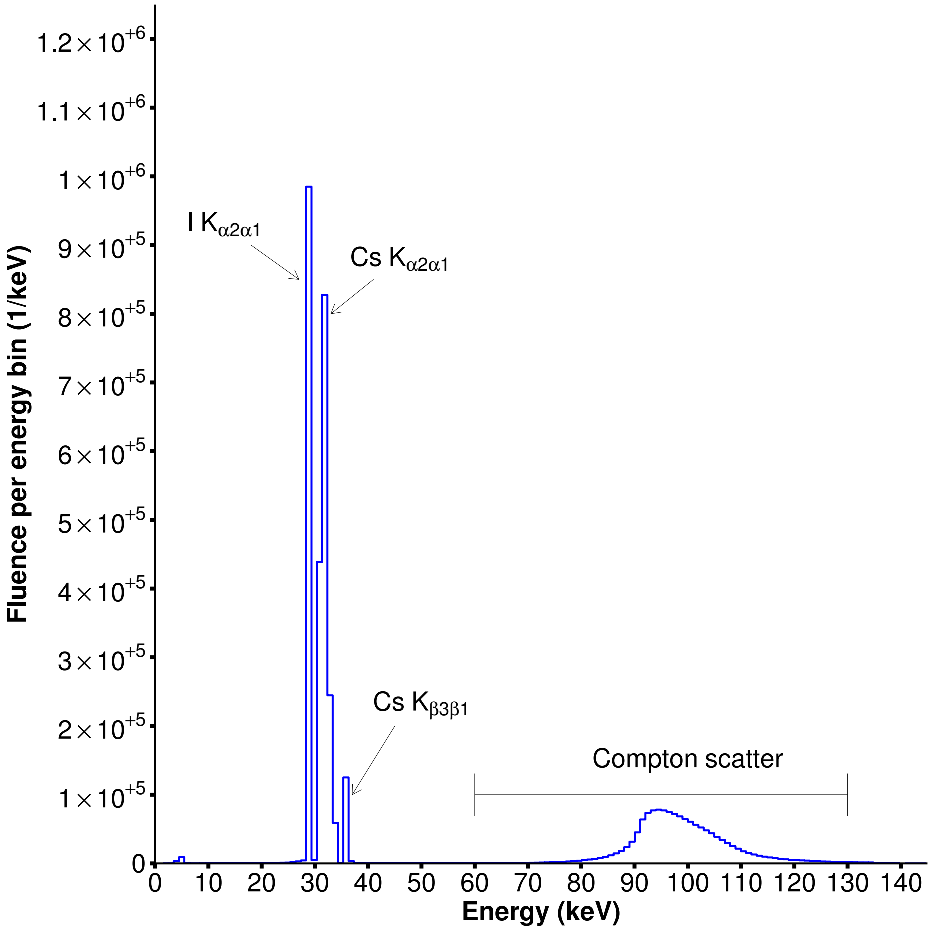

Figure 4.9: 40 hours' simulation of the distribution of photon fluence within a measurement accumulator from the 1500 µm caesium iodide using a 140.5 keV mono-energetic photon source for the portion of the principal K_{α}, K_{β} peaks within the energy range 1 keV to 140 keV. The number of simulated primary photon histories was 1.60 x 10^{8}. The caesium and iodine principal $K_{\alpha1}$ peaks are shown. The caesium $K_{\beta3\beta1}$ peak is also shown. The large off-scale 140.5 keV photon peak was excluded.

Source photons	Transmitted photons*	Backscattered photons*	Absorbed photons
6.89 x 10^7	3.96 x 10^6	51.19 x 10^6	6.38 x 10^7
Fraction	5.86 x 10^{-2} ± 9.6 x 10^{-5}	2.97 x 10^{-2} ± 8.7 x 10^{-5}	9.25 x 10^{-1} ± 9.5 x 10^{-5}

Table 4.6: PENELOPE simulation results showing transmitted, backscattered and absorbed photons, * relative to the direction of the source photons through the 8000 µm caesium iodide crystal. The simulated number of primary photons was 6.89 x 10^7.

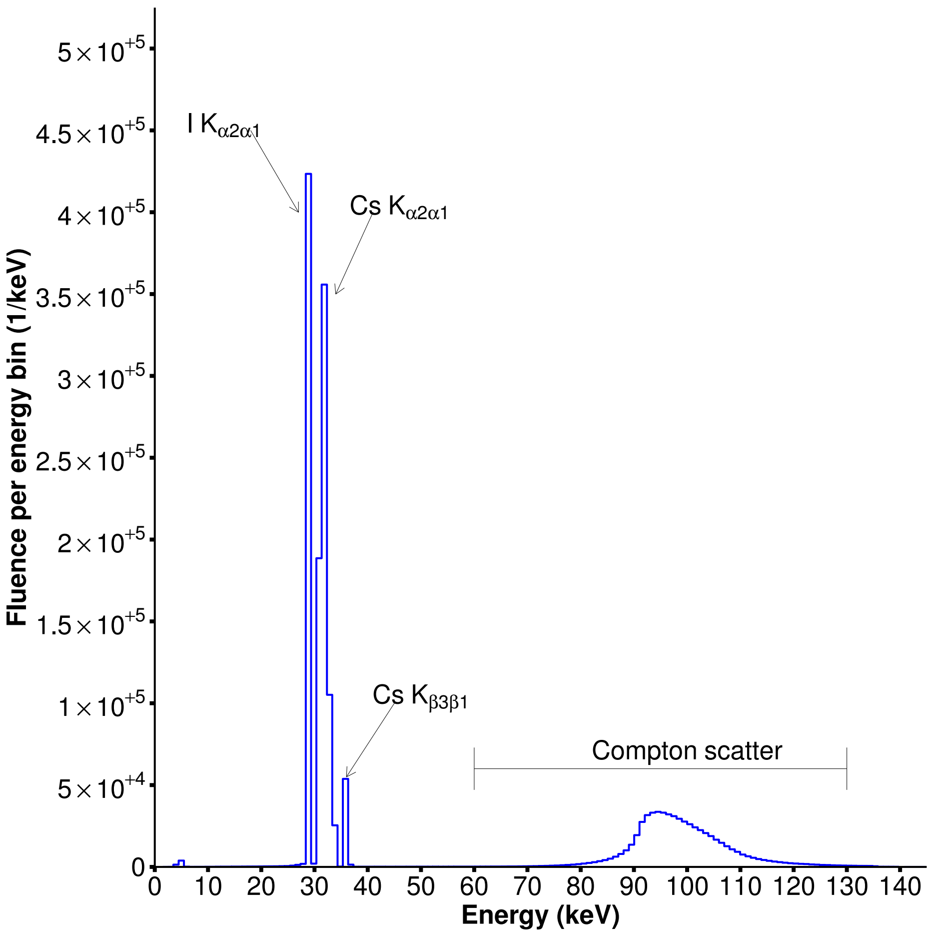

Figure 4.10: 40 hours' simulation of the distribution of photon fluence within a measurement accumulator from the 8000 µm caesium iodide using a 140.5 keV mono-energetic photon source for the portion of the principal K_α, K_β peaks within the energy range 1 keV to 140 keV. The number of simulated primary photon histories was 6.89 x 10^7. The caesium and iodine principal $K_{\alpha1}$ peaks are shown. The caesium $K_{\beta3\beta1}$ peak is also shown. The large off-scale 140.5 keV photon peak was excluded.

The caesium and iodine principal $K_{\alpha 1}$ peaks are tabulated in Table 4.7.

caesium iodide thickness	Source photons	iodine $K_{\alpha 2 \alpha 1}$	caesium $K_{\alpha 2 \alpha 1}$
600 μm	3.62 x 10^8	(1.95 ± 0.02) x 10^6	(1.60 ± 0.02) x 10^6
Fraction	-	(5.39 ± 0.02) x 10^{-3}	(4.42 ± 0.02) x 10^{-3}
1500 μm	1.06 x 10^8	(2.04 ± 0.02) x 10^6	(1.72 ± 0.02) x 10^6
Fraction	-	(1.27 ± 0.02) x 10^{-2}	(1.07 ± 0.02) x 10^{-2}
8000 μm	6.89 x 10^7	(2.04 ± 0.02) x 10^6	(1.72 ± 0.02) x 10^6
Fraction	-	(2.96 ± 0.02) x 10^{-2}	(2.50 ± 0.02) x 10^{-2}

Table 4.7: The fractional amplitude of caesium and iodine principal $K_{\alpha 1}$ peaks, * relative to the direction of the source photons collected by the fluence accumulator.

4.4.3 Discussion

Effect of increasing crystal thickness.

Figures 4.7, 4.9 and 4.10 which show the distribution of photon fluence within these measurement accumulators with increasing thickness of caesium iodide crystal. The fractional amplitude of caesium and iodine principal $K_{\alpha 1}$ peaks relative to the direction of the source photons collected by the fluence accumulator was found to increase with increasing crystal thickness.

The fluence accumulator at the egress surface of the caesium iodide crystal records any transmitted photons. The modelled transmission at 140.5 keV through the 600 μm, 1500 μm and 8000 μm thick caesium iodide crystals was 0.82, 0.66 and 0.06 respectively; these were consistent with the analytical model in Figure 4.8.

Also in Figures 4.7, 4.9 and 4.10 the amount of Compton scatter may be derived from the area under each curve for each Compton scatter profile. An estimate of the area under the curve representing the Compton scatter between 60 keV to 130 keV may be calculated from the difference in the cumulative sum of the fluence at 130 keV and the cumulative sum of the fluence at 60 keV; the integral is the product of this difference and the number of energy bins within this energy interval (i.e. between 60 keV and 130 keV). The amount of Compton scatter within the fluence accumulators from the fluence distributions Figures 4.7, 4.9 and 4.10 decreases with increasing thickness of the crystal as demonstrated in Table 4.8.

Thickness of CsI / µm	Difference in cumulative sums
600	5.22 x 10^6
1500	2.67 x 10^6
8000	1.42 x 10^6

Table 4.8: Difference in the cumulative sums derived for the Compton scatter within the energy interval between 60 keV and 130 keV.

This is because the probability of absorption of Compton scatter events within the caesium iodide increases with increasing thickness of crystal. This implies that by using a thicker scintillator crystal there is an increase of photoabsorption within the crystal and decrease in the Compton component of the fluence from the crystal. This is beneficial for the imaging signal, as the full energy peak from photoabsorption is maximised and Compton scatter which degrades the spatial resolution of the image is minimised. In a gamma camera as the photopeak has a finite width (given by the FWHM), the system's pulse height analyser can be adjusted to accommodate a range of energies to be accepted around the photopeak energy. Typically for a LFOV gamma camera this energy window is set to ± 20% of the photopeak energy. However, windowing around the photopeak energy also means that some Compton scattered events (around 30%) will be included within the image.

The Monte Carlo fluence distributions for the monolithic caesium iodide crystals above are postulated to be similar for photoabsorption when using close packed columnar crystals. However, the proportion of Compton scattering and Rayleigh scattering would be likely to be greater owing to the scattering boundaries between the crystal columns, and in a real crystal, scattering from the crystal base where there will be unstructured caesium iodide, as shown in Figure 7.3 for a sample of 600 μm columnar caesium iodide crystal. Another important consideration is that where scintillation photons are created they are more likely to be absorbed with a thicker crystal. Thus there is a trade-off in maximising scintillator thickness for a given Z and reducing the amount of scintillation photons that are self-absorbed in the crystal.

4.5 Modelling of the energy deposited within the silicon detector

4.5.1 Method

The two preceding sections demonstrated the fluence egress from the caesium iodide crystal. In a real detector system, this fluence would be the source of photons for a silicon detector. The actual detector used in our two SFOV systems is the e2v CCD97-00 back illuminated EMCCD [e2vTechnologies, 2004]; the Monte Carlo simulation models the detector as 5 μm thick silicon. In this section, the PENELOPE Monte Carlo simulation follows the fluence egress from the caesium iodide crystal and was used to determine the distribution of energy deposited within a 5 μm thick silicon detector. No scintillations photons from the caesium iodide crystal are included in the PENELOPE Monte Carlo [Salvat et al., 2011] code nor does it incorporate modelling of detector noise.

Distribution of the energy deposited with the silicon detector

A schematic showing an energy deposition accumulator used to accumulate the distribution of energy deposited within the silicon detector is illustrated in Figure 4.11. A 140.5 keV mono-energetic conical photon source with a 5 degree semi-angle was used with full coverage of the simulated detector; the photon source energy used corresponds to the principal gamma emission energy for technetium-99m. A monolithic 600 μm thick caesium iodide crystal of area 8 mm x 8 mm was positioned 10 cm centrally away perpendicular to the plane of the crystal. A 5 μm thick silicon detector was abutted directly to the egress face of the caesium iodide crystal (no gap). The Monte Carlo energy deposition accumulator was positioned such that it occupies the whole volume of the 8 mm x 8 mm x 5 μm silicon detector. This particular accumulator determines the distribution of the energy deposited by incident photons within the specified volume.

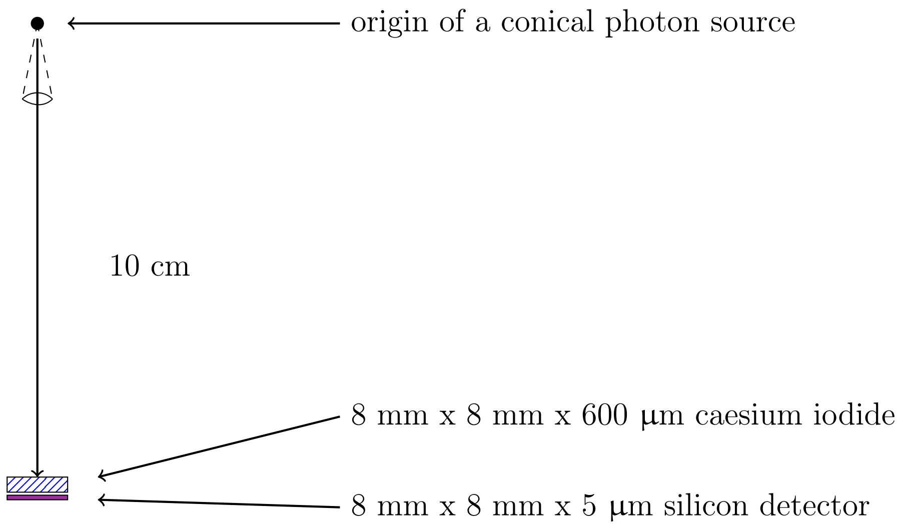

Figure 4.11: Schematic to assess the distribution of energy deposited within an event accumulator in 5 µm silicon layer using a 140.5 keV mono-energetic conical photon source.

4.5.2 Results

Distribution of energy deposition within 5 µm silicon

For brevity the distribution of energy deposited within the 5 µm silicon is only shown for the intervening 600 µm thick caesium iodide crystal Figure 4.12 since the energy spectra were found to be similar when using either 1500 µm or 8000 µm thick caesium iodide crystals abutted to the 5 µm silicon detector. The source of this distribution of energy deposited arises from the fluence subtended from the caesium iodide crystals and accumulated within the respective 5 µm silicon event accumulators within the silicon detector.

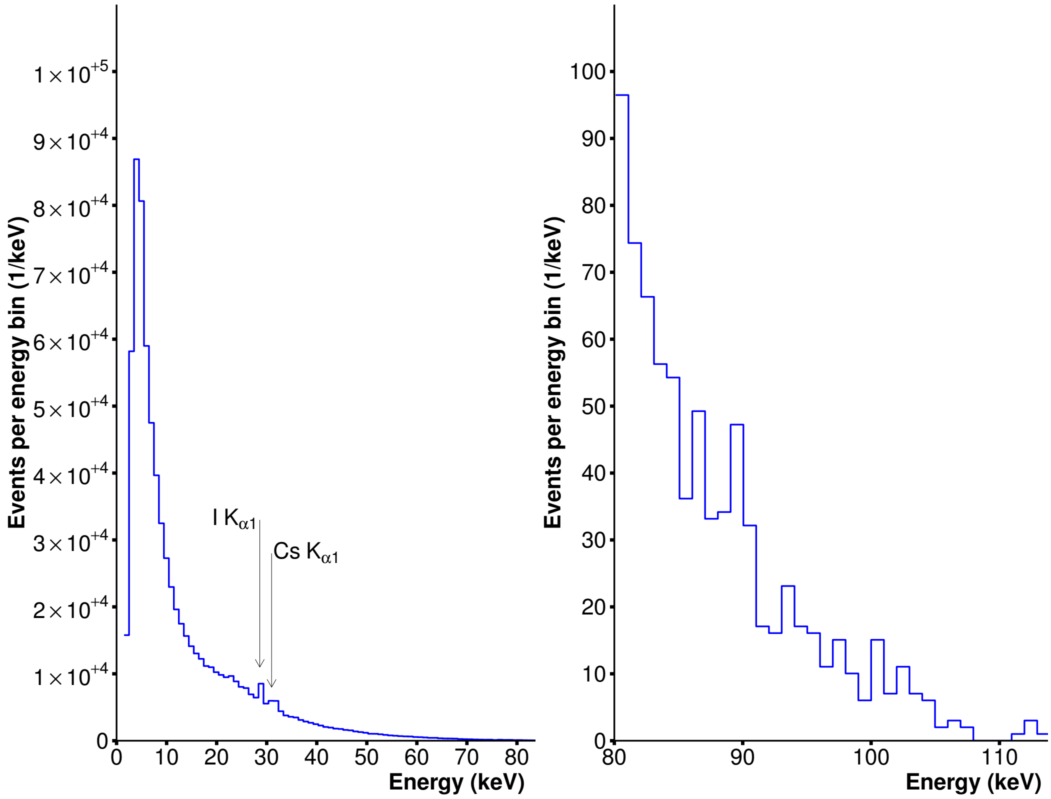

Figure 4.12: 40 hours' simulation of the distribution of energy deposition within an event accumulator in the 5 µm silicon due to fluence from 600 µm thick caesium iodide for the portion within the energy range a: 1 keV to 80 keV and b: 80 keV to 110 keV. The number of simulated primary photon histories was 3.48 x 10^8. The caesium and iodine principal $K_{\alpha 1}$ peaks are shown.

4.5.3 Discussion

Distribution of the energy deposited within 5 µm silicon layer

The distribution of the energy deposited within the 5 µm thick silicon was determined using an energy deposition encompassing the whole volume occupied by the silicon detector. However, the mean free path of the principal fluorescence photons was derived in silicon for the caesium $K_{\alpha 1}$ fluorescence and iodine $K_{\alpha 1}$ fluorescence were 3.15 mm and 4.23 mm respectively. Thus not all of the caesium $K_{\alpha 1}$ fluorescence and iodine $K_{\alpha 1}$ fluorescence created will be accumulated in this energy deposition accumulator, which reflects their small amplitude in Figure 4.12a.

The plot shows a peak response at 3.6 ± 0.5 keV and 4.5 ± 0.5 keV with a fall off either side of these peaks. This is because at low energies the partial photon mass attenuation coefficients for photoabsorption and Rayleigh scattering is larger than at higher photon energies; this response for silicon for incident energies up to 70 keV is shown in Figure 2.2. The tail in the energy spectra from the peak response in the energy spectra to about 110 keV, Figure 4.12b is due to Compton scatter originating from the caesium iodide crystal as any Compton scattered photons egressing from the caesium iodide only deposit part of their energy within the accumulator occupying the volume of the silicon.

We recall from section 3.5 that the detector sensitivity for photons across the cross-section of the 5 μm silicon detector for a 140.5 keV point source was derived to be 0.17%, such that most of the gamma photons at 140.5 keV pass through the 5 μm silicon detector. Using Equation 2.2 for fluence photons of energy 124.3 keV from the caesium iodide crystal (see section 4.3, with the scattering angle of the Compton scattered photon relative to the direction of the impinging photon is $\theta = \pi/3$, the Compton scattered photons have a maximum energy of 110.8 keV. This is consistent with the tail in the energy spectra in Figure 4.12b. There was no difference in the profiles of the energy deposition spectra within 5 μm silicon other than the relative events when using either 1500 μm or 8000 μm thick caesium iodide crystals abutted to the 5 μm silicon detector.

4.6 Conclusions

Several Monte Carlo simulations were successfully used to investigate the individual components used within the design of the Compact Gamma Camera as incident photons were directed towards them. This systematic approach allowed modelling of the distribution of energy deposition within caesium iodide, the distribution of photon fluence from caesium iodide, and also the distribution of energy deposition in a silicon detector.

In the case of energy deposition accumulators although these simulations performed well compared to the referenced data [Chu et al., 1999], the modelled fluorescence intensities do not record some of these K_α and K_β fluorescence photons if the source event originated close to the boundary of the accumulator i.e. less than its mean free path λ .

The distribution of photon fluence within each fluence accumulators at the egress of the caesium iodide crystal also demonstrated the Compton continuum and fluorescence X-rays corresponding to the iodine $K_{\alpha 1}$, caesium $K_{\alpha 1}$ and caesium $K_{\beta 3,\beta 1}$ fluorescence peaks. The model was consistent with the referenced database [Chu et al., 1999].

Using selected thicknesses the probability of absorption of Compton scatter events within the caesium iodide increases with increasing thickness of crystal. This implies that using by using a thicker scintillator crystal there is a proportioned increase of photoabsorption and decrease in the Compton component of the fluence from the crystal.

The modelling in this chapter used a monolithic 5 μm silicon detector representative of an EMCCD. However, the EMCCD used in the CGC and PIXS detector is pixelated which creates an underlying variance in distribution of charge collected. The following chapter 5 explores the experimental findings for a such a bare pixelated silicon detector.

Chapter 5

Experimental Response of the PIXS detector

5.1 Introduction

The Compact Gamma Camera [CGC] uses the same bare silicon detector as the Portable Imaging X-ray Spectrometer detector [PIXS] both introduced in chapter 3. The silicon detector used is the e2v CCD97-00 back illuminated EMCCD [e2vTechnologies, 2004], which was chosen due to its large signal to noise ratio and high spatial resolution. It is beneficial to understand the experimental response of this silicon detector as a baseline response for the CGC. This chapter begins by describing the calibration of the bare silicon detector using both americium-241 and cadmium-109 radionuclides to calibrate the EMCCD ADU channels to energy in keV. Then the detector response from a cadmium-109 radionuclide was compared with the Monte Carlo simulations in chapter 3. A schematic of the PIXS detector is shown in Figure 5.1

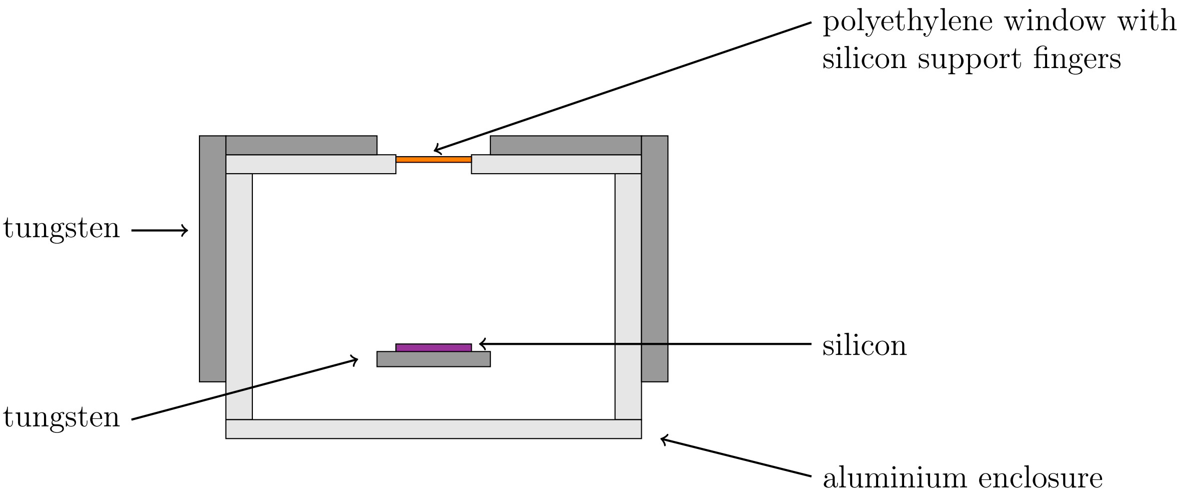

Figure 5.1: A schematic of the PIXS detector

The entrance window of the PIX detector has a 4 µm thick layer of interleaved silicon fingers supporting a polyethylene layer. The 5 µm thick silicon detector represents the depletion layer of an EMCCD with active area of 8 mm x 8 mm which is within an evacuated aluminium chamber at 1.3 x 10^{-3} Pa. This simplified model does not include backscatter from the substrate nor thermoelectric cooler. Shielding from extraneous scatter is provided by a 3 mm thick tungsten partial enclosure. Another reason for the aluminium housing is to mitigate against fluorescence from the housing interfering with the silicon detector. The spectral response for the aluminium fluorescence is shown in Figure 3.11 on page 69 which demonstrates the energy deposition within an event accumulator in a 8 mm x 8 mm x 5 µm thick silicon detector using a full spectral cadmium-109 source. The aluminium fluorescence energy for the $Ag\ K_{\alpha 1,2}$ is 1.4 keV, which is too low to resolve for the PIXS detector owing to detector noise as demonstrated later in this section.

An additional investigation was performed using the cadmium-109 radionuclide for assessing the amount of charge sharing amongst the EMCCD pixel array for these incident photon events. Events recorded within the EMCCD pixel array are clusters of pixels marking the position whereby a charge cloud has been generated along the trajectory of incident photons, and has diffused outwards within the silicon depletion layer. Each cluster of pixels is surrounded by non activated pixels but bounded by the dimensions of the pixel array. This aspect of charge sharing is important in the context of accurately determining the location of a detected event. In both sets of investigation the statistical uncertainty in the ordinate was respectively $\pm 1/\sqrt{N}$ for N EMCCD counts recorded; the statistical uncertainty for the abscissa was $\pm$ 0.1 keV but both sets of error bars were not shown in the following plots for clarity.

5.2 Energy calibration of the EMCCD using americium-241 and cadmium-109 radionuclides

5.2.1 Method

In order to evaluate the experimental response of the EMCCD within the PIXS detector the following radioactive sources and their activity were used for experiments in this chapter as shown in Table 5.1.

Isotope	Reference Radioactivity/ MBq	On Reference Date	Calculated Radioactivity/ MBq
Americum-241	370	05/1985	351± 19
cadmium-109	740	03/2013	84 ± 9

Table 5.1: Radioactive sources used for experiments in this chapter

The cadmium-109 radionuclide source was positioned approximately 5 cm away, centrally and perpendicular to the entrance face of the PIXS detector as shown in Figure 5.2. This distance was used to ensure an uniform flux of photons irradiated the entrance window of the PIXS detector. Although the PIXS detector has a 4 μm polyethylene entrance window, a black polythene liner was used to cover this window since this detector has high sensitivity to ambient optical photons.

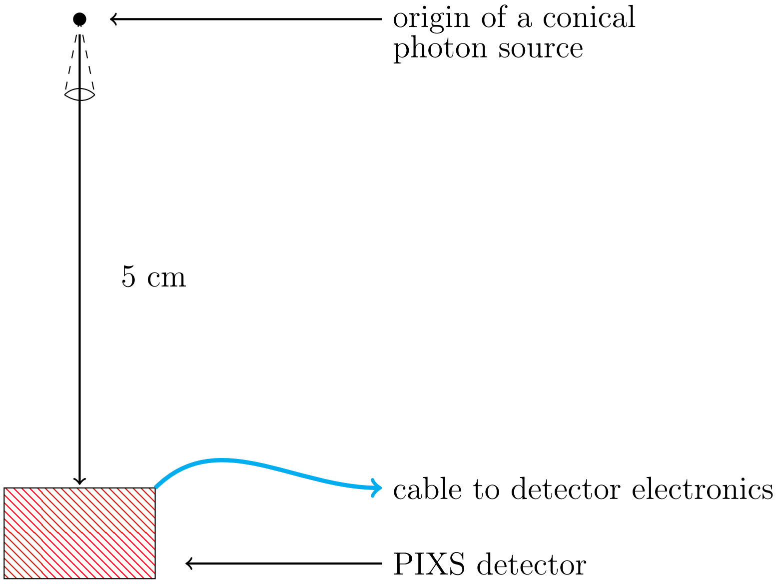

Figure 5.2: The set-up used to record the EMCCD response using the PIXS detector.

The EMCCD uses a thermoelectric cooler and prior to any measurements the EMCCD was cooled to 256.0 ± 0.1 K in order to reduce thermal noise. The gain of the EMCCD was adjusted by changing its gain potential difference Φ_{HV}; this potential difference creates impact ionisation established between ϕ_2 and ϕ_{dc} as discussed in section 1.5. A series of 10,000 frames were collected in turn with Φ_{HV} set consecutively to 33.5 V, 35.5 V, 37.5 V and 39.5 V for each measurement. In each case a region of 128 x 128 pixels was formed over each of the EMCCD frames and the EMCCD counts per ADU channel recorded. The full-frame of 142 x 132 was not used owing to the presence of a hot pixel near the periphery. These results were analysed by exporting the EMCCD counts per ADU channel data for off-line analysis using the **R** programming language. From this data the photopeak channel was plotted against Φ_{HV}. Note the gain of our e2v CCD97-00 back illuminated EMCCD can be set to unity when Φ_{HV}= 20 V. At high values of Φ_{HV} ($>$ 40 V) the shot noise is also increased but this is counteracted by the large gain in signal.

Two further experiments were performed in order to calibrate the ADU channel measurements against keV. The first calibration experiment used cadmium-109 radionuclide source positioned approximately 5 cm away centrally and perpendicular to the entrance face of the PIXS detector as shown in Figure 5.2. This distance was used to ensure an uniform flux of photons irradiated the entrance window of the PIXS detector. As described above a region of 128 x 128 pixels was formed over the EMCCD frames and 60,000 frames collected to improve count statistics. The EMCCD counts per ADU channel were recorded and analysed by exporting this data for off-line analysis. The experiment was then repeated using the americium-241 source as described above.

5.2.2 Results

The variation of the gain of the EMCCD with its gain potential difference Φ_{HV}.

Using the cadmium-109 radioactive source, the variation of the gain of the EMCCD with its gain potential difference Φ_{HV} is shown in Figure 5.3. The identification of the cadmium-109 photochannel signal peaks is discussed in the following subsection.

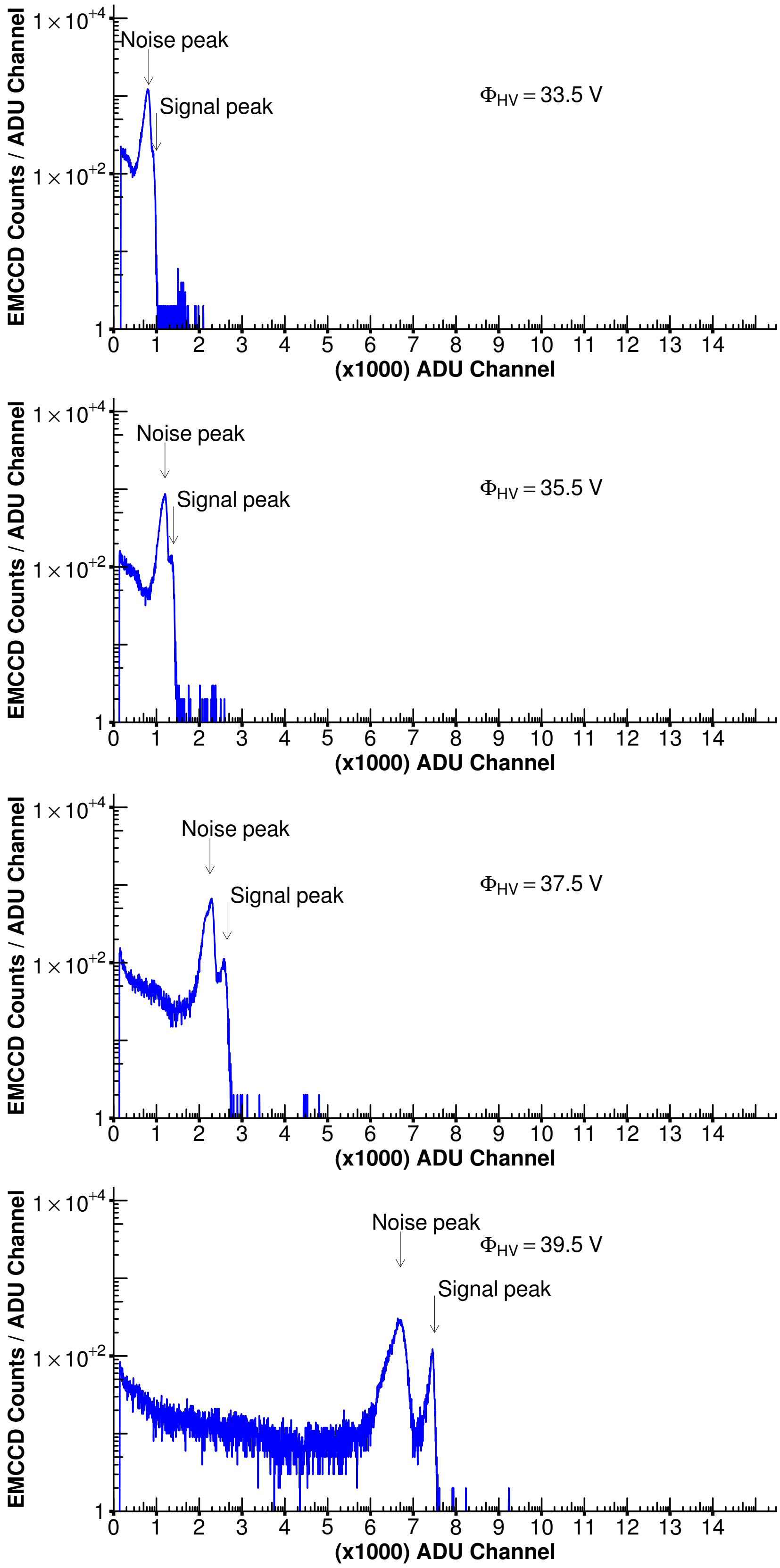

Figure 5.3: EMCCD counts per ADU channel for single pixel events using cadmium-109 with the gain potential difference Φ_{HV}= 33.5 V, 35.5 V, 37.5 V and 39.5 V. The EMCCD was cooled to 256.0 $\pm$ 0.1 K.

The first peak in the plot is the noise peak, and the second peak, where resolvable, is the photochannel signal peak. There are counts at ADC channels higher than the photopeak channel owing to pile-up pulses. For the subsequent measurements the median value of the gain potential difference Φ_{HV}=37.5 V was arbitrarily chosen as this corresponds to the point at which it is clearly possible to separate the noise and signal peaks; this also means that the shot noise from the image and storage areas of the EMCCD is minimised at the output amplifier. The photopeak channel was plotted against the Φ_{HV} to show the effect of adjusting this gain potential difference and is shown in Figure 5.4. This curve has been fitted as an exponential with R^2= 0.98 although there is a trend away from the fit for Φ_{HV}= 33.5 V and Φ_{HV}= 34.5 V as it is difficult to separate the noise and signal peaks.

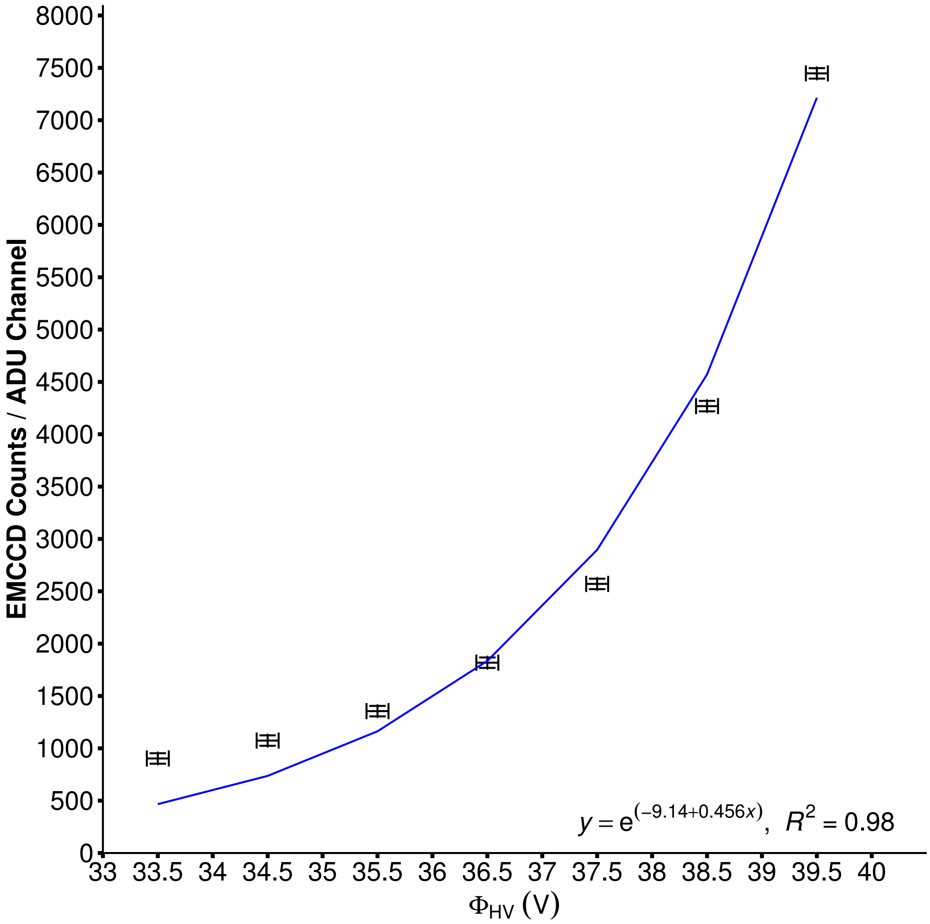

Figure 5.4: The photopeak channel versus the gain potential difference Φ_{HV}. The EMCCD was cooled to 256.0 ± 0.1 K and 10,000 frames were acquired for each gain potential difference Φ_{HV}.

5.2.3 The calibrated spectrum for cadmium-109

The calibrated energy deposition spectrum for cadmium-109 is shown in Figure 5.5. The EMCCD was cooled to 256.0 ± 0.1 K, with Φ_{HV} set to 37.5 V and 60,000 frames were acquired. The tail of the noise spectrum has been thresholded using the noise peak plus 5σ and extends from 1 keV to about 15 keV; the noise peak is off-scale. The large peak at 22.1 keV and the smaller peak at 24.9 keV were identified as the $Ag\ K_{\alpha 1 \alpha 2}$ peaks and $Ag\ K_{\beta 1 \beta 2 \beta 3}$ peaks respectively. The ratio of the larger peak to smaller peak is 6.8 ± 0.1, consistent with the referenced database [Chu et al., 1999] tabulated in Table 3.3. In order to calibrate the EMCCD response a second radionuclide americium-241 was required.

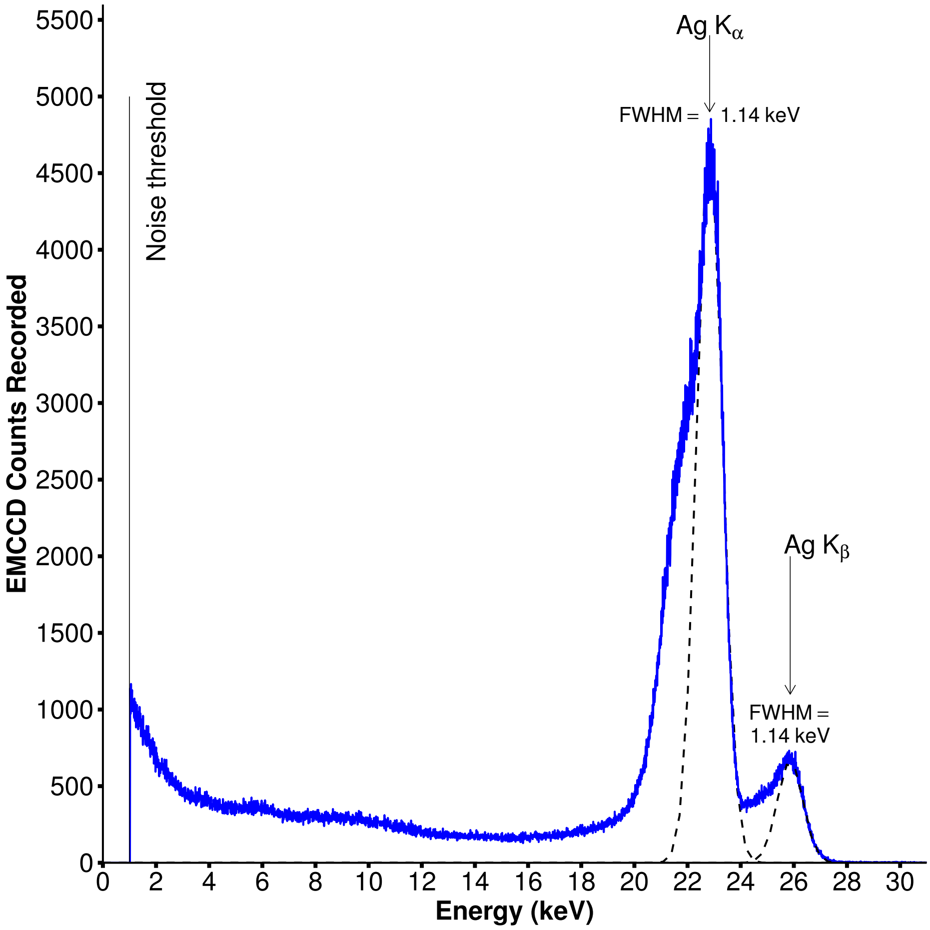

Figure 5.5: EMCCD Counts for all events recorded in silicon per keV for cadmium-109 showing the principal $Ag\ K_{\alpha,\beta}$ peaks. The EMCCD was cooled to 256.0 $\pm$ 0.1 K, with Φ_{HV} set to 37.5 V and 60,000 frames were acquired.

5.2.4 The calibrated spectrum for americium-241

Figure 5.6 shows the energy deposition spectrum for an americium-241 source. The EMCCD was cooled to 256.0 $\pm$ 0.1 K, with Φ_{HV} set to 37.5 V and 60,000 frames were acquired. The tail of the noise spectrum is seen in the interval between 1 keV to about 15 keV, and has been thresholded using the noise peak plus 5σ; this noise peak is off-scale. There was a single principal peak identified as the principal gamma at 59.5 keV with FWHM= 2.28 keV; there are several other peaks identified as shown using the Laboratoire National Henri Becquerel LNHB 2011/53 database [Be et al., 2011]. The EMCCD counts recorded will be scaled according to the response of silicon as a function of energy as shown on Figure 2.2, i.e. the probability of photoabsorption is greater for lower incident energies. Since americium-241 decays by alpha transitions to neptunium-237, the recorded response for the americium-241 source in Figure 5.6 is a complex admixture of gamma photons; the reader may refer to Laboratoire National Henri Becquerel LNHB 2011/53 database [Be et al., 2011] for the relative amplitudes for each type of emission.

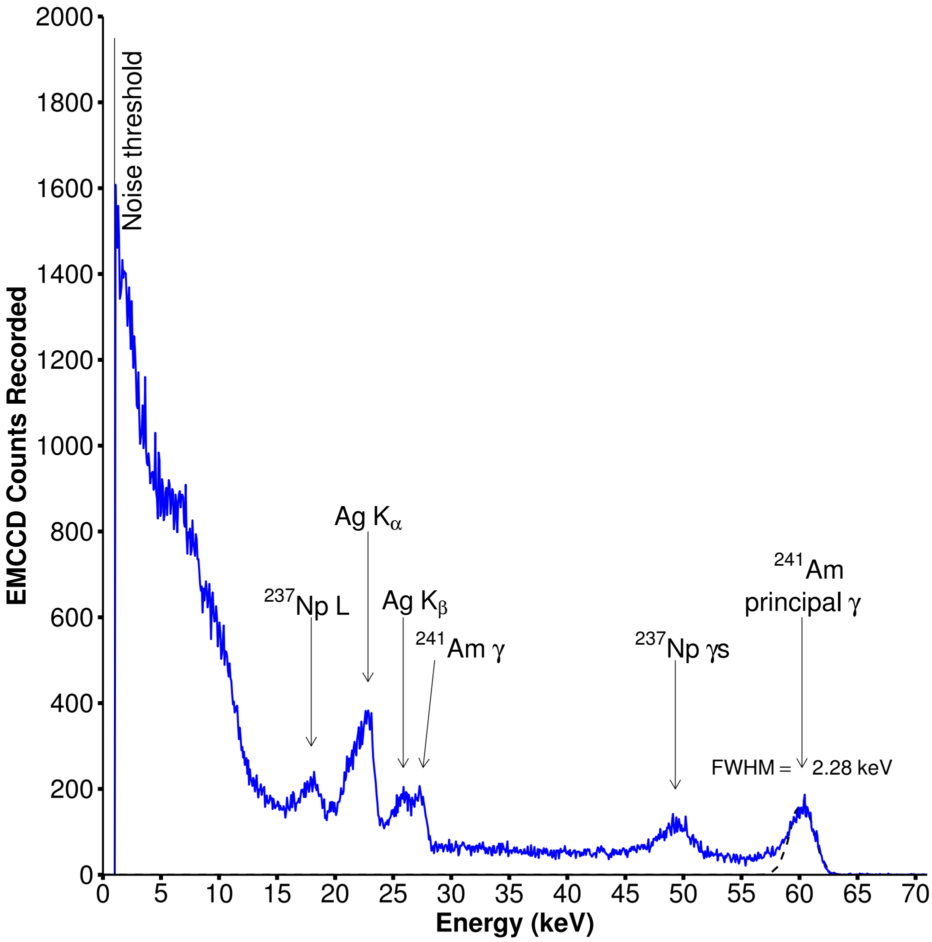

Figure 5.6: EMCCD Counts for all events recorded in silicon per keV showing the americium-241 principal γ peak at 59.5 keV. The EMCCD was cooled to 256.0 ± 0.1 K, with Φ_{HV} set to 37.5 V and 60,000 frames were acquired.

The principal peaks in the energy deposition spectrum for the americium-241 principal γ peak at 59.5 keV and cadmium-109 $AgK_{\alpha1,\alpha2}$ peaks were each fitted to a Gaussian profile. Table 5.2 shows the FWHM for these principal peaks for both radionuclides, where the FWHM is given by Equation 5.1.

$$FWHM = 2\sigma\sqrt{2ln2} \tag{5.1}$$

By fitting these principal peaks the calibration value was calculated to be 118.8 ± 4.7 ADU Channel/ keV for gain potential difference Φ_{HV}= 37.5 V with the EMCCD cooled to 256.0 ± 0.1 K. This calculation of the calibration value used the principal gammas from two different radionuclides across the widest energy interval, then compared this calibration value with that for the cadmium-109 $AgK_{\beta1,\beta2}$ peaks. This value was corroborated using the cadmium-109 $AgK_{\beta1,\beta2}$ peaks.

radionuclide	ADU Channel	Energy/ keV	FWHM / keV
americium-241 principal γ peak	7450	59.5	2.28
cadmium-109 principal $AgK_{\alpha1,\alpha2}$ peaks	2825	22.1	1.14
cadmium-109 $AgK_{\beta1,\beta3}$ peaks	3200	24.9	1.14
Difference between principal peaks	7450 -2825 =4625	59.5 -22.1 =37.4	-

Table 5.2: The peaks were fitted to a Gaussian profile with mean m and standard deviation σ. The calibration value between ADU Channel and keV was calculated to be 118.8 ± 4.7 ADU Channel/ keV using the difference between the principal peaks for the americium-241 principal γ peak at 59.5 keV and cadmium-109 $AgK_{\alpha1,\alpha2}$ peaks. The gain potential difference Φ_{HV}= 37.5 V and the EMCCD was cooled to 256.0 ± 0.1 K.

5.2.5 Discussion

In the preliminary experiment to assess the response of the EMCCD by adjusting its gain potential difference Φ_{HV} between 33.5 V to 39.5 V, a noise peak is initially seen, followed along the abscissa in increasing ADU channel units by the photochannel signal peak (where this is resolvable), as shown by the plots in Figure 5.3. The noise peak is expected since shot noise from the image and storage regions of the EMCCD is multiplied by the gain register and dominates the Gaussian readout noise from the output amplifier, [Robbins, 2011, Zhang et al., 2009]. When an EMCCD operates in photon counting mode, the distribution of photoelectrons from the amplifier is stochastic, as described in section 2.3. For a low input flux of photons of $\ll$ one photon per pixel during the frame exposure time, the output signal from the EMCCD can be counted as either due to single or zero photoelectrons. This is done by assigning thresholds (above the readout noise) for the resulting output from the amplifier, from which the number of source photo-electrons may be estimated by [Basden et al., 2003]. At higher input photon flux > 0.5 photon per pixel, the probability that two incident photons will be absorbed by a single pixel increases.

In Figures 5.6 and 5.5, the noise peak has been thresholded using the noise peak plus 5σ. If the total mean electron gain in the gain register $G \gg \sigma_{readout}$ where $\sigma_{readout}$ is the standard deviation of the readout noise, then a signal above this threshold is treated as a photoelectron event. This readout noise is independent of gain in terms of electrons, and is thresholded at 5σ to distinguish between zero and single input photoelectrons [Zhang et al., 2009]. Using Equation 2.7 in section 2.3.2 [Zhang et al., 2009] the probability distribution of the number of electrons out of the gain register will have a distribution $z(x)$ given $n = 1$ input photoelectron as Equation 5.2.

$$z(x) = \frac{exp(-1/G)}{G^n} \qquad (5.2)$$

where G is the total mean electron multiplication gain derived from Equation 2.9. The premise of distinguishing between zero and single photoelectron as an input, with thresholding of the output signal from the amplifier using the noise peak plus 5σ, can be justified as the plot of photochannel versus Φ_{HV} between 33.5 V to 39.5 V in Figure 5.4 correlates well with exponential model, Equation 5.2 with R^2=0.98.

The calibration plots for Figures 5.6 and 5.5 were used to calculate the calibration value of 118.8 $\pm$ 4.7 ADU Channel/ keV for gain potential difference Φ_{HV}= 37.5 V with the EMCCD cooled to 256.0 $\pm$ 0.1 K. The FWHM of the americium-241 principal γ peak was 2.28 keV, and that for the cadmium-109 principal $AgK_{\alpha1,\alpha2}$ peak was 1.14 keV. As mentioned in section 2.3.3, in the absence of a scintillator, the energy resolution of semiconductor detectors ΔE can be described by three terms as in Equation 2.10, [Owens et al., 1996, Lees, 2010]. The first term is the intrinsic variance of the number of primary electron hole pairs, ΔE can be calculated as 509 eV at 22.1 keV, using ω= 7.8 eV as the electron hole pair creation energy, F=0.27 as the Fano factor and E= 22.1 keV as the incident photon energy. A Monte Carlo simulation of the Fano limited response in the recorded response for the 5 µm silicon layer is shown in Figure 3.12. The $Ag\ K_\alpha$ and $Ag\ K_\beta$ peaks can be seen and are consistent with the line intensities for the referenced database [Chu et al., 1999] in Table 3.3. There are also adjacent peaks at 20.2 $\pm$ 0.1 keV and 20.3 $\pm$ 0.1 keV owing to fluorescence from each parent peak which causes escape events. In each case the accumulator records an event equivalent to a photon with energy given by the difference between the parent photon energy and the respective silicon K_α

fluorescence photon. This Fano limited response can be compared with Figure 5.5 which shows the EMCCD Counts for all events recorded in silicon for cadmium-109 with broadening of the $Ag\ K_{\alpha\beta}$ peaks; the silicon escape peaks are masked by the noise floor preceding the $Ag\ K_{\alpha}$ peak.

Using quadrature subtraction, the sum of the second and third terms in Equation 2.10 was derived to be 631 eV. The second term comprises of the noise due to incomplete charge collection, drift and transfer through the shift and gain registers, and the third term due to noise from the detector readout. For an EMCCD with Φ_{HV}= 37.5 V and cooled to 256.0 ± 0.1 K, the readout noise for the e2v CCD97-00 back illuminated EMCCD is 4 electrons per pixel per frame with each pixel size of 16 μm x 16 μm with 30 Hz frame rate and gain of 1000 [e2vTechnologies, 2004]. Each 16 μm x 16 μm pixel in the silicon array is binned by four within the EMCCD, so the effective "pixel size" is 64 μm x 64 μm. Therefore the readout noise with Φ_{HV}= 37.5 V and cooled to 256.0 ± 0.1 K, is 16 electrons per effective pixel size per frame. While using Φ_{HV}= 37.5 V and cooling to 256.0 ± 0.1 K is beneficial to resolve the photochannel peak from the gain noise peak, increasing Φ_{HV} beyond 40 V to 42 V also increases the shot noise contribution to the second term in Equation 2.10. To put this dark noise into perspective, for our e2v CCD97-00 back illuminated EMCCD used in the CGC shows the readout noise increases when Φ_{HV}= 42 V and cooled to 263.0 ± 0.1 K, equal to 330 electrons per effective pixel size per frame [Bugby, 2015].

The transfer of charge through the shift and gain registers is determined by the charge transfer efficiency. This is the ratio of the generated to induced charge at the detector quoted as being 99.999% as the reverse bias fully depletes the silicon layer [Short et al., 2002]. However the charge transfer efficiency is not specified by the manufacturer for our EMCCD [e2vTechnologies, 2004]. Nonetheless the lag in the collection of charge is not likely to be a major contribution to the second term in Equation 2.10 with CTE almost 100%. Hence this was approximated to 100%. It should be noted that if the solid state crystal is of poor quality then there are likely to be sites of charge trapping. In our EMCCD even though the silicon is of high quality, over several thousand cycles of charge transfer through the shift and gain registers there will be variance in the transfer and collection within the potential wells under each pixel. Incomplete charge collection is discussed in the following section in the context of charge sharing amongst the pixelated silicon detector.

5.3 Experiment to assess the charge sharing in the silicon pixel array

5.3.1 Method

When X-ray and gamma events are detected by the silicon pixel array, the charge cloud generated in the silicon layer may be distributed over several pixels. For our e2v CCD97-00 back illuminated EMCCD, analysis of the events recorded per frame were performed for the cadmium-109 and americium-241 to determine how these events were distributed. These events per frame were assessed to be either single pixel (mono-pixel), shared between two pixels (bi-pixel) or three pixels (tri-pixel) or four pixels (quad-pixel) as shown in an example 4 x 4 pixel array, Figure 5.7. The algorithm used to assess their distribution over the frame [Hansford, 2006] identifies any pixels with adjacent connections within the cluster then classifies them according to whether they were mono-pixel event or shared with several other adjacent pixels. The classification algorithm matches the experimental data to predefined clusters with known arrangements of attached pixels. For the analysis a full-frame region of 128 x 128 pixels was formed over each of the EMCCD frames and 60,000 frames collected. The shape matching algorithm identifying these event types was used to process each of these 60,000 frames by analysing the charge sharing amongst the pixel array.

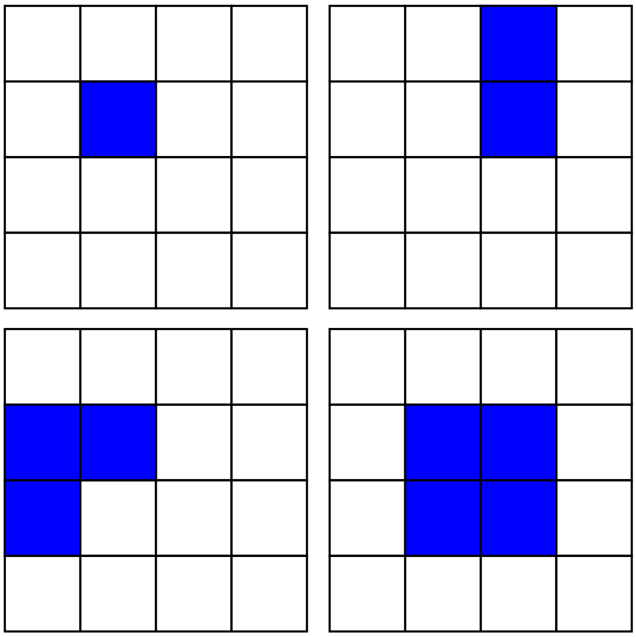

Figure 5.7: Example of four 4 x 4 silicon pixel arrays each for a single EMCCD frame showing a single event detected over either one pixel (mono-pixel), or two pixels (bi-pixel) or three pixels (tri-pixel) or four pixels (quad-pixel). No dead space is shown between pixels within each silicon array as the fill factor is 100% [e2vTechnologies, 2004].

5.3.2 Results

Each of the mono-pixel, bi-pixel, tri-pixel, quad-pixel events that the EMCCD recorded for cadmium-109 is shown in Figure 5.8. This demonstrates the proportion of charge sharing to the total of all events. There are a large number of mono-pixel events and bi-pixel events with a lower proportion of tri-pixel and quad-pixel events with their amplitudes tabulated in Table 5.3.

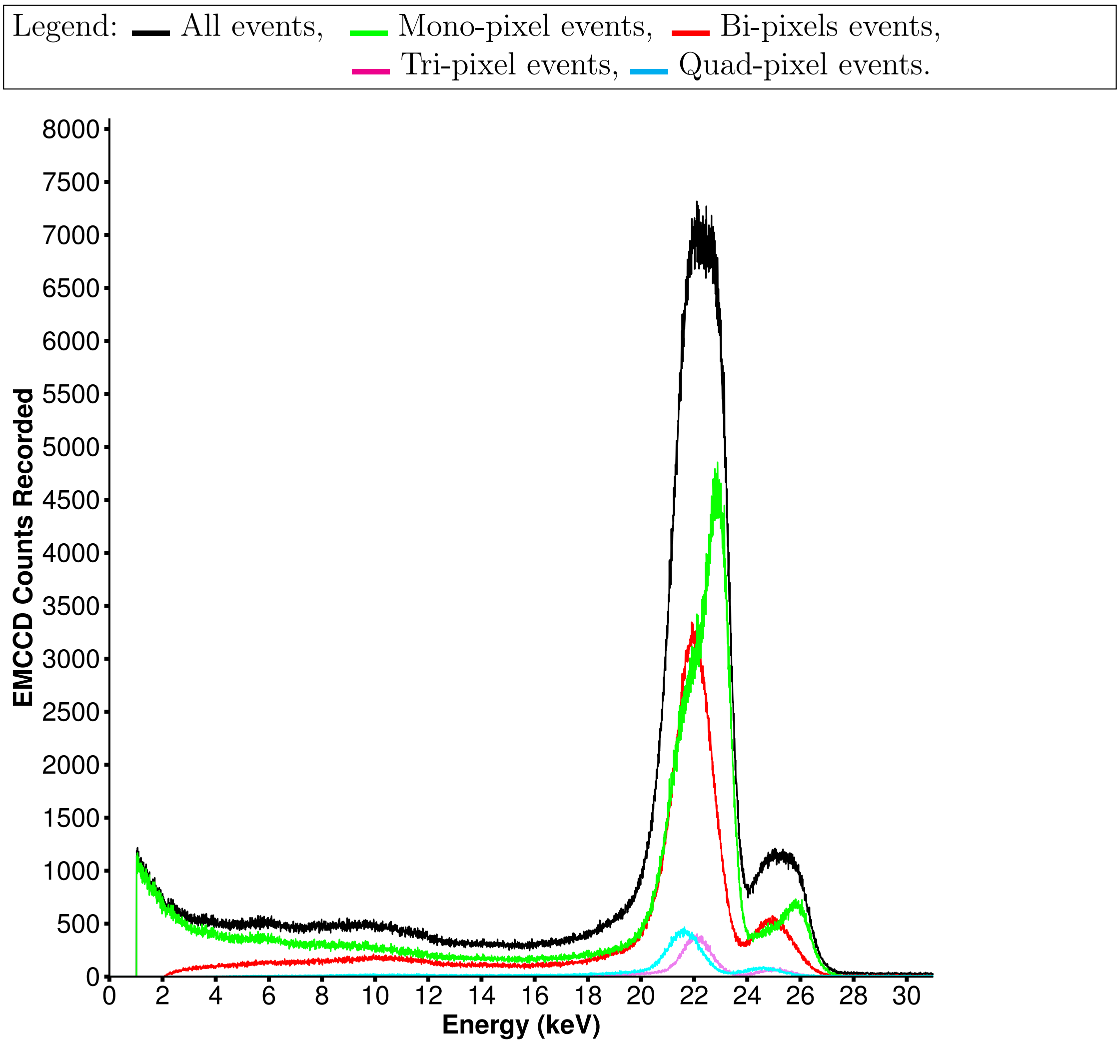

Figure 5.8: EMCCD recorded counts for All, Mono-pixel, Bi-pixel, Tri-pixel and Quad-pixel events for the principal $AgK_{\alpha,\beta}$ peaks of the cadmium-109 spectrum. The EMCCD Gain was 37.5 V and 60,000 frames were acquired. The EMCCD was cooled to 256.0 $\pm$ 0.1 K.

The principal peaks for the cadmium-109 spectrum were fitted to a Gaussian profile and are tabulated in Table 5.3 where m is the mean and σ is the standard deviation of the fitted peak. The full-width half-maximum [FWHM] for the peaks are also shown.

Events	Principal Peak EMCCD Counts ± 10	Gaussian fit: m keV ± 0.1	Gaussian fit: σ keV ± 0.05	FWHM $2\sigma\sqrt{2.ln2}$ keV ± 0.12
All	7350	22.2	0.82	1.93
Mono-pixel	4500	22.8	0.48	1.13
Bi-pixel	3350	22.0	0.73	1.72
Tri-pixel	420	21.7	0.61	1.44
Quad-pixel	380	22.0	0.57	1.34

Table 5.3: The principal peaks for the cadmium-109 multi-pixel spectra were each fitted to a Gaussian profile with mean m and standard deviation σ. The EMCCD gain potential difference Φ_{HV}= 37.5 V and the EMCCD was cooled to 256.0 $\pm$ 0.1 K. The full-width half-maximum [FWHM] for the peaks are also shown.

In the case of the americium-241 spectrum, the findings for each of the mono-pixel, bi-pixel, tri-pixel, quad-pixel events that the EMCCD recorded is shown in Figure 5.9.

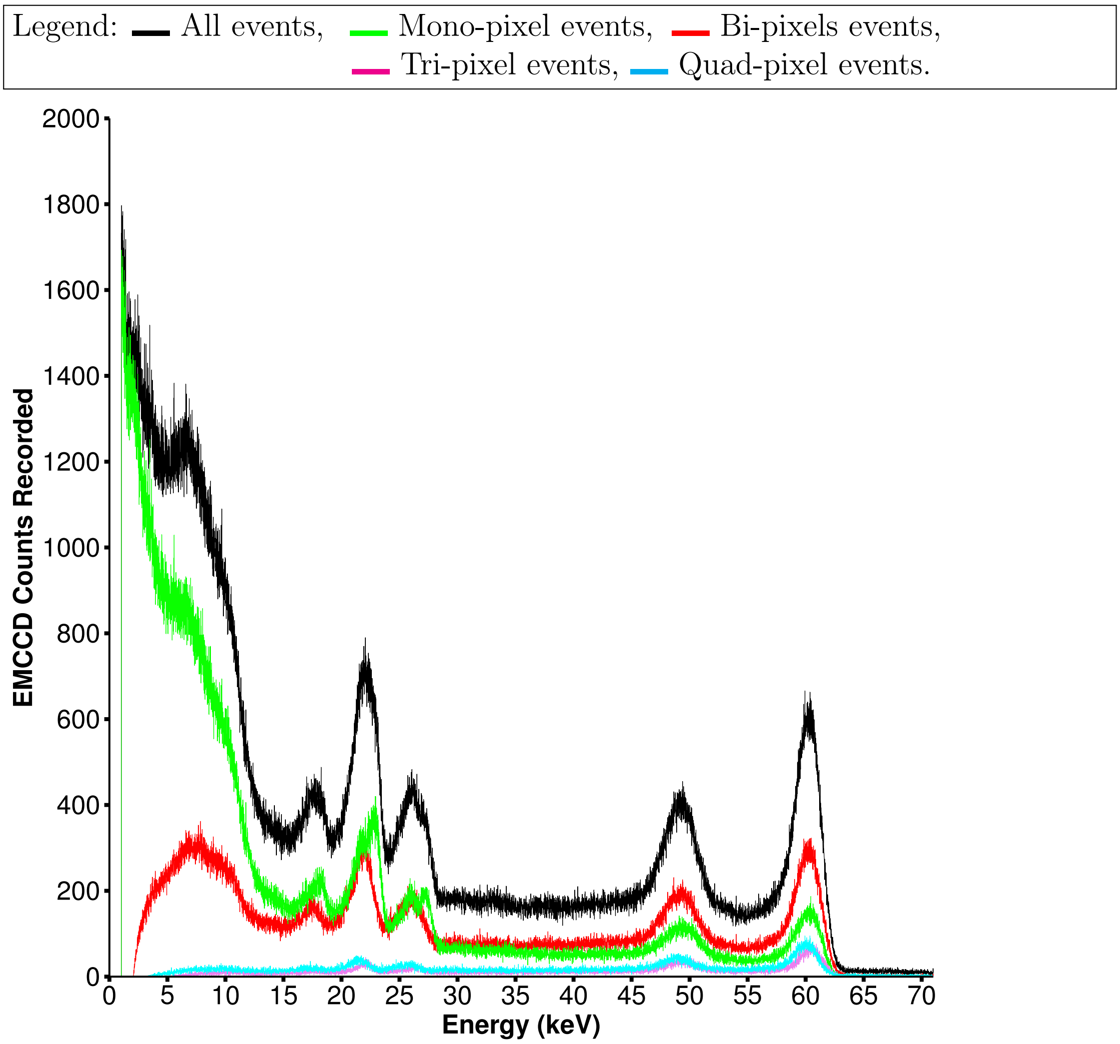

Figure 5.9: EMCCD recorded counts for All, Mono-pixel, Bi-pixel, Tri-pixel and Quad-pixel events for the americium-241 spectrum. The EMCCD Gain was 37.5 V and 60,000 frames were acquired. The EMCCD was cooled to 256.0 ± 0.1 K.

The principal γ peak for Amercium-241 multi-pixel spectra were fitted to a Gaussian profile and are tabulated in Table 5.4.

Events	Principal Peak EMCCD Counts ±10	Gaussian fit: m keV ±0.1	Gaussian fit: σ keV ±0.05	FWHM $2\sigma\sqrt{2.ln2}$ keV ±0.12
All	650	60.2	1.0	2.35
Mono-pixel	175	60.2	1.0	2.35
Bi-pixel	300	60.2	1.0	2.35
Tri-pixel	80	59.8	1.0	2.35
Quad-pixel	75	60.3	1.0	2.35

Table 5.4: The principal γ peak at 59.5 keV for the americium-241 multi-pixel spectra were each fitted to a Gaussian profile with mean m and standard deviation σ. The EMCCD gain potential difference Φ_{HV}= 37.5 V and the EMCCD was cooled to 256.0 ± 0.1 K. The full-width half-maximum [FWHM] for the peaks are also shown.

5.3.3 Discussion

Using the cadmium-109 source the EMCCD Counts for all events recorded in silicon per keV is shown in Figure 5.5. The energy resolution of these principal $Ag\,K_{\alpha,\beta}$ peaks was broad compared to the corresponding Monte Carlo simulation in the absence of noise as shown in Figure 3.12. The FWHM for these principal $Ag\,K_{\alpha,\beta}$ peaks were tabulated in Table 5.2. Notice that both the low energy edges of these AgK_α and AgK_β peaks were broadened. In the case of the principal γ peak at 59.5 keV for the americium-241 spectrum in Figure 5.6, this also shows broadening of its low energy edge. The FWHM for this principal γ peak at 59.5 keV is also shown in Table 5.2.

As the charge cloud diffuses outwards, the probability distribution of charge collected within the potential wells across several pixels manifests as a shift of the centroid peak of multi-pixel events towards lower energies, [Owens et al., 1994]. The broadening of the low energy edge is caused by charge sharing between the pixels of the silicon array owing to:

- the depth-of-interaction and photoelectron range
- diffusion of electron and hole to the electrodes and,
- fluorescence X-rays.

If the impinging gamma photon is absorbed in the depletion layer, the lateral spreading of the charge cloud may be described by analytical models as a cascade of photoelectrons which are generated until a charge cloud with thermalised electrons is produced [McCarthy et al., 1995, Popp et al., 2000, Lees, 2010]. These photoelectrons drift under the $\mathbf{E}-$field as electron hole pairs are generated along their trajectory. The path of the photoelectrons is non-linear and if the distribution of electron hole pairs is created near the periphery of the detector, some of this electrons may also leave the detector in this early stage of the cascade of photoelectrons. The charge collected by the detector represents the radius of the charge cloud, amount of recombination, charge losses and any partial reflection of thermalised electrons near the Si-SiO_2 surface layer, [McCarthy et al., 1995, Lees, 2010]. The depth of the interaction of the gamma photon also determines the radius of the charge cloud, [McCarthy et al., 1995, Short et al., 2002, Lees, 2010].

Multi-pixel events are expected since the charge spread is given as the full-width at (1/e) maximum FW as Equation 5.3, [Nilsson et al., 2002]

$$FW = 4\sqrt{D_n t} \tag{5.3}$$

where D_n is the diffusion coefficient for electrons and t is the drift time for the electrons to reach their electrode. For semiconductors D_n is given by the Einstein relationship, Equation 5.4 for charge q, Boltzmann constant k= 8.62 10^{-5} eV.K^{-1}, temperature T and electron mobility μ_n as

$$\frac{D_n}{\mu_n} = \frac{kT}{q} \tag{5.4}$$

Since the EMCCD was cooled to 256.0 K, $kT/q \simeq 22$ mV. For silicon the electron mobility $\simeq$1000 $\mathrm{cm^2\,V^{-1}s^{-1}}$[Howe and Sodini, 1997], D_n is the diffusion coefficient for electrons $\simeq$ 26 $\mathrm{cm^2\,s^{-1}}$. The electron carrier drift velocity $\simeq$ 10^6 $\mathrm{cm\,s^{-1}}$, so the drift time across a 5 μm silicon detector would be 5 ps. Using Equation 5.3 and assuming a drift time of 5 ps, then the full-width at (1/e) maximum for the charge spread is $\simeq$ 46 μm across. Each 16 μm x 16 μm pixel in the silicon array is binned by four within the EMCCD, so the effective "pixel size" is 64 μm x 64 μm. However, the trajectory of the charge cloud is not necessarily orthogonal to silicon pixel array so multi-pixel events are expected. The ratio of mono-pixel events to bi-pixel events in Tables 5.3 and 5.4 implies that it is more probable for width of the charge cloud to be across a couple of pixels instead of a single pixel at higher incident photon energies. There are a couple of points to bear in mind about this analysis. The drift time is dependent on the energy of the incident photon and its depth-of-interaction within silicon. Secondly, the assumption of a Gaussian charge dispersion of the measured charge at the electrodes provided by [Nilsson et al., 2002, Wang et al., 2011] needs to be justified.

Fluorescence X-rays occur when incident gamma and X-ray photons are photoabsorbed in silicon followed by relaxation as described in section 2.2. The $Ag\ K_{\alpha\beta}$ X-ray photons may be absorbed in the silicon contributing to the spread of the charge cloud however since the silicon layer is only 5 μm thick, it is likely to leave unimpeded; for a X-ray photon of energy 21.9 keV, its range in silicon is 1.24 mm. The range of the primary photoelectron in silicon is 5.72 μm from photoabsorption of a 21.9 keV source photon. Both ranges were calculated using PENELOPE. High energy X-rays are more likely to cause the photoelectrons generated to spread over many pixels, [Nelms et al., 2002]. The decomposition of the EMCCD recorded counts for all events shows a large number of mono-pixel events and bi-pixel events with a lower proportion of tri-pixel and quad-pixel events with their amplitudes tabulated in Table 5.3. Below about 28 keV the proportion of mono-pixel events is greater than bi-pixel events. Then above 28 keV, the proportion of bi-pixel events is greater than mono-pixel events. This effect is demonstrated in Figure 5.9 for americium-241.

5.4 Conclusions

This chapter has demonstrated the response of our e2v CCD97-00 back illuminated EMCCD [e2vTechnologies, 2004] with its gain potential difference Φ_{HV} using cadmium-109 when the EMCCD was cooled to 256.0 $\pm$ 0.1 K. As the distribution of photoelectrons from the amplifier is stochastic, the thresholding scheme of using noise peak plus 5σ worked well for gain potential difference Φ_{HV} between 33.5 V and 39.5 V. This thresholding scheme is only valid for low input photon flux, and is the case for our EMCCD which is operated at 10 frames per second.

Comparing the Fano-limited Monte Carlo simulation performed in chapter 3 using a 5 μm thick silicon detector of cross-section 8 mm x 8 mm, in the absence of noise, with the experimental response of the EMCCD using cadmium-109 showed broadening of the $Ag\,K_{\alpha,\beta}$ peaks. This was consistent with the energy resolution (in the absence of a scintillator) being broadened owing to incomplete charge collection, drift and transfer through the shift and gain registers, and also due to noise from the detector readout, described earlier in section 2.3.

There was an additional finding within the experimental responses using amerium-241 and cadmium-109 which showed that low energy edges of the principal γ peak at 59.5 keV and the $AgK_{\alpha\beta}$ peaks were respectively broadened. This additional low energy edge broadening was deemed to be caused by charge sharing between the pixels of the silicon array. The generation of the charge cloud owing to its depth-of-interaction and non-linear photoelectron range, in combination with its trajectory as determined by the distribution of electron hole charge carriers and their diffusion, all affect the collection of charge at the silicon pixel array. The probability distribution of charge collected within the potential wells across several pixels manifests as a shift of the centroid peak of multi-pixel events towards lower energies. Existing models of the Gaussian charge dispersion of the measured charge at the electrodes provided by [Nilsson et al., 2002, Wang et al., 2011] require further investigation in order to be justified.

Lastly, the decomposition of the EMCCD recorded counts for all events using americium-241 showed that the proportion of mono-pixel events is greater than bi-pixel events below an incident photon energy of about 28 keV. Then above 28 keV, the proportion of bi-pixel events is greater than mono-pixel events. This effect warrants using either analytical or Monte Carlo modelling to compare the incident photon energy with this effect occurring in relation to the silicon pixel size. If the silicon pixel array is coarser than that used in our EMCCD less charge sharing is expected; however, this effect would be counteracted by higher energy photons which are more likely to cause the photoelectrons generated to spread over many pixels.

This chapter has considered the same bare silicon detector used in both the Portable Imaging X-ray Spectrometer detector [PIXS] and the Compact Gamma Camera [CGC]. The following chapter adds both a monolithic and columnar 1500 μm thick caesium iodide scintillator to consider the propagation of optical photons and their detection by the silicon detector.

Chapter 6

GEANT4 Optical simulations of a caesium iodide scintillator - silicon detector model

6.1 Introduction

In Small Field-Of-View gamma photon imaging systems employing scintillators and solid state devices an important aspect of the imaging process requires an understanding of the frequency distribution of the optical photons that are generated within the scintillator, and their frequency distribution when impacting on the silicon detector. In this chapter the term frequency refers to number frequency not radiation frequency. To facilitate this, Monte Carlo simulations of the transport of gamma, X-ray and optical photons through a caesium iodide scintillator-silicon detector were modelled. In the wider scope scintillator and silicon based detectors are wide-spread in other types of clinical imaging [van Eijk, 2003, Roncali et al., 2017].

The transport of optical photons within the caesium iodide crystal can be simulated using Monte Carlo codes with appropriate models of the physics describing their interactions; these processes are either Rayleigh scattering or Mie scattering, together with Fresnel reflection and Fresnel refraction. There are several optical Monte Carlo codes which may be used to simulate the transport of optical scintillations and these include using dedicated Monte Carlo codes:

- MANTIS [Badano and Sempau, 2006]
- HybridMANTIS [Sharma et al., 2012]

and general purpose codes:

- GEANT4 [Agostinelli et al., 2003]
- GATE [Jan et al., 2004], (essentially a front-end wrapper for GEANT4).

The choice for the required simulation depends on the ease in creating a representation of the scintillator and its accuracy in modelling optical surface parameters derived from experiment. Scattering of optical photons occurs in the scintillator, some of which causes optical blurring in the detector and others which potentially escape from the scintillator crystal avoiding detection. Optical blur is further increased because the primary photons from the source can be scattered causing secondary particles (photoelectrons and lower energy X-ray photons). The primary photons will interact at various depths within the scintillator. This depth-of-interaction within columnar structured scintillators has been modelled by Badano [2003], who assessed its effect on the Line Spread Function (LSF) and Modulation Transfer Function [(MTF), the optical blur and optical photon collection efficiency. The modulation transfer function (MTF) is derived from the Fourier Transform of the LSF. The modelled scintillator comprised of a square grid of 1000 x 1000 columns, each of diameter 9 μm with intra-column vacuum spacing of 1 μm. However there was a limitation to that study viz. the absence of the scattering due to secondary particles.

An improved version of their Monte Carlo code called MANTIS coupled the tracking of secondary photons generated from PENELOPE to the creation and transport of scintillation photons [Badano and Sempau, 2006]. Their model accounted for the small angle columnar tilt found in structured caesium iodide (up to 5 degrees away from the orthonormal to the crystal base), greater column packing density (85%), and included the unstructured scintillation layer at the base of columns (15%) and a passive substrate layer (amorphous carbon). This may be seen for example in Figure 7.3 in the following chapter. MANTIS uses input files to describe the optical properties of the medium as a function of photon wavelength λ. These include the linear absorption coefficient μ_a and refractive index n; the linear scattering coefficient μ_s as a function of wavelength is given by Rayleigh's law for which μ_s is proportional to λ^{-4}. Optical photons were modelled as having isotropic scattering or having Rayleigh scattering for unpolarised light with angular dependence given by $(1 + 2cos\,\theta)$ where θ is the angle between incident and scattered photons [Badano and Sempau, 2006].

Both MANTIS and the updated Monte Carlo code HybridMANTIS by the same group [Sharma et al., 2012] can be coupled to the *a priori* transport of gamma photons using the PENELOPE physics models. However, MANTIS [Badano and Sempau, 2006] has a typical computational speed of one optical photon history per second and the construction of a geometry file used for the Monte Carlo simulation can be complex as it uses several quadric surfaces, (see section 3.2). HybridMANTIS uses graphical processing compute units (GPUs) which allows the optical transport to be simulated more efficiently; however, the simulation may have overlapping geometric structures as these are created dynamically during the simulation. Nonetheless a second feature of this latter code is that optical cross-talk through a columnar caesium iodide scintillator may be simulated. In GATE [Strul et al., 2003, Jan et al., 2004, Staelens et al., 2003] scintillator structures may be readily created. All three Monte Carlo codes use selected experimental crystal surface parameters based on Lambertian (diffuse) and specular reflections as described for MANTIS [Freed et al., 2009], HybridMANTIS [Sharma et al., 2012] and GATE/ GEANT4 [Janecek, 2012, Galasso et al., 2015]. A Lambertian reflection distribution is the scalar product (cosine dependence) of the surface normal and the angle of incidence relative to the surface normal.

The probability that an optical photon is detected at the silicon detector is given by the frequency distribution of the scintillation photons that are generated within the scintillator, those that are directed towards the silicon detector, as well as matching the emission spectrum of the scintillator to the spectral sensitivity of the silicon detector. Aside from optical simulations based on MANTIS [Badano, 2003, Badano et al., 2006, Freed et al., 2009] and HybridMANTIS [Sharma et al., 2012, Sharma and Badano, 2013], GATE has been used to simulate the optical transport through a Positron Emission Tomographic detector module comprising of monolithic scintillator (LYSO:Ce) [van der Laan et al., 2010]. However, it was hampered by a limited number of optical surface parameters at the time of this work.

6.2 GEANT4 Optical simulation

This chapter uses a different Monte Carlo code to PENELOPE v2008 used in earlier chapters called GEANT4 [Agostinelli et al., 2003]. GEANT4 was used to model the transport of gamma and X-ray photons, and in addition that of the optical photons created within a caesium iodide scintillator (recalling that PENELOPE v2008 does not include scintillation photons). GEANT4 provides a framework of C++ libraries [GEANT4 Collaboration - G4Applications, 2018] which allows different models of physics to be simulated. Compared to alternative Monte Carlo codes, GEANT4 is preferred for the modelling of the caesium iodide scintillator-silicon detector as it:

- Incorporates the transport of gamma, X-ray and optical photons
- Allows greater flexibility in the geometrical design used to model the detector compared to quadrics
- Incorporates a PENELOPE physics model used in earlier chapters
- Incorporates the optical surface properties of the target materials in these simulations.

An important aspect of the G4 Optical physics model "G4 Optical" to consider [Gumplinger, 2002, GEANT4 Collaboration - G4Applications, 2018, GEANT4 Collaboration - G4Physics, 2018] is that GEANT4 gamma and X-ray photons are simulated by using a different physics model compared to that for optical photons. Although a photon is considered as optical when its wavelength is much greater than the atomic spacing, GEANT4 does not have a smooth transition between the X-ray and gamma photon wavelength range to optical photon wavelengths. In GEANT4 simulations, the processing of the parent gamma photon is suspended when the scintillation photon is generated; then the tracking of scintillation photons is continued until the optical photon is absorbed or outside the geometry of the detector. The electromagnetic models used in this work include the GEANT4 C++ coding of PENELOPE v2008 called "G4 EmPENELOPE". As such, the photon interactions used in this chapter include photoabsorption, Compton scatter and Rayleigh scatter. Chapter 2 provided an overview of these photon interactions but the specifics of the GEANT4 simulations may be found in GEANT4 version 10.5 Physics Reference manual [GEANT4 Collaboration - G4Physics, 2018]. Table 6.1 provides a summary of "G4 EmPENELOPE" physics used in this work.

Electromagnetic Model	“G4 EmPENELOPE” physics
Energy range	100 eV to 1 GeV
Photoabsorption	G4PenelopePhotoElectric
Compton Scatter	G4PenelopeCompton
Rayleigh Scatter	G4PenelopeRayleigh
De-excitation	Bearden Fluorescence
Interaction cross-sections	EPDL97

Table 6.1: The “G4 EmPENELOPE” electromagnetic model comprises of physics for the PENELOPE v2008 including photoabsorption, Compton scatter, Rayleigh scatter, the Bearden fluorescence model [Bearden and Burr, 1967] and interaction cross-sections of EPDL97 are the Lawrence Livermore Evaluated Photon Data Libraries respectively, `https://www-nds.iaea.org/epdl97/`.

For photoabsorption “G4 EmPENELOPE” uses differential cross-sections derived from EPDL97. For Compton scatter, “G4 EmPENELOPE” uses an analytical form for Klein-Nishina accommodating both atomic binding effects and Doppler broadening as described in section 2.1. The GEANT4 tracking of atomic de-excitation is simulated using the Bearden fluorescence model [Bearden and Burr, 1967].

In this work, the frequency distribution of the optical photons were recorded rather than its energy spectrum as GEANT4 does not conserve energy once the optical photons are created from the primary photon(s) and propagated to produce secondary photon tracks [GEANT4 Collaboration - G4Physics, 2018].

6.3 GEANT4 Models

The following sections describe Monte Carlo simulations which use the GEANT4 optical physics model alongside the “G4 EmPENELOPE” physics model. At the time of writing a systematic approach to simulate the frequency distribution of the scintillation photons that are generated within the scintillator and the frequency distribution of the scintillation photons impacting on a silicon detector has not previously been published for a low energy source photon flux (less than 200 keV) used in clinical imaging. The modelling included the photoabsorption and Compton scattering of the source photon flux. The emission of scintillation photons was isotropic, and the transport of optical photons included Rayleigh scattering.

The following cases were considered for both monolithic and columnar caesium iodide crystals to evaluate the frequency distribution of optical photons generated. In GEANT4 interfaces between surfaces are treated as dielectric-dielectric where optical photons are either absorbed, Fresnel reflected, Fresnel refracted or undergo total internal reflection [GEANT4 Collaboration - G4Physics, 2018]. Alternatively where appropriate optical surfaces are treated as dielectric-metal where the optical photons are either absorbed or reflected. Both the caesium iodide crystal and silicon detector had areas of 8 mm x 8 mm in the following cases referring to Figure 6.1:

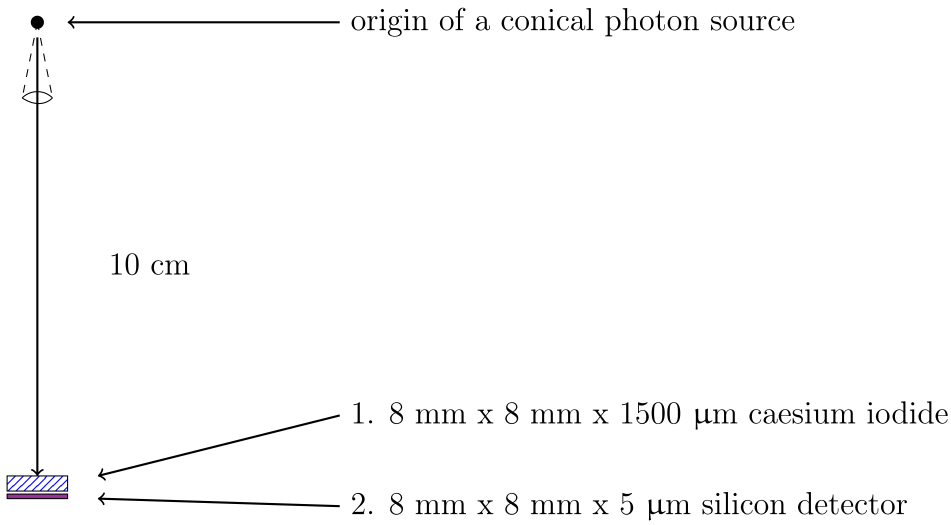

Figure 6.1: Using a 140.5 keV mono-energetic conical photon source, the schematic shows how the frequency distribution of scintillation photons was determined within an event accumulator in: 1. 1500 µm thick caesium iodide, 2. with a 5 µm silicon layer added.

Cases simulated:

1. Scintillation photons accumulated within a 1500 µm thick monolithic caesium iodide.

2. Scintillation photons impacting onto a 5 µm silicon detector abutted directly to the egress face of the 1500 µm thick monolithic caesium iodide.

3. As model #2 but with the 1500 µm thick monolithic caesium iodide wrapped with 1 µm thick aluminium on its lateral faces relative to the direction of the incoming photons.

4. As model #2 but with columnar 1500 µm thick caesium iodide comprised of columns 100 µm x 100 µm x 1500 µm thick, as shown in Figure 6.2. This represents the closest approximation to the real detector.

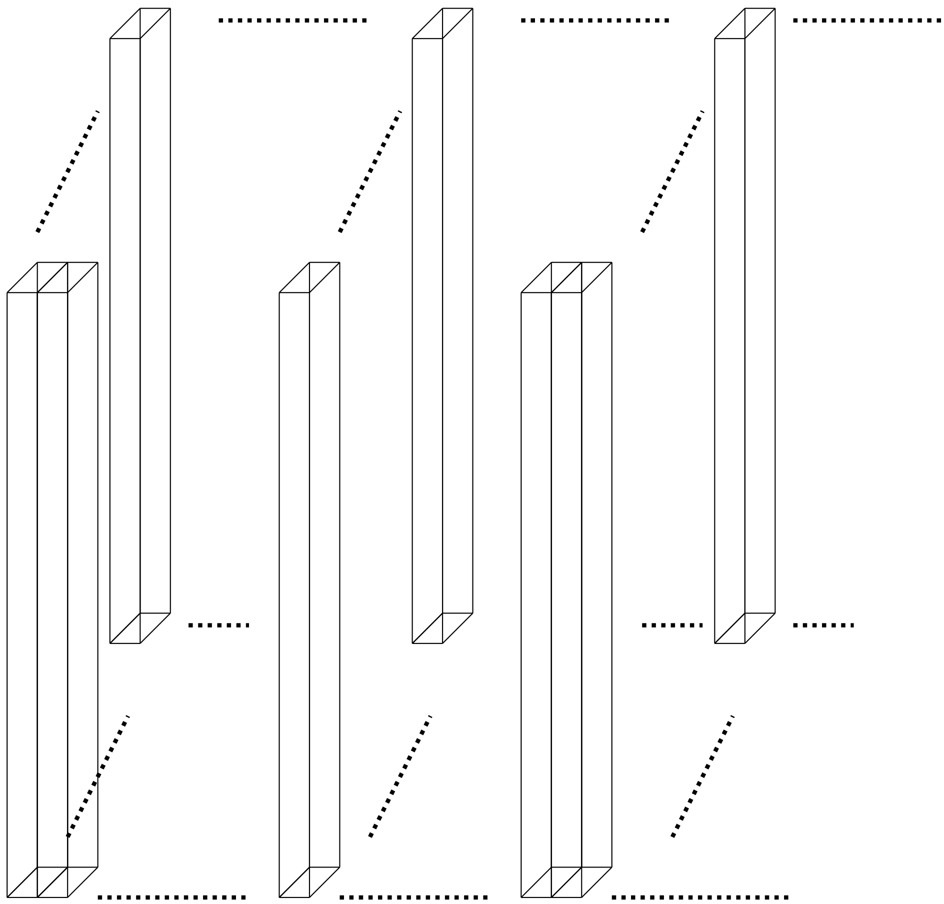

Figure 6.2: A model of a columnar crystal comprised of columns 100 μm x 100 μm x 1500 μm thick. (Only a few columns are shown but they populate the whole crystal volume).

In all simulations the source mono-energetic technetium-99m photon flux was modelled as a cone of 5 degree semi-angle which was centrally directed orthogonal to the plane of the target crystal. No coupling media was used between the egress face of the caesium iodide and the 5 μm thick silicon detector, which was abutted directly to the scintillator without a gap in between. The optical emission spectrum for caesium iodide was derived from a technical publication although the amount of trace thallium doping was unknown [Hamamatsu-Photonics, 2019]; Knyazev et al. [2019] indicate trace thallium doping of $\approx 0.1\%$. No Poisson noise was added to the simulations. The surface pixel properties of the silicon detector including reflectivity of the individual pixels and pixel array dead space were not modelled.

6.4 GEANT4 Optical simulation parameters

There are several parameters required for the simulation of scintillation photons in GEANT4. The scintillation yield of the caesium iodide was set to 54 photons per keV [Blasse, 1994]. The refractive index of caesium iodide was set to 1.79 for optical photons within the energy range 2.3864 eV to 3.447 eV [Blasse, 1994]. The ratio of the fast to slow scintillation components was set to 0.8 [Dorenbos et al., 1995], with their optical decay time constants set to 2.1 ns and 1000.0 ns respectively [Blasse, 1994], as shown in Table 2.1. This is because radiative emission of optical photons occurs as the self-trapped excitons relax or as the excited luminescent ions returns to ground state. The relaxation of excited luminescent ions to ground state may be considered to be comprised of three energy transfer processes [Dietrich and Murray, 1972] viz.:

1. The prompt creation of an excited thallium ion, $\mathrm{Tl}(^{1+})^*$
2. The diffusion of a self-trapped hole and capture by neutral thallium to create excited thallium ion, $\mathrm{Tl}(^{1+})^*$
3. The diffusion of a self-trapped hole and capture by an excited thallium ion, $\mathrm{Tl}(^{2+})^*$. This is followed by a thermally released electron from neutral thallium and its capture by the excited thallium ion $\mathrm{Tl}(^{2+})^*$ to create $\mathrm{Tl}(^{1+})^*$.

Thus the optical decay times arise from the lifetime of the excited state in case #1, the diffusion rate of the self-trapped hole in case #2, and diffusion time of the thermally released electron in case #3. The latter two cases are responsible for the slow component of the scintillation decay time constant. Kerisit et al. [2008] extended the model of Dietrich and Murray [1972] to include the prompt relaxation of self-trapped excitons.

If there is a cluster of excited molecules along the incoming primary photon, de-excitation can be caused without photon emission ("quenching effect"), with the overall scintillation modulated by the Birks constant. The optical light output is described by Birks law, Equation 6.1 [Abreu et al., 2011]

$$\frac{dL}{dx} = \frac{A(\frac{dE}{dx})}{1 + K_B(\frac{dE}{dx})} \tag{6.1}$$

where K_B is Birks constant which is an empirical value determined from experiment, dL/dx is the light output per unit length, dE/dx is the energy loss per unit length and A is the absolute scintillator efficiency. The latter parameter will depend on the depth-of-interaction of the source photons within the scintillator. The scintillation yield of the caesium iodide was set to $A = 54$ photons per keV [Blasse, 1994]. For small dE/dx, Equation 6.1 is approximated by Equation 6.2 for fast electrons created during the scintillation process.

$$\frac{dL}{dx} \approx A\frac{dE}{dx} \tag{6.2}$$

The quenching of optical photon output caused by the scintillation is described using Birks constant and was set to 0.126 µm per keV [Abreu et al., 2011].

In all simulations the optical absorption length as a function of wavelength was derived [Knyazev et al., 2019] and its average value was taken to be 33.0 cm. Knyazev et al. [2019] used a spectrophotometer with two beams of light; one for sampling the attenuation length through caesium iodide, and the other as the reference. The spectral range covered the caesium iodide emission peak 350 nm to 800 nm as shown in Figure 6.8. They derived the optical absorption length as a function of wavelength $L(\lambda)$ as Equation 6.3,

$$L(\lambda) \approx \frac{t/ln10}{A + 2log(1 - R(\lambda)} \tag{6.3}$$

where t is the length of the crystal, A is the attenuation of the light derived from the Beer-Lambert equation, and $R(\lambda)$ is the reflection at the entrance and egress faces of the crystal, derived from Fresnel equations.

In Monte Carlo simulations design parameters can be varied, however where experimental data is often unavailable or limited the simulation is difficult to model. However, one such model of the surface property of scintillators uses the GLISUR surface description, [GEANT4 Collaboration - G4Applications, 2018]. The surface property of the scintillator crystal will be affected by the crystal coating, structure, and optical reflectivity [Roncali et al., 2017]. This surface model allows the user to select the finish pertaining to the smoothness of the crystal surface with a polish of unity enabling Snell's Law for Fresnel reflection whereas polish tending towards zero creates optical reflection with a Lambertian distribution. This simplification does not represent actual crystal surfaces but provides a first order approximation. Although GEANT4 also provides an alternative surface description "UNIFIED" this uses surfaces comprised of a several surface micro-facets; it's use is hampered by lack of experimentally derived data to fulfil its various parameters. However, optical surface models can be determined from the Fresnel transmission and reflection coefficients, or from predefined surface types which are either optically transparent, perfect reflector, Lambertian diffuse reflector, specular reflector or a perfect absorber.

In the following graphs showing the frequency distribution of events per bin, the statistical uncertainty in the ordinate was $\pm\sqrt{N}$ for N events but its error bars were not shown for clarity.

6.5 Scintillation photons generated within 1500 µm thick monolithic caesium iodide.

6.5.1 Method

An initial GEANT4 optical simulation was created with a monolithic caesium iodide crystal of area 8 mm x 8 mm and 1500 µm thick positioned 10 cm away from a mono-energetic technetium-99m conical photon source. The conical photon source had a 5 degree semi-angle which was centrally directed orthogonal to the surface of the target crystal. A schematic of this set-up is shown in Figure 6.3. The "G4 EmPENELOPE" electromagnetic model was used for the photon interactions and the G4 Optical physics model was used for the generation and transport of scintillation photons. This optical simulation used the GLISUR model of optical surface parameters [GEANT4 Collaboration - G4Applications, 2018] and a dielectric-dielectric surface was used for the caesium iodide crystal to allow the optical photons to be either absorbed, Fresnel reflected or Fresnel refracted.

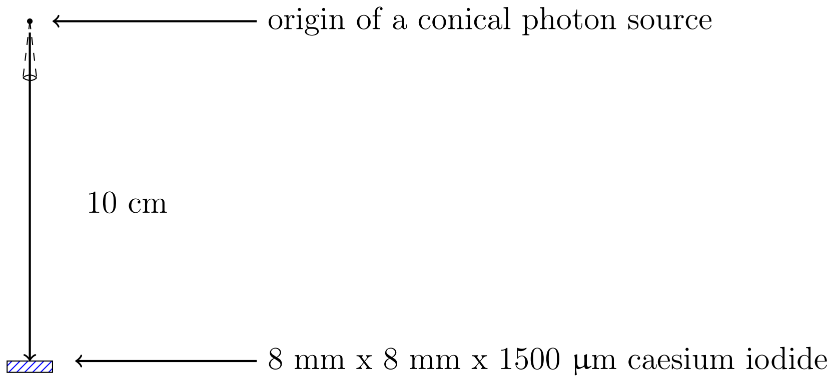

Figure 6.3: Schematic of the model to assess the frequency distribution of scintillation photons generated within a monolithic 1500 µm caesium iodide crystal using a mono-energetic technetium-99m conical photon source.

The Monte Carlo simulation was performed using GEANT4 with the total number of simulated primary photon histories set as 1.0 x 10^9, and used to determine the frequency distribution of scintillation photons generated within the monolithic scintillator crystal. One hundred GEANT4 threads were used, each simulating 1.0 x 10^7 primary photon histories. The GEANT4 population accumulator occupied the whole volume of the scintillation crystal.

6.5.2 Results

The frequency distribution of scintillation photons generated within the 1500 μm thick monolithic caesium iodide crystal using a mono-energetic technetium-99m photon source with a 5 degree semi-angle and centrally directed orthogonal to the plane of the target crystal is shown in Figure 6.4.

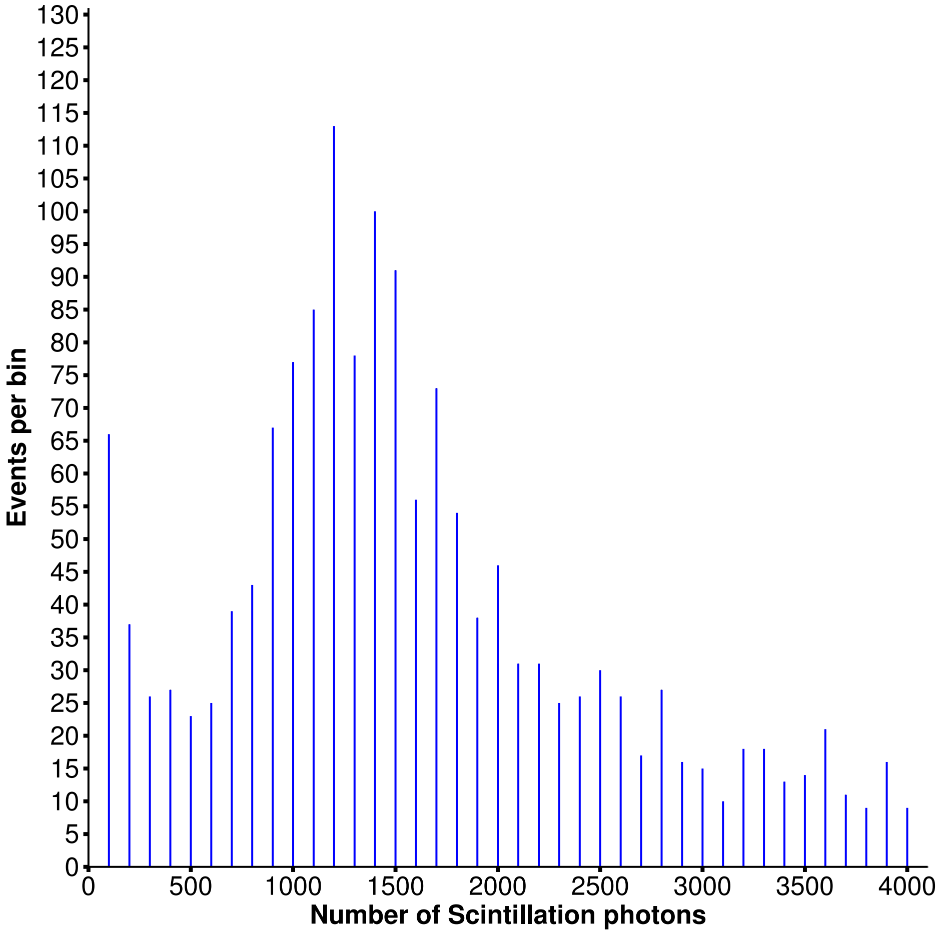

Figure 6.4: 20 hours' multi-threaded "G4 EmPENELOPE" plus G4 Optical physics model simulation of the frequency distribution of scintillation photons generated within monolithic 1500 μm thick caesium iodide using a mono-energetic technetium-99m photon flux source. The total number of simulated primary photon histories was 1.0 x 10^9.

The tails of each of the two peaks in Figure 6.4 may be fitted to two exponential curves.

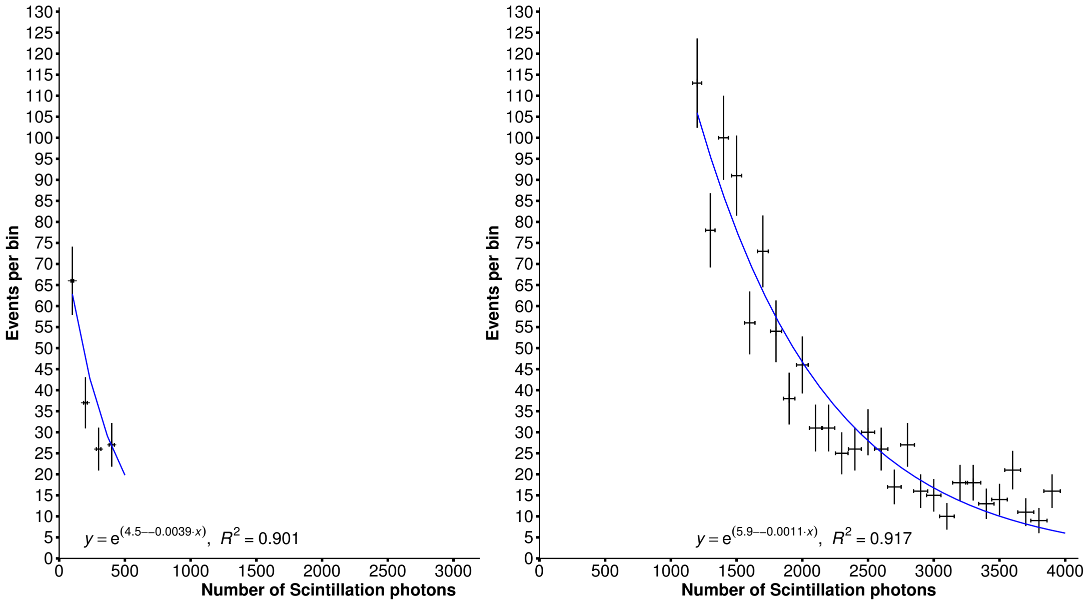

Figure 6.5: Exponential fitting of each of the tails of these two peaks in the frequency distribution of scintillation photons generated within monolithic 1500 μm thick caesium iodide using a mono-energetic technetium-99m photon flux source.

6.5.3 Discussion

Figure 6.4 shows a frequency distribution of scintillation events per bin within monolithic 1500 μm thick caesium iodide crystal. In Figure 6.4 there is a peak amplitude clustered around approximately 1400 scintillation photons. This frequency distribution of scintillation events per bin also shows a smaller amplitude clustered around approximately 100 scintillation photons. The ratio of the smaller peak amplitude to the higher one is approximately 0.65. Both peak amplitudes have a tail which incorporates the fast to slow scintillation decay components collected over the duration of the simulation [Dorenbos et al., 1995]. The mean number of scintillation photons in this frequency distribution is 1,686. Figure 6.5 shows the exponential fitting of each of the tails of these two peaks in the frequency distribution of scintillation photons generated within monolithic 1500 μm thick caesium iodide. By taking account of the range along the abscissa, the exponential decay constants of these tails were found to be similar (Λ=0.36). This suggests that the smaller amplitude clustered around approximately 100 scintillation photons is likely to be a reflected cluster from within the crystal originating from the peak amplitude clustered around approximately 1400 scintillation photons. This is consistent with an analytical model [Galasso et al., 2015] which derived the radial distribution of scintillation light in a monolithic crystal with a single optical reflection from the inner entrance surface back towards the egress surface.

In section 4.2.2 the energy deposition within a model of a 600 μm thick Caesium Iodide crystal was investigated (in the absence of scintillation photons) using PENELOPE v2008 [Salvat et al., 2011]. As the PENELOPE energy deposition accumulator was positioned wholly within the volume occupied by the caesium iodide crystal, it accumulated the energy deposited by photons which undergo photoabsorption, Compton scatter and from fluorescence in the crystal. Photoabsorption creates photoelectrons of energy 139.9 keV, which have a mean free path of 0.113 μm for inelastic scattering within caesium iodide (calculated using PENELOPE for source photons of energy 140.5 keV and a mean excitation energy for caesium iodide of 0.553 keV, obtained from PENELOPE simulation tables). The subsequent de-excitation creates fluorescence X-rays and secondary knock-on electrons which gradually dissipate their energy within the crystal. The energy deposited by these photons interactions, fluorescence X-rays and photoelectron inelastic scattering together create the profile for the frequency distribution of scintillation events per bin in Figure 6.4.

Within caesium iodide of density ρ= 4.51 gcm^{-3}, the photon mean free path for photoabsorption of gamma rays is 3.2155 mm (derived using PENELOPE v2008 [Salvat et al., 2011]), which is greater than the thickness of the 1500 μm thick caesium iodide crystal. Although the physical interpretation is that the majority of gamma photons pass through the 1500 μm thick caesium iodide crystal, the photoabsorption and Compton scattering still contributes to the population of optical photons created. This transmission of gamma photons through the crystal is 0.83, 0.63 and 0.08 respectively for the 600 μm, 1500 μm and 8000 μm thick caesium iodide crystals, as shown in Figure 4.8. In chapter 3 section 3.5.3, the detector efficiency as a function of energy deposited within the 1500 μm thick caesium iodide monolithic crystal E_{CsI} for a point source was 0.3165 and is used to generate scintillation photons.

In GEANT4, the population of optical photons accumulated n_{ph} is sampled from a Gaussian distribution with an expectation value $\bar{n}_{ph}$ [GEANT4 Collaboration - G4Applications, 2018], Equation 6.4,

$$\bar{n}_{ph} = E_0 \bar{Y} \tag{6.4}$$

where E_0= 140.5 keV is incident gamma photon energy, and $\bar{Y}$= 54 photons per keV is the scintillation yield. The expectation value $\bar{n}_{ph}$ was calculated to be 7587 photons. In Figure 6.4 the mean number of scintillation photons in this frequency distribution is 1,686. For n independent observations for each bin, the variance $\hat{\mu}_2$ as given by the second central moment in Equation 2.14. For a Poisson distribution with n=1.0 x10^8 the variance can be derived to be $(7587 - 1686)^2$ x 10^{-8}=0.348.

The proportion of the mean number of scintillation photons in this frequency distribution to the expectation value $\bar{n}_{ph}$ is 0.22. This proportion is less than the unity owing to the detector efficiency as a function of energy deposited (0.3165) within the 1500 μm thick caesium iodide monolithic crystal, the depth-of-interaction of the primary photons within the caesium iodide crystal, and the transport of scintillation photons out of the volume occupied by the GEANT4 accumulator collecting the optical events.

6.6 Scintillation photons impacting onto a 5 μm silicon detector with an intervening unwrapped monolithic caesium iodide crystal

6.6.1 Method

In this section a GEANT4 optical simulation was initially created with the monolithic caesium iodide crystal of area 8 mm x 8 mm and 1500 μm thick positioned 10 cm away from a mono-energetic technetium-99m conical photon source. In addition a 5 μm thick silicon detector of area 8 mm x 8 mm was abutted directly without any space to the egress face of the caesium iodide crystal relative to the direction of the incoming source of photons. A mono-energetic technetium-99m source of 5 degree semi-angle was centrally directed orthogonal to the plane of the target crystal. A schematic of this set-up is shown in Figure 6.6.

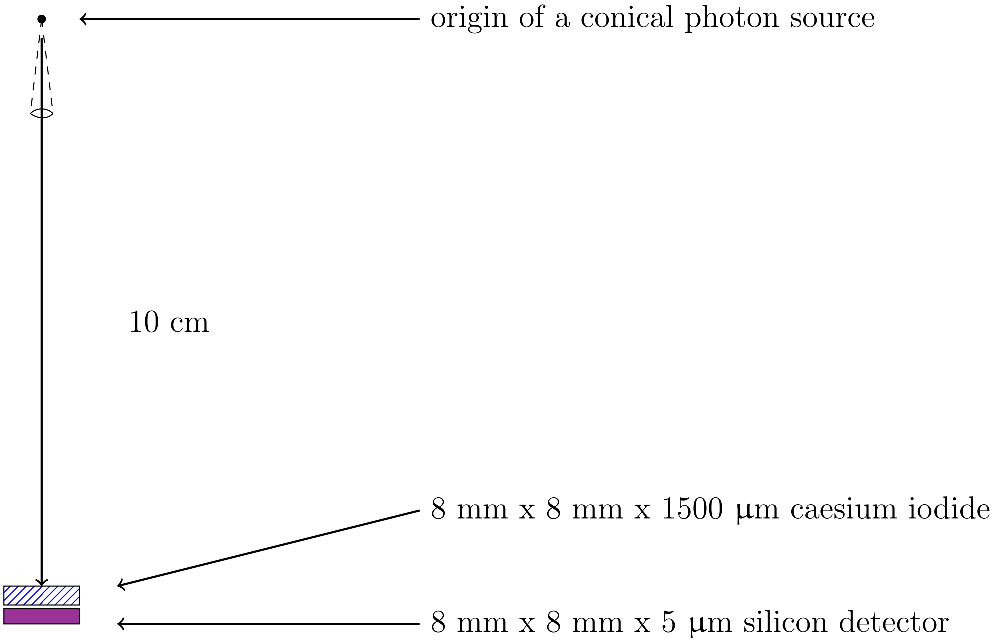

Figure 6.6: Schematic of the model to assess the distribution of energy deposited within an event accumulator positioned within 5 µm silicon for an intervening unwrapped monolithic caesium iodide crystal 1500 µm thick, using a mono-energetic technetium-99m source.

The "G4 EmPENELOPE" electromagnetic model was used for the gamma and X-ray photons photon interactions and the G4 Optical physics model was used for the scintillation photons. The frequency distribution of scintillation photons within the 5 µm thick silicon was recorded noting that GEANT4 does not continue to track the primary photon interactions once the scintillation photons are created and propagated. The GEANT4 optical simulation used the GLISUR model of optical surface parameters [GEANT4 Collaboration - G4Applications, 2018] and a dielectric-dielectric surface was used for the caesium iodide crystal to allow the photons to be either absorbed, Fresnel reflected or Fresnel refracted. The optical surface of the scintillator was set as polished with reflectivity of unity for optical photons within the range 2.0 eV to 4.0 eV. The same modelled scintillation parameters were used for the monolithic caesium iodide as in section 6.5. The optical surface of the 5 µm silicon was set as dielectric-metal with a polished finish and its reflectivity was unity. When the GLISUR model is specified, the only surface finish options available are polished or ground. For dielectric-metal surfaces, the GLISUR G4OpBoundaryProcess also defaults to unit reflectivity and zero detection efficiency [GEANT4 Collaboration - G4Physics, 2018]. Thus any optical photons which were not absorbed, were either back-scattered into the scintillator or scattered away and not accumulated. The number of simulated primary photon histories was 1.0 x 10^8.

6.6.2 Results

Figure 6.7 shows the frequency distribution of scintillation photons impacting onto the 5 μm thick silicon with an intervening unwrapped monolithic 1500 μm thick caesium iodide crystal.

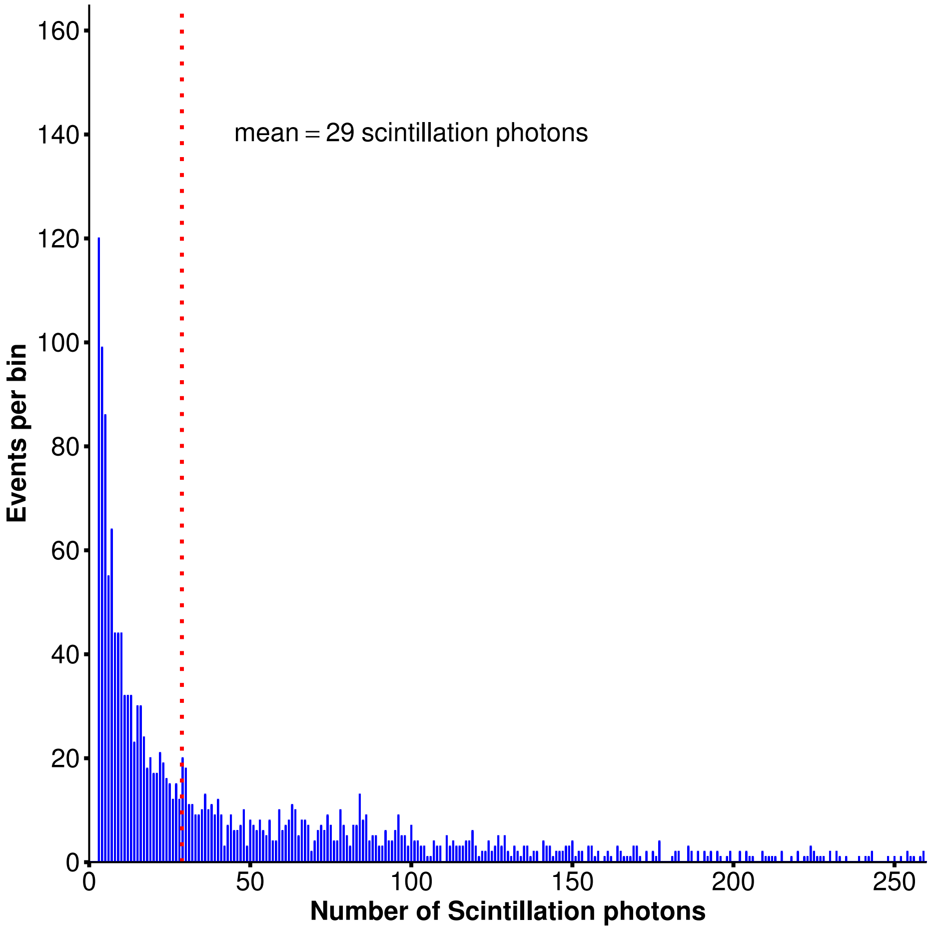

Figure 6.7: 15 hours' G4 EmPENELOPE plus G4 Optical physics model simulation of the frequency distribution of scintillation photons impacting onto the 5 μm thick silicon detector using a mono-energetic technetium-99m and unwrapped monolithic 1500 μm thick caesium iodide intervening between the source and detector. The number of simulated primary photon histories was 1.0 x 10^8.

6.6.3 Discussion

The 5 μm thick silicon detector is representative of the EMCCD whose quantum efficiency peaks in the optical wavelength range as shown in Figure 6.8. This matching of spectra to the emission spectrum of the scintillation photons is an important feature to aid their detection.

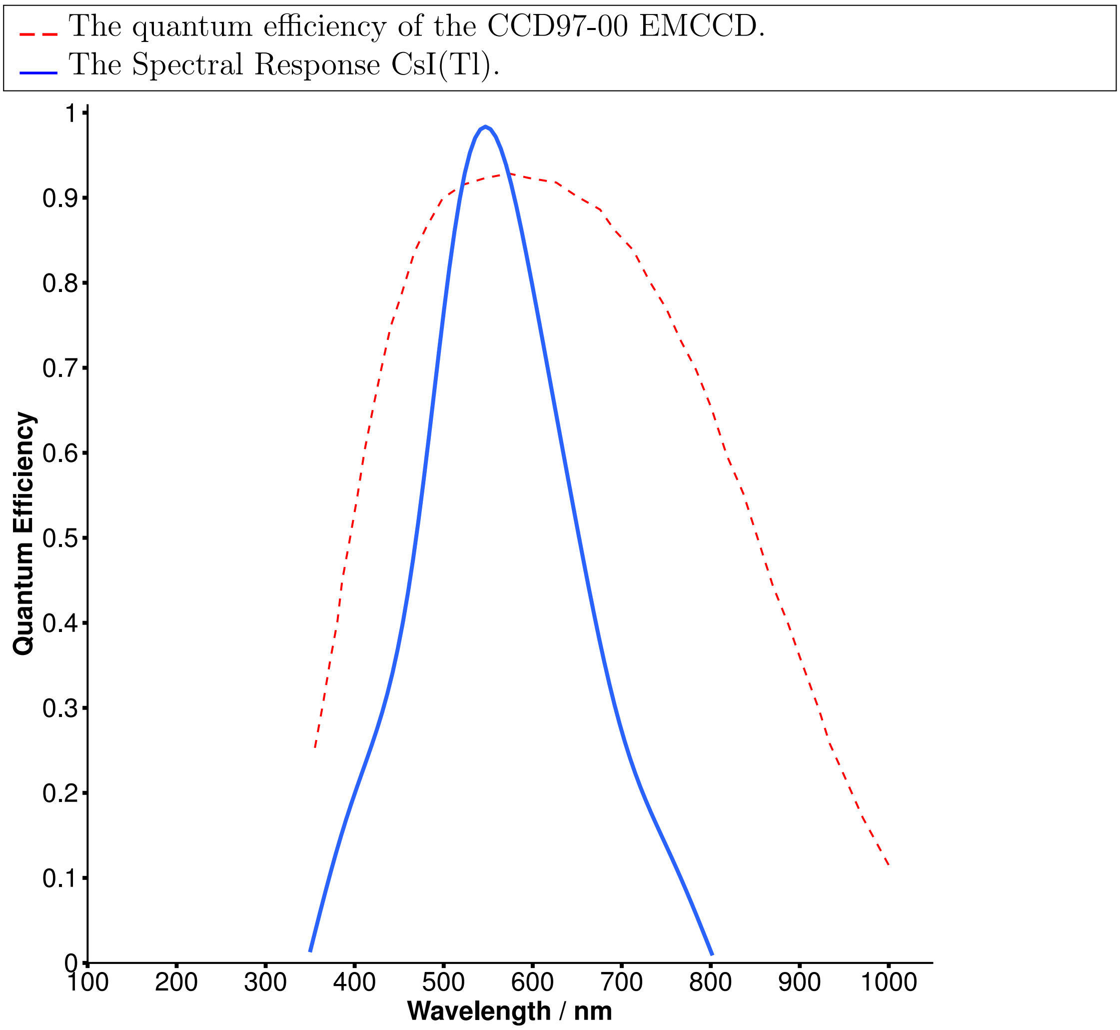

Figure 6.8: The quantum efficiency of the CCD97-00 EMCCD (dashed), permission to use data courtesy of Archie Barrow, Teledyne e2v and the spectral response of CsI(Tl)[Hamamatsu-Photonics, 2019]

The peak of the optical emission spectrum will be proportional to the energy deposition by the primary photons impinging the scintillator and will be reduced by any optical photon losses in the collection en route to the detector. As pointed out [Roncali et al., 2017], any self-absorption or scattering in the crystal bulk should be minimised to increase the collection yield of optical quanta.

The optical photons impacting on the silicon detector will depend on the spatial distribution of the scintillation photons directed towards it, the scintillator's surface properties, any absorption or scattering within the scintillator crystal, the probability of collection of optical quanta by the detector, the detector's surface properties, the quantum efficiency of the detector. The surface pixel properties of the silicon detector including reflectivity of the individual pixels and pixel array dead space were not modelled. Noise within the silicon detector was not modelled in this optical model but was discussed in detail in section 2.3 and in the preceding chapter in the context of the e2v CCD97-00 back illuminated EMCCD [e2vTechnologies, 2004].

6.7 Scintillation photons impacting onto a 5 μm silicon with an intervening monolithic caesium crystal laterally wrapped with 1 μm aluminium.

6.7.1 Method

In this case the simulation above using the monolithic caesium iodide crystal in section 6.6.1 was repeated with the addition of an 1 μm aluminium wrapper surrounding the lateral surfaces of the 1500 μm monolithic caesium iodide crystal, as referenced to the direction of the impinging photon beam. A 5 μm thick silicon detector of area 8 mm x 8 mm was abutted directly to the egress face of the wrapped caesium iodide crystal. The number of simulated primary photon histories was 1.0×10^{8}. The GEANT4 optical simulation used the GLISUR model of optical surface parameters [GEANT4 Collaboration - G4Applications, 2018] and a dielectric-metal surface was used for the aluminium to allow the photons to be either absorbed or scattered. The optical surface of the scintillator was set as polished with reflectivity of unity for optical photons within the range 2.0 eV to 4.0 eV. The same modelled scintillation parameters were used for the monolithic caesium iodide as in section 6.5. The 1 μm aluminium wrapper was defined to be polished and assigned reflectivities of 1.0 for optical photon energies in the range 2.0 eV to 4.0 eV. There was no optical coupling between the caesium iodide crystal and silicon detector.

6.7.2 Results

The frequency distribution of optical photons impacting onto the 5 μm thick silicon detector using the aluminium wrapped 1500 μm thick monolithic caesium iodide is shown in Figure 6.9.

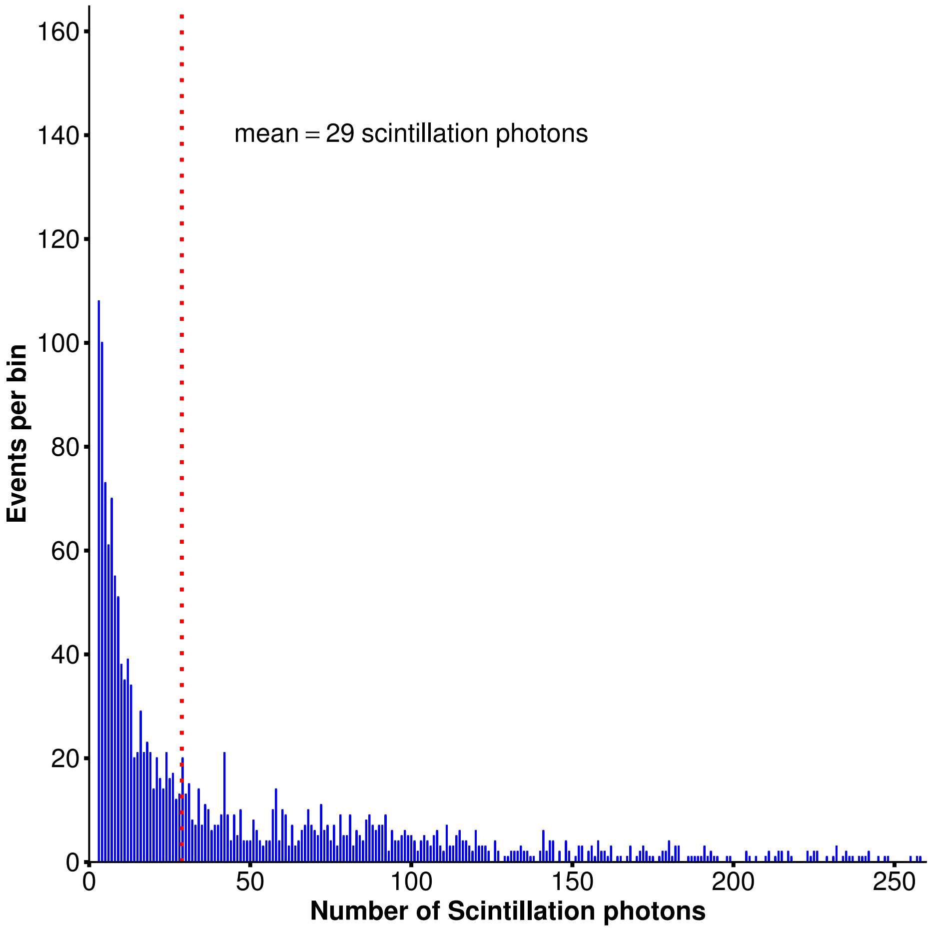

Figure 6.9: 15 hours' G4 EmPhysics plus G4 Optical physics model simulation of the frequency distribution of scintillation photons impacting onto a 5 μm thick silicon detector using a mono-energetic technetium-99m source and 1 μm aluminium laterally wrapping the monolithic 1500 μm thick caesium iodide. The number of simulated primary photon histories was 1.0 x 10^8.

The frequency distribution of scintillation photons impacting onto the 5 μm thick silicon detector in Figure 6.9 show a similar profile to the corresponding unwrapped simulation using monolithic caesium iodide in Figure 6.7. One may have expected the peak events per bin to be higher than the corresponding unwrapped intervening monolithic caesium iodide. In the unwrapped monolithic scintillator crystal optical photons created near all the surface of the crystal can escape from the bulk, whereas for the wrapped monolithic scintillator crystal, only optical photons created near the entrance and egress surfaces of the crystal can escape. The remaining optical photons created near the lateral wrapped surfaces of the monolithic scintillator crystal can be reflected back into the bulk to be absorbed or scattered.

6.7.3 Discussion

There is no significant difference in the mean number of scintillation photons with the addition of a 1 μm thick aluminium wrapper as shown in Figure 6.7 and Figure 6.9. In both these cases, there is a significant reduction in the mean number of scintillation photons impacting the silicon detector (=29), from their production in the caesium iodide crystal. In Figure 6.4 the mean number of scintillation photons in this frequency distribution generated within 1500 μm thick caesium iodide 1,686. For n=1.0 x 10^8 independent observations, the variance $\hat{\mu}_2$ as given by the second central moment in Equation 2.14. As the number of optical photons impacting the silicon detector is a small proportion of those scintillation photons generated within the caesium iodide crystal, the detected photons will follow a Poisson distribution. For a Poisson distribution with n=1.0 x 10^8 the variance can be derived to be $(7587-29)^2$ x 10^{-8}=0.571.

Figure 6.10 shows the cumulative distribution function of the unwrapped monolithic and monolithic 1500 μm thick caesium iodide crystal wrapped with a 1 μm thick aluminium. The two sample Kolmogorov-Smirnov test for difference between these two cumulative distribution function curves gives a D statistic D_n of 0.02810. At a 95% confidence interval, the critical value D_{crit} is approximately given by Equation 6.5

$$D_{crit} = 1.36\sqrt{\left[\frac{1}{n_1} + \frac{1}{n_2}\right]} \tag{6.5}$$

For n_1=n_2=260 data values along the abscissa, D_{crit}=0.1193. Thus as $D_n \ll D_{crit}$ with p=1, there is no significant difference in these two cumulative distribution function curves.

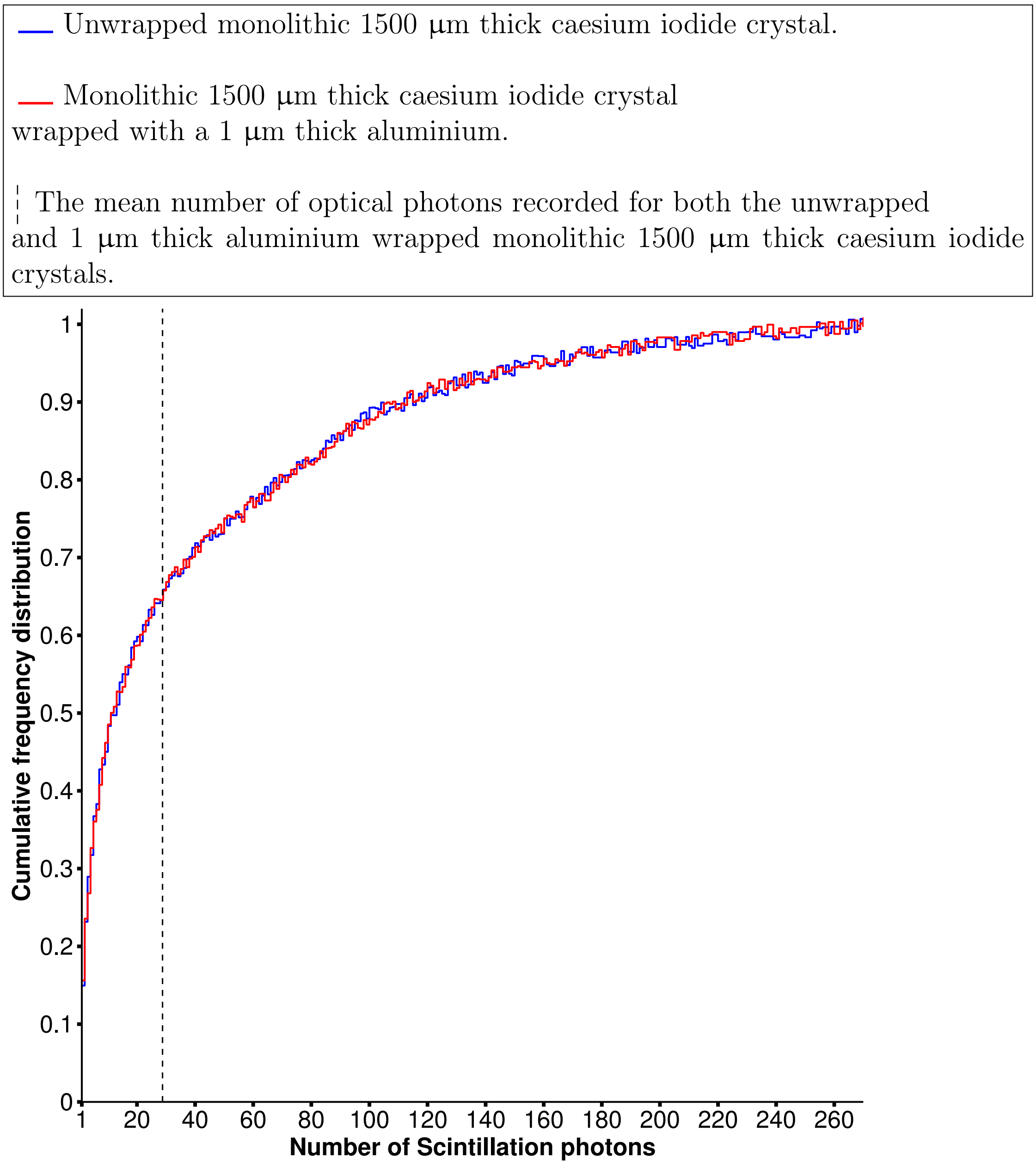

Figure 6.10: The cumulative distribution functions for both the monolithic 1500 μm thick caesium iodide crystals, unwrapped then laterally wrapped with a 1 μm thick aluminium. The dashed vertical line is the mean number of optical photons recorded for both the unwrapped and laterally wrapped with 1 μm thick aluminium simulations.

The total attenuation of optical photons in the bulk of the caesium iodide crystal λ_t is given by Equation 6.6

$$\frac{1}{\lambda_t} = \frac{1}{\lambda_s} + \frac{1}{\lambda_a} \tag{6.6}$$

where λ_s and λ_a are the optical scattering and absorption lengths respectively. The simulation suggests that the optical photons reflected from the inner aluminium surface are absorbed in the bulk of the caesium iodide crystal, or emitted away from the entrance face of the crystal; a proportion will be reflected towards the silicon detector. This finding is consistent with a narrow specular reflection width (FWHM $\approx$ 20 degrees) of a 30 µm aluminium foil noted for angles of incidence to the normal surface between 14 degrees to 78 degrees [Janecek, 2012]. However, Janecek [2012] used a photodiode array over 2π to measure reflectance of a 440 nm laser from 30 µm aluminium foil as 0.787 ± 0.014 relative to four layers of teflon with unity reflectance. This simulation used an estimated reflectivities of 1.0 for optical photon energies in the range 2.0 eV to 4.0 eV in the absence of further experimental data.

In the physical construction of SFOV systems the coupling of the reflector may be via wrapping, gluing or coating all of whose optical surface properties needs to be taken into account. In addition, at interfaces there may well be multiple reflections of optical photons [van der Laan et al., 2010] which affect the number of optical photons propagated to the silicon detector [Roncali et al., 2017]. Recent improvements to GEANT4 include a set of Look-Up-Tables for both surface reflectivity and optical cross-talk between crystal columnar and pixelated structures for several scintillator crystals and common types of reflectors, [Stockhoff et al., 2017].

6.8 Scintillation photons impacting onto a 5 μm silicon detector with an intervening columnar caesium iodide crystals with and without lateral wrapping of 1 μm aluminium.

6.8.1 Method

The above methodology in the previous sections 6.6.1 and 6.7.1 respectively, was repeated for a columnar scintillator in lieu of the monolithic scintillator. The columnar 1500 μm thick caesium iodide was comprised of columns 100 μm x 100 μm. The same optical surface parameters were used for the columnar caesium iodide scintillator and the silicon as mentioned above for the monolithic crystal. The columnar scintillator crystal and silicon detector each had an area 8 mm x 8 mm; the silicon detector as previously described was 5 μm thick. A mono-energetic technetium-99m source of 5 degree semi-angle was centrally directed orthogonal to the plane of the target crystal. The columnar caesium iodide crystal was unwrapped in the first simulation, then the simulation was repeated with the addition of an 1 μm aluminium wrapper surrounding the lateral surfaces of the 1500 μm monolithic caesium iodide crystal, as referenced to the direction of the impinging photon beam. The number of simulated primary photon histories in each case was 1.0 x 10^8.

6.8.2 Results

Figure 6.11 shows the frequency distribution of scintillation photons recorded within the 5 μm thick silicon with an intervening unwrapped columnar 1500 μm thick caesium iodide crystal.

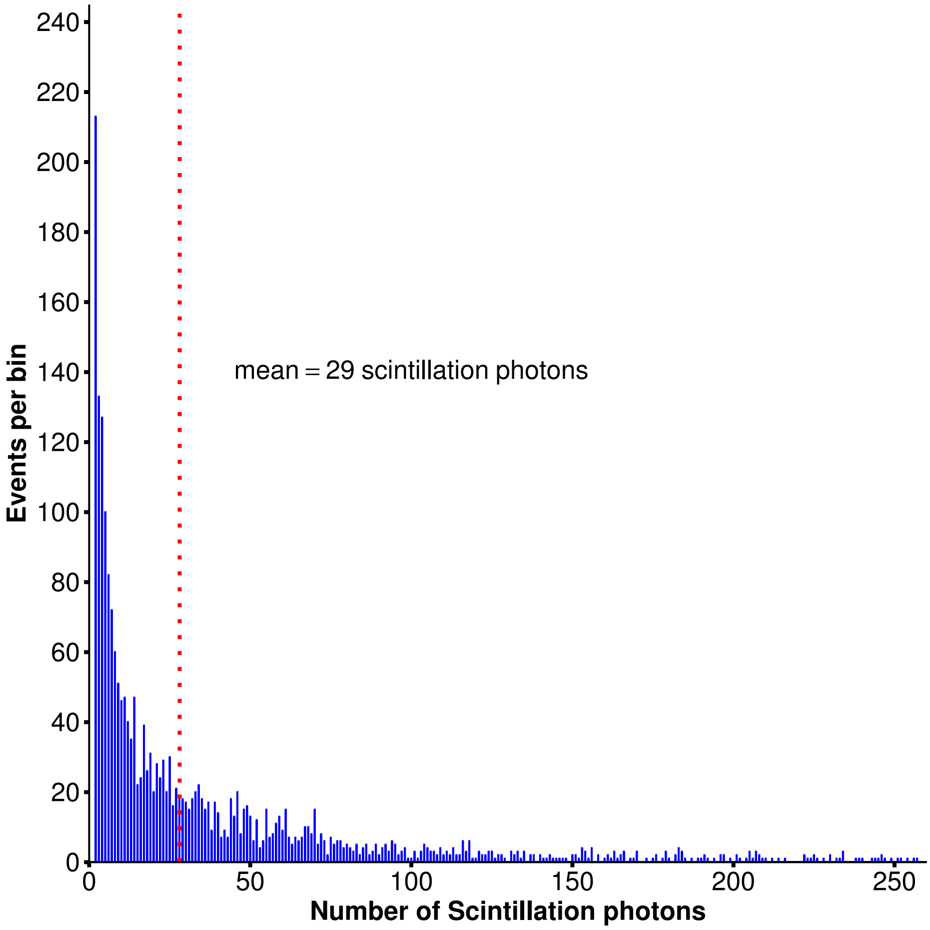

Figure 6.11: 94 hours' G4 EmPENELOPE plus G4 Optical physics model simulation of the frequency distribution of scintillation photons impacting onto a 5 μm thick silicon detector using a mono-energetic technetium-99m and intervening unwrapped columnar 1500 μm thick caesium iodide. The number of simulated primary photon histories was 1.0 x 10^8.

Figure 6.12 shows the frequency distribution of scintillation photons recorded within the 5 μm thick silicon with an intervening columnar 1500 μm thick caesium iodide wrapped with 1 μm aluminium.

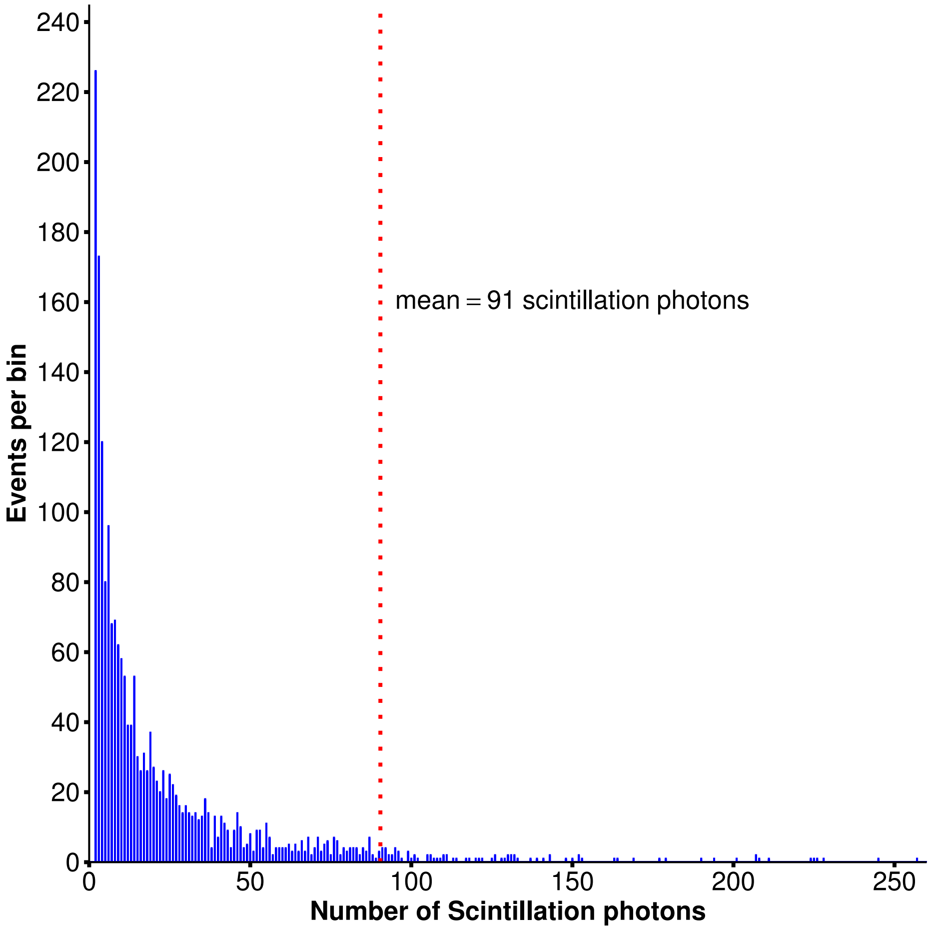

Figure 6.12: 14 hours' G4 EmPENELOPE plus G4 Optical physics model simulation of the frequency distribution of scintillation photons impacting onto a 5 μm thick silicon detector using a mono-energetic technetium-99m and intervening wrapped columnar 1500 μm thick caesium iodide. The columnar 1500 μm thick caesium iodide was laterally wrapped with 1 μm aluminium. The number of simulated primary photon histories was 1.0 x 10^8.

6.8.3 Discussion

In Figure 6.11 the frequency distribution of scintillation photons impacting onto the 5 µm thick silicon detector demonstrates that the peak events per bin is higher for the unwrapped columnar caesium iodide compared to that for the corresponding monolithic caesium iodide. This arises because the columnar caesium iodide crystal has surfaces which create internal reflections as the optical photons propagate towards the 5 µm thick silicon detector [GEANT4 Collaboration - G4Physics, 2018]. This implies that more events for low frequency scintillation photons are channelled towards the 5 µm thick silicon detector compared to the monolithic caesium iodide crystal. In the monolithic caesium iodide the optical photons are created and distributed over 4π, such that a higher proportion (relative to the columnar crystal) are directed away from the 5 µm thick silicon detector, and are optically scattered and absorbed in the bulk crystal.

When the columnar caesium iodide crystal was wrapped with 1 µm thick aluminium on its lateral faces relative to the impinging gamma photon beam, the mean number of scintillation photons increased from 29 to 91 photons respectively in the case of the unwrapped columnar caesium iodide crystal compared to the wrapped one. This implies that when scintillation events create a large cluster of optical photons, the optical photons can be transmitted through the columns and escape through the lateral wall of the crystal. In the case of the wrapped columnar caesium iodide crystal, 1 µm thick aluminium reflects these cluster of optical photons back into the columns; these optical photons then propagate towards the 5 µm thick silicon detector. This efficiency in collection of optical photons at the 5 µm thick silicon detector is demonstrated in the reduction in the simulation time of 94 hours in Figure 6.11 to 14 hours in Figure 6.12. For n=1.0 x 10^8 independent observations, the variance $\hat{\mu}_2$ as given by the second central moment in Equation 2.14. For a Poisson distribution with n=1.0 x 10^8

the variance can be derived to be $(7587 - 91)^2$ x 10^{-8}=0.562. This is slightly less than that for the unwrapped columnar caesium iodide crystal, and less than that for either the wrapped monolithic caesium iodide crystal with 1 μm thick aluminium or the unwrapped monolithic caesium iodide crystal.

Figure 6.13 shows the cumulative distribution function showing the unwrapped columnar and columnar 1500 μm thick caesium iodide crystal laterally wrapped with a 1 μm thick aluminium. The two sample Kolmogorov-Smirnov test for difference between these two cumulative distribution function curves gives a D statistic D_n of 0.0667. At a 95% confidence interval, for n_1=n_2=260 data values along the abscissa, the critical value D_{crit}=0.1193. Thus as D_n<D_{crit} with p<0.05, there is a moderate difference in these two cumulative distribution function curves.

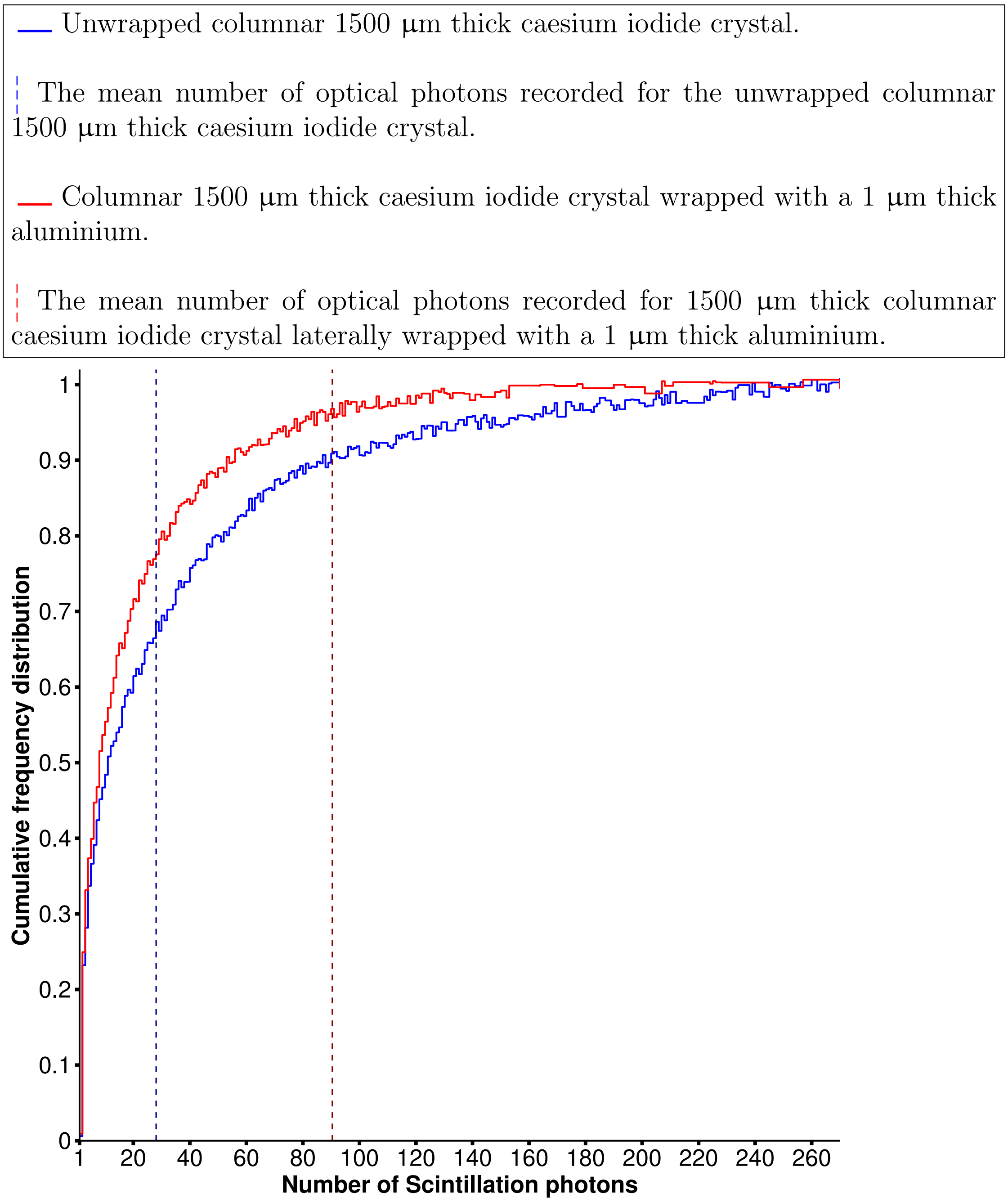

Figure 6.13: The cumulative distribution functions for both the columnar 1500 µm thick caesium iodide crystals, unwrapped then laterally wrapped with a 1 µm thick aluminium. The dashed vertical lines are the mean number of optical photons recorded for the unwrapped and laterally wrapped with 1 µm thick aluminium simulations.

Recalling that the cumulative distribution functions plotted above are:

- Figure 6.10 for the cumulative distribution functions for both the monolithic 1500 µm thick caesium iodide crystals, unwrapped then laterally wrapped with a 1 µm thick aluminium, and
- Figure 6.13 for the cumulative distribution functions for both the columnar 1500 µm thick caesium iodide crystals, unwrapped then laterally wrapped with a 1 µm thick aluminium.

these may be used to estimate the total number of photons impacting the silicon detector. These values were derived using the product of the cumulative sum of these cumulative distribution functions and the number of scintillation photon bins within this intervals along the abscissae. Table 6.2 shows the estimated total number of photons impacting the silicon detector based on these simulated cases, as previously described in section 6.3,

Cases:	cumsum()	Number of optical photons impacting the silicon detector $N \pm \sqrt{N}$	*Proportion of optical photons impacting the silicon detector
1: monolithic, unwrapped	225,377	1.76 x 10^9±4.20 x 10^4	0.0023
2: monolithic, wrapped	225,254	1.76 x 10^9±4.20 x 10^4	0.0023
3: columnar, unwrapped	219,683	1.72 x 10^9±4.15 x 10^4	0.0023
4: columnar, wrapped	707,833	5.54 x 10^9±7.44 x 10^4	0.0073
*Derived from the ratio of the numbers of optical photons impacting the silicon detector to scintillation photons generated within the caesium iodide crystal.			

Table 6.2: The estimated total number of optical photons impacting the silicon detector based on these simulated cases, as previously described in section 6.3, was derived using the product of the cumulative sum, cumsum(), of these cumulative distribution functions and the number of scintillation photon bins within these intervals. The caesium iodide crystal thicknesses used were 1500 µm thick crystal and the lateral wrapping of the crystal (where used) was 1 µm thick aluminium. The number of simulated primary photon histories was 1.0 x 10^8. The proportion of optical photons impacting the silicon detector was derived from the ratio of the number of optical photons impacting the silicon detector to the number of scintillation photons generated within the caesium iodide crystal.

As noted in Equation 6.2 for fast electrons created during the scintillation process, dL/dx which is the light output per unit length is proportional to the energy loss per unit length dE/dx. The constant of proportionality in Equation 6.2 is the absolute scintillator efficiency which for caesium iodide was set to 54 photons per keV. In these simulations above, the number of simulated primary photon histories was 1.0 x 10^8. The number of scintillation photons expected was calculated to be 10^8 x 140.5 x 54=7.587 x 10^{11}, where the mono-energetic technetium-99m conical photon source has energy 1405. keV and the scintillation yield of the caesium iodide was set to 54 photons per keV. The proportion of scintillation photons impacting the silicon detector to those created in the caesium iodide crystal was derived and shown in Table 6.2. The Monte Carlo estimate of the detection efficiency for case #4 which represents the closest approximation to the real detector is low. The Monte Carlo estimate may be compared to the geometrical detection efficiency derived as follows. Assuming the scintillation photons are emitted over 4π and no optical photon collection losses between the caesium iodide crystal and the silicon detector, the solid angle subtended by the silicon detector is given by Equation 6.7, [Khadjavi, 1968]

$$\Omega(a,b,d) = 4.cos^{-1}\sqrt{\frac{1+\alpha^2+\beta^2}{(1+\alpha^2)(1+\beta^2)}} \tag{6.7}$$

where $\alpha = a/(2d)$ and $\beta = b/(2d)$ for a silicon detector of area a x b=8 mm x 8 mm at a distance d=10 cm away from the conical photon beam source. Ω was derived to be 0.0064 radians. The Monte Carlo estimate of the detection efficiency for case #4, the simulation model with a columnar 1500 μm thick caesium iodide crystal, laterally wrapped with a 1 μm thick aluminium which represents the closest approximation to the real detector, is slightly bigger than the geometrical detection efficiency consistent with the fact that the columns channel optical photons towards the silicon detector. The Monte Carlo estimate of the detection efficiency is therefore good. However the geometrical detection efficiency described above depends on the depth-of-interaction. In this work no depth-of-interaction was investigated but should be considered for future investigation. As each incident gamma photon interacts at different depths in the scintillator then this leads to broadening of the light splash across the EMCCD pixel array. At low EMCCD frame rates (10 frames per second) there may well be overlapping of event profiles ("pile-up") which makes the extraction of the event position difficult. Modelling of these profiles is needed to assess depth-of-interaction effects in the scintillator. In terms of clinical imaging it is paramount to ensure the correct physiological mapping to the collated EMCCD image frames so positional accuracy of the event is critical. A suitable technique to extract this event profile may use Scale Space transformation, [Bart and Romeny, 1996] or more recently use of the second moment of the statistical light distribution within the monolithic crystal, [Conde et al., 2015].

6.9 Conclusions

The Monte Carlo simulations in this chapter have successfully used the GEANT4 optical physics model alongside the "G4 EmPENELOPE" physics model. At the time of writing this systematic approach to simulate the frequency distribution of the optical photons that are generated within the scintillator and the frequency distribution of the optical photons impacting onto a silicon detector has not been previously published for a low energy source photon flux (less than 200 keV) used by SFOV gamma cameras.

The proportion of optical photons created and impacting on the silicon detector is greater in the case of the columnar caesium iodide crystal laterally wrapped with 1 µm aluminium, compared either to an unwrapped columnar crystal, laterally wrapped monolithic or unwrapped monolithic crystals. The GEANT4 optical modelling carried out in this chapter also highlighted the requirement to improve the simulations with more accurate experimentally derived parameters and this is discussed in the future work section. These include:

- The optical absorption length of caesium iodide as a function of wavelength,
- The reflectivity of the caesium iodide crystal, aluminium wrapper, individual silicon pixels within the array (in the absence of dead space in between),
- The refractive index of the optical coupling between the caesium iodide crystal and silicon detector, as a function of wavelength.

The columnar 1500 μm thick caesium iodide was comprised of columns 100 μm x 100 μm x 1500 μm thick. In the physical columnar caesium iodide crystal, these columns are 10 μm x 10 μm x 1500 μm, however simulating this geometry requires GEANT4 to be used in multi-threaded mode in future work. The Monte Carlo estimate of detection efficiency was found to be 0.0073 for the simulation model with a columnar 1500 μm thick caesium iodide crystal, laterally wrapped with a 1 μm thick aluminium, which represents the closest approximation to the real detector. However, by comparing this detection efficiency with an analytical calculation, the Monte Carlo estimate of the detection efficiency was good. For a SFOV gamma camera, the Monte Carlo simulations may be extended to improve the detection efficiency of optical photons by using a scintillator of high mass attenuation coefficient to attenuate these optical photons, and with higher optical yield. Future work should also extend the GEANT4 coding to include the spatial distribution of optical photons which is derived from the depth-of-interaction within the caesium iodide crystal.

Chapter 7

Clinical evaluation of high resolution Small Field-Of-View gamma camera systems

7.1 Detection problem and clinical impact.

Manufacturers of LFOV gamma cameras have routinely used standardised protocols such as the National Electrical Manufacturers' Association (NEMA) Standard [Chapman et al., 2007] and International Electrotechnical Commission IEC 60789 Standard [IEC60789-Subcommittee:62C, 2005] for assessing the performance and providing specifications of their cameras. For the clinical environment, modified protocols which arise from these standards have been developed for ease of use and examples of these in the U.K. are found in the Institute of Physics and Engineering in Medicine IPEM Report 86 [Bolster et al., 2003]. The European Directive 97/43/EURATOM mandates a quality assurance programme with suitable quality control for medical devices including gamma camera systems [EURATOM, 1997]. Routine quality control recommendations for LFOV gamma cameras and hand-held gamma probes are well documented by the European Association of Nuclear Medicine EANM [Busemann Sokole et al., 2010b, Dondi et al., 2009]. While LFOV gamma cameras are routinely tested using these standardised protocols [Chapman et al., 2007, Busemann Sokole et al., 2010b, Bolster et al., 2003] they are not always appropriate or easily translated to SFOV gamma cameras. For example, qualitative assessment of the image quality for LFOV gamma cameras use specifically designed phantoms [Chapman et al., 2007, Bolster et al., 2003, Busemann Sokole et al., 2010a,b]. An example of a phantom for LFOV gamma cameras is the ECTphan, `https://www.phantomlab.com/ectphan-330`. However, the design of SFOV gamma cameras has been directed towards sub-millimetre intrinsic spatial resolution so "standard" phantoms are relatively large and unsuitable. If smaller qualitative phantoms are constructed they are required to be precisely manufactured, [Tsuchimochi et al., 2003, Sánchez et al., 2006, Lees et al., 2010]. This chapter has proposed updated procedures for evaluating the imaging parameters of SFOV gamma cameras based on modifications to the NEMA NU1-2007 standard [Chapman et al., 2007]. It is envisaged that these will provide a more appropriate scheme for equipment characterisation assessing the quality of imaging carried out with these high resolution SFOV gamma camera systems.

7.2 Rationale

Regardless of the size and type of gamma camera they should all undergo acceptance testing after installation, and after this quality control on a regular basis throughout the instrument's working lifetime as mandated by the European Directive [EURATOM, 1997], and [Busemann Sokole et al., 2010a,b]. For these purposes the following parameters are routinely assessed:

- Spatial Resolution (Intrinsic and System),
- Spatial Distortion,
- Spatial Uniformity,
- Count-rate Capability,
- System Sensitivity,
- Energy Resolution.

In the subsequent sections each performance parameter is outlined with reference to the current standard approach used in LFOV systems and, if necessary, how it needs to be modified for assessing SFOV systems. In order to improve Poisson statistics sufficient counts should be acquired per pixel. For both LFOV and SFOV gamma cameras approximately 10^4 counts per pixel for standard point sources should be acquired [Chapman et al., 2007]. Additional performance tests for collimator performance and shield leakage are described elsewhere [Busemann Sokole et al., 2010a,b].

At the time of preparation of this chapter, there was a variation in methodology for characterising SFOV systems with some imaging performance characteristics not performed. This warranted some guidelines to ensure consistency in comparison for future SFOV systems which are decribed by the author [Bhatia et al., 2015]. The characterisation methodology was reviewed for the following SFOV systems, and individual SFOV system performance characteristics can be found in the respective references:

1. The IP Guardian2 [Ferretti et al., 2013] consisted of a CsI(Tl) scintillator crystal array composed of 18 x 18 elements each with a sensitive area of 2.25 mm x 2.25 mm, and thickness of 5.0 mm with an inter-crystal separation of 2.45 mm. The scintillator was coupled to a position sensitive photomultiplier. The system used a tungsten collimator 24 mm thick with a square pinhole of internal cross-section 200 μm x 200 μm.

2. The Small Semiconductor Gamma Camera (SSGC) [Tsuchimochi et al., 2003] consisted of a 32 x 32 array of CdTe crystals. Each crystal element was 1.2 mm x 1.2 mm x 5 mm and the inter-crystal spacing was 0.2 mm. The system used a tungsten collimator 10 mm thick with a square pinhole of internal cross-section 1.2 mm x 1.2 mm.

3. The Per-Operative Compact Imager (POCI version 1) SFOV system [Menard et al., 1998] consisted of a cerium doped yttrium aluminium perovskite, YAP(Ce) monolithic scintillator cylindrical cut crystal of 24 mm diameter and 2 mm thick. YAP(Ce) has a density of 5.7 gcm^{-3}, light yield of 40% compared to NaI and a fast decay time of 25 ns (see Table 2.1 for comparison). The system used a tungsten collimator comprised of a stack of 60 x 0.2 mm thick plates each 24 mm diameter. The group used two types of collimators one with 1 mm diameter hexagonal parallel holes and another with 0.4 mm circular parallel holes. Each set of holes were arranged in a 5 x 5 matrix, 4 mm apart. The system used a YAP(Ce) scintillator optically coupled using optical grease (Rhodorsil 500) to a custom-made intensified position sensitive diode comprising of back-end multi-channel plate, P47 phosphor plate and 500 μm thick silicon wafer position sensitive diode.

4. The Per-Operative Compact Imager (POCI version 2) SFOV system was modified to incorporate a CsI(Na) monolithic scintillator of 24 mm diameter and 3 mm thickness [Pitre et al., 2003]. The system used a lead collimator 15 mm thick with 1.4 mm hexagonal holes with 0.3 mm septal thickness. The scintillator is coupled to the custom-made intensified position sensitive diode comprising of back-end multi-channel plate, P47 phosphor plate and 500 μm thick silicon wafer position sensitive diode.

5. Sánchez et al. [2004] evaluated their SFOV system using two monolithic scintillators with each individually coupled using an unspecified optical grease to a position sensitive photomultiplier tube; these were a 6 mm thick NaI(Tl) crystal and a 4 mm thick CsI(Na) crystal both 51 mm in diameter so as to fill the useful field-of-view of the PSPMT.

7.2.1 Intrinsic Spatial Resolution.

This is defined as the full-width half-maximum (FWHM) of a Line Spread Function (LSF) or of a Point Spread Function (PSF) without an imaging collimator installed. This measurement may be supplemented by the full-width tenth-maximum (FWTM) as the PSF or LSF may deviate from a Gaussian Profile. This is due to the asymmetry in the low energy edge as this includes non perfect alignment of the slit transmission mask to the orthogonal axes of the detector, part of the noise tail of the noise spectrum for the EMCCD and broadening of the low energy edge as discussed in chapter 5. Standard methodologies for LFOV gamma cameras, [IEC60789-Subcommittee:62C, 2005, Busemann Sokole et al., 2010a,b] may use a collimated radioactive capillary line source of 0.5 mm width filled with about 40 MBq and positioned parallel to the principal orthogonal axes of the camera - otherwise this leads to broadening of the LSF. Alternatively a radioactive point source contained within a lead pot with a central 0.5 mm diameter hole in its base, is placed on the crystal with its aperture at the base. The radioactivity for the point source should be chosen to give approximately 10^4 counts per pixel. Typically intrinsic resolutions of LFOV gamma cameras are about 2-3 mm, [Vesel and Petrillo, 2005, Polemi et al., 2016].

One important aspect in relation to the imaging matrix is the pixel size of the detector. Thus if one uses an imaging matrix of 256 x 256 pixels, then the pixel size of a LFOV gamma camera with a typical diameter of 540 mm is 2.1 mm x 2.1 mm. NEMA NU1-2007 [Chapman et al., 2007] states the "pixel size should be less than or equal to 0.1 x FWHM", i.e. $\leq$ 0.3 mm for a 540 mm diameter gamma camera. The factor of 0.1 is defined from the Rayleigh criteria to allow clear separation of two adjacent profiles of the point spread function. To achieve the specified "pixel size" the analogue to digital conversion gain is increased perpendicular to the line source for each orthogonal axis simultaneously, and the "zoomed" portion of the field-of-view is imaged. For a SFOV gamma camera, if the expected intrinsic resolution is less than 1.0 mm, then the "pixel size" of the imaging matrix should be $\leq$ 0.1 mm, (equal to 0.1 x FWHM). This implies that the width of the standard line source or the diameter of the standard point source would need to have dimensions less than 0.1 mm to obtain the LSF and PSF respectively. In the case of line sources from practical experience uniform filling of capillary tubes of the order of a few hundred microlitres becomes challenging.

An alternative derivation of the FWHM can be obtained using the Edge Response Function (ERF) method for both SFOV and LFOV systems [Chapman et al., 2007, Vayrynen et al., 1980]. This is obtained from a mask with a machined edge, manufactured from a material with low transmission for the gamma photon energies being used. The edge should be perpendicular to the mask surface and straight to an accuracy of at least 10% of the expected spatial resolution. A line slit with two edges may be used. The mask thickness should as a minimum be sufficient to attenuate 99% of photons, although a thicker mask would be preferable to exclude divergent photons; for example using tungsten the thickness of this mask should be > 3.9 mm for a technetium-99m source which was derived from its mass absorption coefficient μ_a as given by Equation 2.24 where μ_a at 140.5 keV $= 6.01 \text{ x } 10^{-1}$ cm^{2}g^{-1}, its density ρ_a= 19.3 gcm^{-3} and its thickness t_a.

When measuring the intrinsic spatial resolution the mask is placed as close as possible to the scintillation crystal. A uniform plane radioactive source or small point source is placed at a sufficient distance from the lead mask such that all incident gamma photons can be assumed to be perpendicular to it. Then the detected counts across the edge of the mask ideally correspond to a step function, and its derivative gives a LSF. The flood source, or point source at a distance of at least 100 times its diameter irradiates the mask with a uniform flux of photons i.e. the incident photons from the source impinge perpendicular to the slit and detector. The source should be perpendicular to the camera face and in line with its centre as shown in Figure 7.1. Measurements should be taken without any scattering media.

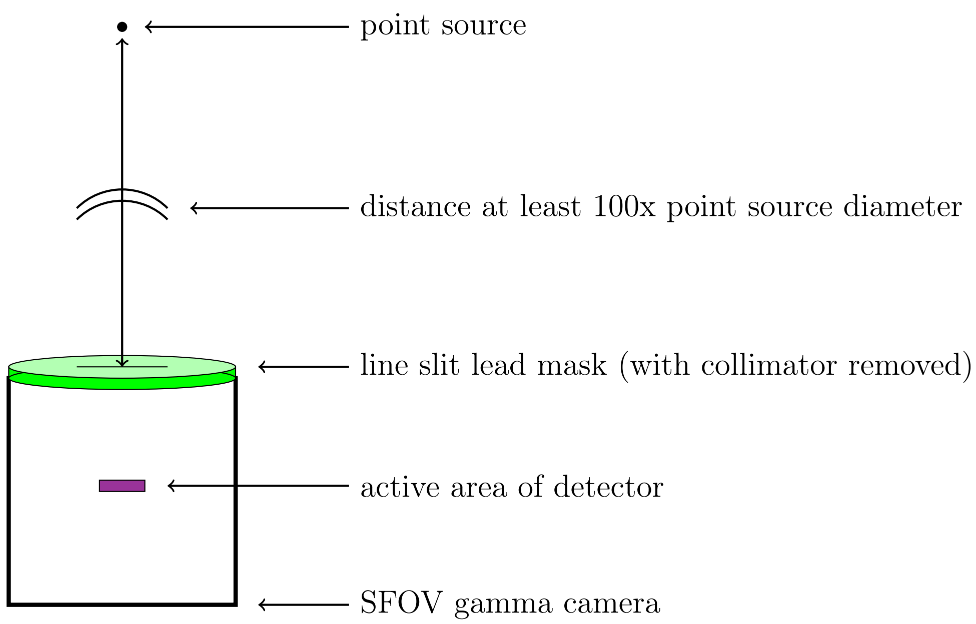

Figure 7.1: Schematic showing the set-up to measure intrinsic spatial resolution

The Shannon sampling theorem [Shannon, 1998] is considered important for measurements of spatial resolution. In order to sample the ERF, the device digitising the data must use a sampling interval that is less than one-half the size of the smallest resolvable feature of the image. In the case of a EMCCD it is not possible to sample at less than one pixel. The value measured in each pixel within the pixel array represents the intensity of the light splash events averaged over the sampling interval. At an insufficient sampling frequency events can be missed and aliasing can arise. So the best intrinsic spatial resolution that can be achieved is two pixels. Measurements should be taken with the edge of the mask aligned to both orthogonal axes of the detector. Intrinsic spatial resolution should be reported as the mean FWHM of the LSF and preferably with its mean FWTM.

7.2.2 System Spatial Resolution.

This is defined as the full-width half-maximum of a LSF or of a PSF with the imaging collimator in place. The protocol for the LFOV gamma camera uses a capillary line source (internal diameter $\leq$ 1.0 mm) with FWHM response measured in air, and with scattering media (such as polyacrylamide) positioned between the line source and the collimator surface, [Chapman et al., 2007]. The polyacrylamide acts to scatter photons as would be expected from a source inside a patient. An in-situ camera collimator will reduce sensitivity therefore longer integration times are needed to obtain sufficient counts. Similar to the intrinsic resolution measurements for SFOV cameras the dimensions of the capillary line source width and point source diameter will need to be smaller, and it may be difficult to produce and fill a phantom with radioactive solution, [Lees et al., 2010]. In this case it may be possible to use a point or line source of a known diameter and then deconvolve its expected profile from the resultant image to determine the resolution; this is not ideal and requires specific knowledge of the expected profile of the source, [Lees et al., 2011]. Typically, LFOV system resolution measurements are stated in the context of the collimator used either at the collimator face or at a known distance (usually 100 mm) away from the collimator.

For SFOV gamma camera systems an appropriate method is to use a capillary tube line source of internal diameter 0.5 mm which is imaged at the collimator face if a parallel-hole collimator is used or at the non-magnifying distance away for a pinhole collimator. The source is imaged in alignment with both orthogonal axes of the detector array. Measurements are to be repeated at five or more distance intervals up to a distance of 100 mm from the collimator face; in each case the intervening gap between the camera face and source should be filled with scattering material such as polyacrylamide or water.

7.2.3 Spatial Distortion.

Spatial Distortion quantifies how accurately the evaluated position of the centre of the event at the detector maps to the actual 2-dimensional event coordinates in the target. It is more convenient to determine spatial non-linearity due to the availability of suitable phantoms. For LFOV gamma cameras, spatial non-linearity is commonly assessed using a lead transmission mask [Chapman et al., 2007]. A least square fit for the imaged line position is calculated. The differences between the imaged and fitted lines at 10 mm intervals are obtained to specify the spatial non-linearity differences across the Geometric Field-Of-View (GFOV) i.e the physical size of the detector entrance window including any in-situ collimator. These difference measurements correspond to NEMA metrics for differential linearity (defined by their standard deviation and mean), and the absolute linearity (maximal deviation). A Parallel Line Equal Spacing (PLES) phantom may also be used [Bolster et al., 2003] which consists of several parallel 1 mm wide grooves filled with lead strips spaced at 20 mm apart, embedded in polyacrylamide. A typical LFOV PLES phantom would be 550 mm square by 0.33 mm thick; the lead parallel lines of thickness 3.175 mm are arranged within a circular diameter of 450 mm. A PLES phantom scaled to approximately 40 mm field-of-view would require precise manufacturing and although possible would be expensive.

For SFOV cameras a more suitable method involves obtaining images using a line transmission mask (e.g. a lead slit machined mask described earlier). The mask is placed as close as possible to the detector as allowed by the camera design. A flood source, or point source located at a distance of at least one hundred times the point source diameter away (section 7.2.1). The spatial non-linearity can then be assessed by rotating this mask in orthogonal directions. Spatial non-linearity should be reported as the mean deviation from the expected linear position of the centre of the imaged line of the transmission mask.

7.2.4 Intrinsic Spatial Uniformity.

Spatial Uniformity describes the variation in counts per pixel within the GFOV relative to the mean counts per pixel over the field-of-view. These measurements are performed with the collimator removed. A point source is placed at a distance of at least one hundred times the point source diameter from the crystal. The integral uniformity can then be defined for the maximal and minimal counts per pixel relative to the mean count for all pixels within the Useful Field-Of-View (UFOV). Standard NEMA equations define both the integral uniformity (across the entire detector) and also the differential uniformity (for localised groups of pixels), [Chapman et al., 2007]. These differential uniformity calculations are based on a small number of pixels within the field-of-view. This method, however, is not robust if pixel value outliers are present in the detector. IPEM Report 86 [Bolster et al., 2003] also defines the coefficient of variation for the counts per pixel in the UFOV (standard deviation of counts per pixel to mean number of counts per pixel) showing the response to photon flux across the flood image – essentially an index of noise within the UFOV. This does not measure uniformity response over adjacent pixels so the differential uniformity is determined using adjacent pixels over the whole field-of-view with five randomly selected adjacent pixels. A histogram for these differential uniformity measurements for each pixel location is plotted; the width of the histogram then indicates the dispersion of the differential uniformity measurements in these pixel clusters. Detailed equations and a sample histogram of differential uniformity measurements can be found in IPEM Report 86, [Bolster et al., 2003].

In the case of a SFOV camera the same procedure and analysis needs to be followed allowing for:

1. The size of the flood source ensuring that it covers the camera face for example a 90 mm diameter Petri dish with radioactive solution of sufficient depth to ensure that the detected count-rate is less than 20 kcounts.s^{-1} thus ensuring a linear count-rate capability [Chapman et al., 2007]. This value of 20 kcounts.s^{-1} is that designated for use for LFOV gamma cameras by NEMA so is considered suitable for SFOV systems for comparative purposes. However it is recognised this target value may need to be adjusted for SFOV systems depending on its count-rate capability.

2. The possible differences in acquisition times as the pixel density of the smaller camera and count-rate capability could require longer imaging times to achieve the same statistical significance per pixel.

7.2.5 Count-rate Capability.

The count-rate capability of a detector is the ability to respond to all incident events such that the observed count-rate increases linearly with the increasing incident flux of photons. The detector will have a finite time to temporally resolve each event, and in the case of high incident flux of photons, "pile-up" of events reduces the count-rate capability so the observed events do not keep up with all incident events. This effect degrades the spatial distortion, spatial uniformity and spatial resolution as Compton scattered events could be added to photopeak events or each Compton scattered event summed as a single event.

Count-rate capability is determined from the count-rate response curve showing the measured count-rate for the uncollimated SFOV system versus the expected count-rate for a single radioactive source. This radioactive source decays within a polyacrylamide well [Chapman et al., 2007]; alternatively several 1 ml point sources with differing known activity may be sited in turn within the polyacrylamide well [IEC60789-Subcommittee:62C, 2005]. The count-rate response curve depends on the energy spectrum of the detected photons, and so depends on the amount of scatter present [Chapman et al., 2007]. The range of expected count rates should at least correspond to those of the clinically injected radioactivity. By recording the count-rate and activity at the time of each measurement, the count-rate response curve can be plotted by allowing the source(s) to decay and performing measurements of count-rate at equal time intervals. The same basic procedure can be used for SFOV cameras with the proviso of matching the source size, position and activities to the characteristics of the type of camera under test.

7.2.6 System Sensitivity.

System sensitivity is determined by the capability of the gamma camera to detect a proportion of the emitted photon flux which is incident on the detector with the system collimator in place. The type of collimator used should be specified when stating the camera sensitivity. For both LFOV and SFOV gamma cameras a uniform planar source covering the GFOV at a known distance away from the camera face can be used. System sensitivity is measured at the collimator surface for those using parallel hole collimators and at the non-magnifying point for gamma camera systems using pinhole collimators. Measurements should be performed up to a distance of 100 mm from the camera face with at least five equidistant intervals. Measurements should be repeated using scattering media (polyacrylamide) between the camera face the radioactive source. System sensitivity should be reported as the ratio of counts incident on the detector, per unit of time per unit of activity, (counts.$s^{-1}MBq^{-1}$ incident) and the type of collimator used.

7.2.7 Energy Resolution.

This measures the detector capability to differentiate between unscattered and scattered incident photons. The energy resolution can be determined from the ratio of the FWHM of the photopeak of the radionuclide being measured to the photopeak energy. The energy spectrum is accumulated using a point source fixed centrally away from the camera face and positioned sufficiently far away so as a uniform photon flux impinges the detector. Measurements should be performed using at least two radionuclides covering the clinically useful energy range, and repeated to ensure the camera is stable with respect to drift of detected photopeak energy. For this type of measurement there is no difference between LFOV and SFOV gamma cameras.

7.3 Results

In this section an appropriate scheme for characterisation of the Compact Gamma Camera [Bhatia et al., 2015] is described. The Compact Gamma Camera (CGC) [Lees et al., 2011], as shown in Figure 7.2, has undergone a full assessment using the procedures outlined in the previous section.

Figure 7.2: The Compact Gamma Camera (CGC, University of Leicester)

The CGC consisted of a thallium-81 doped tightly packed columnar structured caesium iodide scintillator [Hamamatsu, 2016] of 600 μm thickness coupled to an EMCCD, an e2v CCD97-00 back illuminated EMCCD [e2vTechnologies, 2004]. Scanning electron microscope (SEM) images of the tightly packed columnar structured caesium iodide scintillator (type ACS-HL-20-30-600-UK) with each column of diameter approximately 10 μm across are shown in Figure 7.3. The SEM images show that the columns are almost orthogonal to the base of the crystal although there are several dislocations. The columns however increase the optical photon collection by directing the light to the EMCCD.

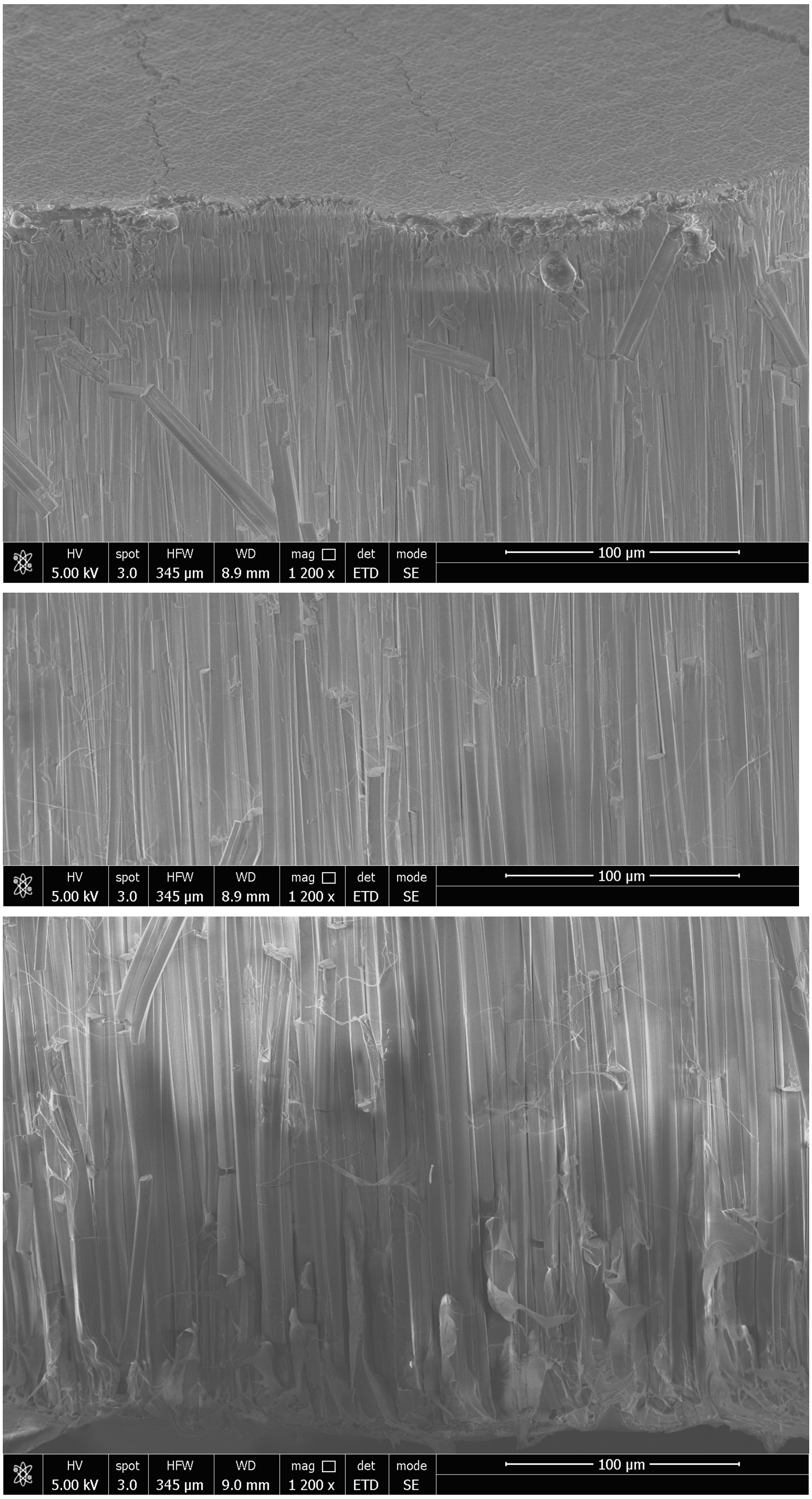

Figure 7.3: Scanning electron microscope cross-section images showing the tightly packed columns within a structured 600 μm thick caesium iodide scintillator with columns of diameter approximately 10 μm across. The top image shows the superior surface, and the bottom image (slightly translated relative to the other images) shows the unstructured scintillator at the base of the crystal.

A schematic of this SFOV gamma camera is shown in Figure 7.4. The EMCCD operates at 10 frames per second and must be cooled with a thermoelectric cooler to reduce dark current noise, described in section 2.3.1. Dark current noise is inherent within the detector whether it operates in counting or integrating mode.

In this section some of the results are described to demonstrate how the protocols have worked in practice. The knife-edge pinhole tungsten collimator is 6 mm thick with a 0.5 mm pinhole and an acceptance angle of 60 degrees. The imaging performance characteristics for the CGC have been jointly published and reproduced from this paper in this chapter, [Bugby et al., 2014]. The protocol was developed by B.S. Bhatia [Bhatia et al., 2015] and experiments were performed by S.L. Bugby with joint discussion. The results in this chapter were analysed independently obtained by the author using the same SFOV gamma camera for corroboration, apart from section 7.3.1 which was developed by S.L. Bugby and the calculation of system sensitivity section 7.3.7 with these results referenced therein. Table 7.1 shows the comparative results for an example Large Field-Of-View and the evaluated Small Field-Of-View gamma camera from the jointly published paper, [Bugby et al., 2014].

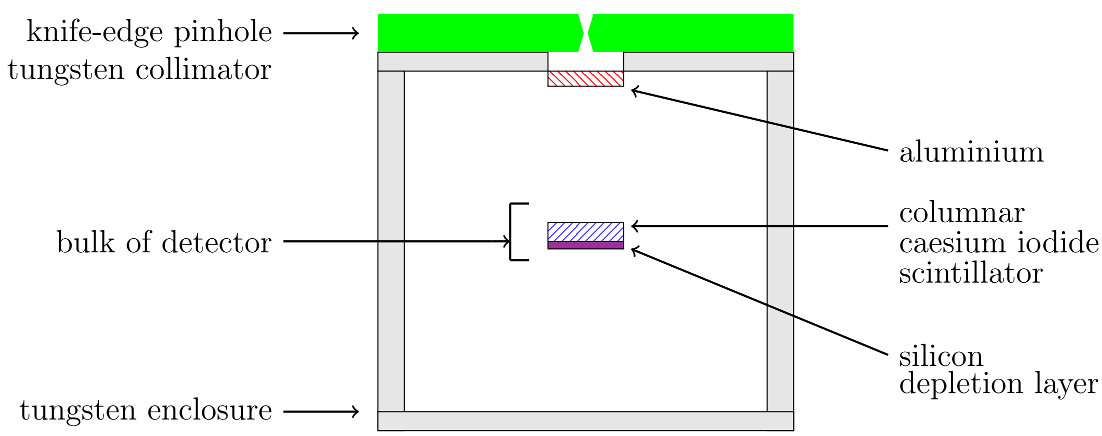

Figure 7.4: Schematic of the Compact Gamma Camera

7.3.1 Image Correction

The frames created by the EMCCD may contain hot pixels, defined as those in more than 5% of frames in a dark image whose counts were above the expected thermal noise threshold [Bugby et al., 2014]. In order to correct the images a flood image and a dark image were acquired. A flood image was taken with a point source at 250 mm away from the uncollimated detector face, and a dark image taken without incident illumination. The flood image and dark image were corrected for hot pixels by replacing the pixels with the mean of their four nearest neighbouring pixels. Then a master flat image was created from the subtraction of the dark image from the flood image; these images had equal exposure times. This master flat image was then normalised to its maximum value, as shown in Figure 7.5. For subsequent acquired images in the following sections, each image would be corrected for flat field effects by subtracting the dark image and then dividing by the master flat image.

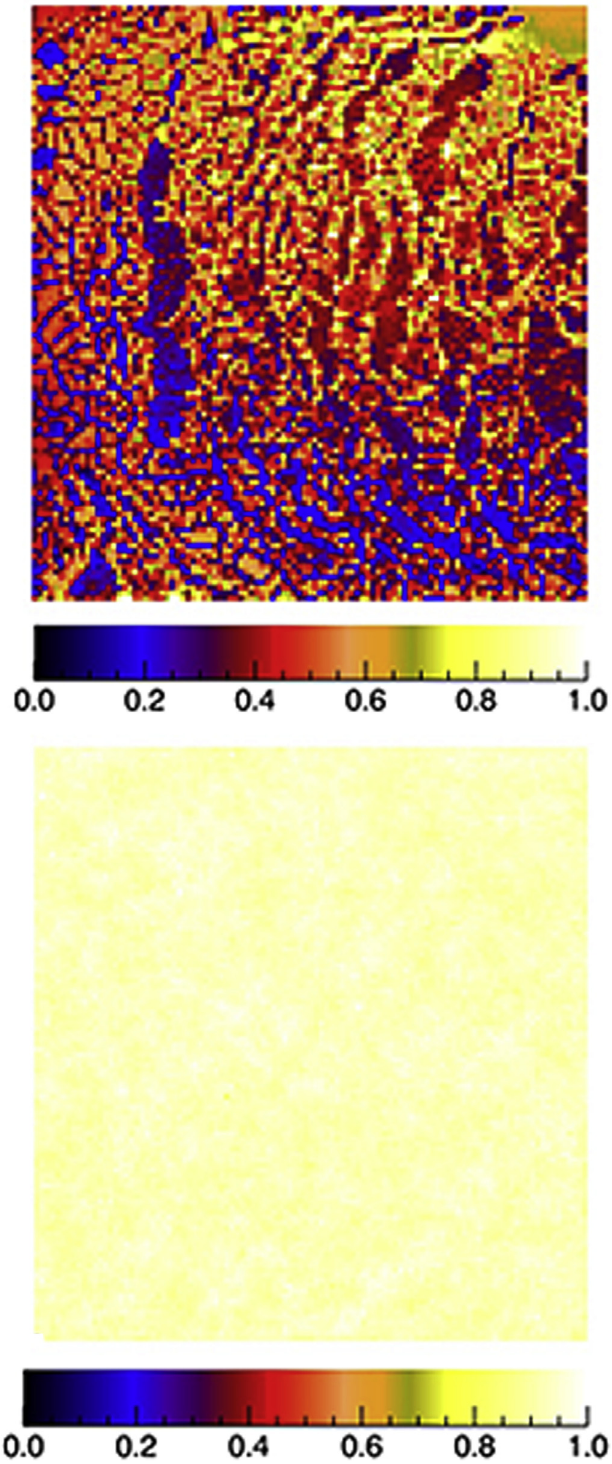

Figure 7.5: Top: Flood image normalised to its maximum value. Bottom: Flat field flood image, normalised to the corrected maximum value. [Bugby et al., 2014]

7.3.2 Intrinsic Spatial Resolution

For evaluation purposes, an existing lead transmission mask of dimensions 10 mm thick, diameter 45 mm and internal line slit dimensions 2 mm x 20 mm was used to measure the intrinsic spatial resolution of the CGC. The transmission mask was placed as close as possible to the scintillator in place of the camera collimator (7 mm from the scintillator face due the design constraints). A 14 MBq point source of 3 mm diameter was placed at 200 mm above the transmission mask. An image of 2,000 frames was acquired with the CGC operating at 10 frames per second (with about 10 counts per frame). Each frame is analysed individually to extract the event position from the detected "light splash" onto the EMCCD [Lees et al., 2011]. An image of the slit transmission mask is shown in Figure 7.6. This image was used to obtain the Edge Response Function measurements by measuring counts across the single non-distorted edge of the mask as shown in Figure 7.7; a least squares fit was used to derive the fitted centre of the imaged slit [Bugby et al., 2014]. Recalling that the detected counts across the edge of the mask ideally correspond to a step function, then its derivative gives a LSF. The intrinsic spatial resolution derived from the LSF, which is the profile of measured counts as a function of position across a line source, is shown in Figure 7.8 which at 7 mm from the scintillator was calculated to be 0.80 $\pm$ 0.02 mm (FWHM). For the e2v CCD97-00 pixels are binned into pixels of size 64 µm by 64 µm [e2vTechnologies, 2004], so the best intrinsic spatial resolution this detector can achieve is 128 µm or two pixels across. The reason for the larger FWHM of 0.8 $\pm$ 0.02 mm compared to 128 µm is discussed in section 7.4.

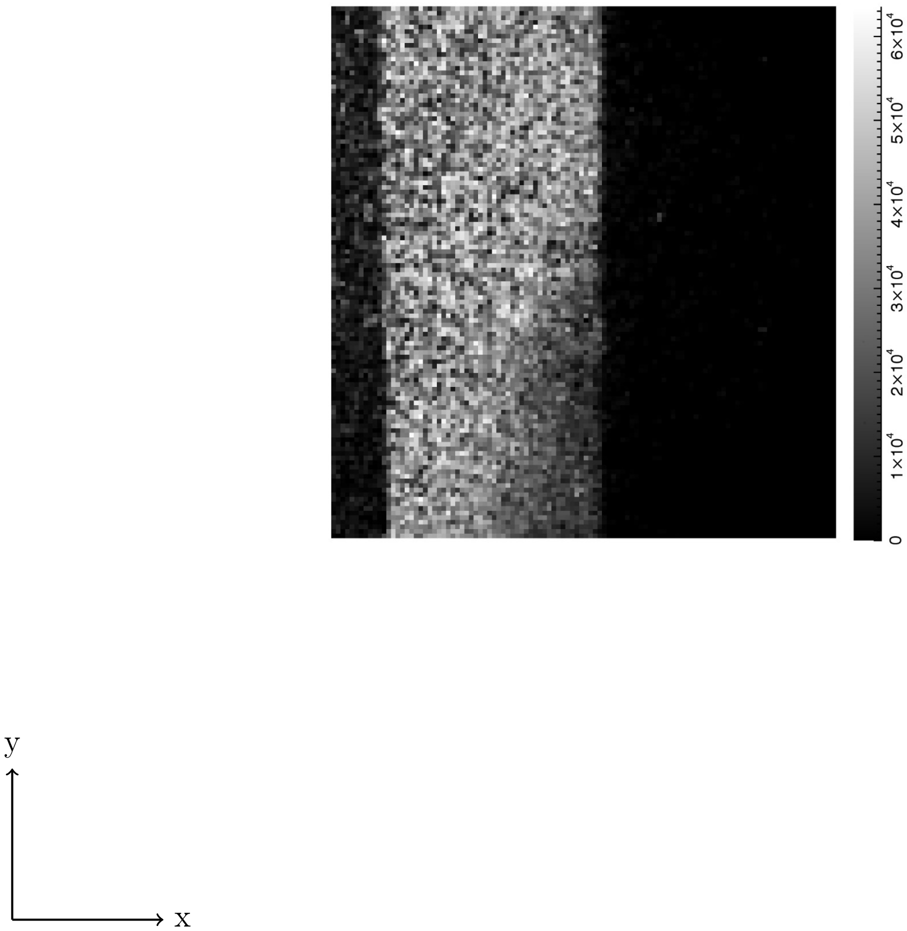

Figure 7.6: SFOV gamma camera image of a 2 mm internal slit width transmission mask normalised to its maximum value for the intrinsic spatial resolution measurement. The slit is almost aligned to the orthogonal axes {xy} of the detector array. Each pixel dimension is 64 μm by 64 μm.

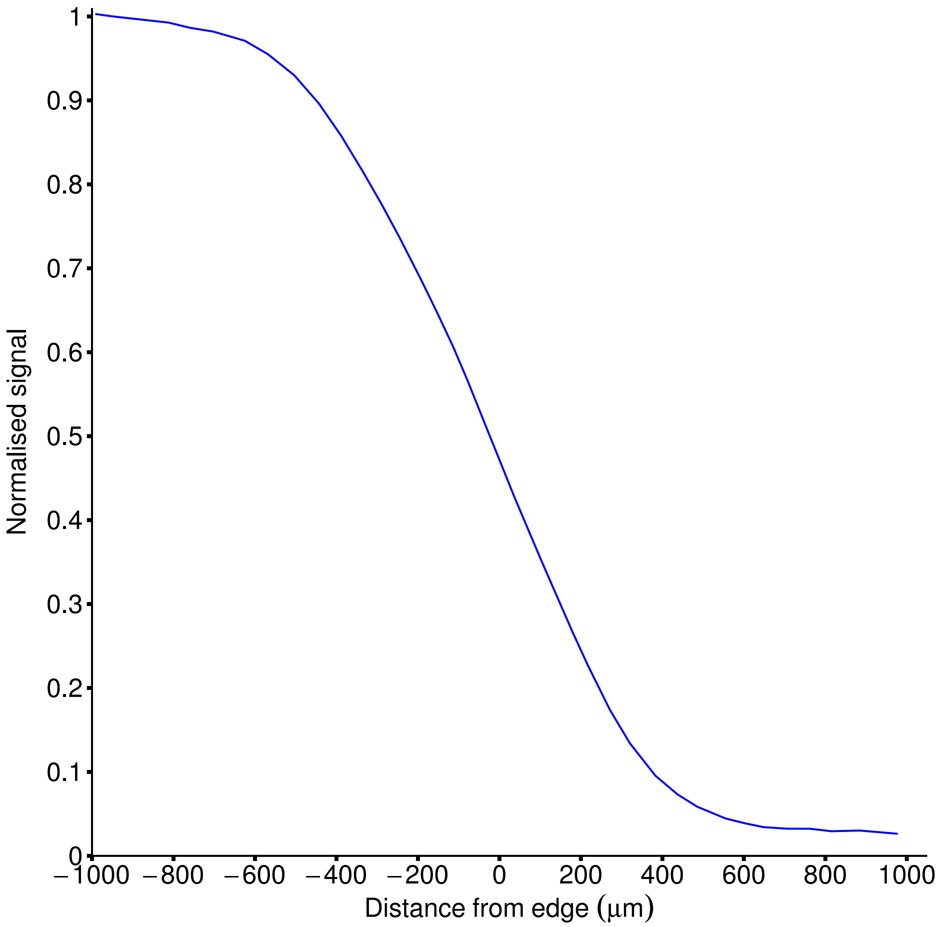

Figure 7.7: An Edge Response Function of the slit image. The edge is taken to be 1 mm away from the fitted centre of the slit image.

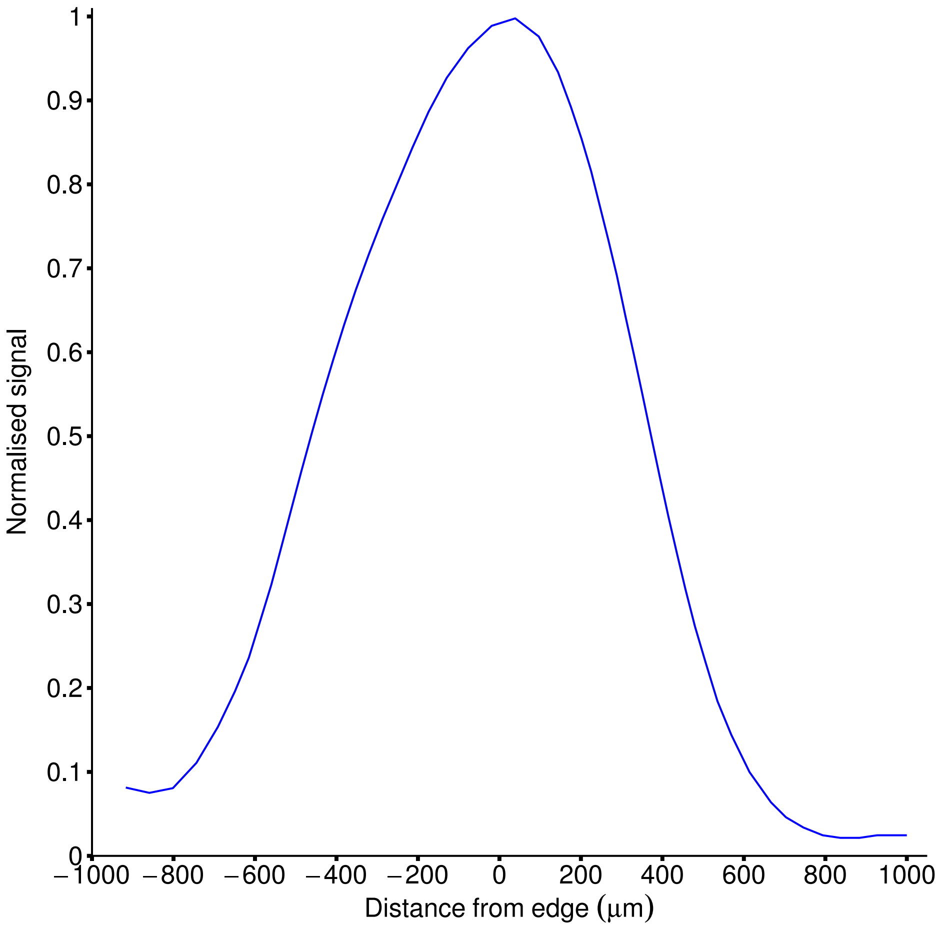

Figure 7.8: Line spread function calculated as the derivative of the ERF.

The slit is almost aligned to the orthogonal axes {xy} of the detector array as this is difficult to achieve in practice. Note the asymmetry of the LSF which arises owing to the variation in measured counts across the two edges of the slit as a function of position along the slit edges as shown in Figure 7.6. This is due to non-uniform coupling of the thallium-81 doped columnar structured caesium iodide scintillator [Hamamatsu, 2016] to the e2v CCD97-00 back illuminated EMCCD [e2vTechnologies, 2004]. This coupling was achieved using a layer of a few microns of Dow Corning grease (compatible for use within the evacuated camera chamber); this uneven coupling is shown as darker pixels in the lower right of the line slit image in Figure 7.6.

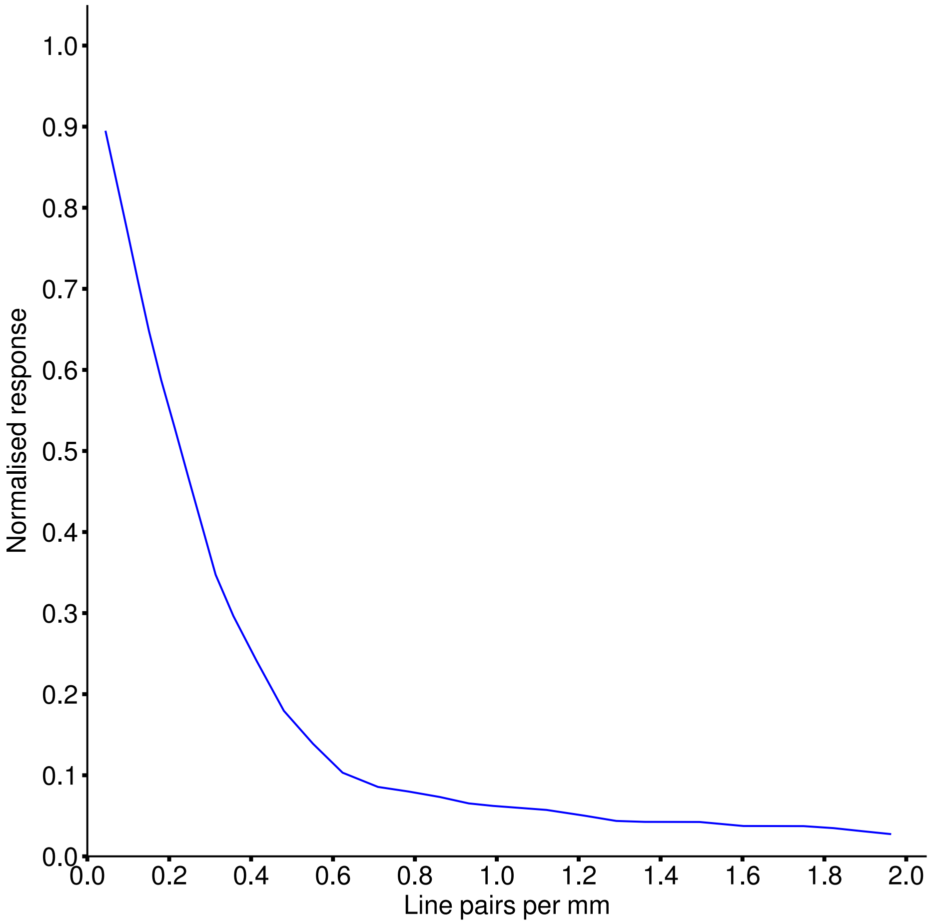

Figure 7.9: The modulation transfer function obtained from the line spread function.

The modulation transfer function (MTF) is shown in Figure 7.9, and is derived from the Fourier Transform of the LSF. As expected the MTF shows the best camera response for low spatial frequencies, and decreases as the spatial frequency increases.

7.3.3 System Spatial Resolution.

For the CGC the spatial resolution was measured with an available 1 mm diameter capillary line source with 40 MBq of technetium-99m and with a 0.5 mm diameter pinhole collimator in place. The 1 mm diameter capillary line source was imaged with polyacrylamide in front of the camera collimator face providing tissue equivalent scattering to a depth of between 5 mm to 30 mm. This collimator centre was 10 mm away from the scintillator surface. 1,000 frames were acquired with the EMCCD operating at 10 frames per second for each measurement. The alignment of the capillary line source or internal slit transmission mask to the camera orthogonal axes may be difficult to achieve in practice and several alignment images should be taken with the SFOV camera prior to measurement of the system spatial resolution. A least squares fit was used to the derive the fitted centre of the imaged 1 mm diameter capillary line source so that its orientation could be adjusted to the orthogonal axes of the detector array.

The system spatial resolution for an expected linear fit using a range of polyacrylamide thicknesses is shown in Figure 7.10. Linear regression was performed using the **R** programming language and has R^2=0.99 which is well matched to theory [Bugby et al., 2014]. As demonstrated in Figure 7.10 system spatial resolution degrades with increasing depth of polyacrylamide.

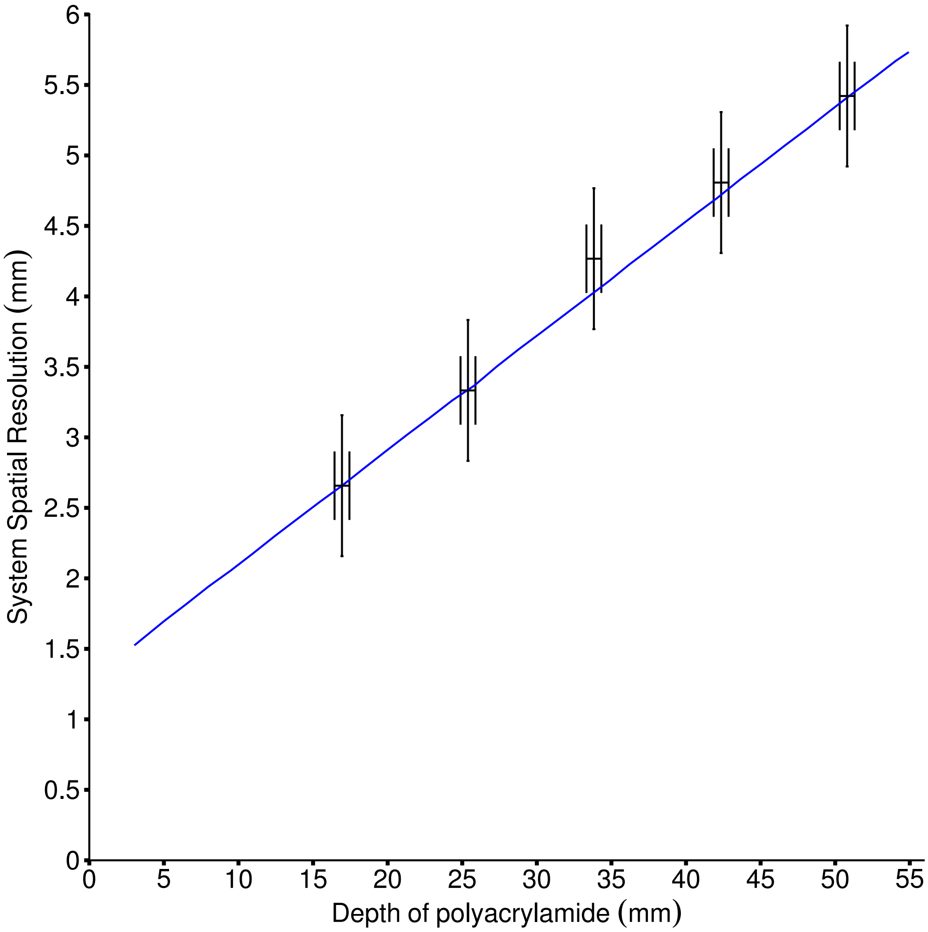

Figure 7.10: System spatial resolution for a linear fit using a range of polyacrylamide (Perspex) thicknesses. The linear fitting is given by $y = 1.3 + 0.0827x$ where x is the depth of polyacrylamide and y is the system spatial resolution, with R^2=0.99.

Using the LSF for the internal slit transmission mask as described in the previous section, the system spatial resolution at the 10 mm from the collimator face for the CGC was determined to be 1.21 mm $\pm$ 0.2 mm (FWHM) [Bugby et al., 2014]; 10 mm from the collimator face is the non-magnifying position of the pin-hole collimator.

7.3.4 Spatial Distortion.

For each image of the slit, a central line of best fit was calculated. By considering each row across the slit, for a slit image aligned to the y-axis, the centre point was compared to its expected position determined by the line of best fit. The process was then repeated for the slit aligned to the x-axis. For both orthogonal directions the mean deviation was calculated to be 0.117 ± 0.002 mm, and a maximum deviation of 0.429 ± 0.002 mm.

7.3.5 Intrinsic Spatial Uniformity.

The intrinsic spatial uniformity was obtained using a 3 mm diameter source containing 25 MBq technetium-99m at a displacement of 250 mm from the uncollimated detector. Although it would have been preferable to increase the source-detector distance to 300 mm so as to ensure a uniform photon flux across the whole of the detector surface (GFOV), 250 mm was chosen as it corresponded to the master flat image which was created from the subtraction of a flood image taken with a point source at 250 mm away from the uncollimated detector face, described in section 7.3.1. Approximately 12000 counts per pixel were recorded. For the UFOV, the integral spatial uniformity was $8.5 \pm 0.9\%$, and the differential spatial uniformity was $1.3 \pm 0.9\%$. The coefficient of variation for the counts per pixel in the UFOV (standard deviation of counts per pixel to mean number of counts per pixel) was $1.6 \pm 0.8\%$. This intrinsic non-uniformity arises owing to a variation in response across the EMCCD pixel array, non-uniformity of the scintillator crystal and non-uniformity of the coupling of the scintillator to the EMCCD. Clinically it is paramount to achieve a spatially uniform response across the UFOV for diagnostic imaging with an intrinsic integral uniformity of 5% and intrinsic differential spatial uniformity of 5% used in routine clinical practice [Bolster et al., 2003]. Whilst the intrinsic differential spatial uniformity is clinically acceptable, that for the intrinsic integral uniformity is not owing to the non-uniform coupling of the scintillator to the EMCCD.

7.3.6 Count-rate Capability.

For each image, incident counts at the detector can be calculated taking into account the initial activity, source detector distance, time of image acquisition and the solid angle subtended by the detector from the source. Incident counts are then plotted against recorded counts to produce a count-rate capability curve. Since the incident counts are accumulated over a sufficiently long duration, negligible dead-time count-rate losses will be included. Linear regression was performed using the **R** programming language for the linear portion of the curve. Incident activity at which the measured counts differ from the linear fit by more than 10% of the expected value is calculated. The maximum measured count-rate should be reported. The frame rate limited count-rate capability for CGC detector is shown in Figure 7.11. Measurements of incident count-rates of > 1200 counts.s^{-1} were not performed at the time owing to the Environmental Agency restriction of on-site radionuclide activity (maximum 300 MBq for technetium-99m). Linear regression was performed using the **R** programming language with R^2=1.0. However, beyond 1200 incident counts.s^{-1} the relationship between incident counts and recorded counts would be expected to be non-linear as the CGC has a finite temporal resolution (the EMCCD operates at 10 frames per second) and its algorithm to separate multiple events within the pixel array is limited, both of which causes loss of measured counts at higher count-rates.

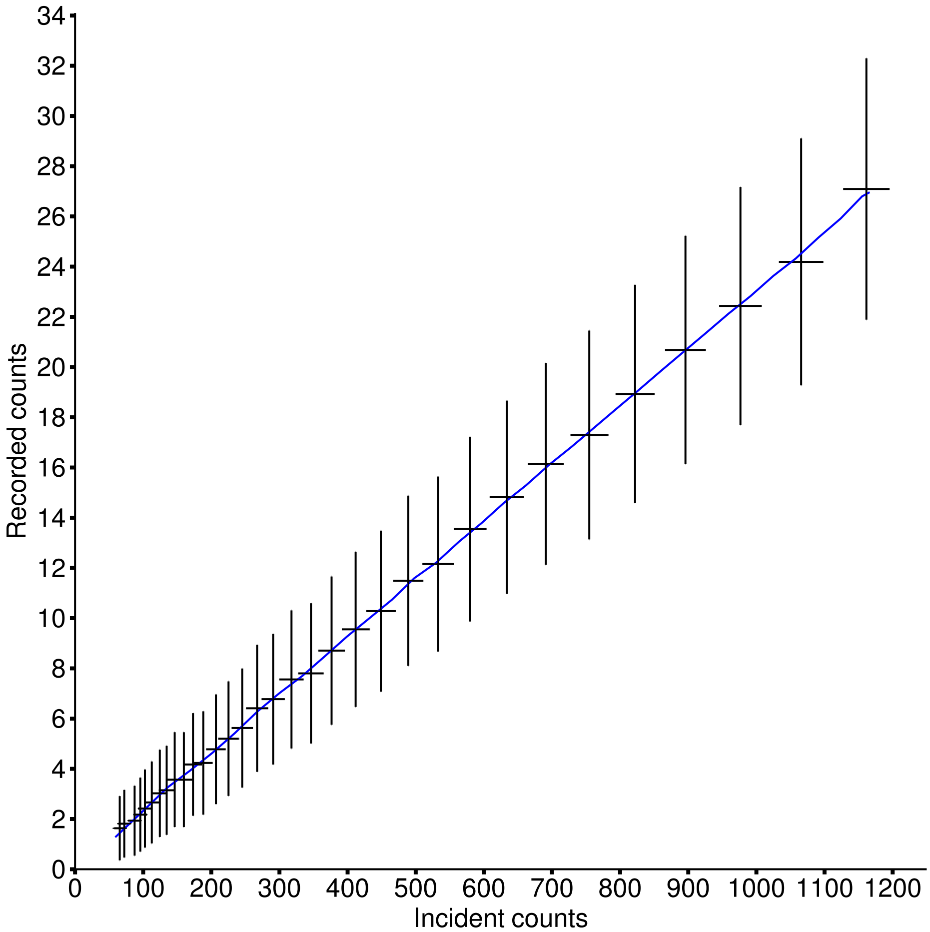

Figure 7.11: Frame rate limited count-rate capability for CGC detector. The e2v CCD97-00 back illuminated EMCCD [e2vTechnologies, 2004] operates at 10 frames per second. The statistical uncertainty in the ordinate and that for the abscissa was $\pm\sqrt{N}$. The linear fitting is given by $y = 0.0672 + 0.023x$ where x is the incident counts and y is the recorded counts, with R^2=1.0

7.3.7 System Sensitivity.

The intrinsic sensitivity of the CGC shown in Figure 7.12 using a 3 mm diameter technetium-99m source of activity 21 MBq at a distance of 350 mm away from the uncollimated detector face. Measurements were performed by adding slabs of polyacrylamide on top of the uncollimated detector face. The decrease in intrinsic sensitivity is shown with increasing slabs of polyacrylamide. Poisson regression was performed using the **R** programming language. The exponent 0.15 is the attenuation coefficient of polyacrylamide was determined from the Poisson regression fitting. The residual deviance is given by the difference between the current Poisson regression model and the maximum deviance of the ideal model (i.e. the observed values). As the residual deviance was small then the goodness of fit χ^2 test was not significant (p>0.05) so this model fitted the data well.

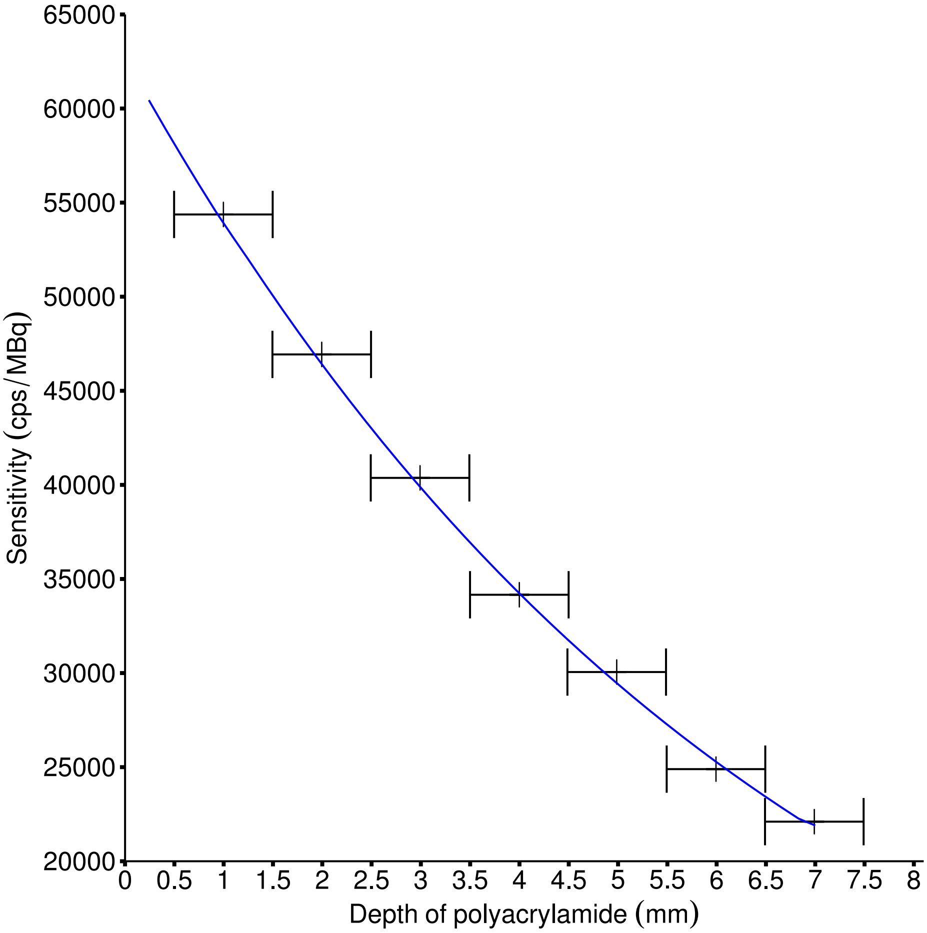

Figure 7.12: Sensitivity of the uncollimated CGC with increasing depths of intervening polyacrylamide. The Poisson regression fitting is given by $y = exp(11-0.15x)$ where x is the depth of polyacrylamide and y is the sensitivity. For Poisson regression fitting the residual deviance was small then the goodness of fit χ^2 test was not significant (p>0.05) so this model fitted the data well.

In order to calculate the system sensitivity, the proportion of incident photons through the pinhole collimator must be taken into account. Pinhole collimators have a height-dependent sensitivity S that can be calculated from Equation 7.1 [Metzler et al., 2001]

$$S = \frac{d^2.sin^3\theta}{16h^2} + \left[\frac{sin^5\theta.tan^2(\alpha/2)}{8h^2\mu^2}\right]\times \left[1 - \frac{cot^2\theta}{tan^2(\alpha/2)}\right]^{0.5}\times \left[1 - \frac{cot^2\theta}{tan^2(\alpha/2)} + \frac{\mu d}{sin\theta tan(\alpha/2)}\right] \tag{7.1}$$

where d=0.5 mm is the diameter of the pinhole, $\theta=\pi/2$ radians is the angle of the source to the pinhole, h=3 mm is the distance from the source to the pinhole centre, $\alpha=\pi/3$ radians is the acceptance angle of the pinhole, and μ= 32.17 cm^{-1} is the linear attenuation coefficient of the tungsten collimator for incident gamma photons at 140.5 keV.

Combining the intrinsic sensitivity and that for the sensitivity of the pinhole collimator, the system sensitivity for the CGC was found to be (214±7) counts.s^{-1}MBq^{-1} at its entrance face, [Bugby et al., 2014].

7.3.8 Energy Resolution.

At least two radionuclide sources are needed for calibration of the energy spectrum, one of which should be technetium-99m since this is the most clinically used radionuclide. The uncollimated detector was irradiated uniformly and an image acquired for each radionuclide used. Energy channels were calibrated using technetium-99m photopeak (140.5 keV) and the principal X-ray peaks of cadmium-109; an example of this calibration plot may be seen [Lees et al., 2011]. The energy resolution for technetium-99m is shown in Figure 7.13. The percentage energy resolution was determined to be $2.35\sigma/140.5 = 56.8\%$ at 140.5 keV with $\sigma \simeq 34$. For the Gaussian regression fitting within the energy interval 40 keV to 240 keV, the residual deviance was large so the goodness of fit χ^2 test was significant ($p<0.05$). This is due to the asymmetry in the low energy edge as this includes non perfect alignment of the slit transmission mask to the orthogonal axes of the detector, part of the noise tail of the noise spectrum for the EMCCD and broadening of the low energy edge as discussed in chapter 5.

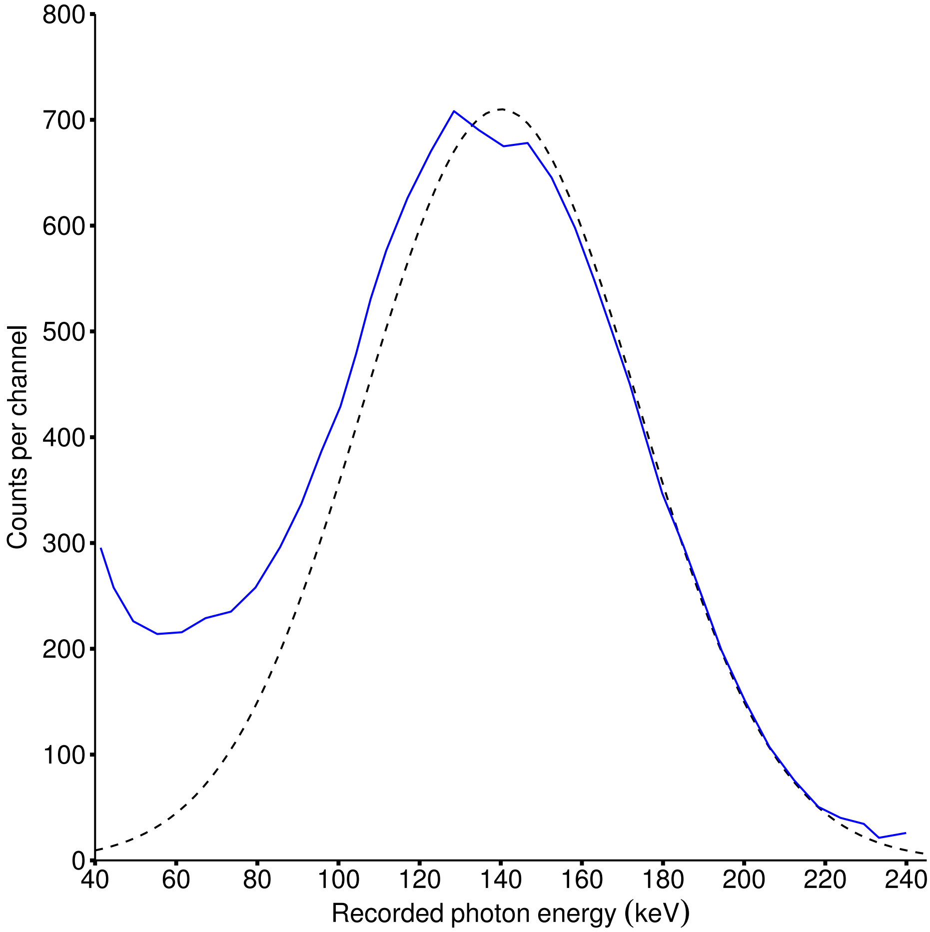

Figure 7.13: The energy resolution measurement using the CGC with a mono-energetic technetium-99m photon source. The dotted line is the Gaussian regression fitting within the energy interval 40 keV to 240 keV, given by $y = a.exp - 0.5((m - x)/\sigma)^2$ where x is the recorded photon energy, y is the counts per channel, with fitted parameters a=710, m=140.5 and σ=34. For the Gaussian regression fitting within the energy interval 40 keV to 240 keV, the residual deviance was large so the goodness of fit χ^2 test was significant ($p<0.05$).

For a LFOV gamma camera a typical energy resolution is of the order of 10% or less at the technetium-99m photopeak [Baechler et al., 2003, Polemi et al., 2016]. Comparative results for the SFOV (Compact Gamma Camera) [Bugby et al., 2014] and for an example LFOV gamma camera (Siemens Ecam) from literature [Baechler et al., 2003] are shown in Table 7.1. As there has not been any significant changes in the design of LFOV gamma camera system [Baechler et al., 2003] has been used for comparative purposes as more recent studies e.g. [Polemi et al., 2016] do not perform complete characterisation.

	LFOV (Siemens Ecam)	SFOV (Compact Gamma Camera)
	[Baechler et al., 2003]	[Bugby et al., 2014]
Intrinsic Spatial Resolution	3.9 mm FWHM 7.4 mm FWTM at crystal face	0.8 mm FWHM at 7 mm from the scintillator
System Spatial Resolution	7.6 mm FWHM at 100 mm away from camera face. Low Energy High Resolution parallel hole collimator	1.21 mm FWHM at 10 mm away from camera face (non-magnifying point). 0.5 mm pinhole collimator
Spatial Distortion	0.55 mm	0.12 mm
Intrinsic Spatial Uniformity	NEMA Integral: 3.00% UFOV 2.37% CFOV NEMA Differential: 1.59% UFOV 1.55% CFOV	NEMA Integral: 8.50% UFOV NEMA Differential: 1.32% UFOV Coefficient of Variation: 1.58% UFOV Spread of the DU 0.6%
Count-rate Capability	count-rate losses $\geq$ 20% 44.8 kcounts.s^{-1}	count-rate losses $\geq$ 20% > 1.2 kcounts.s^{-1}
System Sensitivity	33.0 counts.s^{-1}MBq^{-1} at the camera face. Low Energy High Resolution collimator	214 counts.s^{-1}MBq^{-1} at the camera face. 0.5mm pinhole collimator
Energy Resolution (at 140.5 keV)	10.5%	58%

Table 7.1: Comparative results for an example Large Field-Of-View and the evaluated Small Field-Of-View gamma camera

In Table 7.1 one can see that the CGC has better intrinsic spatial resolution, system resolution, sensitivity and less spatial distortion than the representative LFOV gamma camera. The CGC employs an EMCCD which naturally has a better intrinsic spatial resolution and spatial distortion due to its smaller pixel size compared to the photomultiplier tubes in a LFOV gamma camera. As the system resolution takes into account the type of collimator installed, the observed difference in proportional variation from the camera face in Table 7.1 is due to the different behaviour of pinhole and parallel hole collimation. The CGC shows comparable sensitivity to the LFOV gamma camera, however the use of the pinhole will mean that the sensitivity of the system will drop off faster at distance than parallel hole systems. It should also be noted that the energy resolution and spatial uniformity of the CGC is poor in comparison to the LFOV gamma camera. Whilst the intrinsic differential spatial uniformity is clinically acceptable, that for the intrinsic integral uniformity is not owing to the non-uniform coupling of the scintillator to the EMCCD. The poor energy resolution of the CGC is due to light collection losses from the scintillator and at the scintillator/ detector interface. In addition fluorescence within the tungsten collimator and lead shielding (59 keV to 85 keV) may also be the cause of some the spread in the technetium-99m peak; at the higher energy limit, spreading may also be caused by overlapping light splashes being analysed as a single event. The count rate capability of the CGC is limited by the ability to resolve different light splashes on the detector; its frame rate is 10 Hz and it is found to saturate at 3 events per frame.

7.4 Discussion

The introduction of SFOV gamma cameras into clinical practice has resulted in the need for appropriate quality assurance schemes. This chapter has addressed these issues taking account of the specific requirements for these systems. Although some characterisation protocols have been used for other SFOV systems it is beneficial to have a standard set of tests to address their variation and to ensure measurements were easier to reproduce; these characterisation protocols are described in the following paragraphs for a selection of SFOV systems for each type of test.

For some imaging performance tests, such as system sensitivity and energy resolution, the protocols are equivalent for both LFOV and SFOV gamma cameras. However for the others, although there are similarities, modifications are necessary to account for the SFOV system resolution, pixel arrays and detector characteristics.

7.4.1 Intrinsic and System Spatial Resolution

Quantitative assessment for LFOV gamma cameras uses a standard capillary line source or standard point source. In order to sample the PSF or LSF, NEMA standards require that the "pixel size" should be $\leq$ 0.1 x FWHM [Chapman et al., 2007]. The Rayleigh criterion usually states that the minimum resolvable angular displacement occurs when the maximum belonging to one of the PSFs is positioned over the minimum of the other PSF. This accepted criterion for determining the angular resolution was developed by Lord Rayleigh in the 19th century. However, the factor of 0.1 is defined arbitrarily by NEMA from the Rayleigh criteria to allow clear separation of two adjacent profiles of the point spread function. The intrinsic spatial resolution derived from the LSF for the CGC, which is the profile of measured counts as a function of position across a line source, is shown in Figure 7.8 which at 7 mm from the scintillator was calculated to be 0.80 ± 0.02 mm (FWHM). For SFOV gamma cameras, the tolerances of having line sources and point sources with dimension less than 0.1 mm, and manufacture of bar transmission phantoms with smaller dimensions become progressively more challenging. The ERF Method, [Vayrynen et al., 1980] is better suited as only an edge needs to be imaged. In the evaluated SFOV gamma camera the CGC has on-chip binning giving pixels 64 μm by 64 μm covering an active area of 8 mm by 8 mm, [Lees et al., 2011]. So the best intrinsic spatial resolution this gamma camera can achieve is 128 μm. From experiment the intrinsic spatial resolution was found to be 0.8 mm. An incident gamma photon can produce X-ray fluorescence (providing the gamma photon energy is greater than the K shell binding energy). This X-ray fluorescence can be re-absorbed elsewhere in the scintillator so reducing the intrinsic spatial resolution. The intrinsic spatial resolution may also be broadened by incomplete charge collection, drift and transfer through the shift and gain registers, noise within the detector chain, optical light diffusion and optical light refraction through coupling media between the scintillator and the silicon detector.

System spatial resolution is measured with the collimator in-situ and in the presence of scattering medium simulating thickness of tissue. The collimator type and its dimensions should be stated as in many cases it will be the major limiting factor for system spatial resolution which varies as a function of displacement from the detector face. The thickness of scattering medium simulating tissue should be representative of the clinical situation for imaging. For example for the simulation of imaging deep sentinel nodes which may be found in the axilla of breast tumour patients up to 80 mm of scattering medium should be used, [Pitre et al., 2003].

A summary of alternative SFOV methodology is shown in Table 7.2 with most using the LSF method [Pitre et al., 2003, Sánchez et al., 2004, Tsuchimochi et al., 2003, Ferretti et al., 2013, Tsuchimochi and Hayama, 2013] and Menard et al. [1998] using the PSF method for the system spatial resolution. Only Sánchez et al. [2004] used the slit transmission mask to determine the intrinsic spatial resolution. In the case of line sources from practical experience uniform filling of capillary tubes of the order of a few hundred microlitres becomes challenging. The ERF method is an alternative method which avoids this difficulty.

Reference	System Spatial Resolution
[Ferretti et al., 2013]	LSF extracted from a 1 mm internal diameter capillary tube filled with 1.4 MBq technetium-99m, placed on the surface of the collimator. Obtained the FWHM for the LSF for each additional cm thickness of polyacrylamide
[Tsuchimochi et al., 2003] [Tsuchimochi and Hayama, 2013]	LSF extracted from a 1 mm internal diameter capillary tube filled with 0.37 MBq/ mm technetium-99m, placed on the surface of the collimator. Obtained the FWHM for the LSF for each additional cm thickness of polyacrylamide
[Menard et al., 1998]	PSF extracted from a 0.5 mm diameter collimated Co-57 source (using a 10 mm thick lead plate) placed on the surface of the collimator, Obtained the FWHM for the PSF
[Pitre et al., 2003]	LSF extracted from a 0.5 mm internal diameter capillary tube filled with unquoted activity of technetium-99m, placed on the surface of the collimator. Obtained the FWHM for the LSF for each additional cm thickness of polyacrylamide
[Sánchez et al., 2004]	Intrinsic - 2 mm thick lead transmission mask with slits 1 mm wide separated by 5 mm. An uncollimated technetium-99m 2 mm diameter source was placed at 23 cm from the surface of system in the centre of the UFOV. Orthogonal measurements of intrinsic spatial resolution. System - LSF extracted from a 2 mm internal diameter capillary tube filled with unquoted activity of technetium-99m, placed on the surface of the collimator. Obtained the FWHM for the LSF for 5 cm thickness of polyacrylamide

Table 7.2: Existing system spatial resolution measurements noting the designated collimator is removed for intrinsic spatial resolution and in-situ for system spatial resolution measurements.

7.4.2 Spatial Distortion

The measurement of the spatial distortion for the CGC demonstrated its mean deviation to be 0.117 ± 0.002 mm in both orthogonal directions of the detector array. Given each pixel dimension is 64 μm by 64 μm, this spatial non-distortion is good as it is less than two pixels across. Other methods to measure spatial distortion are shown in Table 7.3 for comparison. Pitre et al. [2003] and Ferretti et al. [2013] both used single point sources translated at known displacement across the GFOV, whereas Menard et al. [1998] and Tsuchimochi et al. [2003] used specifically manufactured transmission masks (i.e. to each SFOV system) to assess spatial distortion. Only Sánchez et al. [2004] the slit transmission mask which is easier to reproduce measurements and is used for the CGC.

Reference	Spatial Distortion
[Ferretti et al., 2013]	Point source technetium-99m 8.5 MBq positioned at different locations within the FOV and compared relative displacements from acquired images.
[Tsuchimochi et al., 2003]	Inferred from transmission bar phantoms for a 289 MBq technetium-99m source positioned 750 mm from each bar phantom. Bar phantoms of width and pitch respectively 1.8 mm / 3.6 mm, 2.4 mm/ 4.8 mm, 3.0 mm/ 6.0 mm and 3.6 mm/ 7.2 mm were used.
[Menard et al., 1998]	Uniform Co-57 source flood source irradiating a 6 mm thick lead transmission mask perforated by a 5 x 5 array with 1 mm diameter holes separated by 4 mm.
[Pitre et al., 2003]	1 mm diameter collimated Co-57 source (using a 10 mm thick lead plate placed) translated in 6 mm steps across the surface of the collimator at an unspecified distance away.
[Sánchez et al., 2004]	2 mm thick lead transmission mask with slits 1 mm wide separated by 5 mm. An uncollimated technetium-99m 2 mm diameter source 2 mm in diameter source was placed at 23 cm from the surface of system in the centre of the UFOV. Orthogonal measurements of spatial linearity.

Table 7.3: Spatial Distortion measurements

7.4.3 Spatial Uniformity

In practice when performing this measurement care should be taken to ensure uniformity of radioactivity within the Petri dish. For comparison alternative methodology to evaluate spatial uniformity is shown in Table 7.4 with [Tsuchimochi et al., 2003, Sánchez et al., 2004, Ferretti et al., 2013] each using a Petri dish filled with a uniform solution of radioactivity. Menard et al. [1998] and Pitre et al. [2003] did not perform this measurement but it is an essential requirement for clinical imaging.

Reference	Spatial Uniformity
[Ferretti et al., 2013]	Filled a 9 cm Petri dish with uniform solution of 115 MBq / 8 ml technetium-99m. Acquired 10 kcounts per pixel. Calculated the integral and differential uniformity.
[Tsuchimochi et al., 2003]	Filled a 85 mm x 85 mm x 15 mm Petri dish with uniform solution of 444 MBq technetium-99m. Acquired image of 600 s duration with the collimator 2 mm away from the surface of the solution. Calculated the variation in counts per pixel over the FOV.
[Menard et al., 1998] [Pitre et al., 2003]	Method not quoted
[Sánchez et al., 2004]	Filled a 25 mm Petri dish with uniform solution of unspecified activity technetium-99m to depth of 1 mm. Acquired 10 kcounts per pixel. Calculated the integral and differential uniformity.

Table 7.4: Spatial Uniformity measurements

7.4.4 Count-rate Capability

Count-rate capability is necessary to assess the SFOV gamma camera performance in the presence of regions of high uptake or injection sites as demonstrated elsewhere, [Tsuchimochi et al., 2003, Tsuchimochi and Hayama, 2013].

Count rates should be measured over the clinical range of administered radioactivity and ideally the camera count-rate response should be linear over this range. From the existing SFOV studies only one had performed this evaluation as shown in Table 7.5. For the CGC, as each incident gamma photon interacts at different depths in the scintillator then this leads to broadening of the light splash across the EMCCD pixel array. At low EMCCD frame rates (10 frames per second) there may well be overlapping of event profiles ("pile-up") which makes the extraction of the event position difficult. The system sensitivity for the CGC was found to be (214±7) counts.$s^{-1}MBq^{-1}$ at its entrance face, [Bugby et al., 2014]. This limits this use of this SFOV system to clinical imaging involving just a few tens of MBq administered activity, for example in lymph node imaging or thyroid imaging using technetium-99m. If one increased the administered activity, then the dose to the patient would increase.

Reference	Count-rate capability
[Ferretti et al., 2013]	Decay method using source activities (24.8 MBq to 1.7 MBq) in 2.5 ml volumes, imaged at 1 hour intervals at the centre of the FOV.
[Tsuchimochi et al., 2003, Tsuchimochi and Hayama, 2013] [Menard et al., 1998] [Pitre et al., 2003] [Sánchez et al., 2004]	Method not quoted

Table 7.5: Count-rate capability measurements

7.4.5 System Sensitivity

The system sensitivity depends on the energy of the radionuclide, the source distribution and position from the gamma camera, the type of collimator used and the mass attenuation coefficient and thickness of the detector. In addition there is a trade-off between system sensitivity and system spatial resolution. Clinically system sensitivity affects the ability to detect small volumes of activity within targeted tissue.

Other methods to obtain the system sensitivity are shown in Table 7.6. [Pitre et al., 2003, Tsuchimochi et al., 2003, Tsuchimochi and Hayama, 2013, Ferretti et al., 2013] each used a point source. Only Ferretti et al. [2013] used polyacrylamide to simulate tissue equivalent thickness whereas Tsuchimochi et al. [2003], Tsuchimochi and Hayama [2013] used a filled water tank. Using polyacrylamide slabs with a point source is a more practical solution.

Reference	Sensitivity
[Ferretti et al., 2013]	Point Source technetium-99m 8.5 MBq on surface of collimator. Determined the depth transmission curve for each additional cm thickness of polyacrylamide. Sensitivity value quoted at the polyacrylamide thickness at which the detected counts decreased to 50%.
[Tsuchimochi et al., 2003] [Tsuchimochi and Hayama, 2013]	Point Source technetium-99m away from the surface of collimator. Sensitivity value quoted but distance from the surface of the system unknown.
[Menard et al., 1998]	Method not quoted
[Pitre et al., 2003]	Point Source technetium-99m away from the surface of collimator. Sensitivity value quoted with 1 cm and 5 cm tissue equivalent thickness
[Sánchez et al., 2004]	Filled a 25 mm Petri dish with uniform solution of unspecified activity technetium-99m to depth of 1 mm. Acquired 10 kcounts per pixel. Sensitivity value quoted at given distance from the surface of the system.

Table 7.6: System sensitivity measurements

7.4.6 Energy Resolution

A key issue is to differentiate unscattered events from scattered events, otherwise this creates blurring in the clinical image. This depends on the gamma ray conversion efficiency, the presence of fluorescence, transmission losses of the optical photons, and the detection efficiency. The percentage energy resolution for the CGC was determined to be about 58% at 140.5 keV. This is worse than for typical LFOV systems, which for example for the NaI(Tl) scintillator based silicon Position Sensitive Photomultiplier Low Profile gamma camera is 10.8% [Polemi et al., 2016]. For solid state detector based gamma cameras without a scintillator the percentage energy resolution is even better, for example for the CdTe Small Semiconductor gamma camera its percentage energy resolution is between 6.9% to 7.8% [Tsuchimochi et al., 2003, Tsuchimochi and Hayama, 2013] at 140.5 keV. A summary of alternative published methodology for testing SFOV systems is shown in Table 7.7. Menard et al. [1998], Pitre et al. [2003], Tsuchimochi et al. [2003], Sánchez et al. [2004] all used a distant point source although Ferretti et al. [2013] did not publish this measurement.

Reference	Energy Resolution
[Ferretti et al., 2013]	Method not quoted
[Tsuchimochi et al., 2003] [Tsuchimochi and Hayama, 2013]	Point Source technetium-99m 18.5 MBq in air at a distance of 100 cm from the surface of the system.
[Menard et al., 1998]	1 mm diameter collimated Co-57 source (using a 10 mm thick lead plate placed) placed on the surface of the collimator
[Pitre et al., 2003]	Point Source technetium-99m of unspecified activity in air at unknown distance from the surface of the system.
[Sánchez et al., 2004]	Lead hole-mask 2 mm thick with 137 holes 1 mm in diameter covering the UFOV of the gamma camera. An uncollimated technetium-99m 2 mm diameter source was placed at 23 cm from the surface of system in the centre of the UFOV.

Table 7.7: Energy Resolution measurements

7.5 Conclusions

The existing protocols used in clinical environments for assessing the performance of Large Field-Of-View (LFOV) gamma cameras need to be adapted for Small Field-Of-View (SFOV) gamma camera systems. Although some characterisation protocols have been used for other SFOV systems it is beneficial to have a standard set of tests to address their variation. The proposed procedures for evaluating the imaging parameters, as outlined in this chapter provide a more appropriate scheme for characterising the high resolution SFOV gamma camera and for optimising image quality.

What is also important for clinical imaging is the time taken to survey a suspect lesion. The clinical operator in theatre has to integrate counts while surveying the target region; how long this takes depends on the confidence of the clinical operator's determination of a true positive lesion. Future protocols should be developed to take into account specific clinical requirements for Small Field-Of-View applications, such as detectability of lesions in sentinel lymph node biopsy or image registration in hybrid camera systems [Bugby et al., 2017].

Chapter 8

Future Work

In this novel work Monte Carlo modelling was used to understand and predict the underlying physics as impinging gamma photons transport through two SFOV systems developed here at the University of Leicester. In doing so, there are several branches of further research which should be explored. Thus starting with Chapter 3, this described Monte Carlo simulations of a model of the CGC with a 0.5 mm diameter cylindrical pinhole tungsten collimator 6 mm thick. However, the actual mechanical design of the collimator hole is tapered with a larger acceptance angle. This consists of a 0.5 mm diameter pinhole with an acceptance angle of 60 degrees in a 6 mm thick tungsten collimator. The aperture penetration and scatter from a tungsten knife-edge pin-hole of diameters between 100 μm to 500 μm for technetium-99m has been investigated using GEANT v4..5.0 [Have and Beekman, 2004]. They reported that the proportion of the detected scatter events to the total detected photons can be of the order of 2-5%. This scatter fraction degrades the spatial resolution [Metzler et al., 2001].

The PENELOPE modelling in this chapter also employed a 1500 μm thick caesium iodide monolithic crystal which was modelled as an approximation to a close-packed (85%) columnar crystal [Hamamatsu-Photonics, 2019]. The cross-section of the 5 μm silicon detector and the 1500 μm thick caesium iodide monolithic crystal were both 8 mm^2. These simulations may be improved by using the more refined geometry construction capabilities of GEANT4 compared to quadrics used in PENELOPE. In such a simulation the geometry simulated would include a 0.5 mm diameter pinhole with an acceptance angle of 60 degrees and a close-packed (85%) columnar caesium iodide crystal. The physical basis for the caesium iodide crystal is demonstrated by scanning electron microscope (SEM) images of the tightly packed columnar structured caesium iodide scintillator (type ACS-HL-20-30-600-UK), with each column of diameter approximately 10 μm across. SEM images show that the columns are almost orthogonal to the base of the crystal although there are several dislocations. The columns however increase the optical photon collection by directing the light to the EMCCD. The GEANT4 C++ coding of PENELOPE v2008 called "G4 EmPENELOPE" should be used for photon interactions at low energies (less than 200 keV), including the small angle columnar tilt found in structured caesium iodide (up to 5 degrees away from the orthonormal to the crystal base) and unstructured scintillation layer at the base of columns (15%) [Badano and Sempau, 2006], the passive substrate layer (amorphous carbon) [Hamamatsu-Photonics, 2019] and back-scatter from the thermoelectric cooler. The surface pixel properties of the silicon detector including reflectivity of the individual pixels and pixel array dead space should also be included.

The systematic approach used to investigate effects of individual components within the SFOV low energy systems was explored in Chapter 4 using PENELOPE. Although the focus of this thesis was on photon interactions including the effects of fluorescence from photoelectron interactions, it did not include detailed interactions of electrons with atoms of the intervening medium. Elastic interactions of electrons are those which preserve the quantum state of the target atom, and may be described by the scattering of the electrons by the charge distribution of the target nucleus and the electron cloud. The energy losses of the projectile electrons is of the order of a few meV and so can be neglected. This is because the target nucleus is much bigger than the mass of the electron. However, there are also inelastic interactions to consider which may create electronic excitations and ionisation in the medium. The energy losses of these projectile electrons undergoing inelastic interactions is of the order of a few eV, and should be considered in future modelling using GEANT4. Photoabsorption creates photoelectrons of energy 139.9 keV, which have a mean free path of 0.113 μm for inelastic scattering within caesium iodide (calculated using PENELOPE for source photons of energy 140.5 keV and a mean excitation energy for caesium iodide of 0.553 keV, obtained from PENELOPE simulation tables). The subsequent de-excitation creates fluorescence X-rays and secondary knock-on electrons which gradually dissipate their energy within the crystal. The influence of photoelectron inelastic scattering should be considered, using for example simulation of inelastic interactions as described in PENELOPE [Salvat et al., 2011] or using the "G4PenelopeIonisationModel" in GEANT4 [GEANT4 Collaboration - G4Physics, 2018].

Chapter 5 evaluated the amount of pixel charge sharing for incident events in the EMCCD pixel array. These events are clusters of pixels marking the position whereby a charge cloud has been generated along the trajectory of incident photons, and has diffused outwards within the silicon depletion layer. The lateral spreading of the charge cloud may be described by analytical models as a cascade of photoelectrons which are generated until a charge cloud with thermalised electrons is produced [Hopkinson, 1987, McCarthy et al., 1995, Lees, 2010]. These photoelectrons drift in non-linear paths under the $\mathbf{E}-$field as electron hole pairs are generated along their trajectory. The charge collected by the detector represents the radius of the charge cloud, amount of recombination, charge losses and any partial reflection of thermalised electrons near the Si-SiO_2 surface layer [McCarthy et al., 1995, Short et al., 2002, Lees, 2010]. More detailed modelling which includes these effects may be simulated using a GEANT4 extension package called G4MicroElec [GEANT4 Collaboration - G4Physics, 2018]. This incorporates the generation and transport of low energy electron as discrete events using the GEANT4 process called "G4MicroElecInelastic". The low energy limit described by the model is 16.7 eV and its experimentally validated upper energy limit is 50 keV [Valentin et al., 2012]. This package also just treats all electron interactions as ionisation neglecting excitation, which may lead to atomic relaxation by fluorescence or Auger electrons. Nonetheless low energy GEANT4 packages like "G4PenelopeIonisationModel" if included within this modelling can fulfil this requirement. Lastly, existing models of the Gaussian charge dispersion of the measured charge at the electrodes provided by [Nilsson et al., 2002, Wang et al., 2011] require further investigation in order to be justified. While GEANT4 has the capability to model electromagnetic fields within the silicon detector, it may also be beneficial to use a multi-physics package open source framework such as Allpix^2 [Spannagel et al., 2018] which incorporates the electric field distribution from technology computer aided design simulations (TCAD), and the charge carrier deposition using GEANT4.

The optical Monte Carlo simulations using GEANT4 carried out in chapter 6 explored the frequency distribution of the optical photons that were generated within the scintillator, and their frequency distribution when impacting onto the silicon detector. This modelling can be extended to include the spatial distribution of the optical photons, not only across the orthogonal dimensions of the pixelated silicon, but also to include their depth-of-interaction in the columnar scintillator. As each incident gamma photon interacts at different depths in the scintillator, creating scintillation photons, then this leads to broadening of the light splash across the pixelated silicon detector. The radius of the light splash across the pixelated silicon detector should be explored along with its distribution as a function of the initial position of the optical photon at the site of creation within the scintillation crystal.

A technique to extract this event profile may use Scale Space transformation, [Bart and Romeny, 1996] however, there is scope to use neural network algorithms to extract the statistical light distribution across the pixelated detector [Babiano et al., 2019]. These methods use the light intensity to estimate the position of the gamma photon interaction and the creation of scintillation photons. However, if the time-stamp of the first scintillation photons on the pixelated silicon are recorded, then it is possible to estimate the position of the depth-of-interaction. The rise and decay time of the scintillator response and the temporal resolution of the pixelated silicon detector would affect the recording of these time-stamps. Early modelling of this time-stamps has been described [Tabacchini et al., 2015] but this should be verified with fast timing experiments with a pixelated silicon detector of the temporal resolution less than a few nanoseconds.

The GEANT4 optical modelling carried out in chapter 6 also highlighted the requirement to use experimentally derived simulation parameters to improve the simulation. The optical absorption length as a function of wavelength can be measured using a spectrophotometer with two beams of light; one for sampling the attenuation length through caesium iodide, and the other as the reference, [Knyazev et al., 2019]. Although a photodiode array over 2π to measure reflectance for a specific wavelength (440 nm) has been used for aluminium foil [Janecek, 2012], a wavelength tunable laser may be used extend this work for caesium iodide crystals and silicon within the optical region 300 - 800 nm, matching the quantum efficiency of the CCD97-00 EMCCD [e2vTechnologies, 2004]. The refractive index of the optical coupling between the caesium iodide crystal and silicon detector, as a function of wavelength within the optical range may be determined using wavelength tunable laser [van Dam et al., 2012]. In the CGC, this optical coupling is provided by layer of a few microns of Dow

Corning grease (compatible for use within the evacuated camera chamber). Transmission measurements of a wavelength tunable laser through the optical coupling create a set of parameters which may be fitted to a single set of Sellmeier coefficients describing the refractive index as a function of wavelength.

Lastly, for the characterisation protocol work performed in chapter 7, future protocols should be developed to take into account specific clinical requirements for small field-of-view applications, such as detectability of lesions in sentinel lymph node biopsy or image registration in hybrid camera systems [Bugby et al., 2017]. From the experimental characterisation the energy resolution of the SFOV gamma camera at 140.5 keV was 58% which is poor and the system sensitivity (214±7) counts.s^{-1}MBq^{-1} at its entrance face, [Bugby et al., 2014], showed comparable sensitivity to the LFOV gamma camera; however the use of the pinhole will mean that the sensitivity of the system will drop off faster at distance than parallel hole systems. Monte Carlo modelling should be used to include not just collimator design and back-scatter from the whole SFOV system, but also explore different modern scintillators. At the time of writing these include for example cerium doped lathanide halides such as $LaBr_3$, cerium doped garnet scintillators such as $Gd_3(Al,Ga)_5O_{12}$ [GAGG] and europium doped strontium iodide SrI_2 [Yanagida, 2018]. Table 8.1 shows a summary of their scintillator properties [Lowdon et al., 2019].

	caesium iodide (thallium doped)	lanthanum bromide	gadolinium oxide garnet (cerium doped)	strontium iodide (europium doped)
Density/ gcm^{-3}	4.51	5.22	6.33	4.55
Emission peak/ nm	560	380	520	435
Light Yield/ photons per keV	54	63	60	80
Decay Time/ ns	2.1, 1000	16	87	1200

Table 8.1: Selection of modern scintillators at the time of writing referenced to thallium doped caesium iodide [Lowdon et al., 2019].

These scintillators have equivalent or higher light yield compared to thallium doped caesium iodide which is important because the energy resolution of the whole SFOV detector correlates with the number of scintillation photons created and collected by the silicon detector (assuming negligible light collection losses between the coupling of the scintillator crystal and the silicon detector). In chapter 6 there was a limitation in the optical modelling in that the frequency distribution of the optical photons were recorded rather than its energy spectrum as GEANT4 does not conserve energy once the optical photons are created from the primary photon(s) and propagated to produce secondary photon tracks [GEANT4 Collaboration - G4Physics, 2018]. This should be addressed with C++ coding development in GEANT4. Table 8.1 also shows that these scintillators have high mass attenuation coefficient to attenuate these optical photons. Clearly, optical simulation parameters would require experiments to assess the optical absorption length, reflectivity and refractive indices as a function of wavelength as described above.

Chapter 9

Summary

In nuclear medicine the physiological function of an organ is imaged by administrating a radiolabelled pharmaceutical either intravenously, intra-dermally, orally, by inhalation or by placement intra-cavity, and collecting the photons emitted from within the patient with a suitable detector. These photons are either photoabsorbed, Compton scattered or Rayleigh scattered. The radio-labelled pharmaceutical component follows the physiological process within the organ and for gamma camera imaging, it is usually labelled with technetium-99m. Sites of tumours and sentinel nodes are imaged by Small Field-Of-View (SFOV) low energy (less than 200 keV) photon imaging systems. These photon imaging systems use detectors which are employed either a solid-state detector on their own, or an inorganic scintillator coupled to a solid-state detector. Some of the known limitations of gamma probes used in surgery (such as spatial resolution and depth of tumours), is addressed by using high resolution SFOV hand-held gamma cameras to provide dynamic images and indeed their development enables imaging procedures to be undertaken at the bedside, within intensive care units, clinics and in the operating theatres. In the wider scope scintillator and silicon based detectors are wide-spread in other types of clinical imaging [van Eijk, 2003, Roncali et al., 2017].

This work is focused on two Small Field-Of-View (SFOV) systems developed at the University of Leicester viz. the Portable Imaging X-ray Spectrometer detector [PIXS], a pre-scintillator system for non-medical use, and the thallium doped caesium iodide scintillator based Compact Gamma Camera [CGC] used for medical imaging. An e2v CCD97-00 back-illuminated Electron Multiplying Charge Coupled Device [e2vTechnologies, 2004] in used in the construction of each system. At the time of writing no publications are described for Monte Carlo simulations of the detailed tracking of these low energy gamma and X-ray photons through the SFOV system. A literature search using the Web of Science (1970-2019) and Scopus (1960-2019) with the keywords "gamma, camera" AND "monte carlo" AND "small" OR "compact" 200 and 215 results respectively are acquired, but without any photon tracking studies. In this work Monte Carlo modelling is used to understand and predict the underlying physics as impinging gamma photons transport through these two models of SFOV systems. In addition, the GEANT4 v10.5 Monte Carlo code [Agostinelli et al., 2003] is used for the optical simulations together with an electromagnetic PENELOPE physics model for interactions of the incident gamma and X-ray photon flux. All Monte Carlo simulations are performed using the ALICE High Performance Computing Facility at the University of Leicester. In this thesis several novel Monte Carlo simulations are described which are used to understand the design of the current SFOV gamma camera and inform its development in order to improve its capability for clinical imaging. Both experimental and analytical validation of the Monte Carlo simulations is also described as appropriate. These SFOV systems are performed with the EMCCD modelled as an 8 mm x 8 mm x 5 μm thick monolithic silicon detector. The clinical context for use of such SFOV imaging systems is established in the first chapter, and includes some of the types of solid state detectors used in SFOV gamma cameras at the time of publication. A summary of the theory used in this work is provided in chapter 2 including aspects of low energy photon interactions, a description of the types of noise in the EMCCD, scintillator crystals and the Monte Carlo method.

By using both PENELOPE v2008 and GEANT4 v10.5 Monte Carlo simulations fascinating insights are provided into the complex physics that occur within these SFOV low energy systems; indeed such Monte Carlo methodology is a useful alternative to purchasing expensive off-the-shelf components prior to their construction. Hence, in chapter 3 a Monte Carlo simulation of a model of the PIXS detector, without detector noise, is described and is used to determine the distribution of energy deposited within the silicon detector. Using an incident 22 keV photon source, an analytical derivation of the proportion of the silicon K X-rays that escape from a finite 8 mm x 8 mm x 5 μm thick silicon detector is calculated, and is used to determine the ratio of the silicon escape peak height to the incident parent peak height as 0.004. In the corresponding Monte Carlo simulation the ratio of the heights of the silicon escape peak to the 22 keV peak is determined as 0.003 ± 0.001 which is in good agreement. Using the full emission spectrum of cadmium-109 as a photon flux, the recorded energy spectrum within the silicon target is demonstrated to be consistent with referenced data [Chu et al., 1999]. In this Monte Carlo simulation a large peak is seen at 3.5 ± 0.2 keV due to Ag L X-rays, owing to the quantum efficiency being higher at this low energy in the silicon detector. In the Monte Carlo simulation of the modelled SFOV detector aluminium fluorescence at 1.4 keV is demonstrated owing to the aluminium enclosure which provides the integrity for the evacuated chamber containing the silicon detector. However, both the aluminium fluorescence and silicon escape peaks are masked by readout noise and detector noise in a real detector. Clearly, it is important to understand these underlying physics interactions in designs employing silicon detectors to validate their detected response to the construction material used and the flux of source photons.

The CGC is designed for clinical imaging in nuclear medicine and has a front-end tungsten pin-hole collimator installed. Any incident gamma and X-ray photons are transmitted through the collimator, caesium iodide scintillator crystal and onto the silicon detector. The detector efficiency as a function of energy deposited for photons within the 5 μm silicon detector for a point source is shown to be 0.17%, consistent with the physical interpretation that the majority of gamma photons pass through the silicon detector.

An important feature of Monte Carlo modelling is that it allows for a systematic approach to investigate the effects of individual components used within the SFOV low energy systems. This is explored in Chapter 4 where the distribution of energy deposited within caesium iodide and the fluence of photons from the egress face of the caesium iodide crystal towards the detector are demonstrated. Following these photons to a silicon detector, the distribution of energy deposited is recorded there. In the Monte Carlo simulations energy deposition and fluence accumulators are used which record the distribution of photons respectively for the energy deposited or population distribution of photons collected within them. However, in the case of energy deposition accumulators, although the energy spectra perform well compared to the referenced data [Chu et al., 1999], not all the modelled fluorescence intensities is not recorded. If some of the K_α and K_β fluorescence photons are created close to the boundary of the accumulator i.e. less than its mean free path, then the intensities of these distributions are not recorded within the Monte Carlo accumulators.

In the design of some low energy SFOV imaging systems, the scintillator is coupled directly to the solid-state detector. In Monte Carlo simulations of the distribution of photon fluence within a fluence accumulator at the egress face of the caesium iodide crystal, Compton continuum and fluorescence X-rays which corresponds to iodine and caesium K_α and K_β fluorescence is demonstrated. Following these photons onto the 5 μm silicon detector, $K_{\alpha 1}$ fluorescence from both caesium and iodine is recorded in the distribution of the energy deposition there. However, as noted, not all these events are collected within the accumulator as its thickness is less than the mean free path of these fluorescence photons. Nonetheless, the profile of this energy distribution within 5 μm silicon is consistent with the response for the photon mass attenuation coefficients of silicon at 140.5 keV.

It is important to corroborate findings either with experiment (where possible) or by analytical means. In chapter 5, for validation purposes, experimental responses are obtained using americium-241 and cadmium-109 sources in order to calibrate a bare silicon PIXS detector without the scintillator being present. In this chapter, the response of the e2v CCD97-00 back illuminated EMCCD with its gain potential difference Φ_{HV} using cadmium-109 is demonstrated (with the EMCCD cooled to 256.0 ± 0.1 K). In the experimental evaluation of this response using cadmium-109, a single photon detection scheme of thresholding using the noise peak plus 5σ is shown to work well for a gain potential difference Φ_{HV} between 33.5 V and 39.5 V. If the total mean electron gain in the gain register $G \gg \sigma_{readout}$, where $\sigma_{readout}$ is the standard deviation of the readout noise, then a signal above this threshold is treated as a photoelectron event. This readout noise is independent of gain in terms of electrons, and is thus thresholded at 5σ to distinguish between zero and single input photoelectrons [Zhang et al., 2009]. The premise of distinguishing between zero and single photoelectron as an input, with thresholding of the output signal from the amplifier using the noise peak plus 5σ is justified. Broadening of the Ag K_α, K_β peaks in the experimental response of the EMCCD using cadmium-109 is also demonstrated and is compared to the Fano-limited Monte Carlo simulation in chapter 3 using a 5 μm thick silicon detector of area 8 mm x 8 mm in the absence of noise. The broadening of the energy resolution (in the absence of a scintillator) is consistent with the accumulative effects of incomplete charge collection, drift and transfer through the shift and gain registers, and noise from the detector readout.

In the final part of chapter 5 the amount of pixel charge sharing for incident events in the EMCCD pixel array is evaluated. Any events which are recorded within the EMCCD pixel array are clusters of pixels marking the position whereby a charge cloud is generated along the trajectory of incident photons, as it diffuses outwards within the silicon depletion layer. As this diffusion occurs, the probability distribution of charge collected within the potential wells across several pixels is manifested as a shift of the centroid peak of multi-pixel events towards lower energies, [Owens et al., 1994]. The broadening of the low energy edge is caused by charge sharing between the pixels of the silicon array owing to: the depth-of-interaction and photoelectron range, diffusion of electron and hole pairs outwards within the silicon depletion layer along the trajectory of incident photons, and fluorescence X-rays.

Lastly, for the decomposition of the EMCCD counts recorded using an americium-241 source it is shown that the proportion of mono-pixel events is greater than bi-pixel events below an incident photon energy of about 28 keV. The charge which is collected by the pixel array represents the radius of the charge cloud, amount of recombination, charge losses and any partial reflection of thermalised electrons near the Si-SiO2 surface layer, [McCarthy et al., 1995, Lees et al., 2010]. The depth of the interaction of the gamma photon also determines the radius of the charge cloud [McCarthy et al., 1995, Short et al., 2002, Lees et al., 2010]. This change in the proportion of bi-pixel events warrants using either analytical or Monte Carlo modelling to compare the incident photon energy with charge collected by the pixel array in relation to the silicon pixel size. If the silicon pixel array is coarser than that used in our EMCCD, less charge sharing is expected. Conversely, higher energy photons are more likely to cause the distribution of photoelectrons generated by the charge cloud to spread over multiple pixels.

The addition of monolithic and columnar 8 mm x 8 mm x 1500 µm thick caesium iodide scintillator crystals is discussed in chapter 6, and the effect of optical photons impacting onto the silicon detector are considered. The columnar 1500 µm thick caesium iodide is modelled using columns 100 µm x 100 µm. In this work the Monte Carlo code GEANT4 v10.4 provides a model for both the transport of gamma and X-ray photons, and that of scintillation photons across crystal surfaces and interfaces. The GLISUR surface description model [GEANT4 Collaboration - G4Applications, 2018] is used and includes a simplified surface description with a polished monolithic scintillator crystal and monolithic silicon detector. The proportion of optical photons which are created and impacting on the silicon detector is greater in the case of the columnar caesium iodide crystal laterally wrapped with 1 µm aluminium, in comparison to either to an unwrapped columnar crystal, laterally wrapped monolithic or unwrapped monolithic crystals.

A more refined model of the frequency distribution of scintillation photons recorded should also include any crystal imperfections within the structure, the probability of collection of optical quanta by the detector via a coupling medium and the detector's surface properties, the spatial distribution of optical photons and the depth-of-interaction effect which creates broadening of the light splash across the EMCCD pixel array. In terms of clinical imaging, accurate physiological mapping for the positional accuracy of the primary emission event from within the patient's body is enhanced when the variance of the spatial resolution in the position of the light splash across the pixels is minimised.

A baseline protocol for the clinical performance evaluation of SFOV gamma cameras in the absence of any previous schema [Bhatia et al., 2015, Bugby et al., 2014] is described in chapter 7. There are a variety of SFOV imaging system designs used in research and although some characterisation protocols have been used for other SFOV systems it is beneficial to have a standard set of tests to address their variation in design. The proposed procedures for evaluating the imaging parameters is demonstrated and this is a more appropriate scheme for characterising the high resolution SFOV gamma cameras.

In this novel work Monte Carlo modelling is used to understand and predict the underlying physics as impinging gamma photons transport through SFOV detectors and in doing so, opens several branches of further research which is described in the section on future work.

Bibliography

A. Abe, N. Takahashi, J. Lee, T. Oka, K. Shizukuishi, T. Kikuchi, T. Inoue, M. Jimbo, H. Ryuo, and C. Bickel. Performance evaluation of a hand-held, semiconductor (CdZnTe)-based gamma camera. *European Journal of Nuclear Medicine and Molecular Imaging*, 30(6):805–811, June 2003. ISSN 1619-7070, 1619-7089. doi: 10.1007/s00259-002-1067-z. URL `http://link.springer.com/10.1007/s00259-002-1067-z`.

Y. Abreu, H. Iwamoto, K. Kiyohara, T. Nagasaki, G. Wakabayashi, Y. Uozumi, and N. Matsufuji. Scintillation Efficiency of Inorganic Scintillators for Intermediate-Energy Charged Particles. *Progress in Nuclear Science and Technology*, 1(0):218–221, February 2011. ISSN 2185-4823. doi: 10.15669/pnst.1.218. URL `http://www.aesj.or.jp/publication/pnst001/data/218.pdf`.

S. Agostinelli, J. Allison, K. Amako, J. Apostolakis, H. Araujo, P. Arce, M. Asai, D. Axen, S. Banerjee, G. Barrand, F. Behner, L. Bellagamba, J. Boudreau, L. Broglia, A. Brunengo, H. Burkhardt, S. Chauvie, J. Chuma, R. Chytracek, G. Cooperman, G. Cosmo, P. Degtyarenko, A. Dell'Acqua, G. Depaola, D. Dietrich, R. Enami, A. Feliciello, C. Ferguson, H. Fesefeldt, G. Folger, F. Foppiano, A. Forti, S. Garelli, S. Giani, R. Giannitrapani, D. Gibin, J.J. Gómez Cadenas, I. González, G. Gracia Abril, G. Greeniaus, W. Greiner, V. Grichine, A. Grossheim, S. Guatelli, P. Gumplinger, R. Hamatsu, K. Hashimoto, H. Hasui, A. Heikkinen, A. Howard, V. Ivanchenko, A. Johnson, F.W. Jones, J. Kallenbach, N. Kanaya, M. Kawabata, Y. Kawabata,

M. Kawaguti, S. Kelner, P. Kent, A. Kimura, T. Kodama, R. Kokoulin, M. Kossov, H. Kurashige, E. Lamanna, T. Lampén, V. Lara, V. Lefebure, F. Lei, M. Liendl, W. Lockman, F. Longo, S. Magni, M. Maire, E. Medernach, K. Minamimoto, P. Mora de Freitas, Y. Morita, K. Murakami, M. Nagamatu, R. Nartallo, P. Nieminen, T. Nishimura, K. Ohtsubo, M. Okamura, S. O'Neale, Y. Oohata, K. Paech, J. Perl, A. Pfeiffer, M.G. Pia, F. Ranjard, A. Rybin, S. Sadilov, E. Di Salvo, G. Santin, T. Sasaki, N. Savvas, Y. Sawada, S. Scherer, S. Sei, V. Sirotenko, D. Smith, N. Starkov, H. Stoecker, J. Sulkimo, M. Takahata, S. Tanaka, E. Tcherniaev, E. Safai Tehrani, M. Tropeano, P. Truscott, H. Uno, L. Urban, P. Urban, M. Verderi, A. Walkden, W. Wander, H. Weber, J.P. Wellisch, T. Wenaus, D.C. Williams, D. Wright, T. Yamada, H. Yoshida, and D. Zschiesche. GEANT4—a simulation toolkit. *Nuclear Instruments and Methods in Physics Research Section A: Accelerators, Spectrometers, Detectors and Associated Equipment*, 506(3):250–303, July 2003. ISSN 01689002. doi: 10.1016/S0168-9002(03)01368-8. URL `http://geant4.web.cern.ch/geant4`.

H.O. Anger. Scintillation Camera with Multichannel Collimators. *Journal of Nuclear Medicine*, 29(1):27–34, 1957. doi: http://dx.doi.org/10.1063/1.1715998.

H.O. Anger. Scintillation Camera with Multichannel Collimators. *Journal of Nuclear Medicine*, 5:515–531, 1964.

V. Babiano, L. Caballero, D. Calvo, I. Ladarescu, P. Olleros, and C. Domingo-Pardo. γ -Ray position reconstruction in large monolithic LaCl3(Ce) crystals with SiPM readout. *Nuclear Instruments and Methods in Physics Research Section A: Accelerators, Spectrometers, Detectors and Associated Equipment*, 931:1–22, July 2019. ISSN 01689002. doi: 10.1016/j.nima.2019.03.079. URL `https://linkinghub.elsevier.com/retrieve/pii/S0168900219304218`.

A. Badano. Optical blur and collection efficiency in columnar phosphors for X-ray imaging. *Nuclear Instruments and Methods in Physics Research Section A: Accelerators, Spectrometers, Detectors and Associated Equipment*, 508(3):467–479, August 2003. ISSN 01689002. doi: 10.1016/S0168-9002(03)01651-6. URL http://linkinghub.elsevier.com/retrieve/pii/S0168900203016516.

A. Badano and J. Sempau. MANTIS: combined x-ray, electron and optical Monte Carlo simulations of indirect radiation imaging systems. *Physics in Medicine and Biology*, 51(6):1545–1561, March 2006. ISSN 0031-9155, 1361-6560. doi: 10.1088/0031-9155/51/6/013. URL http://stacks.iop.org/0031-9155/51/i=6/a=013?key=crossref.eaa68c629a78dc13f5f41c29addfe049.

A. Badano, I.S. Kyprianou, and J. Sempau. Anisotropic imaging performance in indirect x-ray imaging detectors: Anisotropic imaging performance in indirect x-ray imaging detectors. *Medical Physics*, 33(8):2698–2713, July 2006. ISSN 00942405. doi: 10.1118/1.2208925. URL http://doi.wiley.com/10.1118/1.2208925.

S. Baechler, F. Corminbeouf, R. Linder, P.H. Trueb, J. Malterre, B. Delaloye, F. Bochud, and F.R. Verdun. Feasibility of the gamma camera acceptance testing procedure introduced by the Swiss Federal Ofice of Public Health. Technical report, Swiss Federal Ofice of Public Health., 2003.

M. Bart and ter Haar Romeny. Introduction to Scale-Space Theory. In *Fourth International Conference on Visualization in Biomedical Computing*, page 26, Hamburg, Germany, 1996.

A.G. Basden, C.A. Haniff, and C.D. Mackay. Photon counting strategies with low-light-level CCDs. *Monthly Notices of the Royal Astronomical Society*, 345(3):985–991, November 2003. ISSN 00358711, 13652966. doi: 10.1046/j.1365-8711.

2003.07020.x. URL https://academic.oup.com/mnras/article-lookup/doi/10.1046/j.1365-8711.2003.07020.x.

M-M. Be, N. Coursol, B. Duchemin, F. Lagoutine, J. Legrand, K. Debertin, and E. Schonfeld. *Laboaroire NAtional Henri Becquerel 2011/5: Table of Radionuclides*. 2011. URL http://www.nucleide.org/DDEP_WG/DDEPdata.htm.

A.D Beach. Aperture-indexed collimators for gamma cameras with semiconductor detector arrays. *Journal of Physics E: Scientific Instruments*, 2(4): 378–380, April 1969. ISSN 00223735. doi: 10.1088/0022-3735/2/4/424. URL http://stacks.iop.org/0022-3735/2/i=4/a=424?key=crossref.2bb02612fa6c58f048b6b275e1d1c24a.

J.A. Bearden and A.F. Burr. Reevaluation of X-Ray Atomic Energy Levels. *Reviews of Modern Physics*, 39(1):125–142, January 1967. ISSN 0034-6861. doi: 10.1103/RevModPhys.39.125. URL https://link.aps.org/doi/10.1103/RevModPhys.39.125.

S.A. Benjegard, V. Sauret, P. Bernhardt, B. Wangberg, H. Ahlman, and E. Forssell-Aronsson. Evaluation of Three Gamma Detectors for Intraoperative Detection of Tumors Using In-111 Labeled Radiopharmaceuticals. *Journal of Nuclear Medicine*, 40(12):2094–2101, 1999.

M.J. Berger and S.M. Seltzer. Tables of Energy Losses and Ranges of Electrons and Positrons. Technical Report SP-3012, NASA, Washington D.C., 1964.

B.S. Bhatia, S.L. Bugby, J.E. Lees, and A.C. Perkins. A scheme for assessing the performance characteristics of small field-of-view gamma cameras. *Physica Medica*, 31(1):98–103, 2015. ISSN 1724191X. doi: 10.1016/j.ejmp.2014.08.004. URL http://linkinghub.elsevier.com/retrieve/pii/S1120179714005195.

S. Blahuta, B. Viana, A. Bessière, E. Mattmann, and B. LaCourse. Luminescence quenching processes in Gd2O2S:Pr3+,Ce3+ scintillating ceramics. *Optical Materials*, 33(10):1514–1518, August 2011. ISSN 09253467. doi: 10.1016/j.optmat.2011.02.040. URL http://linkinghub.elsevier.com/retrieve/pii/S0925346711001157.

G. Blasse. Scintillator materials. *Chemistry of Materials*, 6(9):1465–1475, September 1994. ISSN 0897-4756, 1520-5002. doi: 10.1021/cm00045a002. URL http://pubs.acs.org/doi/abs/10.1021/cm00045a002.

A. Bolster, J. Hannan, P.S. Cosgriff, A.B. Mostaffa, A. Parkin, P.F. Sharp, D.J. Sumner, H. M. Brash, G.G. Gardiner, P. Jarritt, D. Visvikis, T. Fryer, and A. Houston. *Report 86 Quality Assurance in Gamma Camera Systems*. Institute of Physics and Engineering in Medicine, York, 2003. ISBN 1 903613 13 2. URL http://www.ipem.ac.uk/Publications/IPEMReports.aspx.

S.L. Bugby. *Development of a hybrid portable medical gamma camera*. PhD thesis, Leicester, June 2015.

S.L. Bugby, J.E. Lees, B.S. Bhatia, and A.C. Perkins. Characterisation of a high resolution small field of view portable gamma camera. *Physica Medica*, 30(3): 331–339, May 2014. ISSN 11201797. doi: 10.1016/j.ejmp.2013.10.004. URL http://linkinghub.elsevier.com/retrieve/pii/S1120179713004250.

S.L. Bugby, J.E. Lees, and A.C. Perkins. Hybrid intraoperative imaging techniques in radioguided surgery: present clinical applications and future outlook. *Clinical and Translational Imaging*, 5(4):323–341, August 2017. ISSN 2281-5872, 2281-7565. doi: 10.1007/s40336-017-0235-x. URL http://link.springer.com/10.1007/s40336-017-0235-x.

D. Burt and J. Morcom. CCD Imaging III. Technical report, e2V Technologies Limited, Chelmford, 1987.

E. Busemann Sokole, A. Płachcínska, and A. Britten. Acceptance testing for nuclear medicine instrumentation. *European Journal of Nuclear Medicine and Molecular Imaging*, 37(3):672–681, March 2010a. ISSN 1619-7070, 1619-7089. doi: 10.1007/s00259-009-1348-x. URL http://link.springer.com/10.1007/s00259-009-1348-x.

E. Busemann Sokole, A. Płachcínska, A. Britten, M. Lyra Georgosopoulou, W. Tindale, and R. Klett. Routine quality control recommendations for nuclear medicine instrumentation. *European Journal of Nuclear Medicine and Molecular Imaging*, 37(3):662–671, March 2010b. ISSN 1619-7070, 1619-7089. doi: 10.1007/s00259-009-1347-y. URL http://link.springer.com/10.1007/s00259-009-1347-y.

I. Buvat, I. Castiglioni, J. Feuardent, and M-C. Gilardi. Unified description and validation of Monte Carlo simulators in PET. *Physics in Medicine and Biology*, 50(2):329–346, January 2005. ISSN 0031-9155, 1361-6560. doi: 10.1088/0031-9155/50/2/011. URL http://stacks.iop.org/0031-9155/50/i=2/a=011?key=crossref.a118a968b8eddcdcb256b2aeafdce328.

Carewise. Carewise C-Trak. URL https://carewise.com/c-trak-probes.

I. Castiglioni, I. Buvat, G. Rizzo, M.C. Gilardi, J. Feuardent, and F. Fazio. A publicly accessible Monte Carlo database for validation purposes in emission tomography. *European Journal of Nuclear Medicine and Molecular Imaging*, 32(10):1234–1239, October 2005. ISSN 1619-7070, 1619-7089. doi: 10.1007/s00259-005-1832-x. URL http://link.springer.com/10.1007/s00259-005-1832-x.

J. Chapman, J. Hugg, J. Vesel, C. Bai, I. Blevis, H. Barrett, J. Chen, M. Friedman, D. Fuchs, B. Hasegawa, B. Knoop, T. Lewellen, M. Madsen, M. O'Conner, J. Patton, B. Tsui, T. Turkington, and J. Wiener.

National Electrical Manufacturers Association. NEMA NU 1. Performance measurement of scintillation cameras. Technical report, The National Electrical Manufacturers Association, Rosslyn, VA., 2007. URL http://www.nema.org/standards/Pages/Performance-Measurements-of-Gamma-Cameras.aspx.

S.Y.F. Chu, L.P. Ekström, and R.B. Firestone. *Table of Radioactive Isotopes, Version 2.0, TORI Data.* 1999. URL http://nucleardata.nuclear.lu.se/toi/.

P. Conde, A.J. Gonzalez, A. Gonzalez, L. Hernandez, P. Bellido, E. Crespo, A. Iborra, L. Moliner, J.P. Rigla, M.J. Rodriguez-Alvarez, F. Sanchez, M. Seimetz, A. Soriano, L.F. Vidal, and J.M. Benlloch. Analysis of the Statistical Moments of the Scintillation Light Distribution With dSiPMs. *IEEE Transactions on Nuclear Science*, 62(5):1981–1988, October 2015. ISSN 0018-9499, 1558-1578. doi: 10.1109/TNS.2015.2473695. URL http://ieeexplore.ieee.org/document/7283674/.

G.A. de Vree, A.H. Westra, I. Moody, F. van der Have, K.M. Ligtvoet, and F.J. Beekman. Photon-counting gamma camera based on an electron-multiplying CCD. *IEEE Transactions on Nuclear Science*, 52(3):580–588, June 2005. ISSN 0018-9499. doi: 10.1109/TNS.2005.851443. URL http://ieeexplore.ieee.org/document/1487686/.

S. E. Derenzo, M. J. Weber, E. Bourret-courchesne, and M. K. Klintenberg. The Quest for the Ideal Inorganic Scintillator. *Nuclear Instruments and Methods in Physics Research Section A: Accelerators, Spectrometers, Detectors and Associated Equipment*, 2002:1–8, 2002.

R. Devanathan, L.R. Corrales, F. Gao, and W.J. Weber. Signal variance in gamma-ray detectors—A review. *Nuclear Instruments and Methods in Physics Research Section A: Accelerators, Spectrometers, Detectors and Associated*

Equipment, 565(2):637–649, September 2006. ISSN 01689002. doi: 10.1016/j.nima.2006.05.085. URL http://linkinghub.elsevier.com/retrieve/pii/S0168900206009089.

H.B. Dietrich and R.B. Murray. Kinetics of the diffusion of self-trapped holes in alkali halide scintillators. *Journal of Luminescence*, 5(3):155–170, July 1972. ISSN 00222313. doi: 10.1016/0022-2313(72)90039-7. URL https://linkinghub.elsevier.com/retrieve/pii/0022231372900397.

N. Dinu, T. A. Imando, A. Nagai, L. Pinot, V. Puill, S. Callier, B. Janvier, C. Esnault, M-A. Verdier, L. Raux, V. Vandenbussche, Y. Charon, and L. Menard. SiPM arrays and miniaturized readout electronics for compact gamma camera. *Nuclear Instruments and Methods in Physics Research Section A: Accelerators, Spectrometers, Detectors and Associated Equipment*, 787:367–372, July 2015. ISSN 01689002. doi: 10.1016/j.nima.2015.01.083. URL http://linkinghub.elsevier.com/retrieve/pii/S0168900215001230.

M. Dondi, S. Palm, E. Busemann Sokole, R.Z. Stodilka, A.V. Wegst, and R.E. Zimmerman. Quality Assurance for SPECT Systems. In *IAEA Human Health Series*, number 6, pages 1–263. IAEA, Vienna, 2009. ISBN 978 92 0 103709 1. URL http://www.iaea.org/Publications/index.html.

Y. Dong, W. Wang, D. Lei, X. Gong, Q. Zhou, S. Y. Lee, W.K. Loke, S-F. Yoon, E. S Tok, G. Liang, and Y-C. Yeo. Suppression of dark current in germanium-tin on silicon p-i-n photodiode by a silicon surface passivation technique. *Optics Express*, 23(14):18611, July 2015. ISSN 1094-4087. doi: 10.1364/OE.23.018611. URL https://www.osapublishing.org/abstract.cfm?URI=oe-23-14-18611.

P. Dorenbos, J.T.M. de Haas, C.W.E. Van Eijk, C.L. Melcher, and J.S.

Schweitzer. Non-linear response in the scintillation yield of Lu2SiOs:Ce3+. *IEEE Transactions on Nuclear Science*, 41(4):735–737, 1994.

P. Dorenbos, J.T.M. de Haas, and C.W.E. Van Eijk. Non-proportionality in the scintillation response and the energy resolution obtainable with scintillation crystals.. *IEEE Transactions on Nuclear Science*, 42(6):2190–2202, 1995. doi: 10.1109/23.489415.

J. Duch. Portable gamma cameras: the real value of an additional view in the operating theatre. *European Journal of Nuclear Medicine and Molecular Imaging*, 38(4):633–635, April 2011. ISSN 1619-7070, 1619-7089. doi: 10.1007/s00259-011-1761-9. URL http://link.springer.com/10.1007/s00259-011-1761-9.

C. Dujardin, E. Auffray, E. Bourret-Courchesne, P. Dorenbos, P. Lecoq, M. Nikl, A. N. Vasil'ev, A. Yoshikawa, and R.-Y. Zhu. Needs, Trends, and Advances in Inorganic Scintillators. *IEEE Transactions on Nuclear Science*, 65(8):1977–1997, August 2018. ISSN 0018-9499, 1558-1578. doi: 10.1109/TNS.2018.2840160. URL https://ieeexplore.ieee.org/document/8364630/.

e2vTechnologies. CCD97 00 Back Illuminated 2 Phase IMO Series Electron Multiplying CCD Sensor. Technical report, e2vTechnologies Limited, 2004.

EURATOM. *EURATOM regarding the health protection of individuals against the damages of ionizing radiation in relation to medical exposure.* 1997. URL http://www.eur-lex.europa.eu.

A. Ferretti, S. Chondrogiannis, A. Marcolongo, and D. Rubello. Phantom study of a new hand-held gamma-imaging probe for radio-guided surgery. *Nuclear Medicine Communications*, 34(1):86–90, January 2013. ISSN 0143-3636. doi: 10.1097/MNM.0b013e32835a7ccd.

URL http://content.wkhealth.com/linkback/openurl?sid=WKPTLP:landingpage&an=00006231-201301000-00014.

R.W. Fink, R.C. Jopson, and C.D. Swift. Atomic fluorescence yields. *Reviews of Modern Physics*, 38:513–540, 1996.

M.P. Fioratti and S.R. Piermattei. Calculation of the Escape Peak for Ge-Li and NaI Radiation Detectors. *Nuclear Instruments and Methods*, 96:605–608, 1971.

R.A. Forster, L.J. Cox, R.F. Barrett, T.E. Booth, J.F. Briesmeister, F.B. Brown, J.S. Bull, G.C. Geisler, J.T. Goorley, R.D. Mosteller, S.E. Post, R.E. Prael, E.C. Selcow, and A. Sood. MCNP™ Version 5. *Nuclear Instruments and Methods in Physics Research Section B: Beam Interactions with Materials and Atoms*, 213:82–86, January 2004. ISSN 0168583X. doi: 10.1016/S0168-583X(03)01538-6. URL http://linkinghub.elsevier.com/retrieve/pii/S0168583X03015386.

M. Freed, S. Miller, K. Tang, and A. Badano. Experimental validation of Monte Carlo (MANTIS) simulated x-ray response of columnar CsI scintillator screens. *Medical Physics*, 36(11):4944–4956, October 2009. ISSN 00942405. doi: 10.1118/1.3233683. URL http://doi.wiley.com/10.1118/1.3233683.

O. Gal, M. Gmar, O.P. Ivanov, F. Lainé, F. Lamadie, C. Le Goaller, C. Mahé, E. Manach, and V.E. Stepanov. Development of a portable gamma camera with coded aperture. *Nuclear Instruments and Methods in Physics Research Section A: Accelerators, Spectrometers, Detectors and Associated Equipment*, 563(1):233–237, July 2006. ISSN 01689002. doi: 10.1016/j.nima.2006.01.119. URL http://linkinghub.elsevier.com/retrieve/pii/S0168900206002038.

M. Galasso, C. Borrazzo, and A. Fabbri. A scintillation light radial distribution model for monolithic crystal gamma cameras. *Nuclear Instruments and Methods in Physics Research Section A: Accelerators, Spectrometers,* *Detectors and Associated Equipment*, 786:40–46, June 2015. ISSN 01689002. doi: 10.1016/j.nima.2015.03.035. URL http://linkinghub.elsevier.com/retrieve/pii/S0168900215003514.

F. Garibaldi, E. Cisbani, S. Colilli, F. Cusanno, F. Giuliani, M. Gricia, M. Lucentini, L. Pierangeli, F. Santavenere, G.M. Urciuoli, R. Pani, R. Pellegrini, M.N. Cinti, and R. Scafe. Scintillator and photodetector array optimization for functional breast imaging. *Nuclear Instruments and Methods in Physics Research Section A: Accelerators, Spectrometers, Detectors and Associated Equipment*, 497(1):51–59, January 2003. ISSN 01689002. doi: 10.1016/S0168-9002(02)01892-2. URL https://linkinghub.elsevier.com/retrieve/pii/S0168900202018922.

GEANT4 Collaboration - G4Applications. GEANT4 User's Guide for Application Developers. Technical report, GEANT4 Collaboration, 2018. URL https://geant4.web.cern.ch/support/userdocumentation.

GEANT4 Collaboration - G4Physics. Physics Reference Manual. Technical report, GEANT4 Collaboration, 2018. URL https://geant4.web.cern.ch/support/userdocumentation.

D. Ghosh, N.V. Michalopoulos, T. Davidson, F. Wickham, N.R. Williams, and M.R. Keshtgar. Sentinel node detection in early breast cancer with intraoperative portable gamma camera: UK experience. *The Breast*, 32:53–59, April 2017. ISSN 09609776. doi: 10.1016/j.breast.2016.12.013. URL http://linkinghub.elsevier.com/retrieve/pii/S0960977616302806.

J.T. Goorley, M.R. James, T.E. Booth, J.S. Bull, L.J. Cox, J.W. Jr. Durkee, J.S. Elson, M.L. Fensin, R.A. III Forster, J.S. Hendricks, H. G. III Hughes, R.C. Johns, B.C. Kiedrowski, R.L. Martz, S. Mashnik, G.W. McKinney, D.B. Pelowitz, R.E. Prael, J.E. Sweezy, L.S. Waters, T. Wilcox, and A.J. Zukaitis.

Initial MCNP6 Release Overview - MCNP6 version 1.0. Technical Report LA-UR-13-22934, 1086758, Los Alamos, Los Alamos National Laboratory, June 2013. URL `http://www.osti.gov/servlets/purl/1086758/`.

C. Greskovich and S. Duclos. Ceramic Scintillators. *Annual Review of Materials Science*, 27(1):69–88, August 1997. ISSN 0084-6600. doi: 10.1146/annurev.matsci.27.1.69. URL `http://www.annualreviews.org/doi/10.1146/annurev.matsci.27.1.69`.

P. Gumplinger. Optical Photon Processes in GEANT4. In *TRIUMF/GEANT4 Users' Workshop*, page 25, Stanford Linear Accelerator Center, 2002.

Hamamatsu. X-ray Scintillator ACS. Hamamatsu, Japan, 2016. URL `www.hamamatsu.com`.

Hamamatsu-Photonics. Silicon Photodiodes - Emission spectrum of CsI(Tl) scintillator and spectral response. page 28. Hamamatsu, Japan, cspd0001e13 edition, April 2019. URL `https://www.hamamatsu.com/resources/pdf/ssd/e09handbookxraydetectors.pdf`.

G. Hansford. Internal Users Guide to the CCD Data Analysis Program. Technical report, University of Leicester, 2006.

Frans van der Have and Freek J Beekman. Photon penetration and scatter in micro-pinhole imaging: a Monte Carlo investigation. *Physics in Medicine and Biology*, 49(8):1369–1386, April 2004. ISSN 0031-9155, 1361-6560. doi: 10.1088/0031-9155/49/8/001. URL `http://stacks.iop.org/0031-9155/49/i=8/a=001?key=crossref.d3b2adf892a4b099a7024a928ac49701`.

H. Hayashi, T. Ochiai, M. Mori, T. Karube, T. Suzuki, Y. Gunji, S. Hori, N. Akutsu, H. Matsubara, and H. Shimada. Sentinel lymph node mapping for gastric cancer using a dual procedure with dye- and gamma probe-guided techniques. *Journal of the American College of Surgeons*, 196(1):68–74, January 2003. ISSN 10727515. doi: 10.1016/S1072-7515(02)01594-6. URL `http://linkinghub.elsevier.com/retrieve/pii/S1072751502015946`.

J.W.T. Heemskerk, A.H. Westra, P.M. Linotte, K.M. Ligtvoet, W. Zbijewski, and F.J. Beekman. Front-illuminated versus back-illuminated photon-counting CCD-based gamma camera: important consequences for spatial resolution and energy resolution. *Physics in Medicine and Biology*, 52(8):N149–N162, April 2007. ISSN 0031-9155, 1361-6560. doi: 10.1088/0031-9155/52/8/N01. URL `http://stacks.iop.org/0031-9155/52/i=8/a=N01?key=crossref.bf64f91987ebb164922f07c5734d2ecd`.

K.F.J. Heinrich. The Electron Microprobe. *Berichte der Bunsen-Gesellschaft für physikalische Chemie.*, 70(8):933, 1966. ISSN 0005-9021. doi: 10.1002/bbpc.19660700842.

S. Heller and P. Zanzonico. Nuclear Probes and Intraoperative Gamma Cameras. *Seminars in Nuclear Medicine*, 41(3):166–181, May 2011. ISSN 00012998. doi: 10.1053/j.semnuclmed.2010.12.004. URL `http://linkinghub.elsevier.com/retrieve/pii/S0001299810001613`.

H. Hirayama, Y. Namito, A.F. Bielajew, S.J. Wilderman, and W.R. Nelson. The EGS5 Code System. Technical Report SLAC-R-730, 877459, Stanford Linear Accelerator Center, January 2016. URL `http://www.osti.gov/servlets/purl/877459-sHotCs/`.

G.R. Hopkinson. Analytic Modelling of Charge Diffusion in Charge-Coupled-Device Imagers. *Optical Engineering*, 26(8):767, 1987.

R.T. Howe and C.G. Sodini. Microelectronics: an Integrated Approach. Prentice Hall, 1997.

C.B. Hruska, M.K. O'Connor, and D.A. Collins. Comparison of small field of view gamma camera systems for scintimammography. *Nuclear Medicine Communications*, 26(5):441–445, May 2005. ISSN 0143-3636. doi: 10.1097/00006231-200505000-00008. URL https://insights.ovid.com/crossref?an=00006231-200505000-00008.

J H Hubbell, D E Cullen, and Kissel L. EPDL97 : The Evaluated Photon Data Library , 1997 Version. Technical report, Livermore, 1997.

IEC60789-Subcommittee:62C. *International Electrotechnical Commission. IEC 60789. Medical electrical equipment. Characteristics and test conditions of radionuclide imaging devices Anger type gamma cameras.* International Electrotechnical Commission., Geneva, 2005. ISBN 0 580 47176 4. URL https://webstore.iec.ch/publication/3441.

J.E. Inglesfield. Surface electronic structure. *Reports on Progress in Physics*, 45: 223, 1982. ISSN 0034-4885. doi: 10.1088/0034-4885/45/3/001.

Intramedical. *Node Seeker.* URL https://www.intramedicalimaging.com/node-seeker.html.

S. Jan, G. Santin, D. Strul, S. Staelens, K. Assié, D. Autret, S. Avner, R. Barbier, M. Bardiès, P.M. Bloomfield, D. Brasse, V. Breton, P. Bruyndonckx, I. Buvat, A.F. Chatziioannou, Y. Choi, Y.H. Chung, M.C. Comtat, D. Donnarieix, L. Ferrer, S.J. Glick, C.J. Groiselle, D. Guez, P-F. Honore, S. Kerhoas-Cavata, A.S. Kirov, V. Kohli, M. Koole, M. Krieguer, D.J. van der Laan, F. Lamare, G. Largeron, C. Lartizien, D. Lazaro, M.C. Maas, L. Maigne, F. Mayet, F. Melot, C. Merheb, E. Pennacchio, J. Perez, U. Pietrzyk, F.R. Rannou, M. Rey, D.R. Schaart, C.R. Schmidtlein, L. Simon, T.Y. Song, J-M. Vieira, D. Visvikis, R. van de Walle, E. Wieërs, and C. Morel. GATE: a simulation toolkit for PET and SPECT. *Physics in Medicine and Biology*, 49(19):4543–

4561, October 2004. ISSN 0031-9155, 1361-6560. doi: 10.1088/0031-9155/49/19/007. URL http://stacks.iop.org/0031-9155/49/i=19/a=007?key=crossref.be1d0bbaf1d502515584e510c77393cb.

M. Janecek. Reflectivity Spectra for Commonly Used Reflectors. *IEEE Transactions on Nuclear Science*, 59(3):490–497, June 2012. ISSN 0018-9499, 1558-1578. doi: 10.1109/TNS.2012.2183385. URL http://ieeexplore.ieee.org/document/6168236/.

S. Kerisit, K.M. Rosso, and B.D. Cannon. Kinetic Monte Carlo Model of Scintillation Mechanisms in CsI and CsI(Tl). *IEEE Transactions on Nuclear Science*, 55(3):1251–1258, June 2008. ISSN 0018-9499. doi: 10.1109/TNS.2008.922830. URL http://ieeexplore.ieee.org/document/4545140/.

A. Khadjavi. Calculation of Solid Angle Subtended by Rectangular Apertures. *Journal of the Optical Society of America*, 58(10):1417–1418, 1968. doi: https://doi.org/10.1364/JOSA.58.001417.

I.V. Khodyuk, P.A. Rodnyi, and P. Dorenbos. Nonproportional scintillation response of NaI:Tl to low energy x-ray photons and electrons. *Journal of Applied Physics*, 107(11):113513, June 2010. ISSN 0021-8979, 1089-7550. doi: 10.1063/1.3431009. URL http://aip.scitation.org/doi/10.1063/1.3431009.

D. Kieper, S. Majewski, B. Kross, V. Popov, A.G. Weisenberger, B. Welch, R. Wojcik, M.B. Williams, A.R. Goode, M. More, and G. Zhang. Optimization of breast imaging procedure with dedicated compact gamma cameras. *Nuclear Instruments and Methods in Physics Research Section A: Accelerators, Spectrometers, Detectors and Associated Equipment*, 497(1):168–173, January 2003. ISSN 01689002. doi: 10.1016/S0168-9002(02)01907-1. URL http://linkinghub.elsevier.com/retrieve/pii/S0168900202019071.

A. Knyazev, J. Park, P. Golubev, J. Cederkäll, H. Alvarez-Pol, P. Cabanelas, E. Casarejos, L. Causeret, D. Cortina-Gil, P. Díaz Fernández, M. Feijoo, D. Galaviz, E. Galiana, R. Gernhäuser, A.-L. Hartig, A. Heinz, B. Heiss, A. Ignatov, H. Johansson, P. Klenze, T. Kröll, T. Nilsson, A. Perea, H.-B. Rhee, O. Tengblad, and P. Teubig. Properties of the CsI(Tl) detector elements of the CALIFA detector. *Nuclear Instruments and Methods in Physics Research Section A: Accelerators, Spectrometers, Detectors and Associated Equipment*, 940:393–404, October 2019. ISSN 01689002. doi: 10.1016/j.nima.2019.06.045. URL `https://linkinghub.elsevier.com/retrieve/pii/S0168900219308903`.

M. Kotzassarlidou, B. Hatzipavlidou, A. Makridou, P. Kostaki, and N. Salem. Practical considerations in selecting and using intraoperative gamma probes. *Nuclear Instruments and Methods in Physics Research Section A: Accelerators, Spectrometers, Detectors and Associated Equipment*, 527(1-2):110–112, July 2004. ISSN 01689002. doi: 10.1016/j.nima.2004.03.085. URL `http://linkinghub.elsevier.com/retrieve/pii/S0168900204004541`.

K.S. Krane. *Introductory Nuclear Physics.* John Wiley and Sons, 1988. ISBN 0-471-85914-1.

P. Lecoq. Development of new scintillators for medical applications. *Nuclear Instruments and Methods in Physics Research Section A: Accelerators, Spectrometers, Detectors and Associated Equipment*, 809:130–139, February 2016. ISSN 01689002. doi: 10.1016/j.nima.2015.08.041. URL `http://linkinghub.elsevier.com/retrieve/pii/S0168900215009754`.

J.E. Lees. Spectroscopic model for SiC X-ray detectors. *Nuclear Instruments and Methods in Physics Research Section A: Accelerators, Spectrometers, Detectors and Associated Equipment*, 613(1):98–105, January 2010. ISSN 01689002.

doi: 10.1016/j.nima.2009.11.037. URL `http://linkinghub.elsevier.com/retrieve/pii/S0168900209022177`.

J.E. Lees, D.J. Bassford, P.E. Blackshaw, and A.C. Perkins. Design and use of mini-phantoms for high resolution planar gamma cameras. *Applied Radiation and Isotopes*, 68(12):2448–2451, December 2010. ISSN 09698043. doi: 10.1016/j.apradiso.2010.06.005. URL `http://linkinghub.elsevier.com/retrieve/pii/S0969804310002411`.

J.E. Lees, D.J. Bassford, O.E. Blake, P.E. Blackshaw, and A.C. Perkins. A high resolution Small Field Of View (SFOV) gamma camera: a columnar scintillator coated CCD imager for medical applications. *Journal of Instrumentation*, 6(12):C12033–C12033, December 2011. ISSN 1748-0221. doi: 10.1088/1748-0221/6/12/C12033. URL `http://stacks.iop.org/1748-0221/6/i=12/a=C12033?key=crossref.75b9f0a9a843fb7f5fabc70e55f8f8eb`.

C.S. Levin. Detector design issues for compact nuclear emission cameras dedicated to breast imaging. *Nuclear Instruments and Methods in Physics Research Section A: Accelerators, Spectrometers, Detectors and Associated Equipment*, 497(1):60–74, January 2003. ISSN 01689002. doi: 10.1016/S0168-9002(02)01893-4. URL `http://linkinghub.elsevier.com/retrieve/pii/S0168900202018934`.

M. Ljungberg. *The SIMIND Monte Carlo Program.* December 2017. ISBN 978-1-4398-4109-9 978-1-4398-4110-5. doi: 10.1201/b13073-8. URL `http://www.crcnetbase.com/doi/abs/10.1201/b13073-8`.

A. Lombardi, G. Nigri, F. Scopinaro, S. Maggi, M. Mattei, A. Bonifacino, M. Parisella, A. Soluri, and C. Amanti. High-resolution, handheld camera use for occult breast lesion localization plus sentinel node biopsy (SNOLL): A single-institution experience with 186 patients. *The Surgeon*, 13(2):69–

72, April 2015. ISSN 1479666X. doi: 10.1016/j.surge.2013.10.005. URL http://linkinghub.elsevier.com/retrieve/pii/S1479666X1300125X.

M. Lowdon, P.G. Martin, M.W.J. Hubbard, M.P. Taggart, Dean T. Connor, Y. Verbelen, P.J. Sellin, and T.B. Scott. Evaluation of Scintillator Detection Materials for Application within Airborne Environmental Radiation Monitoring. *Sensors*, 19(18):3828, September 2019. ISSN 1424-8220. doi: 10.3390/s19183828. URL https://www.mdpi.com/1424-8220/19/18/3828.

Mammotome. *Neoprobe.* URL http://www.mammotome.com/neoprobe/.

R. Massari, A. Ucci, C. Campisi, F. Scopinaro, and A. Soluri. A novel fully integrated handheld gamma camera. *Nuclear Instruments and Methods in Physics Research Section A: Accelerators, Spectrometers, Detectors and Associated Equipment*, 832:271–278, October 2016. ISSN 01689002. doi: 10.1016/j.nima.2016.06.124. URL http://linkinghub.elsevier.com/retrieve/pii/S0168900216306945.

K.J. McCarthy, A. Owens, A.D. Holland, and A.A. Wells. Modelling the X-ray response of charge coupled devices. *Nuclear Instruments and Methods in Physics Research Section A: Accelerators, Spectrometers, Detectors and Associated Equipment*, 362(2-3):538–546, August 1995. ISSN 01689002. doi: 10.1016/0168-9002(95)00376-2. URL http://linkinghub.elsevier.com/retrieve/pii/0168900295003762.

L. Menard, Y. Charon, M. Ricard, and L. Valentin. POCI: A Compact High Resolution gamma Camera for Intra-Operative Surgical Use. *IEEE Transactions on Nuclear Science*, 45(3 Part 2):1293–1297, 1998.

S.D. Metzler, J.E. Bowsher, M.F. Smith, and R.J. Jaszczak. Analytic determination of pinhole collimator sensitivity with penetration. *IEEE*

Transactions on Medical Imaging, 20(8):730–741, 2001. doi: 10.1109/42.938241.

W.E. Meyerhof. *Elements of Nuclear Physics.* McGraw-Hill, New York, 1967. ISBN ISBN 10: 0070417458 ISBN 13: 9780070417458.

N. Nelms, D.F. Anagnostopoulos, O. Ayranov, G. Borchert, J-P. Egger, D. Gotta, M. Hennebach, P. Indelicato, B. Leoni, Y.W. Liu, B. Manil, L.M. Simons, and A. Wells. A large area CCD X-ray detector for exotic atom spectroscopy. *Nuclear Instruments and Methods in Physics Research Section A: Accelerators, Spectrometers, Detectors and Associated Equipment*, 484(1-3):419–431, May 2002. ISSN 01689002. doi: 10.1016/S0168-9002(01)02051-4. URL `http://linkinghub.elsevier.com/retrieve/pii/S0168900201020514`.

M. Nikl, P. Bohacek, E. Mihokova, S. Baccaro, A. Vedda, M. Diemoz, E. Longo, M. Kobayashi, E. Auffray, and P. Lecoq. Radiation damage processes in wide-gap scintillating crystals. New scintillation materials. *Nuclear Physics B - Proceedings Supplements*, 78(1-3):471–478, August 1999. ISSN 09205632. doi: 10.1016/S0920-5632(99)00589-7. URL `http://linkinghub.elsevier.com/retrieve/pii/S0920563299005897`.

M. Nikl, A. Yoshikawa, A. Vedda, and T. Fukuda. Development of novel scintillator crystals. *Journal of Crystal Growth*, 292(2):416–421, July 2006. ISSN 00220248. doi: 10.1016/j.jcrysgro.2006.04.048. URL `http://linkinghub.elsevier.com/retrieve/pii/S0022024806003472`.

H-E Nilsson, E Dubarić, M Hjelm, and K Bertilsson. Simulation of photon and charge transport in X-ray imaging semiconductor sensors. *Nuclear Instruments and Methods in Physics Research Section A: Accelerators, Spectrometers, Detectors and Associated Equipment*, 487(1-2):151–162, July 2002. ISSN

01689002. doi: 10.1016/S0168-9002(02)00959-2. URL http://linkinghub.elsevier.com/retrieve/pii/S0168900202009592.

P. Olcott, G. Pratx, D. Johnson, E. Mittra, R. Niederkohr, and C.S. Levin. Clinical evaluation of a novel intraoperative handheld gamma camera for sentinel lymph node biopsy. *Physica Medica*, 30(3):340–345, May 2014. ISSN 11201797. doi: 10.1016/j.ejmp.2013.10.005. URL http://linkinghub.elsevier.com/retrieve/pii/S1120179713004262.

J. Ortega, J. Ferrer-Rebolleda, N. Cassinello, and S. Lledo. Potential role of a new hand-held miniature gamma camera in performing minimally invasive parathyroidectomy. *European Journal of Nuclear Medicine and Molecular Imaging*, 34(2):165–169, February 2007a. ISSN 1619-7070, 1619-7089. doi: 10.1007/s00259-006-0239-7. URL http://link.springer.com/10.1007/s00259-006-0239-7.

J. Ortega, J. Ferrer-Rebolleda, N. Cassinello, and S. Lledo. Short communication. Potential role of a new hand-held miniature gamma camera in performing minimally invasive parathyroidectomy. *European Journal of Nuclear Medicine and Molecular Imaging*, 34:165–169, 2007b. doi: 10.1007/s00259-006-0239-7.

A. Owens, T. Mineo, K.J. McCarthy, and A. Wells. Event recognition in X-ray CCDs. *Nuclear Instruments and Methods in Physics Research Section A: Accelerators, Spectrometers, Detectors and Associated Equipment*, 346(1-2): 353–365, July 1994. ISSN 01689002. doi: 10.1016/0168-9002(94)90723-4. URL http://linkinghub.elsevier.com/retrieve/pii/0168900294907234.

A. Owens, G.W.E. Fraser, A.F. Abbey, A. Holland, . McCarthy, A. Keay, and A. Wells. The X-ray energy response of silicon (B): Measurements. *Nuclear Instruments and Methods in Physics Research Section A: Accelerators, Spectrometers, Detectors and Associated Equipment*, 382(3):503–510, November 1996. ISSN 01689002. doi: 10.1016/S0168-9002(96)00822-4. URL http://linkinghub.elsevier.com/retrieve/pii/S0168900296008224.

S.P. Pederson, R.A. Forster, and T.E. Booth. Confidence Interval Procedures for Monte Carlo Transport Simulations. *Nuclear Science and Engineering*, 127(1):54–77, September 1997. ISSN 0029-5639, 1943-748X. doi: 10.13182/NSE97-A1921. URL https://www.tandfonline.com/doi/full/10.13182/NSE97-A1921.

A.C. Perkins and J.G. Hardy. Intra-operative nuclear medicine in surgical practice. *Nuclear Medicine Communications*, 17:1006–1015, 1996.

S. Pitre, L. Ménard, M. Ricard, M. Solal, J-R. Garbay, and Y. Charon. A hand-held imaging probe for radio-guided surgery: physical performance and preliminary clinical experience. *European Journal of Nuclear Medicine and Molecular Imaging*, 30(3):339–343, March 2003. ISSN 1619-7070, 1619-7089. doi: 10.1007/s00259-002-1064-2. URL http://link.springer.com/10.1007/s00259-002-1064-2.

A.M. Polemi, J. Niestroy, A. Stolin, G. Jaliparthi, R. Wojcik, S. Majewski, and M.B. Williams. Design and characterization of a low profile NaI(Tl) gamma camera for dedicated molecular breast tomosynthesis. In *Proc. SPIE - Int. Soc. Opt. Eng.*, page 99690O, San Diego, California, United States, August 2016. doi: 10.1117/12.2246561. URL http://proceedings.spiedigitallibrary.org/proceeding.aspx?doi=10.1117/12.2246561.

M. Popp, R. Hartmann, H. Soltau, L. Struder, N. Meidinger, P. Holl, N. Krause, and C. van Zanthier. Modeling the energy response of pn-CCDs in the 0.2 - 10 keV band. *Nuclear Instruments and Methods in Physics Research Section*

A: Accelerators, Spectrometers, Detectors and Associated Equipment, 439:567–574, 2000.

E. Porras, B. Escat, J.M. Benlloch, D. Kadi-Hanifi, S. López, N. Pavón, J.A. Ruiz, F. Sánchez, and A. Sebastià. Portable mini gamma camera for medical applications. *Nuclear Instruments and Methods in Physics Research Section A: Accelerators, Spectrometers, Detectors and Associated Equipment*, 486(1-2):186–190, June 2002. ISSN 01689002. doi: 10.1016/S0168-9002(02)00700-3. URL `http://linkinghub.elsevier.com/retrieve/pii/S0168900202007003`.

S.R. Povoski, R.L. Neff, C.M. Mojzisik, D.M. O'Malley, G.H. Hinkle, N.C. Hall, D.A. Murrey, M.V. Knopp, and E.W. Martin. A comprehensive overview of radioguided surgery using gamma detection probe technology. *World Journal of Surgical Oncology*, 7(1):11, 2009. ISSN 1477-7819. doi: 10.1186/1477-7819-7-11. URL `http://wjso.biomedcentral.com/articles/10.1186/1477-7819-7-11`.

S.J.B. Reed and N.G. Ware. Escape peaks and internal fluorescence in X-ray spectra recorded with lithium drifted silicon detectors. *Journal of Physics E: Scientific Instruments*, 5(6):582–583, June 1972. ISSN 0022-3735. doi: 10.1088/0022-3735/5/6/029. URL `http://stacks.iop.org/0022-3735/5/i=6/a=029?key=crossref.4a915ba44b514adb1b12e06330db5926`.

L. Riccardi, M. Gabusi, M. Bignotto, M. Gregianin, A. Vecchiato, and M. Paiusco. Assessing good operating conditions for intraoperative imaging of melanoma sentinel nodes by a portable gamma camera. *Physica Medica*, 31(1):92–97, February 2015. ISSN 11201797. doi: 10.1016/j.ejmp.2014.10.079. URL `http://linkinghub.elsevier.com/retrieve/pii/S1120179714006231`.

M.S. Robbins. Electron-Multiplying Charge Coupled Devces -EMCCDs. In

Single-Photon Imaging, number 160 in Springer Series in Optical Sciences, pages 103–121. Springer-Verlag, Berlin, 2011. ISBN 978-3-642-18442-0.

M.S. Robbins and B.J. Hadwen. The noise performance of electron multiplying charge-coupled devices. *IEEE Transactions on Electron Devices*, 50(5):1227–1232, May 2003. ISSN 0018-9383. doi: 10.1109/TED.2003.813462. URL http://ieeexplore.ieee.org/document/1210766/.

E. Roncali, M. Mosleh-Shirazi, and A. Badano. Modelling the transport of optical photons in scintillation detectors for diagnostic and radiotherapy imaging. *Physics in Medicine and Biology*, 62(20):R207–R235, October 2017. ISSN 1361-6560. doi: 10.1088/1361-6560/aa8b31. URL http://stacks.iop.org/0031-9155/62/i=20/a=R207?key=crossref.6909faa0cc8b25b0e36de4d9be42e07a.

R. Ruano, M. Ramos, J.R. Garcia-Talavera, E. Serrano, A. de Arriba, J. Gonzalez-Orus, M. Iglesias, and M.C. Macias. Staging the Axilla with selective sentinel node biopsy in patients with previous excision of non-palpable and palpable breast cancer. *European Journal of Nuclear Medicine and Molecular Imaging*, 35:1299–1304, 2008. doi: 10.1007/s00259-008-0730-4.

D. Rubello and G. Mariani. Hand-held gamma probe or hand-held miniature gamma camera for minimally invasive parathyroidectomy: competition, evolution or synergy? *European Journal of Nuclear Medicine and Molecular Imaging*, 34(2):162–164, February 2007. ISSN 1619-7070, 1619-7089. doi: 10.1007/s00259-006-0250-z. URL http://link.springer.com/10.1007/s00259-006-0250-z.

D. Rubello, M.D. Gross, G. Mariani, and A. AL-Nahhas. Scintigraphic techniques in primary hyperparathyroidism: from pre-operative localisation to intra-operative imaging. *European Journal of Nuclear Medicine and*

Molecular Imaging, 34(6):926–933, May 2007. ISSN 1619-7070, 1619-7089. doi: 10.1007/s00259-007-0388-3. URL http://link.springer.com/10.1007/s00259-007-0388-3.

F. Salvat. The PENELOPE code system. Specific features and recent improvements. *Annals of Nuclear Energy*, 2015. ISSN 18732100. URL 10.1016/j.anucene.2014.08.007.

F. Salvat, J.M. Fernández-Varea, and J. Sempau. PENELOPE-2011 A Code System for Monte Carlo Simulation of Electron and Photon Transport. Technical report, NUCLEAR ENERGY AGENCY Organisation for Economic Co-operation and Development, 2011.

F. Sánchez, J.M. Benlloch, B. Escat, N. Pavón, E. Porras, D. Kadi-Hanifi, J.A. Ruiz, F.J. Mora, and A. Sebastià. Design and tests of a portable mini gamma camera. *Medical Physics*, 31(6):1384–1397, May 2004. ISSN 00942405. doi: 10.1118/1.1755570. URL http://doi.wiley.com/10.1118/1.1755570.

F. Sánchez, M.M. Fernández, M. Giménez, J.M. Benlloch, M.J. Rodriguez-Alvarez, F. Garcia de Quirós, C.W. Lerche, N. Pavón, and J.A. Palazón. Performance tests of two portable mini gamma cameras for medical applications. *Medical Physics*, 33(11):4210–4220, 2006.

M. Sanchez del Rio, A. Brunetti, B. Golosio, A. Somogyi, and A. Simionovici. XRAYLIB tables (X-ray fluorescence cross-section). Technical report, European Synchrotron Radiation Facility and University of Sassari, 2003.

D. Schilling, U. Boekeler, G. Gakis, C. Schwentner, S. Corvin, K. Sotlar, A-C. Müller, R. Bares, and A. Stenzl. Modified concept for radioisotope-guided sentinel lymph node dissection in prostate cancer. *World Journal of Urology*, 28(6):715–720, December 2010. ISSN 0724-4983, 1433-8726.

doi: 10.1007/s00345-010-0533-7. URL `http://link.springer.com/10.1007/s00345-010-0533-7`.

J.W. Scuffham, M.D. Wilson, P. Seller, M.C. Veale, P.J. Sellin, S.D.M. Jacques, and R.J. Cernik. A CdTe detector for hyperspectral SPECT imaging. *Journal of Instrumentation*, 7(08):P08027–P08027, August 2012. ISSN 1748-0221. doi: 10.1088/1748-0221/7/08/P08027. URL `http://stacks.iop.org/1748-0221/7/i=08/a=P08027?key=crossref.f9234478a32e47b5f751dd13fcb094ae`.

C.E. Shannon. Communication in the Presence of Noise. *Proceedings of the IEEE*, 86(2):11, 1998.

D. Sharma and A. Badano. Validation of columnar CsI x-ray detector responses obtained with hybridMANTIS, a CPU-GPU Monte Carlo code for coupled x-ray, electron, and optical transport. *Medical Physics*, 40(3):031907, February 2013. ISSN 00942405. doi: 10.1118/1.4791642. URL `http://doi.wiley.com/10.1118/1.4791642`.

D. Sharma, A. Badal, and A. Badano. hybridMANTIS: a CPU-GPU Monte Carlo method for modeling indirect x-ray detectors with columnar scintillators. *Physics in Medicine and Biology*, 57(8):2357–2372, April 2012. ISSN 0031-9155, 1361-6560. doi: 10.1088/0031-9155/57/8/2357. URL `http://stacks.iop.org/0031-9155/57/i=8/a=2357?key=crossref.7b8b7c4870b7feaaa99b7240f5b1e213`.

S. Shokouhi, S.D. Metzler, D.W. Wilson, and T.E. Peterson. Multi-pinhole collimator design for small-object imaging with SiliSPECT: a high-resolution SPECT. *Physics in Medicine and Biology*, 54(2):207–225, January 2009. ISSN 0031-9155, 1361-6560. doi: 10.1088/0031-9155/54/2/003. URL `http://stacks.iop.org/0031-9155/54/i=2/a=003?key=crossref.f400b70f602ec2427b83427d15aaed09`.

A.D. Short, R.M. Ambrosi, and M.J.L. Turner. Spectral re-distribution and surface loss effects in Swift XRT (XMM-Newton EPIC) MOS CCDs. *Nuclear Instruments and Methods in Physics Research Section A: Accelerators, Spectrometers, Detectors and Associated Equipment*, 484(1-3):211–224, May 2002. ISSN 01689002. doi: 10.1016/S0168-9002(01)02053-8.

H.A. Smith and M. Lucas. Gamma-Ray Detectors. In *Passive Nondestructive Assay Nuclear Materials*, number LA-UR-90-9, page 43064. Los Alamos National Laboratory, 1999. ISBN 0-16-032724-5. URL http://www.lanl.gov/orgs/n/n1/panda/00326398.pdf.

S. Spannagel, K. Wolters, D. Hynds, N. Alipour Tehrani, M. Benoit, D. Dannheim, N. Gauvin, A. Nürnberg, P. Schütze, and M. Vicente. Allpix2: A modular simulation framework for silicon detectors. *Nuclear Instruments and Methods in Physics Research Section A: Accelerators, Spectrometers, Detectors and Associated Equipment*, 901:164–172, September 2018. ISSN 01689002. doi: 10.1016/j.nima.2018.06.020. URL https://linkinghub.elsevier.com/retrieve/pii/S0168900218307411.

S. Staelens, D. Strul, G. Santin, S. Vandenberghe, M. Koole, Y. D Asseler, I. Lemahieu, and R. van de Walle. Monte Carlo simulations of a scintillation camera using GATE: validation and application modelling. *Physics in Medicine and Biology*, 48(18):3021–3042, September 2003. ISSN 0031-9155, 1361-6560. doi: 10.1088/0031-9155/48/18/305. URL http://stacks.iop.org/0031-9155/48/i=18/a=305?key=crossref.4ce6c675424c7763d2d6e25a18f6455c.

M. Stockhoff, S. Jan, A. Dubois, S.R. Cherry, and E. Roncali. Advanced optical simulation of scintillation detectors in GATE V8.0: first implementation of a reflectance model based on measured data. *Physics in Medicine and Biology*, 62(12):L1–L8, June 2017. ISSN 0031-9155, 1361-6560. doi: 10.1088/

1361-6560/aa7007. URL http://stacks.iop.org/0031-9155/62/i=12/a=L1?key=crossref.1f1deba8a23d0f15299a13375ce9d05a.

D. Strul, G. Santin, V. Breton, and C. Morel. GATE (GEANT4 Application for Tomographic general purpose simulation platform Emission): a PET/SPECT genral purpose simulation platform. *Nuclear Physics B - Proceedings Supplements*, 125:75–79, 2003. URL http://opengatecollaboration.healthgrid.org/.

Valerio Tabacchini, Giacomo Borghi, and Dennis R Schaart. Time-based position estimation in monolithic scintillator detectors. *Physics in Medicine and Biology*, 60(14):5513–5525, July 2015. ISSN 0031-9155, 1361-6560. doi: 10.1088/0031-9155/60/14/5513. URL http://stacks.iop.org/0031-9155/60/i=14/a=5513?key=crossref.443f2861ef25ac1ba756a46e50dafddb.

H. Takeuchi, H. Fujii, N. Ando, S. Ozawa, Y. Saikawa, K. Suda, T. Oyama, M. Mukai, T. Nakahara, A. Kubo, M. Kitajima, and Y. Kitagawa. Validation Study of Radio-Guided Sentinel Lymph Node Navigation in Esophageal Cancer. *Annals of Surgery*, 249(5):757–763, May 2009. ISSN 0003-4932. doi: 10.1097/SLA.0b013e3181a38e89. URL https://insights.ovid.com/crossref?an=00000658-200905000-00013.

S.E.J. Terwisscha Van Scheltinga, F.C. Den Boer, R. Pijpers, G.A. Meyer, A.F. Engel, R. Silvis, S. Meijer, and J.R.M. Van Der Sijp. Sentinel node staging in colon carcinoma: Value of sentinel lymph node biopsy with radiocolloid and blue staining. *Scandinavian Journal of Gastroenterology*, 41(sup243):153–157, January 2006. ISSN 0036-5521, 1502-7708. doi: 10.1080/00365520600664524. URL http://www.tandfonline.com/doi/full/10.1080/00365520600664524.

C. Trotta, R. Massari, N. Palermo, F. Scopinaro, and A. Soluri. New high spatial resolution portable camera in medical imaging. *Nuclear Instruments and Methods in Physics Research Section A: Accelerators, Spectrometers, Detectors and Associated Equipment*, 577(3):604–610, July 2007. ISSN 01689002. doi: 10.1016/j.nima.2007.03.037. URL http://linkinghub.elsevier.com/retrieve/pii/S0168900207005268.

M. Tsuchimochi and K. Hayama. Intraoperative gamma cameras for radioguided surgery: Technical characteristics, performance parameters, and clinical applications. *Physica Medica*, 29(2):126–138, March 2013. ISSN 11201797. doi: 10.1016/j.ejmp.2012.05.002. URL http://linkinghub.elsevier.com/retrieve/pii/S1120179712000397.

M. Tsuchimochi, H. Sakahara, K. Hayama, M. Funaki, R. Ohno, T. Shirahata, T. Orskaug, G. Maehlum, K. Yoshioka, and E. Nygard. A prototype small CdTe gamma camera for radioguided surgery and other imaging applications. *European Journal of Nuclear Medicine and Molecular Imaging*, 30(12):1605–1614, December 2003. ISSN 1619-7070, 1619-7089. doi: 10.1007/s00259-003-1301-3. URL http://link.springer.com/10.1007/s00259-003-1301-3.

J.H. Tutt, D.J. Hall, A.D. Holland, N.J. Murray, and J. Endicott. Developing a high-resolution x-ray imager using electron-multiplying (EM) CCDs. In M. Fiederle, A. Burger, L. Franks, and R.B. James, editors, *Hard X-Ray, Gamma-Ray, and Neutron Detector Physics XV*, page 885217, September 2013. doi: 10.1117/12.2023317. URL http://proceedings.spiedigitallibrary.org/proceeding.aspx?doi=10.1117/12.2023317.

A. Valentin, M. Raine, J.-E. Sauvestre, M. Gaillardin, and P. Paillet. Geant4 physics processes for microdosimetry simulation: Very low energy electromagnetic models for electrons in silicon. *Nuclear Instruments and Methods in Physics Research Section B: Beam Interactions with Materials* *and Atoms*, 288:66–73, October 2012. ISSN 0168583X. doi: 10.1016/j.nimb.2012.07.028. URL https://linkinghub.elsevier.com/retrieve/pii/S0168583X12004314.

H.T. van Dam, S. Seifert, W. Drozdowski, P. Dorenbos, and D. R. Schaart. Optical Absorption Length, Scattering Length, and Refractive Index of ${\rm LaBr}_{3}\!\!:\!\!{\rm Ce}^{3+}$. *IEEE Transactions on Nuclear Science*, 59(3):656–664, June 2012. ISSN 0018-9499, 1558-1578. doi: 10.1109/TNS.2012.2193597. URL http://ieeexplore.ieee.org/document/6200009/.

D.J.(Jan) van der Laan, D.R. Schaart, M.C. Maas, F.J. Beekman, P. Bruyndonckx, and C.W.E. van Eijk. Optical simulation of monolithic scintillator detectors using GATE/GEANT4. *Physics in Medicine and Biology*, 55(6):1659–1675, March 2010. ISSN 0031-9155, 1361-6560. doi: 10.1088/0031-9155/55/6/009. URL http://stacks.iop.org/0031-9155/55/i=6/a=009?key=crossref.85a99e5be09f070b21dc8586c2fe5dbc.

C.W.E. van Eijk. Instrumentation for Detection of Radiation. *Radiation Protection Dosimetry*, 77(4):245–252, June 1998. ISSN 0144-8420, 1742-3406. doi: 10.1093/oxfordjournals.rpd.a032319. URL https://academic.oup.com/rpd/article-lookup/doi/10.1093/oxfordjournals.rpd.a032319.

C.W.E. van Eijk. Inorganic-scintillator development. *Nuclear Instruments and Methods in Physics Research Section A: Accelerators, Spectrometers, Detectors and Associated Equipment*, 460(1):1–14, 2001. ISSN 01689002. doi: 10.1016/S0168-9002(00)01088-3.

C.W.E. van Eijk. Inorganic scintillators in medical imaging detectors. *Nuclear Instruments and Methods in Physics Research Section A: Accelerators, Spectrometers, Detectors and Associated Equipment*, 509(1-3):17–25, August

2003. ISSN 01689002. doi: 10.1016/S0168-9002(03)01542-0. URL http://linkinghub.elsevier.com/retrieve/pii/S0168900203015420.

T. Vayrynen, U. Pitkanen, and K. Kiviniitty. Methods for measuring the modulation transfer function of gamma camera systems. *European Journal of Nuclear Medicine*, 5(1):19–22, February 1980. ISSN 0340-6997, 1619-7089. doi: 10.1007/BF00261201. URL http://link.springer.com/10.1007/BF00261201.

M.C. Veale, J. Kalliopuska, H. Pohjonen, H. Andersson, S. Nenonen, P. Seller, and M.D. Wilson. Characterization of M-π-n CdTe pixel detectors coupled to HEXITEC readout chip. *Journal of Instrumentation*, 7(01):C01035–C01035, January 2012. ISSN 1748-0221. doi: 10.1088/1748-0221/7/01/C01035. URL http://stacks.iop.org/1748-0221/7/i=01/a=C01035?key=crossref.2953dfd1eeb0abb88899b0f1f5bd71c0.

L. Vermeeren, R.A. Valdés Olmos, W. Meinhardt, A. Bex, H.G. van der Poel, W.V. Vogel, F. Sivro, C.A. Hoefnagel, and S. Horenblas. Intraoperative radioguidance with a portable gamma camera: a novel technique for laparoscopic sentinel node localisation in urological malignancies. *European Journal of Nuclear Medicine and Molecular Imaging*, 36(7):1029–1036, July 2009. ISSN 1619-7070, 1619-7089. doi: 10.1007/s00259-009-1100-6. URL http://link.springer.com/10.1007/s00259-009-1100-6.

J. Vesel and M. Petrillo. Improved gamma camera performance using event positioning method based on distance dependent weighting. In *IEEE Nuclear Science Conference Record*, volume 5, pages 2445–2448, 2005.

S. Vidal-Sicart, L. Vermeeren, O. Solà, P. Paredes, and R.A. Valdés-Olmos. The use of a portable gamma camera for preoperative lymphatic mapping: a comparison with a conventional gamma camera. *European Journal of Nuclear*

Medicine and Molecular Imaging, 38(4):636–641, April 2011. ISSN 1619-7070, 1619-7089. doi: 10.1007/s00259-010-1682-z. URL http://link.springer.com/10.1007/s00259-010-1682-z.

X. Wang, D. Meier, S. Mikkelsen, G.E. Maehlum, D.J. Wagenaar, B.M.W. Tsui, B.E. Patt, and E.C. Frey. MicroCT with energy-resolved photon-counting detectors. *Physics in Medicine and Biology*, 56(9):2791–2816, May 2011. ISSN 0031-9155, 1361-6560. doi: 10.1088/0031-9155/56/9/011. URL http://stacks.iop.org/0031-9155/56/i=9/a=011?key=crossref.235160b410ee4dc15a31223697a7fecc.

M. Williams, A. Goode, V. Galbis-Reig, S. Majewski, A. Weisenberger, and R. Wojcik. Performance of a PSPMT based detector for scintimammography. *Physics in Medicine and Biology*, 45(3):781–800, March 2000. ISSN 0031-9155, 1361-6560. doi: 10.1088/0031-9155/45/3/315. URL http://stacks.iop.org/0031-9155/45/i=3/a=315?key=crossref.3d050737fb8d62546cba5469b0fbf00a.

M.D. Wilson, P. Barnes, R.J. Cernik, C.C.T. Hansson, S. Jacques, L.L. Jones, P. Seller, P.J. Sellin, T. Sochi, M.C. Veale, P. Veeramani, P.J. Withers, and C.P. Youd. Comparison of the X ray performance of small pixel CdTe and CZT detectors. In *IEEE Nuclear Science Conference Record*, pages 3942–3946, 2010. doi: 10.1109/NSSMIC.2010.5874554.

S. Yamamoto, H. Watabe, Y. Kanai, M. Imaizumi, T. Watabe, E. Shimosegawa, and J. Hatazawa. Development of a high-resolution Si-PM-based gamma camera system. *Physics in Medicine and Biology*, 56(23):7555–7567, December 2011. ISSN 0031-9155, 1361-6560. doi: 10.1088/0031-9155/56/23/014. URL http://stacks.iop.org/0031-9155/56/i=23/a=014?key=crossref.d7970fc461610f2d836cb57c48eba08d.

Takayuki Yanagida. Inorganic scintillating materials and scintillation detectors. *Proceedings of the Japan Academy, Series B*, 94(2):75–97, 2018. ISSN 0386-2208, 1349-2896. doi: 10.2183/pjab.94.007.

H. Zaidi. Comparative evaluation of photon cross-section libraries for materials of interest in PET Monte Carlo simulations. *IEEE Transactions on Nuclear Science*, 47(6):2722–2735, December 2000. ISSN 00189499. doi: 10.1109/23.901179.

L. Zhang, L. Neves, J.S. Lundeen, and I.A. Walmsley. A characterization of the single-photon sensitivity of an electron multiplying charge-coupled device. *Journal of Physics B: Atomic, Molecular and Optical Physics*, 42(11):114011, June 2009. ISSN 0953-4075, 1361-6455. doi: 10.1088/0953-4075/42/11/114011. URL `http://stacks.iop.org/0953-4075/42/i=11/a=114011?key=crossref.9399450972464c6987fde3bc6b496616`.

W. Zhao, G. Ristic, and J.A. Rowlands. X-ray imaging performance of structured cesium iodide scintillators. *Medical Physics*, 31(9):2594–2605, August 2004. ISSN 00942405. doi: 10.1118/1.1782676. URL `http://doi.wiley.com/10.1118/1.1782676`.